CALCULATION OF THREE-DIMENSIONAL BOUNDARY LAYERS ON TURBOMACHINERY BLADES

by

Wanchai Asvapoositkul

A Dissertation submitted for the degree of Doctor of Philosophy

in Faculty of Engineering, University of London

Department of Mechanical Engineering

University College London

March 1995.

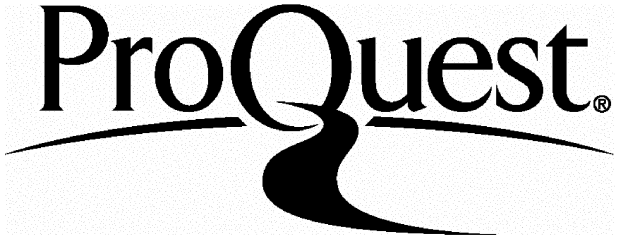

ABSTRACT

The aerodynamic behaviour of turbomachinery is dominated by viscous effects. In the design of a component for the machine, inviscid methods are normally employed. However, it is useful to cover the viscosity in the calculation to achieve a better understanding of the fluid behaviour. This feature can be analysed by using Navier-Stokes calculations or simpler and more approximate techniques such as boundary-layer calculation.

In recent years there have been a considerable number of Navier-Stokes solvers as well as boundary-layer solvers. However, Navier-Stokes methods require a large amount of computer storage and CPU time, which limits the number of grid points that can be used inside the boundary-layer. Hence, boundary-layer techniques become very attractive.

The purpose of this study is to develop a boundary-layer calculation that is efficient, accurate and simple to implement, and can be applied to flow over complex geometry such as turbomachinery blades. To account for the surface curvature and rotation, the three-dimensional unsteady boundary layer equations are expressed in generalised curvilinear co-ordinate system on the body surface with respect to a rotating frame of reference. The equations are solved numerically by using Finite Difference Approximation without employing the similarity transformation. The steady state solutions are obtained by integrating the equations in time.

Two methods, an interactive scheme and FLARE approximation scheme, are described for calculating separated flow. The concept of the interactive approach is general but its application, in this study, is limited to two-dimensional

flow. The viscous losses, expressed in term of entropy generation, is also calculated from the computed flowfield.

Computational results on a wide variety of flow situations and configurations are validated and show good agreement with analytical results and experimental measurements.

Results reveal, in general, that the method holds a practical advantage, in both speed and accuracy of computation, for solving the boundary-layer problems to which it is best suited.

ACKNOWLEDGEMENTS

I would like to express my appreciation to my supervisor, Dr. Mehrdad Zangeneh-Kazemi, for his advice, guidance and encouragement in carrying out this research. He also edited the draft of this dissertation.

I am most grateful to the Government of Thailand for offering me the grant to study at University College London (UCL). This grant is also under the agreement between the Ministry of University Affairs (Thailand) and King Mongkut's Institute of Technology, Thonburi (KMITT). It is a pleasure to acknowledge the co-operation from the Thai Government Students' Office both in Bangkok and London. Also I want to gratefully acknowledge to Professor Prida Wibulswas and colleagues at KMITT for their encouragement to me to get this grant.

A special thanks to all faculty and staff of the Mechanical Engineering Department, UCL for their help during my study. Thanks to wonderful services especially the systems manager, Mr. Mark Iline and Mr. Joe Fletcher, made it possible for me to develop the computational code.

During my stay in England, I have received a considerable help, support and friendliness from Mrs. Siranee Pollakorn, Mr. S. Chutima and friends from Thai Society UCL. I am very grateful to all of them.

Finally, a special note of gratitude goes to my family for their active support and confidence in me. Although we live so far away, we regularly contact: my father through the phone lines, my sisters through the letters and my brothers through e-mail. Sadly, my mother did not have an opportunity to see this dissertation but her kindness is still in my memory.

Wanchai Asvapoositkul
March, 1995.

CONTENTS

LIST OF TABLES

LIST OF FIGURES

NOTATION

SYMBOLS

c_f	skin-friction coefficient
c_p	specific heat at constant pressure
c_v	specific heat at constant volume
h_1, h_2	metric coefficients
H	total enthalpy
H_s	shape factor
I	rothalpy
i, j, k	index of the grid point system
k	thermal conductivity
L	characteristic length, position vector
M	Mach number
n	iteration level, time step, index of time
p	static pressure
Pr	Prandtl number $\left(\frac{c_p \mu}{k}\right)$
Pr_t	turbulent Prandtl number
r	position vector relative to the rotating axis
R	the gas constant = c_p - c_v
Re	Reynolds number
RY	grid growth ratio (Eq. 3.50)
s	outer streamline
T	temperature
t	time
U	velocity vector
u, v, w	velocity components
x, r, θ	cylindrical co-ordinate

x, y, z	Cartesian co-ordinate
α	angle between the lines on the body surface
β	angle between the ξ-axis and the outer streamline
β_w	angle between the wall streamline and the outer streamline
γ	ration of specific heats = c_p/c_v
δ	boundary layer edge
δ_ξ	entropy thickness
δ^*	displacement thickness
δ^{**}	momentum-displacement thickness (Appendix F)
$\Delta n, \Delta\xi, \Delta\eta, \Delta\zeta$	grid spacing in time, ξ, η and ζ co-ordinates
$\Delta x, \Delta y, \Delta z$	grid spacing in x, y, z co-ordinates
ε	convergence criteria
η	Blasius similarity variable
Θ	momentum thickness
μ	dynamic viscosity of fluid
μ_t	turbulent eddy viscosity
ν	kinematics viscosity
$\dot{\xi}$	entropy production
ρ	density
τ	shear stress
Ψ	wall streamline
ω	relaxation factor, safety factor
Ω	angular velocity

SUBSCRIPT

b	at the blade surface
c	crossflow direction
e	outer edge of the boundary layer
i, j, k	denoting co-ordinate direction

s	outer streamline direction
t	turbulent
w	at wall conditions
∞	upstream conditions

SUPER SCRIPT

-	time-averaged quantities
'	fluctuating quantities

CHAPTER 1
INTRODUCTION

1.1 GENERAL

The development of boundary layer has been backed to 1904 when Prandtl proposed the concept of boundary layer that was possible to analyse viscous flows, to the Mathematical Congress in Heidelberg. His paper "On the motion of a fluid with very small viscosity" marked an epoch in the history of fluid mechanics, opening the way for understanding the motion of real fluids (Tani, 1977). He divided the fluid flow about a solid body into two regions (see Fig. 1.1), firstly a very thin layer near of the body where the effects of viscosity are always important and secondly the remaining region outside this layer where the effects of viscosity may be neglected.

Navier-Stokes and Boundary Layer Methods

The viscous flow can be analysed by using Navier-Stokes (NS) calculations or simpler and more approximate techniques such as Boundary-Layer (BL) calculations.

In recent years a considerable number of Navier-Stokes solvers as well as boundary-layer solvers have been developed. The complete Navier-Stokes equations are quite difficult to solve for many reasons. From the mathematical point of view, a large number of quantities are required at each grid point. For example, in three-dimensional flow, one might need five primitive variables, two turbulence properties, and nine or more metric derivatives (McNally, 1985). To capture the viscous layers, a large number of grid points are also required. This calculation is expensive because computational time increases rapidly with the number of grid points used. Therefore, in practice, the number of grid points that

can be used inside the boundary-layer is reduced due to the limitation of computer storage and CPU time. In order to model the effect of viscous layers at the wall and to avoid the need for a very fine mesh near the wall, most of the Navier-Stokes methods employ an empirical wall function. The wall function can be roughly thought of as a solution to the boundary-layer momentum equation using Prandtl's mixing-length turbulence model when convective and pressure gradient terms are insignificant (Anderson et al 1984). Therefore, the wall function can be used in circumstances where the mesh is too coarse to resolve down to viscous layers. This limits the ability of Navier-Stokes methods to accurately predict the viscous effects near the wall.

In application of boundary-layer methods, one of its fundamental concepts is that the effects of viscosity are always important in a very thin layer near the body surface and may be neglected in the remaining region outside this layer. This situation happens when the Reynolds number is very high. As a consequence of this, all viscous terms containing derivatives parallel to the body surface are dropped from the Navier-Strokes equations since they are substantially smaller than viscous terms containing derivatives normal to the wall. Therefore, boundary-layer equations may be considered as an approximate form of the Navier-Strokes equations. Because of their simplicity and the application of no-slip condition (i.e. velocities are zero at the wall), they can resolve the velocities in the viscous layer. The boundary-layer equations are also simpler in form than the Navier-Stoke equations but they are still difficult to solve. One difficulty is to find an appropriate discretization scheme or a marching scheme to satisfy the boundary conditions. The implementation of the marching schemes contributes to the accuracy and efficiency of the solutions, but raises a number of important issues that needs to be solved, such as method of solution. Details of the numerical solution will be discussed in chapter 3.

Three-dimensional boundary layers in turbomachinery

The flow through turbomachinery is dominated by three-dimensional unsteady and viscous effects. In the design of a component for the machine, inviscid methods are normally employed as they are quite efficient computationally. On the other hand, the implementation of viscous flow calculations in turbomachinery is not yet sufficiently well developed to be used for design purposes (Denton, 1986). However, the viscous methods can provide a very good qualitative picture of the flow such as secondary flows in a rotor. This will reflect the flow phenomena in turbomachinery that are not only three-dimensional but also extremely complex because of the interactions between curvature and rotation effects, pressure gradients and turbulence levels. Therefore, several complicating features have also to be considered in the case of three-dimensional problems. These features are presented in the following paragraphs.

In two-dimensional flow, the spanwise distance is assumed to be of infinite length and the flow is identical in that direction. With these simplifications, the streamlines of the outer flow on the plane surface are straight lines perpendicular to the leading edge. A two-dimensional boundary layer flow over a wing section is shown in Fig. 1.2. In this flow, the velocity profiles are identical in the y-direction. However, in three-dimensional flow, the velocity profiles are not identical in the spanwise direction and the fluid flow naturally occurs on curved surfaces or curved external flow. The shape of the body surfaces and the additional component motion make the streamlines of the outer flow curve when observed in a plane parallel to the body surface (see Fig. 1.3). This natural curved streamline can be maintained only when the centrifugal force on the fluid is balanced by the pressure gradient in the spanwise direction. Inside the boundary-layer the pressure gradients remain the same and the fluid velocity decreases due to viscosity. To maintain the balance, the streamlines inside the boundary-layer must be more

highly curved. This limiting streamline is also shown in Fig. 1.3. This gives rise to a velocity component within the boundary-layer normal to the external streamline. This velocity component is called the "secondary flow". It is responsible for transporting the low momentum fluids. Therefore, we can expect that the total velocity is twisting across the boundary layer. An example of three-dimensional boundary layer velocity profile is shown in Fig. 1.4.

The other feature of a three-dimensional boundary-layer is that the secondary flow may change sign during the computations. This means that the limiting streamline is also changed both in direction and magnitude. Johnston (1988) reported that three-dimensional separation occurs when the limiting streamline approaches the crossflow direction. Therefore the viscous flow calculation should have a capability to deal with separated flow since flow in the turbomachinery frequently tends to separate either as a result of free stream separation or due to the intensity of the secondary flow.

1.2 STATEMENT OF PROBLEM

The state of the art in turbomachinery has advanced to the point where further significant improvements will have to come from an increased knowledge of the fluid mechanics. For this reason, in recent years increasing attention and effort have been devoted to experimental and computational investigations on flow phenomena, especially viscous effects, in the machines. The fluid flows in these circumstances are three-dimensional and as a consequence the boundary-layer computations have to be treated as three-dimensional as well. Modern computers offer the possibility of solving complicated systems of partial differential equations numerically. As a result, a number of numerical methods have been developed and are still being developed. The calculations reported to date for three-dimensional flows have employed the usual direct method for

solving the boundary-layer equations. This means that it is not applicable in the case of separated flows. Little is known about the applicability of the inverse boundary-layer approach for fully three-dimensional flows (Anderson et al 1984).

1.3 THE OBJECTIVES OF THE STUDY

The main objective of this study is to develop computational procedure that gives good qualitative predictions of three-dimensional boundary-layer that can be applied to flow over complex geometry such as turbomachinery blades. The proposed method is based on compressible, three-dimensional unsteady, turbulent boundary-layer equations and the solutions are established without employing the similarity transformation. It therefore becomes clear that this method is quite general.

1.4 SCOPE AND LIMITATION

The work will solve unsteady three-dimensional boundary-layer of the rotating cylindrical co-ordinate system as well as Cartesian co-ordinate system by using Finite Difference Approximation. The eddy-viscosity expression used for this study is Baldwin-Lomax model. In the method to be described the effects of the boundary layer on the inviscid flow are represented by the interactive boundary-layer method. FLARE approximation scheme is also described for calculating separated flow.

Among the new significant aspects of the present work are: (1) the treatment of the three-dimensional boundary-layer for application to turbomachinery blades in both direct and inverse modes as well as stationary and rotating blades; (2) the use of viscous-inviscid interaction, with the interactive boundary-layer model, (3) the ability to employ "non-similarity method" to probe

the accuracy of the solutions, and finally; (4) evaluation of the effect of boundary-layer induced loss during passage through turbomachines.

1.5 ORGANISATION OF THE THESIS

The rest of this thesis is organised as follows. Chapter two is devoted entirely to review of developments in the boundary-layer method. The review covers topics in methods of solving boundary-layer equations, numerical methods for the equations, methods applicable to turbomachinery blades, turbulence modelling and loss due to boundary-layer. The next chapter presents the calculation procedure for compressible, three-dimensional unsteady, turbulent boundary layers. Key topics here include governing equations, turbulent model, transformation, discretization and numerical solution algorithm. This mainly deals with the direct implementation of the boundary layer equations. The inverse method for the case of separation flows is presented in chapter four. Three methods, FLARE approximation scheme, conventional inverse scheme and interactive scheme are discussed. The first section of the chapter focuses on FLARE approximation scheme. Then a conventional scheme is presented. In this case, we prescribe displacement thickness to solve the equations. This is because we can interact directly with the interactive boundary-layer model that is presented in the next section. The final section describes loss generation in three-dimensional boundary-layer. Chapter five mainly deals with validation of the boundary layer method. The validations covered a wide variety of flow situations and configurations to show that the code is efficient, accurate and simple to implement. The last chapter consists mainly of conclusions and recommendations for further study. The equation sets derived for preliminary consideration and design have been relegated to the appendixes.

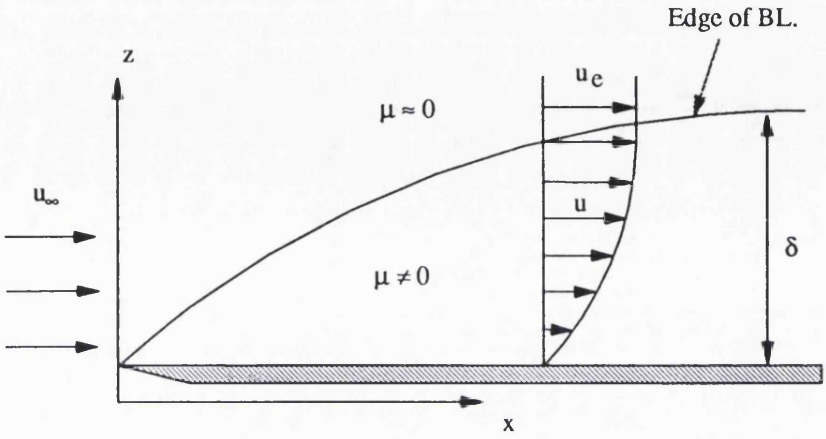

Fig. 1.1 A boundary layer on a flat plate

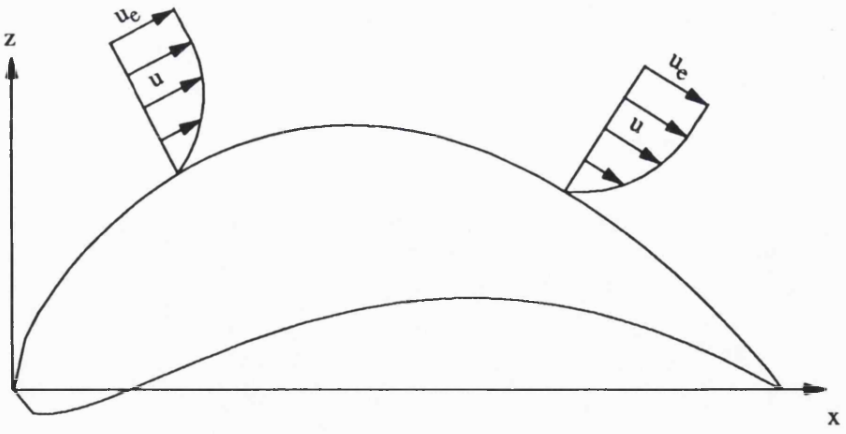

Fig. 1.2 Two-dimensional boundary layer flow

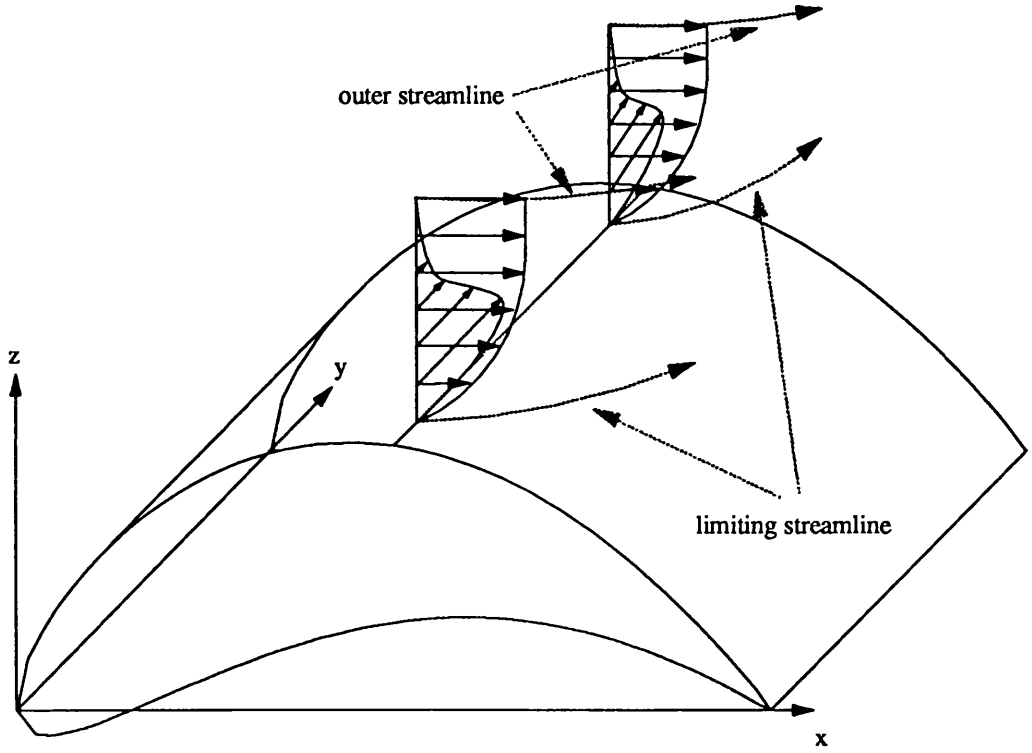

Fig. 1.3 Three-dimensional boundary layer flow

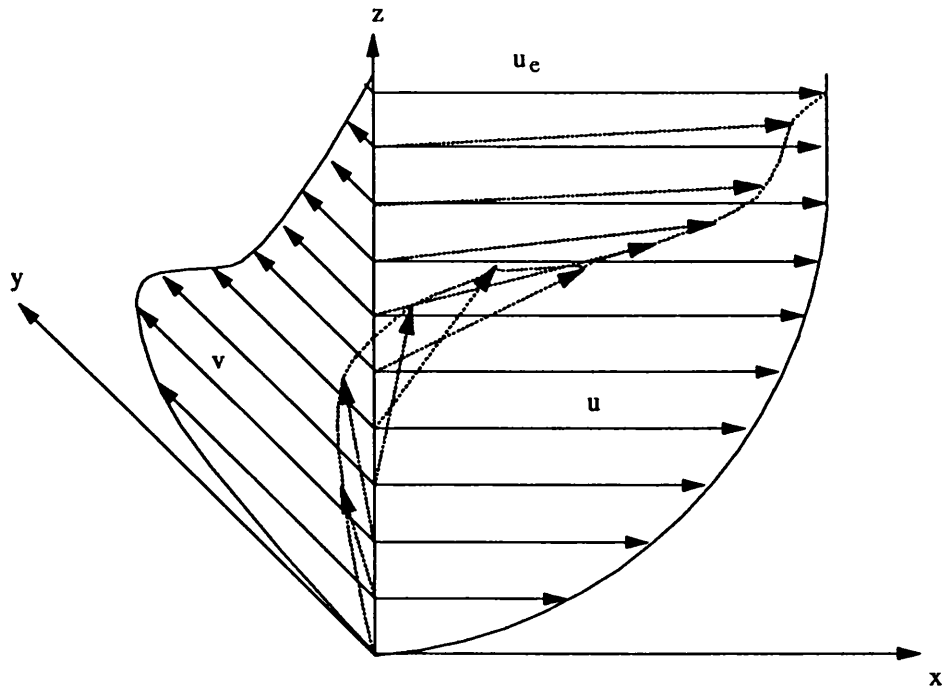

Fig. 1.4 Three-dimensional boundary layer velocity profile

CHAPTER 2
LITERATURE SURVEY

2.1 INTRODUCTION

This chapter gives firstly a brief outline of prediction methods of boundary-layer problems followed by a description of current developments. The review is drawn from a broad structure of the problems and then concentrated on methods applicable to turbomachinery. To make the text readable, the author divides the review into 5 areas of considerations, methods of solving boundary-layer equations, numerical methods for the equations, methods applicable to turbomachinery blades, turbulence modelling and loss due to boundary-layer.

2.2 METHODS OF SOLVING BOUNDARY-LAYER EQUATIONS

In the early stage of solving boundary-layer equations especially when computers were not invented, the solutions were obtained by using simplifications or assumptions. Most early solutions of boundary-layer equations were based on some forms of similarity law using which the partial differential equations of the boundary layer could be reduced to an ordinary differential equation by the use of suitable substitutions. For example, Blasius used it to find the solutions for flow on a flat plate in 1908. In his transformation the independent variables (e.g. x, z, u, w) in the boundary-layer equations are replaced by a function that relates to the Blasius similarity variable (i.e. $\eta = z\sqrt{\frac{u_e}{\upsilon x}}$). Thus the boundary-layer equations are reduced to a form that can be solved with only one function. The application and numerical solutions of this type of transformation for three-dimensional flow over a flat plate can be seen in Appendix C.

The Blasius similarity was extended by Falkner and Skan in 1930 to the case in which the free-stream velocity varies in proportion to x^n. This type of solution can illustrate the flow problem both adverse (decelerating free-stream velocity, i.e. $n<0$) and favourable (accelerating free-stream velocity, i.e. $n>0$) pressure gradients depending the value of n.

In practice, the free-stream velocity will not be characterised by single value of n and the velocity profiles will not be similar at all points along the surface. The solution of the general flow presents considerable numerical and analytical difficulties. This fact has led to the development of calculation methods for finding the solution of boundary-layer equations. Methods of solving the equations fall into two main categories, integral methods and finite difference methods.

Integral method: By integrating the boundary-layer equations with respect to the normal distance to the surface, the partial differential equations of the boundary layer are reduced to one or more ordinary differential equations. This resulting set of ordinary differential equations usually consists of momentum thickness (Θ), displacement thickness (δ^*) and skin friction coefficient (τ_w). In order to close the equations these parameters are then related to form an auxiliary equation that provides a good estimate of flow inside the boundary layer. This auxiliary equation varies depending on the flow situation and assumptions, and may be obtained from direct measurement or empirical relations.

Integral methods can be applied to a wide range of both laminar and turbulent flows. There are many approaches and they cannot all be considered here. For two-dimensional incompressible laminar boundary-layer with pressure gradient, the reader is referred to a work by Thwaites (1949), and for turbulent flow by Truckenbrodt (appeared in Schlichting (1979)), and Das (1988). Reviews

of the methods are given by many authors (e.g. Schlichting (1979) and White (1991)).

Integral methods are simple in terms of formulation and require considerably less computational effort than finite difference methods. They can provide reliable estimates of displacement thickness, momentum thickness, wall shear and skin friction. These parameters are required in most engineering applications and design.

However, the application of the integral methods is not straightforward since the accuracy and reliability of the methods are limited by the available auxiliary equation. For application to turbomachinery, the process of finding suitable relations for the model is a highly complex and inherently unsteady phenomena and its direct measurement is difficult.

Finite difference method: By this method, the boundary layer equations are solved directly in finite-difference form. In fact, any problems that can be solved by an integral method can also be solved by a finite-difference method. A summary of many methods, principally differential methods, was prepared by Cebeci and Smith (1974), and White (1991). Simple methods and numerical considerations related to the finite difference solution of the boundary layer equations were described in two excellent books by Anderson et al (1984) and Fletcher (1991).

In recent years, the finite difference methods are preferred for many reasons (Anderson et al (1984) and Johnston (1988)). First, finite difference methods are, potentially, more generally applicable than integral methods. Finite difference methods are flexible and easy to adapt when boundary or other problem conditions are changed. Second, the accuracy of integral methods is limited by the

available auxiliary equation. Third, powerful computers are available. Integral methods generally provide overall predicted characteristics of the boundary-layer, e.g. displacement thickness, momentum thickness and skin friction, rather than details of the boundary layer flow. This technique makes the boundary-layer equations require considerably less computational effort due to simple forms of the equations. Finite difference methods on the other hand require larger computational resources and can resolve the boundary-layer equations into the flow inside the layer as well as the overall prediction of the flow. Therefore the finite difference methods are admirably suited to use on modern computers.

Comparisons and reviews dealing with the numerical solutions of three-dimension boundary-layer solvers (both integral and finite difference methods) can be seen in Lemmerman and Atta (1980), and Humphreys and Lindhout (1988).

Transformation of Boundary Layer Equations: One of the efficient ways of solving the boundary layer equations is to transform the equations before attempting to solve them. This technique is widely used especially in the finite difference method because it may eliminate singularities at stagnation points or leading edges, and stretch the co-ordinate normal to the surface in order to account for boundary layer growth. Many authors have successfully computed the boundary layer problems using Dorodnitysn-Howarth, Stewartson, Probstein-Elliott, Levy-Lees transformations. Details of these transformations are given in Stewartson (1964), Cebeci and Smith (1970), and Vatsa (1985).

2.3 NUMERICAL METHODS FOR THE BOUNDARY-LAYER EQUATIONS

The methods for solving boundary-layer equations have a common technique that the partial differential equations of the boundary layer are

transformed to one having an algebraic representation (Anderson et al 1984). The methods differ only in the implementation of the marching schemes. Some of the widely used schemes for the numerical solution of the boundary-layer equations are presented in the following paragraphs.

An explicit scheme: By using this scheme, the solutions of boundary-layer equations may be computed directly at each grid point downstream. Since only one unknown appears in each equation, this method is simple. Unfortunately, this standard scheme is conditionally unstable through the von Neumann analysis. A modified explicit scheme called the DuFort-Frankel scheme seems more stable than the standard explicit scheme because it requires information from the two previous streamwise stations. For example, the streamwise derivative first-order derivative in the momentum equation is represented by

$$\frac{\partial u}{\partial x} = \frac{\left(u_{i+1,k} - u_{i,k}\right)}{\Delta x} + 0(\Delta x) \qquad 2.1$$

in the standard explicit method and by

$$\frac{\partial u}{\partial x} = \frac{\left(u_{i+1,k} - u_{i-1,k}\right)}{2\Delta x} + 0(\Delta x)^2 \qquad 2.2$$

in the DuFort-Frankel method. The finite difference grid for both methods is shown in Fig. 2.1.

Pletcher (1969) developed the DuFort-Frankel calculation procedure for turbulent boundary-layer flows. Prandtl's mixing-length concept was used to express the turbulent shearing stress. The predictions agree well with experimental data for both favourable and adverse pressure gradients of flows over a flat plate. The method is stable and no iterative procedures are required. However the

explicit scheme is no longer widely used for boundary layers due to the restrictive stability constraint.

An implicit scheme: Unlike the explicit scheme, the boundary-layer equations of an implicit scheme are formed in a system of simultaneous equations for the unknown functions at each downstream step. This system of equations may be similar to that shows in Fig. 2.2. To obtain the solutions, therefore, the equations must be solved simultaneously by either iteration or matrix inversion. The implicit scheme for boundary-layer problems is unconditionally stable through the von Neumann analysis and provides the basis for several boundary-layer calculations such as the Crank-Nicolson scheme, the Keller's box scheme, the Krause zig-zag scheme.

The Crank-Nicolson scheme: The boundary-layer equations of simple implicit scheme have been formulated as a first-order accurate for the grid arrangement. To achieve higher-order accuracy, all derivatives can be approximated by simple centred differences and two-point average, and the centre of discretization is located at the point $(i+\frac{1}{2},k)$. This type of scheme is called the Crank-Nicolson scheme. A typical grid arrangement is shown in Fig. 2.3. Examples of a fully implicit and the Crank-Nicolson scheme for compressible laminar boundary-layer equations may be seen in Anderson et al (1984).

The Crank-Nicolson procedure can be extended for three-dimensional boundary-layer equations (Anderson et al (1984) and Fletcher (1991)). In this scheme the discretization is centred at $(i+\frac{1}{2}, j+\frac{1}{2}, k)$. The grid arrangement of the scheme is shown in Fig. 2.4. The use of this Crank-Nicolson scheme is limited only when the sign of the crossflow components does not change due to the restriction of zone of dependence concept. The detail of zone of dependence concept will be presented in chapter 3.

The Keller's box scheme: Keller (1978) developed a scheme that is similar to the Crank-Nicolson scheme. The discretization is centred at $(i+\frac{1}{2}, k+\frac{1}{2})$ and the first derivatives are approximated by centred differences and two-point average. The grid points can be constructed involving only the four corners of a grid box. A typical box scheme for boundary-layer equations is shown in Fig. 2.5.

Keller and Cebeci (1972) employed the Keller's box scheme to predict the boundary-layer on laminar flows, turbulent flows and wake flows. The scheme is unconditionally stable but the resulting equations are highly implicit and non-linear. Newton's method and a block tridiagonal system are employed to solve them. In order to improve the accuracy of the numerical solution and reduce the computer time, Richardson extrapolation is also employed. The investigation shows that the scheme is very efficient and is applicable to three-dimensional flows.

The Krause zig-zag scheme: An alternative implicit procedure for three-dimensional flows is the Krause zig-zag scheme. It has been widely used for flows in which the crossflow velocity (v) component changes sign. The centre of discretization is at the point $(i+\frac{1}{2}, j, k)$. In this scheme the y-derivative is approximated by the finite difference relation

$$\left.\frac{\partial v}{\partial y}\right|_{i+\frac{1}{2}} = \frac{v_{j+1} - v + v_{i+1} - v_{i+1,j-1}}{2\Delta y} \qquad 2.3$$

Fig. 2.6 shows a computational grid for the Krause zig-zag scheme of the three-dimensional boundary-layer flows where x is streamline direction with velocity u and y is the crossflow direction with velocity v. The restriction on the meshes (e.g. Δx and Δy) is imposed if crossflow velocity (i.e. v) is negative due to

zone of dependence concept. The stability constraint of this scheme is (Fletcher 1991)

$$u>0, \qquad \left|\frac{v\Delta x}{u\Delta y}\right| \le 1 \qquad 2.4$$

The Kitchens scheme: The Crank-Nicolson and Krause zig-zag schemes can be employed in three-dimensional boundary-layer flows but there is a restriction on Δx to satisfy the zone of dependence concept. Kitchens et al (1975) employed an implicit scheme in their three-dimensional calculation. In this scheme the discretisation is centre at $(i+\frac{1}{2}, j, k)$. The approximation for x-derivative is

$$\frac{\partial u}{\partial x} = \frac{\left(2u_{i+1} - u_{j+1} - u_{j-1}\right)}{2\Delta x} \qquad 2.5$$

The approximation for y-derivative is

$$\frac{\partial u}{\partial y} = \frac{u_{j+1} - u_{j-1}}{2\Delta y} \qquad 2.6$$

The grid configuration of this scheme is shown in Fig. 2.7. The prediction on three-dimensional boundary-layer over flat plate shows that this scheme seems relatively insensitive to violations in the zone of dependence constraint. This means that in some schemes the restriction on grid size (e.g. Δx) may be relaxed. In general, the violations of the zone of dependence rule should be avoided to secure the numerical results.

An upwind scheme: An upwind scheme differs from the schemes described earlier in that this scheme is based on bi-directional marching technique. It's marching scheme changes according to the local values of velocities (e.g. u,

v). This is because the stability constraints for three-dimensional boundary-layer flow depend upon the local values of velocities. This scheme is less straightforward to implement than simple marching schemes but it is attractive since it provides stable solutions when the crossflow is reversed (e.g. $v<0$). Many authors (e.g. Johnston (1990), Steger and Van Dalsem (1985), and Vatsa (1985)) have successfully computed the three-dimensional boundary-layer using this scheme. Detail of the scheme will be discussed in discretization section of chapter 3.

Time marching scheme: An alternative approach to solve the boundary-layer equations is time-marching scheme. The scheme can be approximated for both unsteady and steady-state solutions. The principle and numerical methods are presented in Bradshaw et al (1981), Steger and Van Dalsem (1985), and Warsi (1992). The technique is similar to those of space-marching scheme, but differs in the governing equations in which the unsteady equations are integrated in time. The scheme is not too complex and requires reasonable storage (Lakshminarayana 1991). The solutions can be obtained accurately and robustly.

Van Dalsem and Steger (1984 and 1985) proposed a finite difference method that solved the unsteady three-dimensional boundary-layer equations in the time-accurate or relaxation mode. A complex similarity transformation is avoided and viscous-layer growth is scaled out by co-ordinate transformation. They employ an upwind scheme for spatial derivatives in the streamwise and spanwise directions. By this way, the complex space-marching scheme may be neglected.

Separation and viscous-inviscid interaction: The boundary layer equations have a singularity when there is a flow reversal. One way of dealing with the singularity is by neglecting the product of the streamwise velocity

component and it's streamwise derivative in the governing equations wherever the velocity becomes negative (i.e. the so-called FLARE approximation). This is only relatively accurate for small reverse flow region, usually less than 10% of the local free stream velocity (Anderson et al (1984)). Another way is to solve the equations in the reverse mode by prescribing either displacement thickness or wall shear stress.

In general the boundary layer and inviscid calculations must be iteratively coupled. The surface velocity distribution from the inviscid calculation is used as an input to the boundary layer calculation to determine the displacement thickness. To estimate the effect of the displacement, the inviscid flow solution can be obtained by the use of a small disturbance approximation. This calculation consists of two parts treated alternately: the calculation of the boundary layer (viscous region), and the calculation of the outer flow (inviscid region). This interaction has been widely employed to make engineering predictions of viscous effects in many problems.

There are two methods of combining viscous-inviscid interaction:

1. **The relaxation formula:** In this method, the interaction calculation is initiated by prescribing displacement thickness (δ^*) in the interaction region. For the prescribed distributions of $\delta^*(x)$, solutions for outer flow (u_e) are divided in two parts, one is from a inviscid solver (e.g. Euler method) and the other is from viscous solvers (e.g. Boundary-layer method). Viscous-inviscid interaction is achieved by matching these two solutions. The difference between outer flow calculated both ways (viscous and inviscid solutions) can be used as a potential to calculate an improved distribution for displacement thickness. This iterative updating of the solutions can be effectively carried out by the methods successfully demonstrated by Carter (1978) and, Kwon and Pletcher (1986a, b). The flow chart for this method is presented in Fig. 2.8.

2. **The interactive boundary-layer model**: Interaction between the inviscid and viscous flows is achieved by blowing-velocity (e.g. $w_n = \frac{d}{dx}(u_e \delta^*)$) distribution that is linked to the displacement thickness distribution through the Hilbert integral. This method was developed by Veldman (1981). Cebeci et al (1992) suggested that the method can be viewed as an empirical formula that provides a better approximation to the link between inviscid and viscous flow equations than that the relaxation formula used by Carter (1978) and, Kwon and Pletcher (1986a). The method was applied to airfoil by (subsonic flow) Veldman (1981), and (turbulence flow) Cebeci et al (1992). Recently Jang et al (1991), extended the interactive approach to the calculation of blade boundary layers and compared its predictions with Navier-Stokes calculations. The detail of this method is discussed in chapter 4 and its flow chart is shown in Fig. 4.4.

2.4 METHODS APPLICABLE TO TURBOMACHINERY BLADES

Lakshminarayana (1991) has reviewed and assessed various computational fluid dynamic techniques for the analysis and design of turbomachinery. He recommends that the three-dimensional boundary-layer equations for turbomachinery flow should be written in a curvilinear system and a rotating cylindrical co-ordinate. These will enable the equations to account for the effects of rotation and surface curvature.

In the following paragraphs we present boundary-layer and Navier-Stokes methods for calculating turbomachinery flows.

Boundary Layer Methods

Lakshminarayana and Govindan (1981) developed an integral method for predicting the gross properties of the boundary-layer in turbomachinery blades. The governing equations are based on the incompressible three-dimensional boundary layer of rotation curvilinear system. The integral equations are reduced to two first-order partial-differential equations by using a power law profile for velocities and a skin friction relation based on experimental data. The method uses Head's entrainment equations as a closure model. The numerical solution is compared with the cascade, inducer, compressor, and fan rotor and shows very good agreement in all cases. However, the code is inaccurate if there is a flow reversal.

Karimipanah and Olsson (1992) predicted the three-dimensional turbulent boundary-layer development on a turbomachinery blade and used integral momentum technique. The system of equations is written in an orthogonal curvilinear system. The entrainment equation by Michel is used as an auxiliary equation. The calculations show the influence of rotation and compressibility on the boundary-layer parameters. Momentum thickness and shape factor increase with increasing rotation and decrease when compressible flow is taken into account.

Thompkins and Usab (1982) considered a finite difference method for quasi-three-dimensional boundary-layer on rotating blade rows. The three-dimensional boundary-layer equations are written in an orthogonal curvilinear co-ordinate system and assumed that gradients of all flow properties in the crossflow direction are zero. The Keller's Box scheme is employed to predict the boundary-layer. The results of the calculation are verified to a NASA Low Aspect Ratio transonic compressor stage and show that a rotor performance is influenced by the three-dimensional boundary-layer especially for separated flow.

Yamazaki (1981) derived the three-dimensional boundary-layer equations in a general non-orthogonal co-ordinate system for rotating cylindrical co-ordinate system. His set of equations has been applied to calculate the boundary-layer on propeller blades by Groves and Change (1984) and Oshima (1994).

Groves and Change (1984) predicted the viscous effects on rotating propeller blades by using finite difference approach to approximate the three-dimensional boundary-layer equations. The Keller box scheme is used but the characteristic box scheme is used instead when the crossflow is reversed. The eddy-viscosity factor is defined by applying the Cebeci-Smith model for turbulent flow. Computed results are presented for several blade geometries. Overall, the predicted boundary-layer parameters are shown to give reasonable agreement with experimental data.

Oshima (1994) evaluated the viscous effect on propeller performance by using the three-dimensional boundary-layer theory. The boundary-layer equations are presented in a non-orthogonal co-ordinate system which rotates with the blade. The turbulent terms are defined by an algebraic eddy-viscosity formulation. The system of equations is solved numerically using the finite volume method. The computation is verified with local flows near a propeller blade surface. These flows were measured in the cavitation tunnel by using 3-component Laser Doppler Velocimeter. Calculated velocity profiles in the boundary layer show good agreement with the measured ones.

Vatsa (1985) presented a fully three-dimensional boundary method. The governing equations are written in non-orthogonal body surface and solved numerically by using a finite difference approach. In order to capture the viscous-layer growth, the Levy-Less transformation is introduced in the system of

equations before solving them. He employed a first-order formulation for spatial derivatives and an upwind scheme in the crossflow direction (to capture flow reversal). The resulting linear algebraic equations are solved using a block tridiagonal solver. The predicted viscous flows over a turbine endwall and airfoil suction surfaces are in good agreement with the experimental data.

Anderson (1987) applied the method due to Vatsa for the calculation of heat transfer and streamline flow patterns. He has used experimental surface pressure to solve the Euler equations at the surface. These solutions are used as boundary conditions in the boundary-layer solver in order to obtain the complete edge flow conditions. Solutions for three-dimensional boundary-layer flow over the endwall and suction surface of a stationary turbine cascade and for the pressure surface of a rotating turbine blade are presented and evaluated with experimental data. Predictions show good agreement with the experimental data.

Navier-Stokes Methods

In the current survey, there are a number of studies which have been done to develop a technique to capture viscous flows in turbomachinery by using the Navier-Stokes equations. Some of the Navier-Stokes methods will be discussed in the following.

Three-dimensional inviscid calculations for turbomachinery are now well developed but three-dimensional viscous flow calculations are not yet sufficiently well developed to be used for design purposes. Denton (1986) suggested that there is scope for an intermediate type of method in which a highly developed and comparatively efficient inviscid method is coupled with a simple approximated viscous method. The approximated viscous method is obtained when the viscous terms in the Navier-Stokes equations are replaced by a body force in the momentum equations. The method has been applied to compressor and turbine

blade rows, both rotating and stationary, and good results are obtained. However, it is recognised that many more grid points will be necessary to get accurate solutions by such a method.

Dawes (1987) investigated a three-dimensional viscous compressible flow in turbomachinery by using the Navier-Stokes equations. The unsteady equations are written in an integral form and solved numerically by finite volume formulation. The eddy viscosity (μ_t) is given by Baldwin-Lomax model. The steady state solutions are obtained by applying a multigrid algorithm to accelerate the convergence. This method is applied to the high-speed centrifugal compressor rotor. Computations of the entropy generation rate throughout the flowfield shows that the dominant loss generation is very near to the shroud. The secondary flows are responsible for transporting the low momentum fluid.

Ng and Dawes (1992) developed a technique to capture the viscous effect near the wall of turbomachinery problems using Navier-Stokes equations. The basic concept is to take a quasi-3D Navier-Stokes or Euler solver on a coarse mesh (the "outer code") and couple it to a 2-D space marching parabolised Navier-Stokes solver on a finer sub-mesh (the "inner code"). The FLARE approximation is employed when the flow is reversed in the inner code. The inner and outer codes are coupled in an analogous way to a multigrid method. This technique has been applied to compute viscous flow over a compressor cascade and a turbine cascade, and fairly good correlation has been obtained with experimental data.

Arnone and Swanson (1993) presented a method for solving the Reynolds-averaged full Navier-Stokes equations. A finite-volume approach is applied to discretize the two-dimensional unsteady Navier-Stokes equations. Solutions are advanced in time by a four-stage Runge-Kutta time-stepping scheme

with convergence accelerated to steady state by local time stepping and a full multigrid method. The Baldwin-Lomax eddy-viscosity model is used for turbulent flow. In order to validate the method for turbomachinery applications, computations were performed for bicircular arc cascade and gas turbine rotor blade. Comparisons with experimental data show that the code is an accurate viscous solver and can give very good blade-to-blade predictions for engineering applications.

Liu and Jameson (1993) solved the three-dimensional compressible Reynolds-averaged Navier-Stokes equations by using a finite volume scheme. A multigrid method is used to accelerate convergence. The eddy-viscosity is specified by using the Baldwin-Lomax model. The method has been applied to a three-dimensional low-pressure turbine cascade. The results gave reasonably good agreement when compared with inviscid solutions and experimental data.

2.5 TURBULENCE MODELLING

For turbulent flow, a proper turbulence model should be incorporated into the boundary-layer solvers to predict the results accurately. Turbulence is a property of the flow rather than that of the fluid, hence, empirical correlation is employed to represent the variation of eddy viscosity inside a boundary layer. Turbulence modelling may be classified as follows (White (1991)).

1. Algebraic models
2. One-equation models
3. Two-equation models
4. Reynolds Stress Models (RSM)

Algebraic models

An algebraic turbulence model requires no additional differential equations to be solved. The eddy viscosity distribution is specified in two parts, the inner region and the outer region. Examples of this model are the Cebeci-Smith model and the Baldwin-Lomax model. They are used by many existing calculation methods and seem to be the most popular class of turbulence models (Humphreys and Lindhout (1988)). Lakshminarayana (1991) suggested that the algebraic eddy-viscosity model is strictly valid only for two-dimensional "simple shear flows". He also concluded that:

1. The model is adequate for two-dimensional compressible flows with a mild pressure gradient.

2. The model is suitable for three-dimensional boundary layers with small cross flows.

3. The model is not valid for flows with curvature, rotation, or separation.

4. The model is not valid for pressure or turbulence-driven secondary flows and when abrupt changes in strain or shear rate are presented.

5. The model cannot accurately predict shock-induced separated flow.

One-equation models

In one-equation model, the turbulent eddy viscosity is evaluated by a model of turbulent kinetic energy (k). This model solves only one partial differential equation, therefore, it is less computationally intensive compared with two-equation model.

The use of one-equation models in the 1968 Stanford Conference showing that the results were satisfactory but, apparently, no better than the best algebraic methods that merely used a model for eddy viscosity (White (1991)). The implementation of one-equation model is extremely difficult for extending a

length-scale correlation to complex flows (Lakshminarayana (1991)). These are the reasons why a one-equation model is not presently popular.

Two-equation models

In the two-equation model, the turbulent kinetic energy (k) and dissipation (ε) equations are solved to calculate turbulent eddy viscosity. Lakshminarayana (1991) summarised the model as follows.

1. The k-ε model is much superior to algebraic models.

2. The k-ε model is accurately predicted for most two-dimensional flows.

3. The k-ε model is not good for three-dimensional flows with high cross flows, swirl, rotation, curvature and shock-induced separation. This is because the model assumes an isotropy and low Reynolds number formulation near the wall.

Sondak (1995) developed a method for the application of wall functions to generalised curvilinear co-ordinate systems with non-orthogonal grids. The method has made the use of wall functions and the k-ε turbulent model to accurately predict the viscous effects near the wall in low-Reynolds number models. It has been tested on a flat plate with a non-orthogonal grid and a prolate hemispheroid with an orthogonal grid. The results are compared with experimental data and Baldwin-Lomax model. The k-ε model with the wall function gave good results for both the fine-grid and coarse-grid cases.

Ekaterinaris and Menter (1994) tested one- and two-equation eddy-viscosity models for unsteady massively separated flow. An implicit numerical scheme is used for the integration of the compressible, Reynolds-averaged Navier-Stokes equations. These turbulent models are tested for steady separated flow and for unsteady flow over oscillating airfoils. The selected models include the Baldwin-Barth (B-B) model and the Spalart-Allmaras (S-A) model for one-equation models, the k-ε, the k-ω and the shear stress transport (SST) k-ω models

for two-equation models. The results showed that for the light-stall case the S-A model did not yield sufficient separation and underpredicted the extreme values of the unsteady loads (lift coefficient c_l, drag coefficient c_d, and pitching moment coefficient c_m). The B-B model overpredicted the values for the light-stall case and the attached flow cases. The standard k-ε and the k-ω models did not predict separation even for the deep-stall case. The SST k-ω model gave good predictions for the attached and the light-stall cases.

Reynolds Stress Models (RSM)

RSM is potentially the superior model since it provides a more realistic physical simulation of turbulent flow. RSM is intended to account for complex turbulent effects, such as surface curvature and rotation, in three-dimensional layers. However, the modelled Reynolds stress equations are extremely complicated to solve for a three-dimensional flow since there are about 10-20 transport equations involved (Lakshminarayana (1991)). Zhang and Lakshminarayana (1990) modified a model in conjunction with the k-ε equations. This model is called an algebraic Reynolds stress model (ARSM). ARSM simulates the turbulent stress more realistically by relating the properties to local conditions. This model is efficient and inexpensive and can predict important features of flow in a turbomachinery (e.g. rotation and curvature effects). Therefore ARSM may be used to illustrate the ability of boundary layer codes to predict complex three-dimensional boundary layers.

2.6 LOSS DUE TO BOUNDARY-LAYER

The aerodynamic behaviour of turbomachinery is dominated by viscous effects. The viscous flow, from boundary layer methods or Navier-Stokes methods, can be used to predict the terms such as the boundary-layer blockage and secondary flow. Before taking these quantitative predictions for

turbomachinery design purpose, one should understand the process of loss generation. Denton (1993) showed that the performance of turbomachines is directly related to rate of entropy production in the flowfield. Therefore he preferred to use the word "entropy" rather than the word "loss". The understanding of this process can identify loss sources and its mechanism, and improve design of turbomachines (Dawes (1987)). Denton and Cumpsty (1987) divided the sources of entropy into viscous effects in boundary-layer, viscous effects in mixing process, shock waves, and heat transfer across temperature difference.

Entropy generation in Boundary layers: Denton and Cumpsty (1987) has reviewed the entropy generation in boundary layers in the following way. The entropy is generated in the boundary layer because of viscous friction. Velocity inside the layer changes rapidly near the surface, therefore most of the entropy generation is concentrated in the inner part of the layer and is about 90 percent of the entropy generation in a boundary layer. The total rate of entropy creation is proportional to the area under the τ-v curve. For two-dimensional boundary layer, it may be written as

$$\dot{\xi} = \int_0^{\delta} \frac{1}{T} \tau dv \qquad 2.7$$

$\dot{\xi}$ is the rate of entropy production per unit surface area, T is temperature, τ is shear stress and v is velocity across the boundary layer thickness (δ). He also presented the entropy generation in terms of the dissipation (C_d,non-dimensional form of $\dot{\xi}$) and an entropy thickness (δ_ξ).

$$C_d = \frac{T}{\rho v^3} \dot{\xi} \qquad 2.8$$

$$\delta_\xi = \frac{T_e}{\rho_e v_e^3} \int_0^\delta \rho v (\xi - \xi_e) dz \qquad 2.9$$

The results from the calculations can be used as guidelines and as an aid to understanding the physics of the flow. The principle of entropy production will be discussed in detail in chapter 4 and application of it to real turbomachinery will be presented in chapter 5.

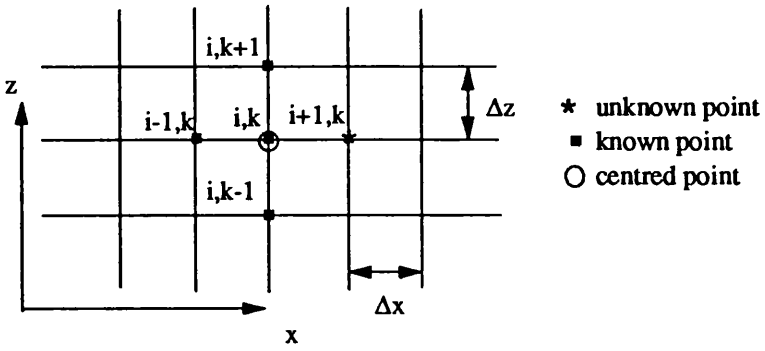

Fig. 2.1 The finite difference grid for explicit scheme

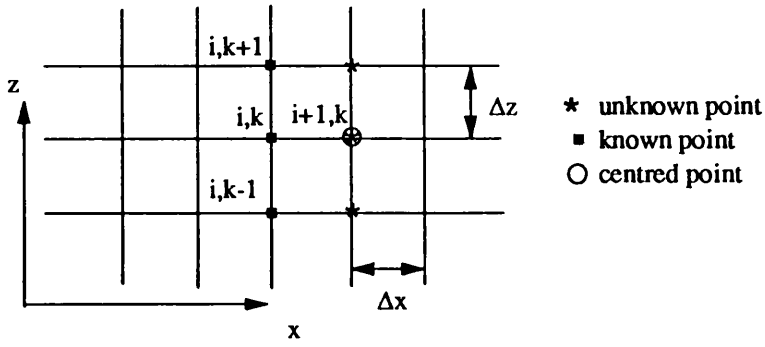

Fig. 2.2 Simple implicit finite difference grid points

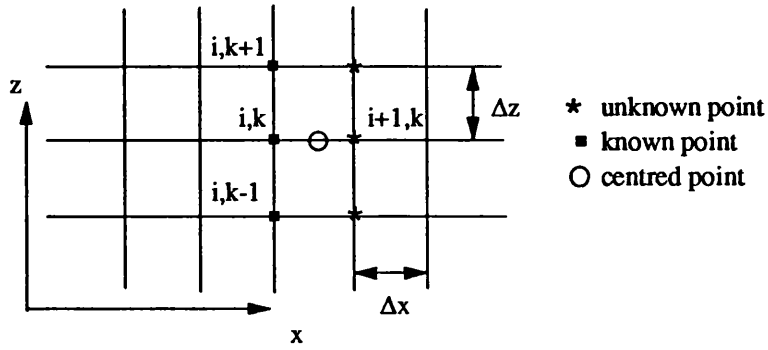

Fig. 2.3 The finite difference grid points for Crank-Nicolson scheme

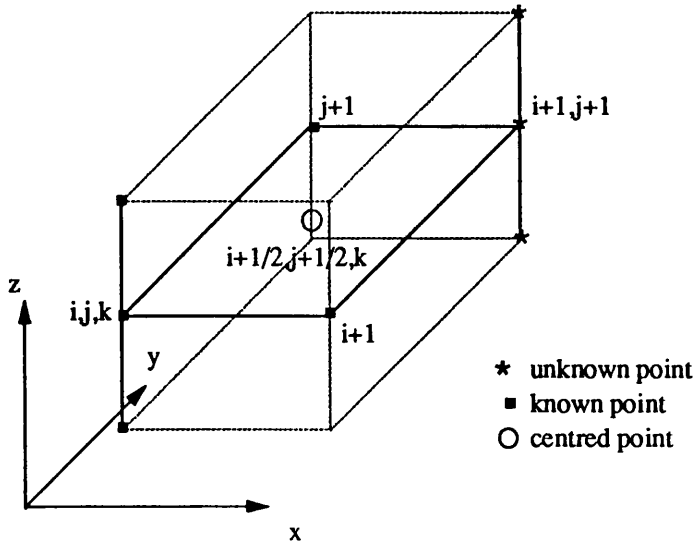

Fig. 2.4 Three-dimensional finite difference grid points for the Crank-Nicolson scheme

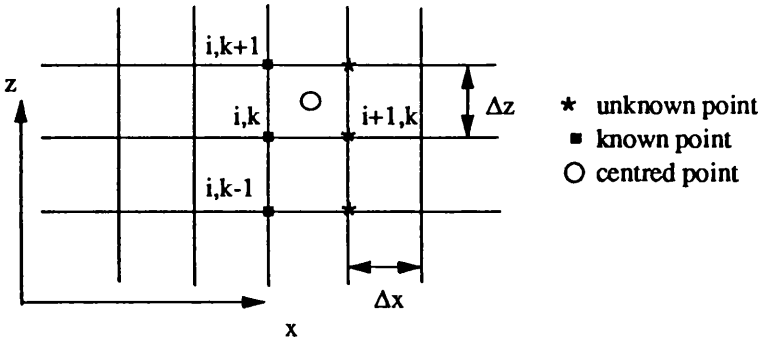

Fig. 2.5 Typical finite difference grid for boundary-layer flows in the Keller's box scheme.

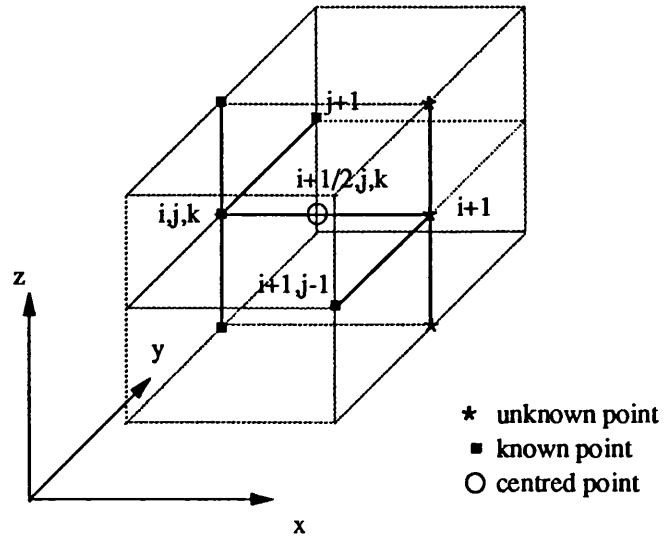

Fig. 2.6 Arrangement for the Krause zig-zag scheme

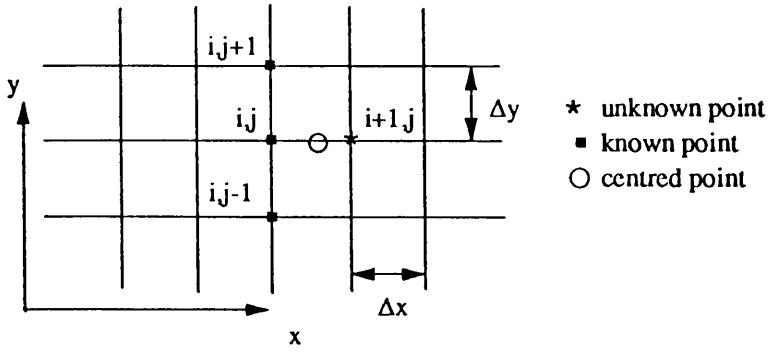

Fig. 2.7 Grid arrangement of Kitchens scheme on x-y plane

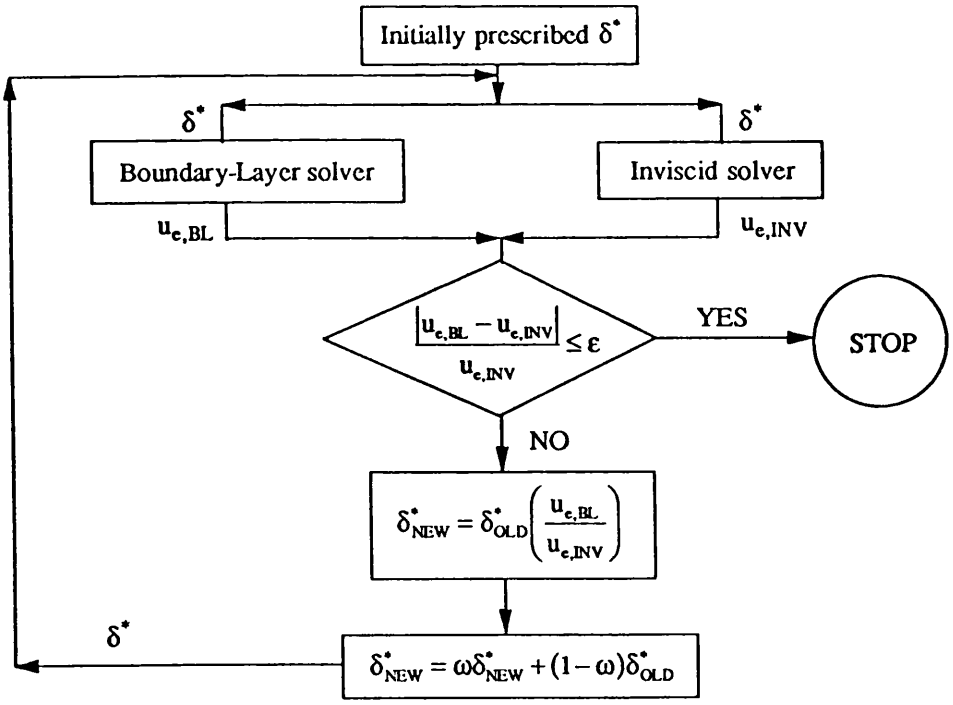

Fig. 2.8 Flow chart for the viscous-inviscid interaction: relaxation formula (Kwon and Pletcher (1986a))

CHAPTER 3
THREE-DIMENSIONAL BOUNDARY LAYERS

3.1 INTRODUCTION

This chapter provides the procedures used to develop a calculation method for three-dimensional boundary-layers on turbomachinery blades. The chapter starts by presenting the boundary-layer governing equations. These equations are three-dimensional unsteady boundary-layer equations. They are expressed in body-fitted non-orthogonal curvilinear co-ordinate system. By using these equations, it is possible to calculate the boundary-layer on curved surfaces. The equations are also written in rotating cylindrical co-ordinates that are best suited to turbomachinery especially when the system is rotating about one axis.

The eddy-viscosity for the turbulent flow based upon Baldwin-Lomax model is presented in the next section. The model was chosen because it uses simple empirical turbulent models and can be applied for three-dimensional separated flows. This model is used in many Navier-Stokes solvers and boundary-layer solvers, and the solution is obtained by direct computation.

The stability and accuracy of the solutions depend on the transformation and discretization methods employed. Since the complex similarity transformations are avoided and the equations are expressed in the physical domain that is non-uniform grid spacing, the grid generation is used to transform this non-uniform grid spacing (physical domain) to a uniform grid spacing (computational domain). This approach is presented in section four.

The discretization scheme that is used is based on an upwind differencing scheme. This is described in section five. The scheme provides a more stable

discretization for predicting problems with flow reversal. It is employed with second-order formulation in the spatial derivatives parallel to the surface. Central differencing is used for the spatial derivatives in the normal direction. Finally the forward differencing with first-order formulation is used for time derivative.

The numerical solution algorithm is defined and discussed in section six of the chapter. The solutions are obtained by time integration that is in a form of a tridiagonal system of equations. Thus the boundary-layer equations can be computed efficiently and accuracy.

Section seven presents the computational procedure. The systems of equations from the previous section are solved in an uncoupled manner. Once the predicted values are obtained, they will be updated and used to predicted the other values. This iteration process will continue until the solutions are converged. To accelerate the process a variable relaxation factor is used.

In the final section, we shall investigate the stability of the boundary-layer equations and describe the zone of dependence concept.

3.2 GOVERNING EQUATIONS

Governing equations of fluid flows consist of three basic laws of conservation of mass, momentum and energy. These conservative laws are the heart of fluid dynamics and the fluid flows have to obey their principles. In fact all the fluid dynamic problems are solved with the same principles but with different assumptions.

The Navier-Strokes equations represent the conservation of momentum and are applicable in describing the motion of fluid. They are used to solve many

fluid flow problems since they can be expressed for steady or unsteady, viscous or inviscid, compressible or incompressible flow, etc.

Boundary layer is formed whenever fluid flows over a solid surface. If Reynolds number is very high, the boundary layer will be a very narrow layer near to a solid surface and the effect of viscosity is significant in this thin layer. Outside the layer, therefore, the effect of viscosity may be ignored. With the help of this assumption and the order of magnitude, all viscous terms containing derivatives parallel to the surface are much smaller than those normal to the wall. These terms are dropped out in the Navier-Stokes equations. The resultant equations are boundary-layer momentum equations that are simpler than the Navier-Stokes equations. These equations together with the energy equation and the continuity equation are used to solve boundary-layer problems. These equations are not applicable to flow near the intersection of two surfaces (e.g. near hub-blade junctions and corners in channels) because stress gradients in two directions are not important in those regions. Other reduced forms of the Navier-Stokes equations can be used to treat the problems. These forms of equations are not considered here and can be seen in Anderson et al (1984).

3.2.1 CONSERVATION EQUATIONS

The equations of continuity, momentum and energy with respect to a frame of reference rotating with a constant angular velocity Ω are given by:

$$\frac{\partial \rho}{\partial t} + \nabla \cdot (\rho \mathbf{U}) = 0 \qquad 3.1a$$

$$\rho \frac{\partial \mathbf{U}}{\partial t} + \rho \mathbf{U} \cdot \nabla \mathbf{U} + 2\rho \boldsymbol{\Omega} \times \mathbf{U} + \rho \boldsymbol{\Omega} \times (\boldsymbol{\Omega} \times \mathbf{r}) = -\nabla p + \nabla \cdot (\mu \nabla \mathbf{U}) \qquad 3.2a$$

$$\rho \frac{\partial I}{\partial t} + \rho \mathbf{U} \cdot \nabla I = \frac{\partial p}{\partial t} + \nabla \cdot \left[\frac{\mu}{Pr} \nabla H + \mu \left(1 - \frac{1}{Pr} \right) \nabla \frac{U^2}{2} \right] \qquad 3.3a$$

U is the velocity relative to the rotating system, p is the pressure, I ($=H-\frac{(\Omega r)^2}{2}$) is the rothalpy, H ($=c_pT+\frac{U^2}{2}$) is the total enthalpy, Pr is the Prandtl number, ρ is the density, μ is the viscosity and **r** is the position vector relative to the rotating axis.

The equations are written in the unsteady forms since they are solved by a time marching scheme. They differ from their steady flow counterparts only through the appearance of the term $\frac{\partial \rho}{\partial t}$ in continuity equation, $\rho\frac{\partial \mathbf{U}}{\partial t}$ in momentum equation and, $\rho\frac{\partial I}{\partial t}$ and $\frac{\partial p}{\partial t}$ in energy equation.

In rotating and non-rotating co-ordinates of the momentum equations (3.2a), there are two additional terms in the former due to the rotation. These terms are $2\Omega\times\mathbf{U}$, the Coriolis acceleration, and $\Omega\times(\Omega\times\mathbf{r})$, the centripetal acceleration. For energy equation, the effect of rotation appears through rothalpy.

The boundary-layer equations of Cartesian co-ordinate are simple and quite straightforward. Therefore we will first illustrate the set of boundary-layer equations in this co-ordinate system. Let $\mathbf{U} = u_x\mathbf{e}_x + u_y\mathbf{e}_y + u_z\mathbf{e}_z$ and the normal distance to the surface is in z-direction, then equations (3.1a-3.3a) for non-rotating Cartesian co-ordinate can be written into the following scalar boundary layer equations:

continuity:

$$\frac{\partial \rho}{\partial t}+\frac{\partial \rho u_x}{\partial x}+\frac{\partial \rho u_y}{\partial y}+\frac{\partial \rho u_z}{\partial z}=0 \qquad 3.1b$$

x-momentum:

$$\rho\frac{\partial u_x}{\partial t}+\rho u_x\frac{\partial u_x}{\partial x}+\rho u_y\frac{\partial u_x}{\partial y}+\rho u_z\frac{\partial u_x}{\partial z}=-\frac{\partial p}{\partial x}+\frac{\partial}{\partial z}\left(\mu\frac{\partial u_x}{\partial z}\right) \qquad 3.2.1b$$

y-momentum:

$$\rho\frac{\partial u_y}{\partial t}+\rho u_x\frac{\partial u_y}{\partial x}+\rho u_y\frac{\partial u_y}{\partial y}+\rho u_z\frac{\partial u_y}{\partial z}=-\frac{\partial p}{\partial y}+\frac{\partial}{\partial z}\left(\mu\frac{\partial u_y}{\partial z}\right) \qquad 3.2.2b$$

z-momentum:

$$\frac{\partial p}{\partial z}\approx 0 \qquad 3.2.3b$$

energy:

$$\rho\frac{\partial H}{\partial t}+\rho u_x\frac{\partial H}{\partial x}+\rho u_y\frac{\partial H}{\partial y}+\rho u_z\frac{\partial H}{\partial z}=\frac{\partial p}{\partial t}+\frac{\partial}{\partial z}\left[\frac{\mu}{Pr}\frac{\partial H}{\partial z}+\frac{\mu}{2}\left(1-\frac{1}{Pr}\right)\frac{\partial U^2}{\partial z}\right] \quad 3.3b$$

Since $|u_z| << |u_x|$ and $|u_y|$, the value of $U^2 = u_x^2 + u_y^2 + u_z^2 \approx u_x^2 + u_y^2$. At the boundary-layer edge, we set $\mathbf{U} = u_{ex}\mathbf{e}_x + u_{ey}\mathbf{e}_y + u_{ez}\mathbf{e}_z$ and $\mu = 0$ in the equations (3.2.1b-3.2.3b) resulting the Euler equations. Since the boundary-layer is very thin, we can assume that p is constant across the layer (see equation 3.2.3b). Therefore we can relate the derivation of pressure term through the Euler equations. Setting $\mu = 0$ in the equations (3.2.1b-3.2.2b) we get

x-momentum:

$$\rho_e\frac{\partial u_{ex}}{\partial t}+\rho_e u_{ex}\frac{\partial u_{ex}}{\partial x}+\rho_e u_{ey}\frac{\partial u_{ex}}{\partial y}+\rho_e u_{ez}\frac{\partial u_{ex}}{\partial z}=-\frac{\partial p}{\partial x} \qquad 3.2.1c$$

y-momentum:

$$\rho_e\frac{\partial u_{ey}}{\partial t}+\rho_e u_{ex}\frac{\partial u_{ey}}{\partial x}+\rho_e u_{ey}\frac{\partial u_{ey}}{\partial y}+\rho_e u_{ez}\frac{\partial u_{ey}}{\partial z}=-\frac{\partial p}{\partial y} \qquad 3.2.2c$$

energy:

$$\rho_e \frac{\partial H_e}{\partial t} + \rho_e u_{ex} \frac{\partial H_e}{\partial x} + \rho_e u_{ey} \frac{\partial H_e}{\partial y} = \frac{\partial p}{\partial t}$$

where a subscript e denotes a quantity at the boundary-layer edge.

The above set of equations (3.1b, 3.2.1b-3.2.3b, 3.3b) is applicable only to a flat plate. In order to get a general form of boundary-layer equations, the shape of the surface on which the boundary layers are formed has to be considered. This will be discussed in the following section.

3.2.2 METRIC COEFFICIENTS

It should be noted that the equations (3.1a-3.3a) are valid for any co-ordinate systems as long as the operation of ∇ is known. Since boundary layers are defined on a surface that the fluid flows, the equations should be transformed to the general curvilinear system ($\bar{\xi}$, $\bar{\eta}$, $\bar{\zeta}$). A straightforward procedure is to use the metric stretching factor h_i (i=1, 2, 3) to relate the curvilinear co-ordinate to a standard co-ordinate system (e.g. Cartesian co-ordinate, cylindrical co-ordinate).

In the following transformation we will relate the general curvilinear system ($\bar{\xi}$, $\bar{\eta}$, $\bar{\zeta}$) to a cylindrical co-ordinate system (x, r, θ). The curvilinear system is defined in an non-orthogonal co-ordinate in order to cover all types of surface shape. This non-orthogonal curvilinear co-ordinate system is shown in Fig. 3.1.

The equations due to Yamazaki (1981) are adapted for unsteady compressible flow. The surface of the body consists of two non-orthogonal surface co-ordinates ($\bar{\xi}$, $\bar{\eta}$) with an angle α between them. The third co-ordinate $\bar{\zeta}$ is the actual distance measured normal to the surface. The system $\bar{\xi}$, $\bar{\eta}$, $\bar{\zeta}$ is

rotating around the x-axis with the constant angular velocity Ω. At time t, the surface itself is defined in terms of cylindrical co-ordinates (x, r, θ) as

$$x = x_b, \qquad r = r_b, \qquad \theta = \theta_b \tag{3.4}$$

where $x_b = x_b(\bar{\xi}, \bar{\eta})$, $r_b = r_b(\bar{\xi}, \bar{\eta})$, $\theta_b = \theta_b(\bar{\xi}, \bar{\eta})$.
A subscript b denotes a quantity at the blade surface (i.e. at $\bar{\zeta} = 0$).

The position vector **L** in the non-orthogonal curvilinear co-ordinate system $\bar{\xi}$, $\bar{\eta}$, $\bar{\zeta}$ may be written as:

$$\mathbf{L} = x\mathbf{e}_x + r\mathbf{e}_r + \theta\mathbf{e}_\theta \tag{3.5}$$

where $\mathbf{e}_x$, $\mathbf{e}_r$, $\mathbf{e}_\theta$ are the constant unit vectors along x, r, θ axes, respectively. The tangential vectors to the co-ordinate lines $\bar{\xi}$, $\bar{\eta}$ and $\bar{\zeta}$ can be obtained by partial derivatives of **L** with respect to $\bar{\xi}$, $\bar{\eta}$, $\bar{\zeta}$ (i.e., $\frac{\partial \mathbf{L}}{\partial \bar{\xi}}$, $\frac{\partial \mathbf{L}}{\partial \bar{\eta}}$, $\frac{\partial \mathbf{L}}{\partial \bar{\zeta}}$), respectively. They are called the base vectors or metric coefficients.

$$h_1 = \left|\frac{\partial \mathbf{L}}{\partial \bar{\xi}}\right| = \sqrt{\left(\frac{\partial x_b}{\partial \bar{\xi}}\right)^2 + \left(\frac{\partial r_b}{\partial \bar{\xi}}\right)^2 + \left(\frac{r_b \partial \theta_b}{\partial \bar{\xi}}\right)^2} \tag{3.6}$$

$$h_2 = \left|\frac{\partial \mathbf{L}}{\partial \bar{\eta}}\right| = \sqrt{\left(\frac{\partial x_b}{\partial \bar{\eta}}\right)^2 + \left(\frac{\partial r_b}{\partial \bar{\eta}}\right)^2 + \left(\frac{r_b \partial \theta_b}{\partial \bar{\eta}}\right)^2} \tag{3.7}$$

$$h_3 = \left|\frac{\partial \mathbf{L}}{\partial \bar{\zeta}}\right| = \sqrt{\left(\frac{\partial x_b}{\partial \bar{\zeta}}\right)^2 + \left(\frac{\partial r_b}{\partial \bar{\zeta}}\right)^2 + \left(\frac{r_b \partial \theta_b}{\partial \bar{\zeta}}\right)^2} \tag{3.8}$$

In cylindrical co-ordinates, the vector displacement between two points on the body surface is given by

$$dL = dx_b\, \mathbf{e}_x + dr_b\, \mathbf{e}_r + r_b d\theta_b\, \mathbf{e}_\theta \qquad 3.9$$

In curvilinear co-ordinates, the analogous displacement is given by

$$dL = dL_1\, \mathbf{e}_1 + dL_2\, \mathbf{e}_2 + dL_3\, \mathbf{e}_3 \qquad 3.10$$

where $\mathbf{e}_1$, $\mathbf{e}_2$, and $\mathbf{e}_3$ are the unit vectors along $\bar{\xi}$, $\bar{\eta}$ and $\bar{\zeta}$, respectively. In the curvilinear co-ordinate system, if $\bar{\xi}$ is increased by $\Delta\bar{\xi}$, then ΔL_1 will be increased by $h_1\Delta\bar{\xi}$ in the $\bar{\xi}$-direction . The other two directions are considered in a similar manner. For boundary layer equations, there is no loss of generality by setting h_3 = 1 since the value of $\bar{\zeta}$ is arbitrary and independent from x_b, r_b, θ_b. The element of length on the surface, |dL| then

$$\begin{aligned} |dL|^2 &= dx_b^2 + dr_b^2 + (r_b d\theta_b)^2 \\ &= (h_1 d\bar{\xi})^2 + (h_2 d\bar{\eta})^2 + 2h_1h_2 \cos\alpha\, d\bar{\xi}\, d\bar{\eta} \end{aligned} \qquad 3.11$$

with $h_1h_2 \cos\alpha = \dfrac{\partial x_b}{\partial\bar{\xi}}\dfrac{\partial x_b}{\partial\bar{\eta}} + \dfrac{\partial r_b}{\partial\bar{\xi}}\dfrac{\partial r_b}{\partial\bar{\eta}} + r_b\dfrac{\partial\theta_b}{\partial\bar{\xi}}r_b\dfrac{\partial\theta_b}{\partial\bar{\eta}}$

Then we can see that

$$\mathbf{e}_1 = \frac{1}{h_1}\frac{\partial L}{\partial\bar{\xi}} = \frac{1}{h_1}\frac{\partial x_b}{\partial\bar{\xi}}\mathbf{e}_x + \frac{1}{h_1}\frac{\partial r_b}{\partial\bar{\xi}}\mathbf{e}_r + \frac{r_b}{h_1}\frac{\partial\theta_b}{\partial\bar{\xi}}\mathbf{e}_\theta \qquad 3.12$$

$$\mathbf{e}_2 = \frac{1}{h_2}\frac{\partial L}{\partial\bar{\eta}} = \frac{1}{h_2}\frac{\partial x_b}{\partial\bar{\eta}}\mathbf{e}_x + \frac{1}{h_2}\frac{\partial r_b}{\partial\bar{\eta}}\mathbf{e}_r + \frac{r_b}{h_2}\frac{\partial\theta_b}{\partial\bar{\eta}}\mathbf{e}_\theta \qquad 3.13$$

The relationships among the unit vectors in $\bar{\xi}$-, $\bar{\eta}$-, $\bar{\zeta}$-directions (i.e., $\mathbf{e}_1$, $\mathbf{e}_2$, $\mathbf{e}_3$) and the unit vectors in x-, r-,θ-directions (i.e., $\mathbf{e}_x$, $\mathbf{e}_r$, $\mathbf{e}_\theta$) are

$$\mathbf{e}_x \cdot \mathbf{e}_x = \mathbf{e}_r \cdot \mathbf{e}_r = \mathbf{e}_\theta \cdot \mathbf{e}_\theta = 1$$

$$\mathbf{e}_\theta \cdot \mathbf{e}_r = \mathbf{e}_r \cdot \mathbf{e}_x = \mathbf{e}_x \cdot \mathbf{e}_\theta = 0$$

$$\mathbf{e}_x \times \mathbf{e}_x = \mathbf{e}_r \times \mathbf{e}_r = \mathbf{e}_\theta \times \mathbf{e}_\theta = 0$$

$$\mathbf{e}_\theta \times \mathbf{e}_x = \mathbf{e}_r$$

$$\mathbf{e}_r \times \mathbf{e}_\theta = \mathbf{e}_x$$

$$\mathbf{e}_x \times \mathbf{e}_r = \mathbf{e}_\theta$$

$$\mathbf{e}_1 \cdot \mathbf{e}_1 = \mathbf{e}_2 \cdot \mathbf{e}_2 = \mathbf{e}_3 \cdot \mathbf{e}_3 = 1$$

$$\mathbf{e}_1 \cdot \mathbf{e}_3 = \mathbf{e}_2 \cdot \mathbf{e}_3 = 0$$

$$\mathbf{e}_1 \cdot \mathbf{e}_2 = \cos \alpha$$

$$\mathbf{e}_1 \times \mathbf{e}_1 = \mathbf{e}_2 \times \mathbf{e}_2 = \mathbf{e}_3 \times \mathbf{e}_3 = 0$$

$$\mathbf{e}_1 \times \mathbf{e}_2 = \mathbf{e}_3 \sin \alpha$$

$$\mathbf{e}_3 \times \mathbf{e}_1 = -\mathbf{e}_1 \frac{\cos \alpha}{\sin \alpha} + \mathbf{e}_2 \frac{1}{\sin \alpha}$$

$$\mathbf{e}_2 \times \mathbf{e}_3 = \mathbf{e}_1 \frac{1}{\sin \alpha} - \mathbf{e}_2 \frac{\cos \alpha}{\sin \alpha} \qquad 3.14$$

and the directional cosines between the systems are

$$\mathbf{e}_1 \cdot \mathbf{e}_\theta = \frac{r_b}{h_1} \frac{\partial \theta_b}{\partial \bar{\xi}}$$

$$\mathbf{e}_1 \cdot \mathbf{e}_r = \frac{1}{h_1} \frac{\partial r_b}{\partial \bar{\xi}}$$

$$\mathbf{e}_1 \cdot \mathbf{e}_x = \frac{1}{h_1} \frac{\partial x_b}{\partial \bar{\xi}}$$

$$\mathbf{e}_2 \cdot \mathbf{e}_\theta = \frac{r_b}{h_2} \frac{\partial \theta_b}{\partial \bar{\eta}}$$

$$\mathbf{e}_2 \cdot \mathbf{e}_r = \frac{1}{h_2} \frac{\partial r_b}{\partial \bar{\eta}}$$

$$\mathbf{e}_2 \cdot \mathbf{e}_x = \frac{1}{h_2}\frac{\partial x_b}{\partial \bar{\eta}}$$

$$\mathbf{e}_3 \cdot \mathbf{e}_\theta = \frac{1}{h_1 h_2 \sin\alpha}\left(\frac{\partial x_b}{\partial \bar{\xi}}\frac{\partial r_b}{\partial \bar{\eta}} - \frac{\partial r_b}{\partial \bar{\xi}}\frac{\partial x_b}{\partial \bar{\eta}}\right)$$

$$\mathbf{e}_3 \cdot \mathbf{e}_r = \frac{1}{h_1 h_2 \sin\alpha}\left(-\frac{\partial x_b}{\partial \bar{\xi}}\frac{r_b \partial\theta_b}{\partial \bar{\eta}} + \frac{r_b \partial\theta_b}{\partial \bar{\xi}}\frac{\partial x_b}{\partial \bar{\eta}}\right)$$

$$\mathbf{e}_3 \cdot \mathbf{e}_x = \frac{1}{h_1 h_2 \sin\alpha}\left(\frac{\partial r_b}{\partial \bar{\xi}}\frac{r_b \partial\theta_b}{\partial \bar{\eta}} - \frac{r_b \partial\theta_b}{\partial \bar{\xi}}\frac{\partial r_b}{\partial \bar{\eta}}\right) \qquad 3.15$$

From equations (3.12-3.15), the unit vector $\mathbf{e}_3$ can be evaluated from

$$\mathbf{e}_3 = \mathbf{e}_1 \times \mathbf{e}_2 \frac{1}{\sin\alpha}$$

$$= \frac{1}{h_1 h_2 \sin\alpha}\left(\frac{\partial r_b}{\partial \bar{\xi}}\frac{r_b \partial\theta_b}{\partial \bar{\eta}} - \frac{r_b \partial\theta_b}{\partial \bar{\xi}}\frac{\partial r_b}{\partial \bar{\eta}}\right)\mathbf{e}_x$$

$$+ \frac{1}{h_1 h_2 \sin\alpha}\left(-\frac{\partial x_b}{\partial \bar{\xi}}\frac{r_b \partial\theta_b}{\partial \bar{\eta}} + \frac{r_b \partial\theta_b}{\partial \bar{\xi}}\frac{\partial x_b}{\partial \bar{\eta}}\right)\mathbf{e}_r$$

$$+ \frac{1}{h_1 h_2 \sin\alpha}\left(\frac{\partial x_b}{\partial \bar{\xi}}\frac{\partial r_b}{\partial \bar{\eta}} - \frac{\partial r_b}{\partial \bar{\xi}}\frac{\partial x_b}{\partial \bar{\eta}}\right)\mathbf{e}_\theta \qquad 3.16$$

Then, the position of a point near the blade surface can be represented as

$$x = x_b + (\mathbf{e}_3 \cdot \mathbf{e}_x)\bar{\zeta}$$

$$r = r_b + (\mathbf{e}_3 \cdot \mathbf{e}_r)\bar{\zeta}$$

$$\theta = \theta_b + (\mathbf{e}_3 \cdot \mathbf{e}_\theta)\frac{\bar{\zeta}}{r} \qquad 3.17$$

It should be noted that there are two normal directions, above and below the surface. If the other direction is required, the unit normal vector $\mathbf{e}_3$ should be negative.

3.2.3 NON-ORTHOGONAL CO-ORDINATE SYSTEM

The boundary layer equations for the non-orthogonal co-ordinate system $\bar{\xi}$, $\bar{\eta}$, $\bar{\zeta}$ now can be derived since the metric coefficients (h_1, h_2, h_3) and the unit vectors ($\mathbf{e}_1$, $\mathbf{e}_2$, $\mathbf{e}_3$) are specified. It should be noted that these values, in general, vary from point to point. For more detail about differential quantities in the new curvilinear co-ordinate system, the reader can refer to Anderson et al (1984) and Warsi (1992). It should be emphasised that velocity **U** must be defined along the surface co-ordinate. In this system, we set $\mathbf{U} = u\mathbf{e}_1 + v\mathbf{e}_2 + w\mathbf{e}_3$. For the boundary layer problems, $|w| << |u|$ and $|v|$, and these velocities (i.e. u, v) are directed along the surface ($\bar{\xi}$, $\bar{\eta}$) with an angle α between the $\bar{\xi}$ and $\bar{\eta}$ curves. Therefore, $U^2 = u^2+v^2+2uv\cos\alpha$. For the method of the velocity transformation between the curvilinear co-ordinate ($\bar{\xi}$, $\bar{\eta}$, $\bar{\zeta}$) and the cylindrical co-ordinate (x, r, θ), the reader can see in Appendix A. The operation of ∇ on the equations (3.1a-3.3a) for the co-ordinate surfaces can be written as:

continuity:

$$\frac{\partial \rho}{\partial t}+\frac{1}{h_1 h_2 \sin\alpha}\left[\frac{\partial(h_2 \sin\alpha \rho u)}{\partial \bar{\xi}}+\frac{\partial(h_1 \sin\alpha \rho v)}{\partial \bar{\eta}}+\frac{\partial(h_1 h_2 \sin\alpha \rho w)}{\partial \bar{\zeta}}\right]=0 \quad 3.18a$$

$\bar{\xi}$-momentum:

$$\rho\frac{\partial u}{\partial t}+\frac{\rho u}{h_1}\frac{\partial u}{\partial \bar{\xi}}+\frac{\rho v}{h_2}\frac{\partial u}{\partial \bar{\eta}}+\rho w\frac{\partial u}{\partial \bar{\zeta}}+K_{11}\rho u^2+K_{12}\rho uv+K_{13}\rho v^2+A_1$$
$$=K_{14}\frac{\partial p}{\partial \bar{\xi}}+K_{15}\frac{\partial p}{\partial \bar{\eta}}+\frac{\partial}{\partial \bar{\zeta}}\left(\mu\frac{\partial u}{\partial \bar{\zeta}}\right) \quad 3.19a$$

$\bar{\eta}$-momentum:

$$\rho\frac{\partial v}{\partial t}+\frac{\rho u}{h_1}\frac{\partial v}{\partial \bar{\xi}}+\frac{\rho v}{h_2}\frac{\partial v}{\partial \bar{\eta}}+\rho w\frac{\partial v}{\partial \bar{\zeta}}+K_{21}\rho u^2+K_{22}\rho uv+K_{23}\rho v^2+A_2$$
$$=K_{24}\frac{\partial p}{\partial \bar{\xi}}+K_{25}\frac{\partial p}{\partial \bar{\eta}}+\frac{\partial}{\partial \bar{\zeta}}\left(\mu\frac{\partial v}{\partial \bar{\zeta}}\right) \quad 3.20a$$

energy:

$$\rho\frac{\partial I}{\partial t}+\frac{\rho u}{h_1}\frac{\partial I}{\partial \bar{\xi}}+\frac{\rho v}{h_2}\frac{\partial I}{\partial \bar{\eta}}+\rho w\frac{\partial I}{\partial \bar{\zeta}}=\frac{\partial p}{\partial t}+\frac{\partial}{\partial \bar{\zeta}}\left[\frac{\mu}{Pr}\frac{\partial H}{\partial \bar{\zeta}}+\frac{\mu}{2}\left(1-\frac{1}{Pr}\right)\frac{\partial U^2}{\partial \bar{\zeta}}\right] \quad 3.21a$$

Equation (3.21a) can be written in the term of total enthalpy as shown in equation (3.21b).

$$\rho\frac{\partial H}{\partial t}+\frac{\rho u}{h_1}\frac{\partial H}{\partial \bar{\xi}}+\frac{\rho v}{h_2}\frac{\partial H}{\partial \bar{\eta}}+\rho w\frac{\partial H}{\partial \bar{\zeta}}=\frac{\partial p}{\partial t}+\frac{\partial}{\partial \bar{\zeta}}\left[\frac{\mu}{Pr}\frac{\partial H}{\partial \bar{\zeta}}+\frac{\mu}{2}\left(1-\frac{1}{Pr}\right)\frac{\partial U^2}{\partial \bar{\zeta}}\right]$$
$$+\frac{\rho u\Omega^2}{h_1 2}\frac{\partial r^2}{\partial \bar{\xi}}+\frac{\rho v\Omega^2}{h_2 2}\frac{\partial r^2}{\partial \bar{\eta}}+\rho\Omega^2 r\left[A_{\omega 2}u+A_{\omega 3}v\right] \quad 3.21b$$

where

$$K_{11}=\frac{\cos\alpha}{h_1h_2\sin^2\alpha}\left[\frac{\partial h_1}{\partial \bar{\eta}}-\frac{\partial h_2\cos\alpha}{\partial \bar{\xi}}\right]$$

$$K_{12}=\frac{1}{h_1h_2\sin^2\alpha}\left[\left(1+\cos^2\alpha\right)\frac{\partial h_1}{\partial \bar{\eta}}-2\cos\alpha\frac{\partial h_2}{\partial \bar{\xi}}\right]$$

$$K_{13}=\frac{1}{h_1h_2\sin^2\alpha}\left[\frac{\partial h_1\cos\alpha}{\partial \bar{\eta}}-\frac{\partial h_2}{\partial \bar{\xi}}\right]$$

$$K_{14}=-\frac{1}{h_1\sin^2\alpha}$$

$$K_{15}=\frac{\cos\alpha}{h_2\sin^2\alpha}$$

$$K_{21}=-\frac{K_{11}}{\cos\alpha}$$

$$K_{22}=\frac{1}{h_1h_2\sin^2\alpha}\left[\left(1+\cos^2\alpha\right)\frac{\partial h_2}{\partial \bar{\xi}}-2\cos\alpha\frac{\partial h_1}{\partial \bar{\eta}}\right]$$

$$K_{23}=-K_{13}\cos\alpha$$

$$K_{24}=-K_{14}\cos\alpha$$

$$K_{25}=-K_{15}\cos\alpha$$

$$A_{\omega 2} = \mathbf{e}_1 \cdot \mathbf{e}_r = \frac{1}{h_1}\frac{\partial r_b}{\partial \xi}$$

$$A_{\omega 3} = \mathbf{e}_2 \cdot \mathbf{e}_r = \frac{1}{h_2}\frac{\partial r_b}{\partial \eta} \qquad 3.22$$

A_1 and A_2 are the terms that involved in the rotation of the axis. Yamazaki (1981) derived A_1 and A_2 by introducing a function A which equals to

$$A = A_1\,\mathbf{e}_1 + A_2\,\mathbf{e}_2$$
$$= 2\rho\Omega\times\mathbf{U} + \rho\Omega\times(\Omega\times\mathbf{r}) \qquad 3.23$$

Let $\mathbf{e}_x = l_1\,\mathbf{e}_1 + l_2\,\mathbf{e}_2 + l_3\,\mathbf{e}_3$

$\mathbf{e}_r = m_1\,\mathbf{e}_1 + m_2\,\mathbf{e}_2 + m_3\,\mathbf{e}_3$

and $\mathbf{e}_\theta = n_1\,\mathbf{e}_1 + n_2\,\mathbf{e}_2 + n_3\,\mathbf{e}_3$ 3.24

and using the unit vectors relation, we get

$$l_1 = \left[(\mathbf{e}_x \cdot \mathbf{e}_1) - (\mathbf{e}_x \cdot \mathbf{e}_2)\cos\alpha\right]\frac{1}{\sin^2\alpha}$$

$$l_2 = \left[(\mathbf{e}_x \cdot \mathbf{e}_2) - (\mathbf{e}_x \cdot \mathbf{e}_1)\cos\alpha\right]\frac{1}{\sin^2\alpha}$$

$$l_3 = \mathbf{e}_x \cdot \mathbf{e}_3$$

$$m_1 = \left[(\mathbf{e}_r \cdot \mathbf{e}_1) - (\mathbf{e}_r \cdot \mathbf{e}_2)\cos\alpha\right]\frac{1}{\sin^2\alpha}$$

$$m_2 = \left[(\mathbf{e}_r \cdot \mathbf{e}_2) - (\mathbf{e}_r \cdot \mathbf{e}_1)\cos\alpha\right]\frac{1}{\sin^2\alpha}$$

$$m_3 = \mathbf{e}_r \cdot \mathbf{e}_3$$

$$n_1 = \left[(\mathbf{e}_\theta \cdot \mathbf{e}_1) - (\mathbf{e}_\theta \cdot \mathbf{e}_2)\cos\alpha\right]\frac{1}{\sin^2\alpha}$$

$$n_2 = \left[(\mathbf{e}_\theta \cdot \mathbf{e}_2) - (\mathbf{e}_\theta \cdot \mathbf{e}_1)\cos\alpha\right]\frac{1}{\sin^2\alpha}$$

$$n_3 = \mathbf{e}_\theta \cdot \mathbf{e}_3 \qquad 3.25$$

If $\Omega = \Omega \mathbf{e}_x$, we can write the term

$$2\rho\Omega \times \mathbf{U} = 2\rho\left[(\Omega \mathbf{e}_x) \times (u\mathbf{e}_1 + v\mathbf{e}_2 + w\mathbf{e}_3)\right]$$

$$= 2\rho\Omega\left[(l_1\mathbf{e}_1 + l_2\mathbf{e}_2 + l_3\mathbf{e}_3) \times (u\mathbf{e}_1 + v\mathbf{e}_2 + w\mathbf{e}_3)\right] \qquad 3.26$$

The resulting equation in non-orthogonal curvilinear co-ordinate is then:

$$2\rho\Omega \times \mathbf{U} = -2\rho\Omega(u\cos\alpha + v)\frac{1}{\sin\alpha}\frac{1}{h_1 h_2 \sin\alpha}\left(\frac{\partial r_b}{\partial \bar{\xi}}\frac{r_b \partial\theta_b}{\partial \bar{\eta}} - \frac{r_b \partial\theta_b}{\partial \bar{\xi}}\frac{\partial r_b}{\partial \bar{\eta}}\right)\mathbf{e}_1$$

$$+2\rho\Omega(u + v\cos\alpha)\frac{1}{\sin\alpha}\frac{1}{h_1 h_2 \sin\alpha}\left(\frac{\partial r_b}{\partial \bar{\xi}}\frac{r_b \partial\theta_b}{\partial \bar{\eta}} - \frac{r_b \partial\theta_b}{\partial \bar{\xi}}\frac{\partial r_b}{\partial \bar{\eta}}\right)\mathbf{e}_2 \qquad 3.27$$

and the term $\rho\Omega\times(\Omega\times\mathbf{r})$ is done in the similar way

$$\rho\Omega \times (\Omega \times \mathbf{r}) = -\rho\Omega^2 r\,\mathbf{e}_r = -\rho\Omega^2 r\frac{1}{\sin^2\alpha}\left(\frac{1}{h_1}\frac{\partial r_b}{\partial \bar{\xi}} - \frac{\cos\alpha}{h_2}\frac{\partial r_b}{\partial \bar{\eta}}\right)\mathbf{e}_1$$

$$-\rho\Omega^2 r\frac{1}{\sin^2\alpha}\left(\frac{1}{h_2}\frac{\partial r_b}{\partial \bar{\eta}} - \frac{\cos\alpha}{h_1}\frac{\partial r_b}{\partial \bar{\xi}}\right)\mathbf{e}_2 \qquad 3.28$$

Therefor $A_1 = -2\rho\Omega\ (u\cos\alpha + v)\frac{1}{\sin\alpha}\frac{1}{h_1 h_2 \sin\alpha}\left(\frac{\partial r_b}{\partial \bar{\xi}}\frac{r_b \partial\theta_b}{\partial \bar{\eta}} - \frac{r_b \partial\theta_b}{\partial \bar{\xi}}\frac{\partial r_b}{\partial \bar{\eta}}\right)$

$$-\rho\Omega^2 r\frac{1}{\sin^2\alpha}\left(\frac{1}{h_1}\frac{\partial r_b}{\partial \bar{\xi}} - \frac{\cos\alpha}{h_2}\frac{\partial r_b}{\partial \bar{\eta}}\right) \qquad 3.29$$

$$A_2 = 2\rho\Omega(u+v\cos\alpha)\frac{1}{\sin\alpha}\frac{1}{h_1 h_2 \sin\alpha}\left(\frac{\partial r_b}{\partial\bar{\xi}}\frac{r_b\partial\theta_b}{\partial\bar{\eta}} - \frac{r_b\partial\theta_b}{\partial\bar{\xi}}\frac{\partial r_b}{\partial\bar{\eta}}\right)$$

$$-\rho\Omega^2 r\frac{1}{\sin^2\alpha}\left(\frac{1}{h_2}\frac{\partial r_b}{\partial\bar{\eta}} - \frac{\cos\alpha}{h_1}\frac{\partial r_b}{\partial\bar{\xi}}\right) \qquad 3.30$$

From equations (3.18a-3.21a), we can see that the velocity vector of inviscid flow has the components $u_e(\bar{\xi}, \bar{\eta}, t)$ and $v_e(\bar{\xi}, \bar{\eta}, t)$, so the pressure distribution in the inviscid flow is a function of $\bar{\xi}$, $\bar{\eta}$ and t (i.e. $p = p(\bar{\xi},\bar{\eta},t)$). The normal pressure gradient $\left(\frac{\partial p}{\partial\bar{\zeta}}\right)$ is zero within the boundary-layer. This gives similar result as those in the simple form of Cartesian co-ordinate as presented in section 3.2.1. Therefore, the derivation of pressure components can be related through the equations (3.31-3.32).

$$\rho_e\frac{\partial u_e}{\partial t} + \frac{\rho_e u_e}{h_1}\frac{\partial u_e}{\partial\bar{\xi}} + \frac{\rho_e v_e}{h_2}\frac{\partial u_e}{\partial\bar{\eta}} + K_{11}\rho_e u_e^2 + K_{12}\rho_e u_e v_e + K_{13}\rho_e v_e^2 + A_1$$

$$= K_{14}\frac{\partial p}{\partial\bar{\xi}} + K_{15}\frac{\partial p}{\partial\bar{\eta}} \qquad 3.31$$

$$\rho_e\frac{\partial v_e}{\partial t} + \frac{\rho_e u_e}{h_1}\frac{\partial v_e}{\partial\bar{\xi}} + \frac{\rho_e v_e}{h_2}\frac{\partial v_e}{\partial\bar{\eta}} + K_{21}\rho_e u_e^2 + K_{22}\rho_e u_e v_e + K_{23}\rho_e v_e^2 + A_2$$

$$= K_{24}\frac{\partial p}{\partial\bar{\xi}} + K_{25}\frac{\partial p}{\partial\bar{\eta}} \qquad 3.32$$

$$\rho_e\frac{\partial H_e}{\partial t} + \frac{\rho_e u_e}{h_1}\frac{\partial H_e}{\partial\bar{\xi}} + \frac{\rho_e v_e}{h_2}\frac{\partial H_e}{\partial\bar{\eta}} = \frac{\partial p}{\partial t} + \frac{\rho_e u_e\Omega^2}{h_1 2}\frac{\partial r_e^2}{\partial\bar{\xi}} + \frac{\rho_e v_e\Omega^2}{h_2 2}\frac{\partial r_e^2}{\partial\bar{\eta}}$$

$$+\rho_e\Omega^2 r_e\left[A_{02}u_e + A_{03}v_e\right]$$

From equations (3.31-3.32), we see that the pressure components are related to the inviscid value of u, v and H. Although the set of the governing equations is expressed in an unsteady form, our method is to solve the equations

for steady flows. According to this, the inviscid terms (e.g. u_e, v_e, H_e) are a function of only $\bar{\xi}$ and $\bar{\eta}$. Therefore $\frac{\partial u_e}{\partial t}, \frac{\partial v_e}{\partial t}, \frac{\partial H_e}{\partial t}$ and $\frac{\partial p}{\partial t}$ are neglected.

The set of the governing equations for laminar flow is now completed through the equation of state (R is the gas constant),

$$p=\rho RT \tag{3.33}$$

Molecular viscosity-temperature relation, assumed to be represented by the Sutherland's law (White (1991))

$$\frac{\mu}{\mu_0} \approx \left(\frac{T}{T_0}\right)^{\frac{3}{2}} \frac{T_0+S}{T+S} \tag{3.34}$$

where S is the Sutherland's constant, μ_0 and T_0 are viscosity and temperature, respectively at reference values.

Sutherland's formula can be approximated by the simple power law

$$\frac{\mu}{\mu_0} = \left(\frac{T}{T_0}\right)^n \tag{3.35}$$

For air, White (1991) recommended the following values.

$$T_0 = 273 \text{ K}$$
$$\mu_0 = 1.716\times10^{-5} \text{ N-s/m}^2$$
$$n = 0.666 \tag{3.36}$$

The boundary conditions for the governing equations are given in equation (3.37a,b).

at the wall $\bar{\zeta}$: the no-slip condition, u = v = w = 0

either a specified temperature, $T = T_w$

or heat-transfer condition, $\frac{\partial T}{\partial \zeta} = q^{\cdot}$ or $H = H_w$ 3.37a

at the edge of the boundary layer $\bar{\zeta} \rightarrow \infty$:

a specified free-stream conditions,

$u = u_e$, $v = v_e$, $T = T_e$ or $H = H_e$ 3.37b

In the above set of equations, all scale factors are calculated at the body surface $\bar{\zeta}$=0 (i.e. x_b, r_b, θ_b). It should be noted that the distance r_b is a function of the surface co-ordinate $\bar{\xi}$, $\bar{\eta}$ only while r is the perpendicular distance of a point from the axis of rotation.

3.2.4 APPROXIMATE EQUATION FOR THE ENERGY EQUATION

From the energy equation (3.21a) if the Prandtl number is unity (a fair approximation for gases), the last term vanishes. When there is no heat transfer at the surface, it implies that $\frac{\partial H}{\partial \bar{\zeta}}$ vanishes at the surface. Therefore the equation becomes $\rho \frac{\partial I}{\partial t} = 0$ or I = constant throughout the boundary layer. This leads to the particular solution to the case of conservation of rothalpy.

$$I = \text{constant} = c_p T_e + \frac{U_e^2}{2} - \frac{\Omega^2 r_e^2}{2} = c_p T + \frac{U^2}{2} - \frac{\Omega^2 r^2}{2} \qquad 3.38$$

Thus the temperature across the boundary layer at an adiabatic wall with Pr=1 can be written as.

$$T = T_e + \frac{(U_e^2 - U^2)}{2c_p} + \frac{\Omega^2(r^2 - r_e^2)}{2c_p} \qquad 3.39a$$

where U_e^2 is the total velocity at the boundary layer edge = $u_e^2 + v_e^2 + 2u_e v_e \cos\alpha$.

r_e is the radius relative to the rotating axis at the boundary layer edge.

The above equation can be used to approximate the energy equation of compressible boundary layers when Pr is near unity and there is no heat transfer at the surface. It should be noted that the equation can be applied for turbulent flow if one makes the assumption $Pr \approx Pr_t \approx 1$ (approximately true for air). The effect of turbulent flow will be presented in section 3.3. For non-rotating co-ordinate system, total enthalpy is conserved and the temperature-velocity relation can be obtained in the similar manner.

3.2.5 NON-DIMENSIONAL EQUATIONS

The boundary-layer equations can be non-dimensionalized by using the following free-stream values:

L (a characteristic length) for all lengths

u_∞ (free-stream velocity) for all velocity vectors

$\rho_\infty u_\infty^2$ (the dynamic head) for pressure

T_∞ (free-stream temperature) for temperature

$c_p T_\infty$ for enthalpy

$\frac{u_\infty}{L}$ for angular velocity

$\frac{L}{u_\infty}$ for time

Normal distance and velocities are also stretched by the square root of the Reynolds number, $Re = \frac{\rho_\infty u_\infty L}{\mu_r}$, where μ_r is the molecular viscosity evaluated at free-stream temperature. The non-dimensional governing equations (3.18a-3.21a and 3.39a) can be expressed as:

continuity:

$$\frac{\partial \rho}{\partial t}+\frac{1}{h_1 h_2 \sin\alpha}\left[\frac{\partial(h_2 \sin\alpha \rho u)}{\partial \bar{\xi}}+\frac{\partial(h_1 \sin\alpha \rho v)}{\partial \bar{\eta}}+\frac{\partial(h_1 h_2 \sin\alpha \rho w)}{\partial \bar{\zeta}}\right]=0 \quad 3.18a$$

$\bar{\xi}$-momentum:

$$\rho\frac{\partial u}{\partial t}+\frac{\rho u}{h_1}\frac{\partial u}{\partial \bar{\xi}}+\frac{\rho v}{h_2}\frac{\partial u}{\partial \bar{\eta}}+\rho w\frac{\partial u}{\partial \bar{\zeta}}+K_{11}\rho u^2+K_{12}\rho uv+K_{13}\rho v^2+A_1$$
$$=K_{14}\frac{\partial p}{\partial \bar{\xi}}+K_{15}\frac{\partial p}{\partial \bar{\eta}}+\frac{\partial}{\partial \bar{\zeta}}\left(\mu\frac{\partial u}{\partial \bar{\zeta}}\right) \quad 3.19a$$

$\bar{\eta}$-momentum:

$$\rho\frac{\partial v}{\partial t}+\frac{\rho u}{h_1}\frac{\partial v}{\partial \bar{\xi}}+\frac{\rho v}{h_2}\frac{\partial v}{\partial \bar{\eta}}+\rho w\frac{\partial v}{\partial \bar{\zeta}}+K_{21}\rho u^2+K_{22}\rho uv+K_{23}\rho v^2+A_2$$
$$=K_{24}\frac{\partial p}{\partial \bar{\xi}}+K_{25}\frac{\partial p}{\partial \bar{\eta}}+\frac{\partial}{\partial \bar{\zeta}}\left(\mu\frac{\partial v}{\partial \bar{\zeta}}\right) \quad 3.20a$$

energy:

$$\rho\frac{\partial H}{\partial t}+\frac{\rho u}{h_1}\frac{\partial H}{\partial \bar{\xi}}+\frac{\rho v}{h_2}\frac{\partial H}{\partial \bar{\eta}}+\rho w\frac{\partial H}{\partial \bar{\zeta}}=\frac{\partial}{\partial \bar{\zeta}}\left[\frac{\mu}{Pr}\frac{\partial H}{\partial \bar{\zeta}}\right]$$
$$+(\gamma-1)M_\infty^2\frac{\partial}{\partial \bar{\zeta}}\left[\frac{\mu}{2}\left(1-\frac{1}{Pr}\right)\frac{\partial U_T^2}{\partial \bar{\zeta}}\right]+(\gamma-1)M_\infty^2\frac{\rho u\Omega^2}{h_1 2}\frac{\partial r^2}{\partial \bar{\xi}}$$
$$+(\gamma-1)M_\infty^2\frac{\rho v\Omega^2}{h_2 2}\frac{\partial r^2}{\partial \bar{\eta}}+(\gamma-1)M_\infty^2\rho\Omega^2 r\left[A_{02}u+A_{03}v\right] \quad 3.21c$$

$$T=T_e+(\gamma-1)M_\infty^2\frac{\left(U_{eT}^2-U_T^2\right)}{2c_p}+(\gamma-1)M_\infty^2\frac{\Omega^2\left(r^2-r_e^2\right)}{2c_p} \quad 3.39b$$

where $M_\infty^2=\dfrac{u_\infty^2}{\gamma R T_\infty}$

R is the gas constant $=c_p-c_v=\dfrac{c_p(\gamma-1)}{\gamma}$.

γ is the ratio of specific heats $= \frac{c_p}{c_v}$.

3.3 TURBULENT MODEL

The governing equations presented in section 3.2 are applicable to laminar flow. Therefore in this section, we will extend the boundary layer equations for the turbulent flow.

It is generally observed that the flow pattern in the boundary layer is laminar for a certain distance from the leading edge then further downstream the flow in the boundary layer becomes turbulent. A good indicator in determining whether the flow is laminar or turbulent is the Reynolds number. When the Reynolds number is very high (say > 10^7), the flow may be expected to become turbulent. Transition from laminar to turbulent flow in a boundary layer is a complex phenomenon and will not be considered in this study.

The flow pattern of turbulent flow is not constant in time but exhibits very irregular, high-frequency fluctuation. This irregular fluctuation may be characterised by random fluctuations of the flow variables around some average values. A method to find the solution of the flow is to replace this disorderly changing flow variables by time averages plus fluctuations about the average. For example, $u = \bar{u} + u''$, where bar superscript indicates the average value and the double prime superscript indicates the variation due to turbulent fluctuation (see Fig. 3.2). The time-average quantity $\bar{u}$ is defined as $\bar{u} = \lim_{\Delta t \to \infty} \frac{1}{\Delta t} \int_{t_0}^{t_0+\Delta t} u\,dt$. We require that Δt be large compared to the period of the random fluctuations associated with the turbulence, but small with respect to the time constant for any slow variations in a flowfield associated with ordinary unsteady flows (Anderson et al 1984). In practice, the limit $\Delta t \to \infty$ is taken to mean a time that is long

compared to a reciprocal of the predominant frequencies of the turbulent fluctuation in the spectrum of u. For a fluctuating quantity u', the time-average, $\overline{u''}$, is zero, whereas $\overline{\rho'' u''} \neq 0$, in general, unless $\rho' = 0$.

In compressible flows, the time averaging procedure creates some additional terms in the governing equations such as a mean-mass term (e.g. $\overline{\rho'' u''}$), momentum transport terms (e.g. $\bar{u}\overline{\rho'' v''}$, $\overline{\rho'' u'' v''}$). These additional terms may be eliminated by the mass-weighted-averaging procedure. We define mass-weighted mean variables according to $\tilde{f} = \frac{\overline{\rho f}}{\bar{\rho}}$, where the bar denotes time averaging and the tilde denotes mass-weighted averaging. The velocity $\tilde{u}$ may then be written as $\frac{\overline{\rho u}}{\bar{\rho}}$. We define new fluctuating quantities by $u = \tilde{u} + u'$ where u' is the superimposed velocity fluctuation. It should also be noted that the time average of the primed function multiplied by the density is equal to zero (e.g. $\overline{\rho u'} = 0$), whereas $\overline{u'} \neq 0$, in general, unless $\rho' = 0$.

In order to get the governing equations for turbulent flow, we substitute all the flow properties in the governing equations with the average and the fluctuation terms. The velocity components and thermal variables are mass averaged. Fluid properties such as density and pressure are time averaged. The entire equations are then time averaged. For further discussions see Cebeci and Smith (1974), and Anderson et al (1984). The new quantities, the turbulent stresses ($-\overline{\rho u'w'}$, $-\overline{\rho v'w'}$) and the turbulent heat flux ($-\overline{\rho w'T'}$), are the additional variables in the governing equations. The governing mean flow equations for compressible turbulent flow are (drop bar for convenience):

continuity:

$$\frac{\partial \rho}{\partial t} + \frac{1}{h_1 h_2 \sin\alpha}\left[\frac{\partial(h_2 \sin\alpha \rho u)}{\partial \bar{\xi}} + \frac{\partial(h_1 \sin\alpha \rho v)}{\partial \bar{\eta}} + \frac{\partial(h_1 h_2 \sin\alpha \rho w)}{\partial \bar{\zeta}}\right] = 0 \quad 3.18b$$

$\bar{\xi}$-momentum:

$$\rho\frac{\partial u}{\partial t}+\frac{\rho u}{h_1}\frac{\partial u}{\partial \bar{\xi}}+\frac{\rho v}{h_2}\frac{\partial u}{\partial \bar{\eta}}+\rho w\frac{\partial u}{\partial \bar{\zeta}}+K_{11}\rho u^2+K_{12}\rho uv+K_{13}\rho v^2+A_1$$

$$=K_{14}\frac{\partial p}{\partial \bar{\xi}}+K_{15}\frac{\partial p}{\partial \bar{\eta}}+\frac{\partial}{\partial \bar{\zeta}}\left(\mu\frac{\partial u}{\partial \bar{\zeta}}-\rho\overline{u'w'}\right) \qquad 3.19b$$

$\bar{\eta}$-momentum:

$$\rho\frac{\partial v}{\partial t}+\frac{\rho u}{h_1}\frac{\partial v}{\partial \bar{\xi}}+\frac{\rho v}{h_2}\frac{\partial v}{\partial \bar{\eta}}+\rho w\frac{\partial v}{\partial \bar{\zeta}}+K_{21}\rho u^2+K_{22}\rho uv+K_{23}\rho v^2+A_2$$

$$=K_{24}\frac{\partial p}{\partial \bar{\xi}}+K_{25}\frac{\partial p}{\partial \bar{\eta}}+\frac{\partial}{\partial \bar{\zeta}}\left(\mu\frac{\partial v}{\partial \bar{\zeta}}-\rho\overline{v'w'}\right) \qquad 3.20b$$

energy:

$$\rho\frac{\partial H}{\partial t}+\frac{\rho u}{h_1}\frac{\partial H}{\partial \bar{\xi}}+\frac{\rho v}{h_2}\frac{\partial H}{\partial \bar{\eta}}+\rho w\frac{\partial H}{\partial \bar{\zeta}}=\frac{\partial}{\partial \bar{\zeta}}\left[\frac{\mu}{Pr}\frac{\partial H}{\partial \bar{\zeta}}-\rho c_p\overline{w'T'}\right]$$

$$+\frac{\partial}{\partial \bar{\zeta}}\left[\frac{1}{2}\left(\mu-\frac{\mu}{Pr}\right)\frac{\partial U_T^2}{\partial \bar{\zeta}}\right]$$

$$+\frac{\partial}{\partial \bar{\zeta}}\left[-\rho u\overline{u'w'}-\rho v\overline{v'w'}-\rho u\overline{v'w'}\cos\alpha-\rho v\overline{u'w'}\cos\alpha\right]$$

$$+\frac{\rho u\Omega^2}{h_1 2}\frac{\partial r^2}{\partial \bar{\xi}}+\frac{\rho v\Omega^2}{h_2 2}\frac{\partial r^2}{\partial \bar{\eta}}+\rho\Omega^2 r[A_{02}u+A_{03}v] \qquad 3.21d$$

By using the mixing length model and the Boussinesq approximation it is possible to express the turbulent stresses in a similar way to laminar shear stresses by defining a turbulent viscosity and conductivity (Cousteix (1987) and Anderson et al (1984)). Therefore, the turbulent stresses ($-\rho\overline{u'w'}$, $-\rho\overline{v'w'}$) and the turbulent heat flux ($-\rho\overline{w'T'}$) may be evaluated in terms of the turbulent viscosity (μ_t) and the turbulent Prandtl number (Pr_t).

$$-\rho\overline{u'w'} = \mu_t \frac{\partial u}{\partial \bar{\zeta}}$$

$$-\rho\overline{v'w'} = \mu_t \frac{\partial v}{\partial \bar{\zeta}}$$

$$-\rho\overline{w'T'} = \frac{c_p \mu_t}{Pr_t} \frac{\partial T}{\partial \bar{\zeta}}$$

The temperature (T) in the energy equation can be expressed in term of H by using the definition of total enthalpy, $H = c_p T + U_T^2$. These substitutions permit the boundary-layer equations to be written as (in non-dimensional terms)

continuity:

$$\frac{\partial \rho}{\partial t} + \frac{1}{h_1 h_2 \sin\alpha}\left[\frac{\partial(h_2 \sin\alpha \rho u)}{\partial \bar{\xi}} + \frac{\partial(h_1 \sin\alpha \rho v)}{\partial \bar{\eta}} + \frac{\partial(h_1 h_2 \sin\alpha \rho w)}{\partial \bar{\zeta}}\right] = 0 \quad 3.18c$$

$\bar{\xi}$-momentum:

$$\rho\frac{\partial u}{\partial t} + \frac{\rho u}{h_1}\frac{\partial u}{\partial \bar{\xi}} + \frac{\rho v}{h_2}\frac{\partial u}{\partial \bar{\eta}} + \rho w \frac{\partial u}{\partial \bar{\zeta}} + K_{11}\rho u^2 + K_{12}\rho uv + K_{13}\rho v^2 + A_1$$
$$= K_{14}\frac{\partial p}{\partial \bar{\xi}} + K_{15}\frac{\partial p}{\partial \bar{\eta}} + \frac{\partial}{\partial \bar{\zeta}}\left(\left[\mu + \mu_t\right]\frac{\partial u}{\partial \bar{\zeta}}\right) \quad 3.19c$$

$\bar{\eta}$-momentum:

$$\rho\frac{\partial v}{\partial t} + \frac{\rho u}{h_1}\frac{\partial v}{\partial \bar{\xi}} + \frac{\rho v}{h_2}\frac{\partial v}{\partial \bar{\eta}} + \rho w \frac{\partial v}{\partial \bar{\zeta}} + K_{21}\rho u^2 + K_{22}\rho uv + K_{23}\rho v^2 + A_2$$
$$= K_{24}\frac{\partial p}{\partial \bar{\xi}} + K_{25}\frac{\partial p}{\partial \bar{\eta}} + \frac{\partial}{\partial \bar{\zeta}}\left(\left[\mu + \mu_t\right]\frac{\partial v}{\partial \bar{\zeta}}\right) \quad 3.20c$$

energy:

$$\rho\frac{\partial H}{\partial t} + \frac{\rho u}{h_1}\frac{\partial H}{\partial \bar{\xi}} + \frac{\rho v}{h_2}\frac{\partial H}{\partial \bar{\eta}} + \rho w \frac{\partial H}{\partial \bar{\zeta}} = \frac{\partial}{\partial \bar{\zeta}}\left[\left(\frac{\mu}{Pr} + \frac{\mu_t}{Pr_t}\right)\frac{\partial H}{\partial \bar{\zeta}}\right]$$
$$+(\gamma - 1)M_\infty^2 \frac{\partial}{\partial \bar{\zeta}}\left[\frac{1}{2}\left(\mu - \frac{\mu}{Pr} + \mu_t - \frac{\mu_t}{Pr_t}\right)\frac{\partial U_T^2}{\partial \bar{\zeta}}\right]$$

$$+(\gamma-1)M_{\infty}^2\frac{\rho u\Omega^2}{h_1 2}\frac{\partial r^2}{\partial\bar{\xi}}+(\gamma-1)M_{\infty}^2\frac{\rho v\Omega^2}{h_2 2}\frac{\partial r^2}{\partial\bar{\eta}}$$

$$+(\gamma-1)M_{\infty}^2\rho\Omega^2 r\left[A_{\omega 2}u+A_{\omega 3}v\right] \qquad 3.21e$$

Therefore a turbulent model must be defined to close the system of boundary-layer solutions. The turbulent Prandtl number (Pr_t) is a well-behaved function across the flow and may assume a constant near one, most commonly, $Pr_t \approx 0.9$ (Anderson et al (1984)). Turbulent problem is thus reduced to the evaluation of the turbulent eddy viscosity (μ_t). The μ_t is not a fluid property but a property of the flow and the geometry. It has the same dimensions as μ.

It should be noted that the equations in the turbulent flow resemble those in the laminar flow except that the former contain a turbulent eddy viscosity (μ_t) and the turbulent Prandtl number (Pr_t).

In this calculation we use the Baldwin-Lomax method (1978) to evaluate μ_t. This method is based on a simple algebraic turbulent model. The original model is derived from thin-layer approximation and modified for three-dimensional flow over a non-orthogonal surface in this study.

Baldwin-Lomax Model

The boundary layer is divided into an inner region and an outer region with a separate equation defining each region. μ_t is given by

$$\mu_t=\begin{cases}(\mu_t)_{inner} & \bar{\zeta}\le\bar{\zeta}_{crossover}\\ (\mu_t)_{outer} & \bar{\zeta}_{crossover}<\bar{\zeta}\end{cases} \qquad 3.40$$

where $\bar{\zeta}$ is the normal distance from the wall and $\bar{\zeta}_{crossover}$ is the smallest value of $\bar{\zeta}$ at which values from the inner and outer formula are equal.

In the Inner Region

Eddy viscosity in the inner region is defined as

$$(\mu_t)_{inner} = \rho\left\{0.4\bar{\zeta}\left(1-e^{\frac{-y^+}{A^+}}\right)\right\}^2 |\omega| \qquad 3.41$$

where $A^+=26$

$$y^+ = \bar{\zeta}\frac{\sqrt{\rho_w \tau_w}}{\mu_w}$$

τ_w = turbulent wall shear stress

$$= \mu_w\left[\left(\frac{\partial u}{\partial \bar{\zeta}}\right)_w^2 + \left(\frac{\partial v}{\partial \bar{\zeta}}\right)_w^2 + 2\cos\alpha\left(\frac{\partial u}{\partial \bar{\zeta}}\right)_w\left(\frac{\partial v}{\partial \bar{\zeta}}\right)_w\right]^{\frac{1}{2}} \qquad 3.42$$

$|\omega|$ = the magnitude of the vorticity

$$= \left[\left(\frac{\partial u}{\partial \bar{\zeta}}\right)^2 + \left(\frac{\partial v}{\partial \bar{\zeta}}\right)^2 + 2\cos\alpha\left(\frac{\partial u}{\partial \bar{\zeta}}\right)\left(\frac{\partial v}{\partial \bar{\zeta}}\right)\right]^{\frac{1}{2}} \qquad 3.43$$

In the Outer Region

In the outer regions, the eddy viscosity becomes

$$(\mu_t)_{outer} = \frac{0.0168 c_{kleb}\rho F_{wake}}{1+5.5\left(\frac{c_{cp}\bar{\zeta}}{\bar{\zeta}_{max}}\right)^6} \qquad 3.44$$

where $c_{kleb}=1.6$ 3.45

$c_{cp}=0.3$ 3.46

$$F_{wake} = \min\left\{\bar{\zeta}_{max}F_{max}, \frac{0.25\bar{\zeta}_{max}u_{dif}^2}{F_{max}}\right\} \qquad 3.47$$

$$u_{dif}^2 = \left(u^2 + v^2 + 2\cos\alpha uv\right)_{max} \qquad 3.48$$

F_{max} and $\bar{\zeta}_{max}$ are determined from the function:

$$F(\bar{\zeta}) = \bar{\zeta}|\omega|\left(1 - e^{\frac{-y^+}{A^+}}\right) \qquad 3.49$$

F_{max} is the maximum value of $F(\bar{\zeta})$ that occurs in a profile and $\bar{\zeta}_{max}$ is the value of $\bar{\zeta}$ at which it occurs.

In a wake, the outer formulation is applied across the entire shear layer and in the Baldwin-Lomax model the exponential term in the $F(\bar{\zeta})$ function is set to zero.

3.4 GRID GENERATION AND TRANSFORMATION

The systems of governing equations are now applicable for laminar or turbulent flow. In order to avoid the complexity of the similarity transformations and to solve the equations directly, we have to scale out the viscous-layer growth by using co-ordinate transformation. This will not only make the equations simple to solve but also make them general to implement.

From section 3.2, the system of governing equations is written in the co-ordinate surface such that $\bar{\xi}$ and $\bar{\eta}$ are the grid lines along the surface with an angle α between them and $\bar{\zeta}$ is in the normal direction. The accurate solution of the boundary-layer equations for the flow using finite difference models that evaluate the flow's properties at all points within the layer requires a very fine mesh near the wall. This is because boundary layer flows contain severe velocity

gradients normal to the surface. In the case of turbulent flow, the grid points have to be located within the viscous sublayer. A technique to generate an unequal grid spacing will be discussed in the next section.

3.4.1 VARIABLE GRID SPACING IN THE NORMAL DIRECTION

In boundary-layer flow problems, the normal cluster grid points near solid boundaries are mandatory to provide adequate resolution of the viscous boundary layer. The variable grid spacing is formed by using a geometric series such that the quotient of two consecutive terms is constant.

$$RY = \frac{\Delta\bar{\zeta}_k}{\Delta\bar{\zeta}_{k-1}} \qquad 3.50$$

where RY is the grid growth ratio which is greater than 1.

From the geometric series theory, we can prove that the distance to the k^{th} grid line is given by

$$\bar{\zeta}_k = \Delta\bar{\zeta}_1 \frac{(RY^{k-1}-1)}{(RY-1)} \qquad 3.51$$

where $\Delta\bar{\zeta}_1$ is the distance from the solid wall to the first grid line. If turbulent flow is computed, $\Delta\bar{\zeta}_1$ is chosen so that the first grid point is placed at approximately $\Delta\bar{\zeta}^+ \approx 1.5$ (defined as $\Delta\bar{\zeta}\frac{(\rho_w\tau_w)^{\frac{1}{2}}}{\mu_w}$) in order to resolve the thin laminar sublayer (Anderson et al (1984)). In the case where $\Delta\bar{\zeta}_1$ is constant for the whole calculation, the grid growth ratio (RY) should be varied at different grid points in the flow direction since the boundary-layer edge is a function of the distance measured from the leading edge. In the above, RY is actually obtained from the solution of equation (3.51) at a specified value of $\bar{\zeta}_{kmax}$. Since the

equation is non-linear, we can get the solution by using Newton's method. For this method, it gives

$$RY_{n+1} = RY_n - \frac{f(RY_n)}{f'(RY_n)} \qquad 3.52$$

where $f(RY_n) = \Delta\bar{\zeta}_1 \frac{(RY_n^{k\max-1} - 1)}{\bar{\zeta}_{k\max}} - (RY_n - 1)$ 3.53

$$f'(RY_n) = \Delta\bar{\zeta}_1 \frac{(k\max - 1)RY_n^{k\max-2}}{\bar{\zeta}_{k\max}} - 1 \qquad 3.54$$

RY_n = RY at the iteration n^{th}

Thus, starting with an initial guess value of RY_n, an improved approximation, RY_{n+1}, can be computed from the above equation. The process is repeated iteratively until $\left|\frac{f(RY_n)}{f'(RY_n)}\right|$ is lower than an allowance value. The procedure usually converges in three or four iterations since the convergence of the Newton's iteration is rapid. Typically in laminar flow RY is set to 1.07 and then $\Delta\bar{\zeta}^+$ is varied. While in turbulent $\Delta\bar{\zeta}^+$ is set to about 1.5 (in order to model the laminar sublayer) and the RY is varied.

3.4.2 UNIFORMLY SPACED GRID EQUATIONS

The governing equations can be solved on a uniformly spaced grid that is more reliable, efficient and simpler than that on a non-uniformly spaced grid by using an appropriate transformation. In the boundary layer equations, we can see that only the normal grid that is not uniform. Therefore, we can relate the non-uniformly grid system ($\bar{\xi}$, $\bar{\eta}$, $\bar{\zeta}$) to the uniformly grid system (ξ, η, ζ) through equation (3.55).

$$\xi = \xi(\bar{\xi})$$

$$\eta = \eta(\bar{\eta})$$
$$\zeta = \zeta(\bar{\xi}, \bar{\eta}, \bar{\zeta}) \qquad 3.55$$

The method of transformation is based on the chain rule of partial differentiation. Therefore, we get

$$\frac{\partial}{\partial \bar{\xi}} = \xi_{\bar{\xi}} \frac{\partial}{\partial \xi} + \zeta_{\bar{\xi}} \frac{\partial}{\partial \zeta}$$
$$\frac{\partial}{\partial \bar{\eta}} = \eta_{\bar{\eta}} \frac{\partial}{\partial \eta} + \zeta_{\bar{\eta}} \frac{\partial}{\partial \zeta}$$
$$\frac{\partial}{\partial \bar{\zeta}} = \zeta_{\bar{\zeta}} \frac{\partial}{\partial \zeta} \qquad 3.56$$

The transformed parameters in the above equations are:

$$\xi_{\bar{\xi}} = 1$$
$$\eta_{\bar{\eta}} = 1$$
$$\zeta_{\bar{\xi}} = \frac{\bar{\zeta}_{\xi}}{\bar{\zeta}_{\zeta}}$$
$$\zeta_{\bar{\eta}} = -\frac{\bar{\zeta}_{\eta}}{\bar{\zeta}_{\zeta}}$$
$$\zeta_{\bar{\zeta}} = \frac{1}{\bar{\zeta}_{\zeta}} \qquad 3.57$$

For general transformation the reader can refer to Anderson et al (1984) and Fletcher (1991). The subscripts by ξ, η and ζ in the equations (3.56-3.57) mean differentiation with respect to ξ, η and ζ,respectively. The barred term is a non-uniformly spaced computational grid.

Suppose we apply the transformation given in equation (3.56) to the governing equations (3.19a-3.21a). The compressible boundary-layer equations

for the unsteady, three-dimensional can be written in the uniformly spaced grid ξ $(\bar{\xi})$, $\eta(\bar{\eta})$, $\zeta(\bar{\xi}, \bar{\eta}, \bar{\zeta})$ co-ordinates as

$$\frac{\partial \rho}{\partial t}+\frac{1}{h_1 h_2 \sin\alpha}\left[\frac{\partial(h_2 \sin\alpha \rho u)}{\partial \xi}+\zeta_{\bar{\xi}}\frac{\partial(h_2 \sin\alpha \rho u)}{\partial \zeta}\right]$$

$$+\frac{1}{h_1 h_2 \sin\alpha}\left[\frac{\partial(h_1 \sin\alpha \rho v)}{\partial \eta}+\zeta_{\bar{\eta}}\frac{\partial(h_1 \sin\alpha \rho v)}{\partial \zeta}\right]$$

$$+\frac{1}{h_1 h_2 \sin\alpha}\left[\zeta_{\bar{\zeta}}\frac{\partial(h_1 h_2 \sin\alpha \rho w)}{\partial \zeta}\right]=0 \qquad 3.58$$

$$\rho\frac{\partial u}{\partial t}+\frac{\rho u}{h_1}\frac{\partial u}{\partial \xi}+\frac{\rho u}{h_1}\zeta_{\bar{\xi}}\frac{\partial u}{\partial \zeta}+\frac{\rho v}{h_2}\frac{\partial u}{\partial \eta}+\frac{\rho v}{h_2}\zeta_{\bar{\eta}}\frac{\partial u}{\partial \zeta}+\rho w\zeta_{\bar{\zeta}}\frac{\partial u}{\partial \zeta}$$

$$+K_{11}\rho u^2+K_{12}\rho uv+K_{13}\rho v^2+A_1$$

$$=K_{14}\frac{\partial p}{\partial \xi}+K_{15}\frac{\partial p}{\partial \eta}+\zeta_{\bar{\xi}}\frac{\partial}{\partial \zeta}\left(\mu\zeta_{\bar{\xi}}\frac{\partial u}{\partial \zeta}\right) \qquad 3.59$$

$$\rho\frac{\partial v}{\partial t}+\frac{\rho u}{h_1}\frac{\partial v}{\partial \xi}+\frac{\rho u}{h_1}\zeta_{\bar{\xi}}\frac{\partial v}{\partial \zeta}+\frac{\rho v}{h_2}\frac{\partial v}{\partial \eta}+\frac{\rho v}{h_2}\zeta_{\bar{\eta}}\frac{\partial v}{\partial \zeta}+\rho w\zeta_{\bar{\zeta}}\frac{\partial v}{\partial \zeta}$$

$$+K_{21}\rho u^2+K_{22}\rho uv+K_{23}\rho v^2+A_2$$

$$=K_{24}\frac{\partial p}{\partial \xi}+K_{25}\frac{\partial p}{\partial \eta}+\zeta_{\bar{\xi}}\frac{\partial}{\partial \zeta}\left(\mu\zeta_{\bar{\xi}}\frac{\partial v}{\partial \zeta}\right) \qquad 3.60$$

$$\rho\frac{\partial H}{\partial t}+\frac{\rho u}{h_1}\frac{\partial H}{\partial \xi}+\frac{\rho u}{h_1}\zeta_{\bar{\xi}}\frac{\partial H}{\partial \zeta}+\frac{\rho v}{h_2}\frac{\partial H}{\partial \eta}+\frac{\rho v}{h_2}\zeta_{\bar{\eta}}\frac{\partial H}{\partial \zeta}+\rho w\zeta_{\bar{\zeta}}\frac{\partial H}{\partial \zeta}$$

$$=\zeta_{\bar{\xi}}\frac{\partial}{\partial \zeta}\left[\frac{\mu}{P_r}\zeta_{\bar{\xi}}\frac{\partial H}{\partial \zeta}+\frac{\mu}{2}\left(1-\frac{1}{P_r}\right)\zeta_{\bar{\xi}}\frac{\partial U_T}{\partial \zeta}\right]$$

$$+\frac{\rho u\Omega^2}{h_1 2}\xi_{\bar{\xi}}\frac{\partial r^2}{\partial \xi}+\frac{\rho v\Omega^2}{h_2 2}\eta_{\bar{\eta}}\frac{\partial r^2}{\partial \eta}+\rho\Omega^2 r\left[A_{02}u+A_{03}v\right] \qquad 3.61$$

3.5 DISCRETIZATION

In order to avoid confusion about the numerical schemes, the discretization of the momentum and the energy equations is considered in this section while that of the continuity equation is presented separately in the continuity equation section of numerical solution algorithm. The discrete form of the equations is centred at (i,j,k,n) where i, j and k are the points in ξ, η and ζ direction, respectively, and n is the n^{th} time level. A solution of the discretized equations is assumed to be known at time n for all i, j and k (i.e. on a whole plane). Therefore the finite-difference forms of the equations are used to predict the solution at the n+1 level. The formulas given below are used to approximate terms involving derivatives with respect to ξ, η, ζ and t. Superscripts and subscripts on the formula are used to specify their position and are not written if their values are unchanged from (i, j, k, n).

Before we discuss further about the discrete forms, one should bear in mind that the same scheme of discretization is used to evaluate the transformation parameters (e.g. $\zeta_{\bar{\xi}}$, $\zeta_{\bar{\eta}}$, $\zeta_{\bar{\zeta}}$) and the derivatives in the governing equations. For this reason, the discrete form of the transformation parameters will not be presented. The same scheme of discretization for geometrical parameters is important to ensure the accuracy of the solutions.

Discretization Schemes for Momentum and Energy Equations

Time derivative

The governing equations are integrated in time. Therefore the time derivative is approximated for an expansion level n+1 with forward differencing. This scheme is first order accurate and can be written as

$$\rho\frac{\partial u}{\partial t}=\rho\frac{u^{n+1}-u}{\Delta t} \qquad 3.62$$

The scheme is applied to the terms with time derivative of the governing equations (3.51-3.54).

ξ- & η-derivatives

For spatial derivatives parallel to the body surface (ξ-, ζ-directions) an explicit second-order accurate upwind difference operator is used. The use of an upwind scheme especially in cross-flow direction will suppress the break down of calculation when reverse flow occurs (e.g. v<0, Johnston (1990)). By using this scheme, the way in which the derivative can be evaluated is subjected to the sign of coefficient term. A convective transport term, e.g. $\frac{\rho u}{h_1}\frac{\partial u}{\partial \xi}$, can be written in an upwind scheme as

$$\frac{\rho u}{h_1}\frac{\partial u}{\partial \xi}=\frac{\rho}{h_1}\left[\frac{(u+|u|)}{2}\frac{1}{\alpha_{i1}\Delta\xi}(\alpha_{i2}u+\alpha_{i3}u_{i-1}+\alpha_{i4}u_{i-2})\right]$$
$$+\frac{\rho}{h_1}\left[\frac{(u-|u|)}{2}\frac{1}{\beta_{i1}\Delta\xi}(\beta_{i2}u+\beta_{i3}u_{i+1}+\beta_{i4}u_{i+2})\right] \qquad 3.63$$

where the coefficients α_{i1}-α_{i4} and β_{i1}-β_{i4} are given in table 3.1. This equation can be applied only to ξ-derivative. A similar expression is used for η-derivative and the coefficients α_{j1}-α_{j4} and β_{j1}-β_{j4} are given in table 3.2.

Table 3.1: The coefficients at various values of i (for momentum and energy equations, see equation 3.63)

i	α_{i1}	α_{i2}	α_{i3}	α_{i4}	β_{i1}	β_{i2}	β_{i3}	β_{i4}
i=2	1	1	-1	0	2	-3	4	-1
3≤i≤iend-2	2	3	-4	1	2	-3	4	-1
i=iend-1	2	3	-4	1	1	-1	1	0
i=iend	2	3	-4	1	1	0	0	0

Table 3.2: The coefficients at various values of j (for momentum and energy equations)

$$\frac{\rho v}{h_2}\frac{\partial u}{\partial \eta} = \frac{\rho}{h_2}\left[\frac{(v+|v|)}{2}\frac{1}{\alpha_{j1}\Delta\eta}\left(\alpha_{j2}u+\alpha_{j3}u_{j-1}+\alpha_{j4}u_{j-2}\right)\right] + \frac{\rho}{h_2}\left[\frac{(v-|v|)}{2}\frac{1}{\beta_{i1}\Delta\eta}\left(\beta_{j2}u+\beta_{j3}u_{j+1}+\beta_{j4}u_{j+2}\right)\right]$$

j	α_{j1}	α_{j2}	α_{j3}	α_{j4}	β_{j1}	β_{j2}	β_{j3}	β_{j4}
j=1	1	0	0	0	2	-3	4	-1
j=2	1	1	-1	0	2	-3	4	-1
3≤j≤jend-2	2	3	-4	1	2	-3	4	-1
j=jend-1	2	3	-4	1	1	-1	1	0
j=jend	2	3	-4	1	1	0	0	0

ζ-derivatives

For spatial derivatives normal to a solid surface (ζ-direction) an implicit second-order accurate central difference operator is used. By applying the scheme to the terms with ζ-derivative, e.g. $\rho w \zeta_{\bar{\zeta}} \frac{\partial u}{\partial \zeta}$, the difference formula can be written as

$$\rho w \zeta_{\bar{\zeta}} \frac{\partial u}{\partial \zeta} = \rho w \zeta_{\bar{\zeta}} \frac{(u_{k+1}-u_{k-1})^{n+1}}{2\Delta\zeta} \qquad 3.64$$

3.6 NUMERICAL SOLUTION ALGORITHM

The discretizations (3.62-3.64) are applied in the momentum and energy equations. The quantities unknown at n+1 level in the equations are obtained by solving a set of tridiagonal matrix system. The truncation error of the difference equations is of order ($\Delta\xi^2$, $\Delta\eta^2$, $\Delta\zeta^2$, Δt) except at lateral boundaries.

3.6.1 ξ-MOMENTUM EQUATION

The u^{n+1} values across the boundary-layer are obtained from ξ-momentum. The tridiagonal matrix is given in equation (3.65)

$$a\, u_{k-1}^{n+1} + b\, u^{n+1} + c\, u_{k+1}^{n+1} = RHS \qquad 3.65$$

where $a = -\frac{\rho u}{h_1}\zeta_{\bar{\xi}}\frac{1}{2\Delta\zeta} - \frac{\rho v}{h_2}\zeta_{\bar{\eta}}\frac{1}{2\Delta\zeta} - \rho w\zeta_{\bar{\zeta}}\frac{1}{2\Delta\zeta} - \frac{\zeta_{\bar{\xi}}}{2\Delta\zeta\Delta\zeta}\left(\mu\zeta_{\bar{\xi}} + \left\langle\mu\zeta_{\bar{\xi}}\right\rangle_{k-1}\right)$

$$b = \rho\frac{1}{\Delta t} + \frac{\zeta_{\bar{\xi}}}{2\Delta\zeta\Delta\zeta}\left(\left\langle\mu\zeta_{\bar{\xi}}\right\rangle_{k-1} + 2\mu\zeta_{\bar{\xi}} + \left\langle\mu\zeta_{\bar{\xi}}\right\rangle_{k+1}\right)$$

$$c = \frac{\rho u}{h_1}\zeta_{\bar{\xi}}\frac{1}{2\Delta\zeta} + \frac{\rho v}{h_2}\zeta_{\bar{\eta}}\frac{1}{2\Delta\zeta} + \rho w\zeta_{\bar{\zeta}}\frac{1}{2\Delta\zeta} - \frac{\zeta_{\bar{\xi}}}{2\Delta\zeta\Delta\zeta}\left(\mu\zeta_{\bar{\xi}} + \left\langle\mu\zeta_{\bar{\xi}}\right\rangle_{k+1}\right)$$

$$RHS = \rho\frac{u}{\Delta t}$$

$$-\frac{\rho}{h_1}\left[\frac{(u+|u|)}{2}\frac{1}{\alpha_{i1}\Delta\xi}\left(\alpha_{i2}u + \alpha_{i3}u_{i-1} + \alpha_{i4}u_{i-2}\right)\right]$$

$$-\frac{\rho}{h_1}\left[\frac{(u-|u|)}{2}\frac{1}{\beta_{i1}\Delta\xi}\left(\beta_{i2}u + \beta_{i3}u_{i+1} + \beta_{i4}u_{i+2}\right)\right]$$

$$-\frac{\rho}{h_2}\left[\frac{(v+|v|)}{2}\frac{1}{\alpha_{j1}\Delta\eta}\left(\alpha_{j2}u + \alpha_{j3}u_{j-1} + \alpha_{j4}u_{j-2}\right)\right]$$

$$-\frac{\rho}{h_2}\left[\frac{(v-|v|)}{2}\frac{1}{\beta_{j1}\Delta\eta}\left(\beta_{j2}u + \beta_{j3}u_{j+1} + \beta_{j4}u_{j+2}\right)\right]$$

$$+\frac{\rho_e}{h_1}\left[\frac{(u_e+|u_e|)}{2}\frac{1}{\alpha_{i1}\Delta\xi}\left(\alpha_{i2}u_e + \alpha_{i3}u_{ei-1} + \alpha_{i4}u_{ei-2}\right)\right]$$

$$+\frac{\rho_e}{h_1}\left[\frac{(u_e-|u_e|)}{2}\frac{1}{\beta_{i1}\Delta\xi}\left(\beta_{i2}u_e + \beta_{i3}u_{ei+1} + \beta_{i4}u_{ei+2}\right)\right]$$

$$+\frac{\rho_e}{h_2}\left[\frac{(v_e+|v_e|)}{2}\frac{1}{\alpha_{j1}\Delta\eta}\left(\alpha_{j2}u_e + \alpha_{j3}u_{ej-1} + \alpha_{j4}u_{ej-2}\right)\right]$$

$$+\frac{\rho_e}{h_2}\left[\frac{(v_e-|v_e|)}{2}\frac{1}{\beta_{j1}\Delta\eta}\left(\beta_{j2}u_e+\beta_{j3}u_{ej-1}+\beta_{j4}u_{ej-2}\right)\right]$$

$$+K_{11}(\rho_e u_e^2-\rho u^2)+K_{12}(\rho_e u_e v_e-\rho uv)+K_{13}(\rho_e v_e^2-\rho v^2)$$

$$+A_{11}2\Omega\left(\{\rho u-\rho_e u_e\}\cos\alpha+\{\rho v-\rho_e v_e\}\right)+A_{12}\Omega^2 r(\rho-\rho_e)$$

$$A_{11}=\frac{1}{\sin\alpha}\frac{1}{h_1h_2\sin\alpha}\left(\frac{\partial r_b}{\partial\bar{\xi}}\frac{r_b\partial\theta_b}{\partial\bar{\eta}}-\frac{r_b\partial\theta_b}{\partial\bar{\xi}}\frac{\partial r_b}{\partial\bar{\eta}}\right)$$

$$A_{12}=\frac{1}{\sin^2\alpha}\left(\frac{1}{h_1}\frac{\partial r_b}{\partial\bar{\xi}}-\frac{\cos\alpha}{h_2}\frac{\partial r_b}{\partial\bar{\eta}}\right)$$

3.6.2 η-MOMENTUM EQUATION

The v^{n+1} values across the boundary layer are obtained from η-momentum with updated values of u^{n+1} from equation (3.65). The tridiagonal matrix is given in equation (3.66).

$$a\,v_{k-1}^{n+1}+b\,v^{n+1}+c\,v_{k+1}^{n+1}=RHS \qquad 3.66$$

$$\text{where } a=-\frac{\rho u^{n+1}}{h_1}\zeta_{\bar{\xi}}\frac{1}{2\Delta\zeta}-\frac{\rho v}{h_2}\zeta_{\bar{\eta}}\frac{1}{2\Delta\zeta}-\rho w\zeta_{\bar{\zeta}}\frac{1}{2\Delta\zeta}-\frac{\zeta_{\bar{\zeta}}}{2\Delta\zeta\Delta\zeta}\left(\mu\zeta_{\bar{\zeta}}+\left\langle\mu\zeta_{\bar{\zeta}}\right\rangle_{k-1}\right)$$

$$b=\rho\frac{1}{\Delta t}+\frac{\zeta_{\bar{\zeta}}}{2\Delta\zeta\Delta\zeta}\left(\left\langle\mu\zeta_{\bar{\zeta}}\right\rangle_{k-1}+2\mu\zeta_{\bar{\zeta}}+\left\langle\mu\zeta_{\bar{\zeta}}\right\rangle_{k+1}\right)$$

$$c=\frac{\rho u^{n+1}}{h_1}\zeta_{\bar{\xi}}\frac{1}{2\Delta\zeta}+\frac{\rho v}{h_2}\zeta_{\bar{\eta}}\frac{1}{2\Delta\zeta}+\rho w\zeta_{\bar{\zeta}}\frac{1}{2\Delta\zeta}-\frac{\zeta_{\bar{\zeta}}}{2\Delta\zeta\Delta\zeta}\left(\mu\zeta_{\bar{\zeta}}+\left\langle\mu\zeta_{\bar{\zeta}}\right\rangle_{k+1}\right)$$

$$RHS=\rho\frac{v}{\Delta t}$$

$$-\frac{\rho}{h_1}\left[\frac{\left(u^{n+1}+\left|u^{n+1}\right|\right)}{2}\frac{1}{\alpha_{i1}\Delta\xi}\left(\alpha_{i2}v+\alpha_{i3}v_{i-1}+\alpha_{i4}v_{i-2}\right)\right]$$

$$-\frac{\rho}{h_1}\left[\frac{\left(u^{n+1}-\left|u^{n+1}\right|\right)}{2}\frac{1}{\beta_{i1}\Delta\xi}\left(\beta_{i2}v+\beta_{i3}v_{i+1}+\beta_{i4}v_{i+2}\right)\right]$$

$$-\frac{\rho}{h_2}\left[\frac{\left(v+|v|\right)}{2}\frac{1}{\alpha_{j1}\Delta\eta}\left(\alpha_{j2}v+\alpha_{j3}v_{j-1}+\alpha_{j4}v_{j-2}\right)\right]$$

$$-\frac{\rho}{h_2}\left[\frac{\left(v-|v|\right)}{2}\frac{1}{\beta_{j1}\Delta\eta}\left(\beta_{j2}v+\beta_{j3}v_{j+1}+\beta_{j4}v_{j+2}\right)\right]$$

$$+\frac{\rho_e}{h_1}\left[\frac{\left(u_e^{n+1}+\left|u_e^{n+1}\right|\right)}{2}\frac{1}{\alpha_{i1}\Delta\xi}\left(\alpha_{i2}v_e+\alpha_{i3}v_{ei-1}+\alpha_{i4}v_{ei-2}\right)\right]$$

$$+\frac{\rho_e}{h_1}\left[\frac{\left(u_e^{n+1}-\left|u_e^{n+1}\right|\right)}{2}\frac{1}{\beta_{i1}\Delta\xi}\left(\beta_{i2}v_e+\beta_{i3}v_{ei+1}+\beta_{i4}v_{ei+2}\right)\right]$$

$$+\frac{\rho_e}{h_2}\left[\frac{\left(v_e+|v_e|\right)}{2}\frac{1}{\alpha_{j1}\Delta\eta}\left(\alpha_{j2}v_e+\alpha_{j3}v_{ej-1}+\alpha_{j4}v_{ej-2}\right)\right]$$

$$+\frac{\rho_e}{h_2}\left[\frac{\left(v_e-|v_e|\right)}{2}\frac{1}{\beta_{j1}\Delta\eta}\left(\beta_{j2}v_e+\beta_{j3}v_{ej+1}+\beta_{j4}v_{ej+2}\right)\right]$$

$$+K_{21}\left(\rho_e\left[u_e^{n+1}\right]^2-\rho\left[u^{n+1}\right]^2\right)+K_{22}(\rho_e u_e{}^{n+1}v_e-\rho u^{n+1}v)+K_{23}(\rho_e v_e{}^2-\rho v^2)$$

$$-A_{11}2\Omega\left(\{\rho u-\rho_e u_e\}+\{\rho v-\rho_e v_e\}\cos\alpha\right)+A_{22}\Omega^2 r(\rho-\rho_e)$$

$$A_{22}=\frac{1}{\sin^2\alpha}\left(\frac{1}{h_2}\frac{\partial r_b}{\partial\eta}-\frac{\cos\alpha}{h_1}\frac{\partial r_b}{\partial\xi}\right)$$

3.6.3 ENERGY EQUATION

The tridiagonal matrix of the energy equation is similar to those of the momentum equations. The H^{n+1} values across the boundary-layer are obtained from the tridiagonal matrix in the equation (3.67) with updated values of u^{n+1} and v^{n+1}.

$$a\,H_{k-1}^{n+1} + b\,H^{n+1} + c\,H_{k+1}^{n+1} = RHS \qquad 3.67$$

where $a = -\frac{\rho u^{n+1}}{h_1}\zeta_{\bar{\xi}}\frac{1}{2\Delta\zeta} - \frac{\rho v^{n+1}}{h_2}\zeta_{\bar{\eta}}\frac{1}{2\Delta\zeta} - \rho w\zeta_{\bar{\zeta}}\frac{1}{2\Delta\zeta}$

$$-\frac{\zeta_{\bar{\zeta}}}{2\Delta\zeta\Delta\zeta}\left(\frac{\mu}{P_r}\zeta_{\bar{\zeta}} + \left\langle\frac{\mu}{P_r}\zeta_{\bar{\zeta}}\right\rangle_{k-1}\right)$$

$$b = \rho\frac{1}{\Delta t} + \frac{\zeta_{\bar{\zeta}}}{2\Delta\zeta\Delta\zeta}\left(\left\langle\frac{\mu}{P_r}\zeta_{\bar{\zeta}}\right\rangle_{k-1} + 2\frac{\mu}{P_r}\zeta_{\bar{\zeta}} + \left\langle\frac{\mu}{P_r}\zeta_{\bar{\zeta}}\right\rangle_{k+1}\right)$$

$$c = \frac{\rho u^{n+1}}{h_1}\zeta_{\bar{\xi}}\frac{1}{2\Delta\zeta} + \frac{\rho v^{n+1}}{h_2}\zeta_{\bar{\eta}}\frac{1}{2\Delta\zeta} + \rho w\zeta_{\bar{\zeta}}\frac{1}{2\Delta\zeta}$$

$$-\frac{\zeta_{\bar{\zeta}}}{2\Delta\zeta\Delta\zeta}\left(\frac{\mu}{P_r}\zeta_{\bar{\zeta}} + \left\langle\frac{\mu}{P_r}\zeta_{\bar{\zeta}}\right\rangle_{k+1}\right)$$

RHS =

$$\rho\frac{H}{\Delta t} + \rho\Omega^2 r\left[A_{\omega 2}u + A_{\omega 3}v\right]$$

$$-\frac{\rho}{h_1}\left[\frac{\left(u^{n+1} + |u^{n+1}|\right)}{2}\frac{1}{\alpha_{i1}\Delta\xi}\left(\alpha_{i2}H + \alpha_{i3}H_{i-1} + \alpha_{i4}H_{i-2}\right)\right]$$

$$-\frac{\rho}{h_1}\left[\frac{\left(u^{n+1} - |u^{n+1}|\right)}{2}\frac{1}{\beta_{i1}\Delta\xi}\left(\beta_{i2}H + \beta_{i3}H_{i+1} + \beta_{i4}H_{i+2}\right)\right]$$

$$-\frac{\rho}{h_2}\left[\frac{\left(v^{n+1} + |v^{n+1}|\right)}{2}\frac{1}{\alpha_{j1}\Delta\eta}\left(\alpha_{j2}H + \alpha_{j3}H_{j-1} + \alpha_{j4}H_{j-2}\right)\right]$$

$$-\frac{\rho}{h_2}\left[\frac{\left(v^{n+1} - |v^{n+1}|\right)}{2}\frac{1}{\beta_{j1}\Delta\eta}\left(\beta_{j2}H + \beta_{j3}H_{j+1} + \beta_{j4}H_{j+2}\right)\right]$$

$$+\frac{\zeta_{\bar{\zeta}}}{2\Delta\zeta\Delta\zeta}\left(\mu\left\{1-\frac{1}{P_r}\right\}\zeta_{\bar{\zeta}} + \left\langle\mu\left\{1-\frac{1}{P_r}\right\}\zeta_{\bar{\zeta}}\right\rangle_{k-1}\right)\frac{\left(U_{T_{k-1}}^{n+1}\right)^2}{2}$$

$$-\frac{\zeta_{\bar{\zeta}}}{2\Delta\zeta\Delta\zeta}\left(\left\langle\mu\left\{1-\frac{1}{P_r}\right\}\zeta_{\bar{\zeta}}\right\rangle_{k-1} + 2\mu\left\{1-\frac{1}{P_r}\right\}\zeta_{\bar{\zeta}} + \left\langle\mu\left\{1-\frac{1}{P_r}\right\}\zeta_{\bar{\zeta}}\right\rangle_{k+1}\right)\frac{\left(U_T^{n+1}\right)^2}{2}$$

$$+\frac{\zeta_{\bar{\xi}}}{2\Delta\zeta\Delta\zeta}\left(\mu\left\{1-\frac{1}{P_r}\right\}\zeta_{\bar{\xi}}+\left\langle\mu\left\{1-\frac{1}{P_r}\right\}\zeta_{\bar{\xi}}\right\rangle_{k+1}\right)\frac{\left(U_{T_{k+1}}^{n+1}\right)^2}{2}$$

$$+\frac{\rho\Omega^2}{h_1 2}\left[\frac{\left(u^{n+1}+\left|u^{n+1}\right|\right)}{2}\frac{1}{\alpha_{i1}\Delta\xi}\left(\alpha_{i2}r^2+\alpha_{i3}r^2{}_{i-1}+\alpha_{i4}r^2{}_{i-2}\right)\right]$$

$$+\frac{\rho\Omega^2}{h_1 2}\left[\frac{\left(u^{n+1}-\left|u^{n+1}\right|\right)}{2}\frac{1}{\beta_{i1}\Delta\xi}\left(\beta_{i2}r^2+\beta_{i3}r^2{}_{i+1}+\beta_{i4}r^2{}_{i+2}\right)\right]$$

$$+\frac{\rho\Omega^2}{h_2 2}\left[\frac{\left(v^{n+1}+\left|v^{n+1}\right|\right)}{2}\frac{1}{\alpha_{j1}\Delta\eta}\left(\alpha_{j2}r^2+\alpha_{j3}r^2{}_{j-1}+\alpha_{j4}r^2{}_{j-2}\right)\right]$$

$$+\frac{\rho\Omega^2}{h_2 2}\left[\frac{\left(v^{n+1}-\left|v^{n+1}\right|\right)}{2}\frac{1}{\beta_{j1}\Delta\eta}\left(\beta_{j2}r^2+\beta_{j3}r^2{}_{j+1}+\beta_{j4}r^2{}_{j+2}\right)\right]$$

The energy equation may be replaced by conservation of rothalpy. The approximate value is obtained by assuming $Pr \approx Pr_t \approx 1$ and the adiabatic wall condition. As a result the temperature across boundary layer is expressed as a function of the velocity. For detail see section 3.2.4 Approximate Equation for the Energy Equation.

3.6.4 FLUID PROPERTY EQUATIONS

The values of density (ρ) at n+1 are computed from the ideal-gas law, once the temperature is known. The fluid's viscosity (μ) is computed from the viscosity law of the fluid. For turbulent flow, the turbulent viscosity (μ_t) is evaluated as prescribed in section 3.3.

$$T^{n+1}=\left[H-\frac{(\gamma-1)M_\infty^2}{2}U_T^2\right]^{n+1} \qquad 3.68$$

$$\rho^{n+1}=\left[\frac{\rho_e T_e}{T}\right]^{n+1} \qquad 3.69$$

$$\mu^{n+1}=\mu_e\left[\frac{T^{n+1}}{T_e}\right]^{0.66} \qquad 3.70$$

3.6.5 DISCRETIZATION SCHEME FOR CONTINUITY EQUATION

Once u, v, H, ρ, μ and μ_t are known at n+1, therefore the value w at n+1 can be computed from the continuity equation (3.18). The formulae given below are used to approximate terms involving derivatives with respect to the spatial co-ordinate directions. The discrete form of the continuity equation is centred at (i, j, $k+\frac{1}{2}$, n+1).

ξ- & η-derivatives

The ξ derivative is approximated with a backward difference second order accurate formula, except at the lateral boundaries. The discretization of this derivative (at i, j, k, n) can be written in the general form with the coefficients α_{i1}-α_{i4} as follows,

$$\frac{\partial(\rho u)}{\partial \xi} = \frac{1}{\alpha_{i1}\Delta\xi}\left(\alpha_{i2}\rho u + \alpha_{i3}\rho u_{i-1} + \alpha_{i4}\rho u_{i-2}\right) \qquad 3.71$$

The η derivative can be expressed in a similar manner, viz.;

$$\frac{\partial(\rho v)}{\partial \eta} = \frac{1}{\alpha_{j1}\Delta\xi}\left(\alpha_{j2}\rho v + \alpha_{j3}\rho v_{j-1} + \alpha_{j4}\rho v_{j-2}\right) \qquad 3.72$$

The values of coefficients α_{i1}-α_{i4} and α_{j1}-α_{j4} are given in table 3.3 and 3.4 respectively.

Table 3.3: The coefficients at various values of i (for continuity equation)

i	α_{i1}	α_{i2}	α_{i3}	α_{i4}
i=2	1	1	-1	0
i≥3	2	3	-4	1

Table 3.4: The coefficients at various values of j (for continuity equation)

j	α_{j1}	α_{j2}	α_{j3}	α_{j4}
j=1	1	0	0	0
j=2	1	1	-1	0
j≥3	2	3	-4	1

ζ-derivative

The discretized formula of ζ-derivative is similar to that presented in equation (3.64) except in this equation the point of consideration is (i,j,k+½). The scheme can be written as

$$\zeta_{\bar{\zeta}}\frac{\partial(\rho w)}{\partial\zeta}=\zeta_{\bar{\zeta}_{k+\frac{1}{2}}}\left[\frac{\rho w_{k+1}-\rho w}{\Delta\zeta}\right]^{n+1} \qquad 3.73$$

Continuity Equation

By applying discretized formulae (3.62, 3.71, 3.72, 3.73) to the continuity equation (3.58), the value of w at (i, j, k+1, n+1) can be evaluated as follow

$$w_{k+1}^{n+1}=\frac{RHS}{Coeff} \qquad 3.74$$

where

$$Coeff=-\frac{\left(\left\langle\zeta_{\bar{\zeta}}\right\rangle_{k+1}+\zeta_{\bar{\zeta}}\right)}{2}\frac{1}{\Delta\zeta}\rho_{k+1}^{n+1}$$

$$RHS=-\frac{\left(\left\langle\zeta_{\bar{\zeta}}\right\rangle_{k+1}+\zeta_{\bar{\zeta}}\right)}{2}\frac{1}{\Delta\zeta}\langle\rho w\rangle^{n+1}+\frac{(\rho_{k+1}+\rho)^{n+1}-(\rho_{k+1}+\rho)}{2\Delta t}$$

$$+\frac{1}{h_1h_2\sin\alpha}\left\langle\frac{1}{2}\frac{1}{\alpha_{i1}\Delta\xi}\left(\alpha_{i2}h_2\sin\alpha\rho u+\alpha_{i3}h_2\sin\alpha\rho u_{i-1}+\alpha_{i4}h_2\sin\alpha\rho u_{i-2}\right)\right\rangle_{k+1}^{n+1}$$

$$+\frac{1}{h_1 h_2 \sin\alpha}\left\langle\frac{1}{2}\frac{1}{\alpha_{i1}\Delta\xi}\left(\alpha_{i2}h_2\sin\alpha\rho u+\alpha_{i3}h_2\sin\alpha\rho u_{i-1}+\alpha_{i4}h_2\sin\alpha\rho u_{i-2}\right)\right\rangle^{n+1}$$

$$+\frac{1}{h_1}\frac{\left(\left\langle\zeta_{\bar{\xi}}\right\rangle_{k+1}+\zeta_{\bar{\xi}}\right)}{2}\frac{1}{\Delta\zeta}\left(\langle\rho u\rangle_{k+1}-\rho u\right)^{n+1}$$

$$+\frac{1}{h_1 h_2 \sin\alpha}\left\langle\frac{1}{2}\frac{1}{\alpha_{j1}\Delta\eta}\left(\alpha_{j2}h_1\sin\alpha\rho v+\alpha_{j3}h_1\sin\alpha\rho v_{j-1}+\alpha_{j4}h_1\sin\alpha\rho v_{j-2}\right)\right\rangle_{k+1}^{n+1}$$

$$+\frac{1}{h_1 h_2 \sin\alpha}\left\langle\frac{1}{2}\frac{1}{\alpha_{j1}\Delta\eta}\left(\alpha_{j2}h_1\sin\alpha\rho v+\alpha_{j3}h_1\sin\alpha\rho v_{j-1}+\alpha_{j4}h_1\sin\alpha\rho v_{j-2}\right)\right\rangle^{n+1}$$

$$+\frac{1}{h_2}\frac{\left(\left\langle\zeta_{\bar{\eta}}\right\rangle_{k+1}+\zeta_{\bar{\eta}}\right)}{2}\frac{1}{\Delta\zeta}\left(\langle\rho v\rangle_{k+1}-\rho v\right)^{n+1}$$

3.7 COMPUTATIONAL PROCEDURE

The solution method is based on time marching and has the capability to calculate the unsteady flow properties. However, the intention of implementing the method is for steady flow. In this calculation a first order accurate time-integral routine is used. Using the discretization described in section 3.5 and the definition of eddy viscosity, the three conservative equations in finite difference form can now be solved in an uncoupled manner. The momentum equations can be solved for u^{n+1} and v^{n+1}, the energy equation for H^{n+1}, the equations of state for T^{n+1}, ρ^{n+1} and the viscosity law for μ^{n+1}. The next step is to solve the continuity equation for w^{n+1}. Finally, the update values are computed μ_t at time n+1 by employing the Baldwin-Lomax model. This sequence represents one cycle of an iteration procedure. The next time step, the values are updated and the calculation replaces to obtain the solutions. For steady flow solutions, the process is repeated until the difference between two successive values of u, v and w, for ζ-η plane, be less than a specific number of a convergence criterion. A suitable convergent criterion can be defined in terms of u. The equation is given as

$$\text{MAX}\left|u^{n+1} - u\right| \leq \varepsilon \qquad \text{for all j,k} \qquad 3.75$$

where ε is the convergence criterion (usually $\approx 1\times10^{-4}$).

We use u as a convergence criterion because it is a base parameter in the governing equations. If the convergence criterion (3.75) is not satisfied, all the parameters are updated and the process repeats. The equation used for updating the values before the next time iteration is

$$u_{new} = \omega\, u^{n+1} + (1-\omega)\, u_{old} \qquad 3.76$$

where ω is relaxation factor

Once the convergence criterion (3.75) for the whole plane of spanwise direction is satisfied at the i^{th} downstream, the boundary layer solution is marched to the $(i+1)^{th}$ downstream. This process is repeated until the final n^{th} downstream is reached.

The numerical procedure of this method is outline in Fig. 3.3 .

One of the problems in solving the equations is convergence. Many researchers have accelerated the convergence by using multigrid method. The application of multigrid method in boundary-layer problem is complicated since we have to recalculate all the transformed parameters every time we upgrade the grid construction. The more the levels we apply the more complex the equations. From our study, it has been shown that over relaxation and under relaxation factors do not much effect to the results, if the solution is converged. But a faster rate of convergence is obtained by using over relaxation factor. In many applications the over relaxation factor cannot be implemented since the solution

oscillates or sometime does not converge. This can be eliminated by using very low relaxation factor but it slows the convergence rate. We can accelerate the convergence rate in a similar way as that in the multigrid method by adapting relaxation factor according to the convergence rate. That is to say when the convergence rate is high we use over relaxation, and when the convergent rate is slow we use under relaxation. We switch back to over relaxation factor when the convergence rate is high again. The implementation of this method is less complex than that of multigrid one and can accelerate the convergence. The speed of convergence depends upon the quality of the update procedure.

3.8 STABILITY AND ZONE OF DEPENDENCE CONCEPTS

Stability Analysis

To study the stability concept one can use the von Neumann analysis. In this method a partial differential equation is approximated to a linear equation by using a linear constant coefficient model. The equation is then implemented in a finite difference approximation and its stability is investigated by using a Fourier analysis. Since our solutions are obtained from a tridiagonal matrix, we can analyse the stability concept of the equations with a tridiagonal constraint.

Anderson et al (1984) show that the implicit scheme for boundary-layer flows is unconditionally stable in the von Neumann analysis. However, numerical instability of this equation can occur if the choice of grid spacing permits the algebraic model to be an inaccurate representation for a viscous flow. This is because the diagonal dominance of a tridiagonal matrix is not maintained.

The algorithm of the tridiagonal elimination scheme is very efficient since it requires only 5N-4 operations when N is the matrix size. It is possible to prove that the solutions of the tridiagonal matrix will not lead to any stability problems if

the diagonal terms are dominated. Therefore, to avoid the numerical difficulty it is necessary that (Anderson et al (1984) and Fletcher (1991))

$$|b| > |a| + |c| \qquad 3.77$$

where a is sub-diagonal of the matrix

b is diagonal of the matrix

c is super-diagonal of the matrix

This property can be used as a stability analysis of our equations. For simplification, the equation (3.65) of incompressible flow on a flat plate can be written as

$$a\, u_{k-1}^{n+1} + b\, u^{n+1} + c\, u_{k+1}^{n+1} = RHS \qquad 3.78$$

where $a = -\rho w \frac{1}{2\Delta z} - \frac{\mu}{\Delta z \Delta z}$

$$b = \rho \frac{1}{\Delta t} + \frac{2\mu}{\Delta z \Delta z}$$

$$c = \rho w \frac{1}{2\Delta z} - \frac{\mu}{\Delta z \Delta z} \qquad 3.79$$

Equation (3.77) can also be written as

$$b^2 > a^2 + c^2 \qquad 3.80$$

Substitute the values of a, b and c from equation (3.79) in equation (3.80) and rearrange, the inequality becomes:

$$\frac{2\rho^2\Delta z^4}{\mu^2\Delta t^2}+8\frac{\rho\Delta z^2}{\mu\Delta t}+4>\frac{\rho^2 w^2\Delta z^2}{\mu^2} \qquad 3.81$$

If we assume that $\Delta t >> \Delta z$ (approximately true in our case), the first two terms may be neglected. Then the stability of the equation requires that

$$\frac{\rho|w|\Delta z}{\mu}<2 \qquad 3.82$$

Therefore, normal grid point (Δz) should be small enough to hold the above condition. This agrees with the boundary layer assumption that the viscous effect is important in the narrow region. On the other hand, this condition also contributes to the fact that the viscosity effect can be captured if the fine mesh in the normal direction (Δz) is used.

In the case of three-dimensional flow, we will get the similar condition if $\left\langle\mu\zeta_{\bar{\xi}}\right\rangle_{k+1}=\left\langle\mu\zeta_{\bar{\xi}}\right\rangle_{k-1}=\left\langle\mu\zeta_{\bar{\xi}}\right\rangle$. In the discretized form it yields:

$$\left|\frac{u\zeta_{\bar{\xi}}}{h_1}+\frac{v\zeta_{\bar{\eta}}}{h_2}+w\zeta_{\bar{\zeta}}\right|\frac{\rho\Delta\zeta}{\mu\zeta_{\bar{\zeta}}^{\,2}}<2 \qquad 3.83$$

Zone of Dependence Concept

Kitchens et al (1975) show that the concepts of stability and zone of dependence are not the same. The constraints imposed by both methods may coincide in some cases (Anderson et al (1984)). The zone of dependence condition is required for three-dimensional boundary-layer equations because the equations have a hyperbolic character in the plane parallel to the surface (e.g. x-y plane) on which the boundary-layer develops. This comes from the fact that in the x- and y-directions, only convective term occurs in the equations, while in the z-

direction both convection and diffusion (second derivative term in z-direction for the momentum equations) occur.

If we imagine that the fluid is passing through point p in the boundary layer (see Fig. 3.4), there are two extreme lines, the external streamline and the limiting streamline, bounding the flow. Then extending downstream of these lines passing through A-B is the zone of dependence and that upstream is the zone of influence. The identified regions of zones of dependence and influence vary depending on the direction of local streamlines across the boundary-layer (i.e. $\frac{dy}{dx} = \frac{v}{u}$). This feature can be seen in Fig. 3.5 that is taken from Cousteix (1987). In Fig. 3.5 a, the wall and external streamlines are drawn when both u and v in the boundary layer are positive. When the local velocities (e.g. u, v) are changed, we can see that the angle between the two outer most streamlines is also changed. The angle is widest when both u and v are negative (see Fig. 3.5c). In Fig. 3.5c, there is possible that the region of dependence may cover the unknown quantities (denote as +).

The hyperbolic behaviour of the equation implies that the predicted conditions at p come from the domain of dependence. This constraint results in implementation of the zone of dependence principle. It requires that the numerical domain may include more than, but not less than, the physical zone. The exact quantitative statement of the zone of dependence principle depends upon the difference molecule employed (Anderson et al (1984)). For implicit scheme, the zone of dependence principle would require that (Kitchens et al (1975))

$$u > 0, \qquad \left|\frac{v\Delta x}{u\Delta y}\right| \leq 1 \qquad 3.84$$

This constraint will limit the size of Δx and Δy. The calculated values of zone of dependence will be presented in chapter 5, computational results.

3.9 CLOSURE

The equations and procedures described in section 3.3 through 3.8 are general and can be applied to flow over complex geometry such as turbomachinery blades. Its implementation and application are simple and straightforward since the governing equations are solved directly without employing similarity transformation. The time integration makes the discretization scheme less complex. The convergence of the solutions is fast since the tridiagonal elimination scheme is formed and a multi-relaxation factor method is used. However, its application restricts to the flow that is not separated. In order to cope with the separation flow, the method has to be solved inversely. This will be presented in the next chapter.

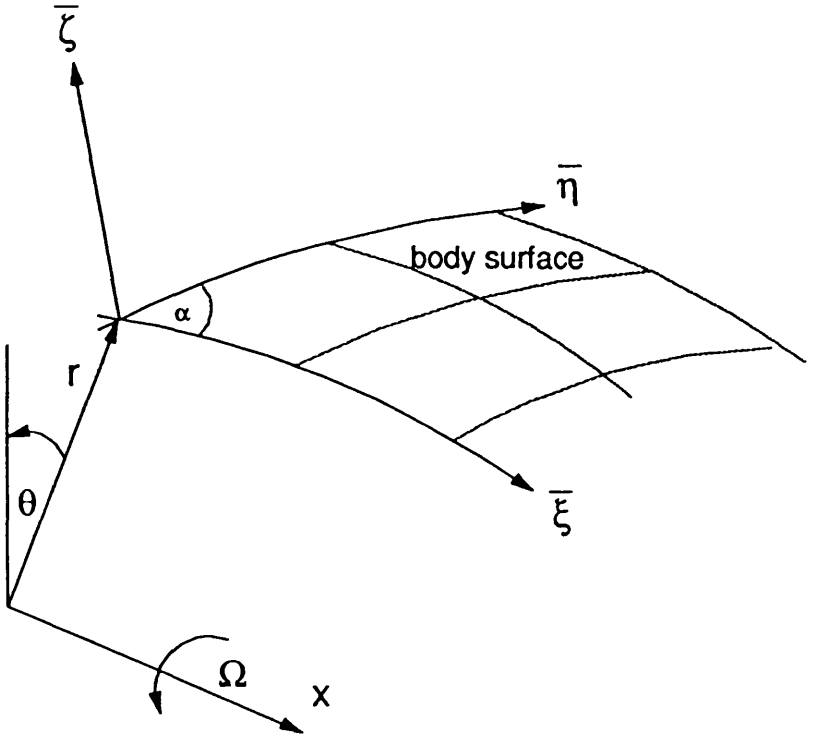

Fig. 3.1 Non-orthogonal curvilinear co-ordinate system on the body surface with angular velocity Ω.

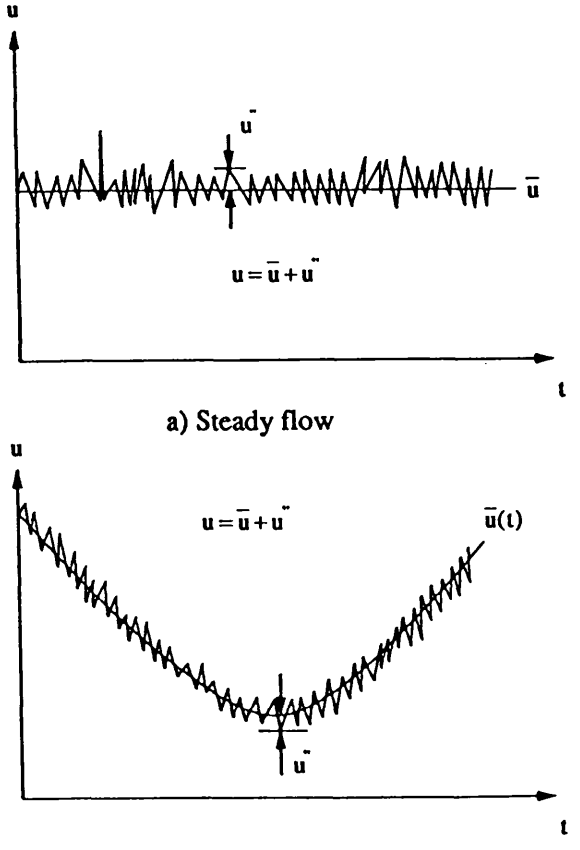

Fig. 3.2 Relationship between u, $\bar{u}$ and u' (Anderson et al 1984)

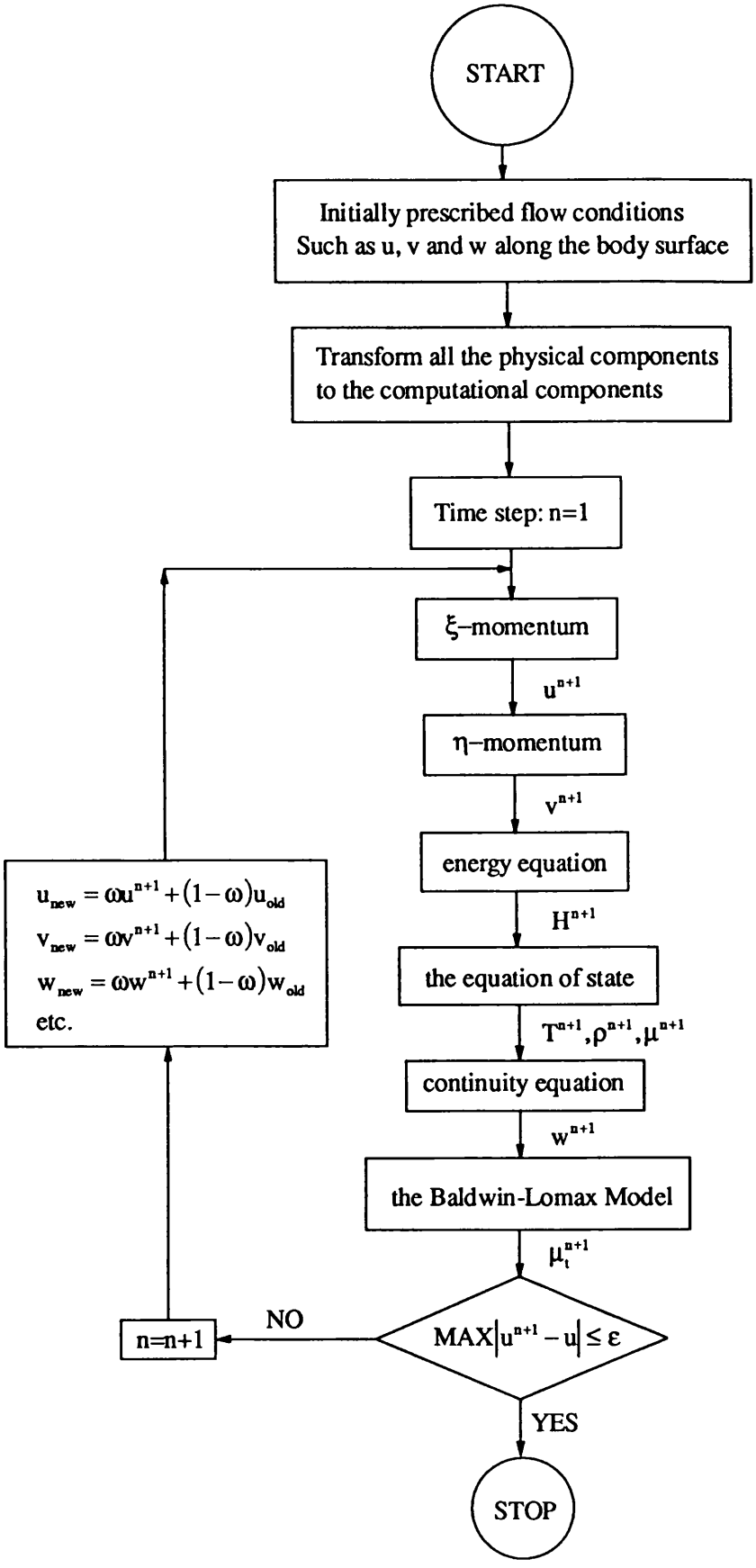

Fig. 3.3 Flow diagram for the boundary layer method (at i^{th} downstream)

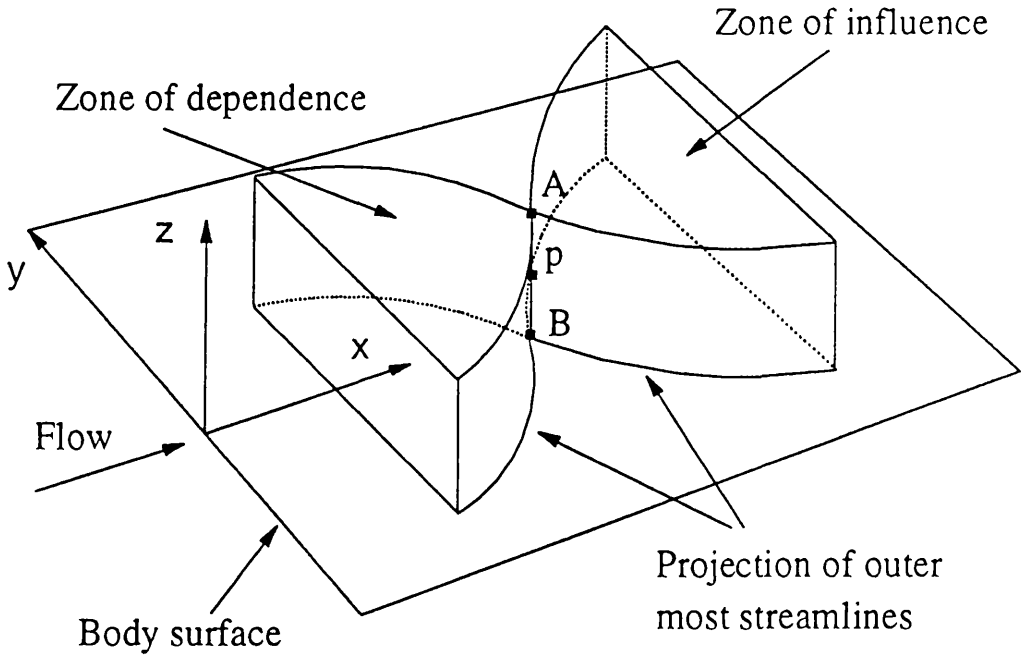

Fig. 3.4 Zones of dependence and influence in three-dimensional boundary layers (Anderson et al 1984).

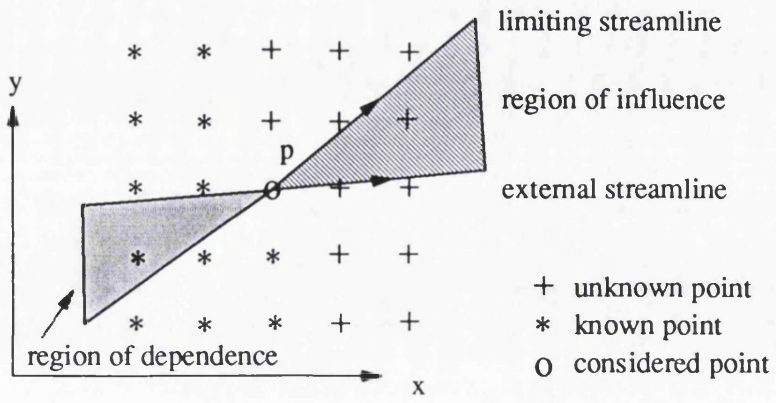

a) when both u and v in the boundary layer are positive

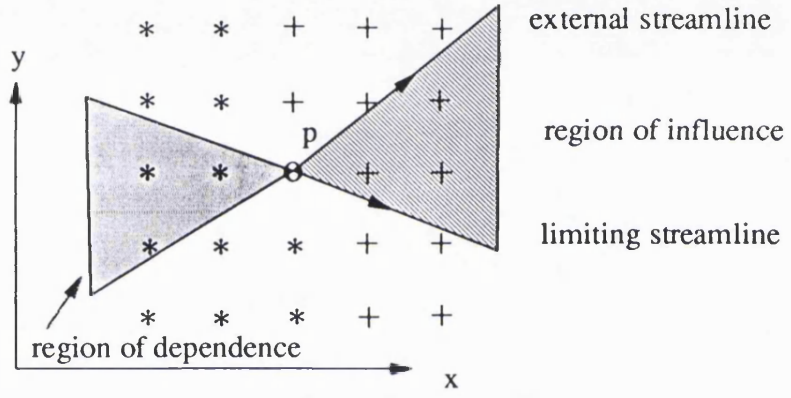

b) when u is positive across the layer and v is negative near the wall

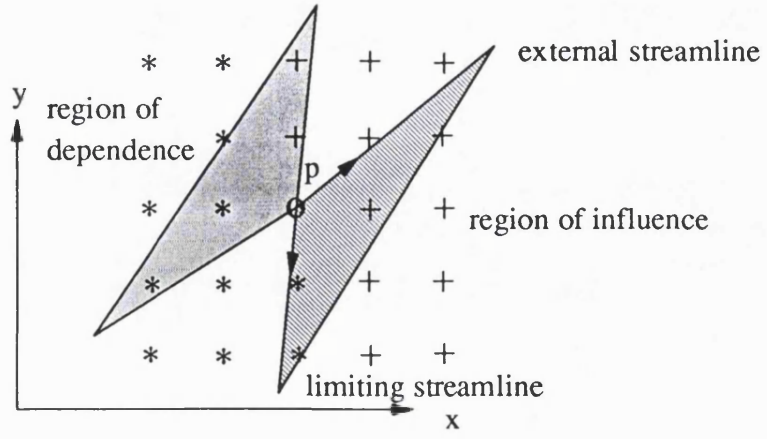

c)when both u and v are negative

Fig. 3.5 Zone of dependence concept when freestream velocities u and v are positive (Cousteix, 1987)

CHAPTER 4
SEPARATION AND VISCOUS-INVISCID INTERACTION

4.1 INTRODUCTION

The previous chapter described the standard method or "direct method" of solving the boundary layer equations. In this method, the boundary layer flow is computed by specifying the no-slip conditions at the wall and inviscid properties at the boundary layer edge. The parameters such as momentum thickness (Θ), displacement thickness (δ^*), wall shear stress (τ_w) and skin friction (c_f) are obtained as parts of the solutions. However, boundary layer equations as implemented under the direct approach have a singularity when there is a flow reversal as a result of boundary layer separation. In this chapter different ways of solving boundary equations in case of flow reversal will be discussed.

The next section presents a brief overview of boundary layer separation in two- and three-dimensional flow. The discussion will be limited to qualitative description of this important phenomenon. The general background of the separation and simple treatment of this phenomenon is also presented.

The prediction of flow separation is the most difficult aspects of the boundary layer approach. In recent years much effort has been devoted to develop methods for predicting separation of boundary layer. In this chapter we will consider only three methods, the FLARE approximation method, the simple inverse method and the interactive method.

In the case when the reverse flow velocity is small compared with the outer velocity, one can remove the instability by using a simple technique known as the FLARE approximation. In this method the calculation procedure is the

same as that in the direct method except that the streamwise convective term (e.g. $u\frac{\partial u}{\partial x}$) is neglected when the velocity is negative (i.e. $u<0$). This method is presented in section three.

Catherall and Mangler (1966) demonstrated that the boundary-layer equations are not singular at separation when displacement thickness is prescribed instead of free-stream velocity. This technique is known as the "inverse method". It is the boundary condition that differs between the direct and the inverse methods. The simple technique of the inverse method is discussed in section four.

Once a solution is obtained by the inverse method, more accurate solutions of the boundary layer equations can be generated by using viscous-inviscid interaction methods. The best approach, at the moment, is the "interactive method" due to Veldman (1981). The essence of the method is that both the free-stream velocity and displacement thickness are treated as boundary condition that couple through the use of a Hilbert integral. This method is presented in two- and three-dimensional flow in section five.

To appreciate the importance of separation, we should consider loss generation due to viscous effect in turbomachinery. The accurate prediction of flow is an important information in the design process since the performance of the machine is governed by the flow behaviour. If the flow remains attached to the wall, the loss associated with viscous effects is small compared with the case when the flow is separated. This loss can be approximated in term of entropy generation that can be consulted in the final section of this chapter.

4.2 BOUNDARY LAYERS AND SEPARATION

4.2.1 SEPARATION IN TWO-DIMENSIONAL FLOW

From the boundary-layer theory, the velocity inside the layer must change rapidly from the free-stream value at the layer edge to zero at the wall to satisfy the no-slip condition. In the region near the surface, the momentum of the fluid is small therefore the fluid behaviour is controlled by pressure and viscous shear force. The viscous shear force retards the flow across the viscous region. At the surface (i.e. z=0), the x-momentum equation for flow over flat-plate can be written as

$$\frac{\partial}{\partial z}\left(\mu\frac{\partial u}{\partial z}\right)=\frac{\partial p}{\partial x} \qquad 4.1$$

If the pressure gradient along the flow direction is zero, the velocity gradient close to the wall is constant and equals to τ_w/μ. Therefore, velocity profile is decelerated across the layer. This decelerated flow makes the boundary layer thickness grow higher in the flow direction.

If there is a pressure gradient in the flow direction, the rates of change of the boundary layer thickness and the velocity profile are altered. In the inviscid flow, the pressure gradient is results from changes in the free-stream velocity. When the pressure decreases along the flow, the free-stream velocity is accelerated. Therefore the term $\frac{\partial}{\partial z}\left(\mu\frac{\partial u}{\partial z}\right)$ in equation (4.1) is negative and the boundary layer is thinned. This is sometime called favourable pressure gradient.

If, on the other hand, the pressure increases in the flow direction, the free-stream velocity is decelerated. This is known as adverse pressure gradient. In this case $\frac{\partial}{\partial z}\left(\mu\frac{\partial u}{\partial z}\right)$ is positive and the boundary layer is thickened. The velocity

profile is shown in Fig. 4.1. If the positive pressure gradient is too large it can lead a value $\frac{\partial u}{\partial z}$ to go to zero. Under this condition the flow near the wall will stagnate or reverse as presented in Fig. 4.1. This provides some explanation for the nature of separation in two-dimensional flow.

It is observed that laminar separation can occur even in a small adverse pressure gradient. Turbulent boundary layers, on the other hand, are able to adhere to the surface for a greater distance than the laminar boundary layers. In order to prevent the separation problems, most of turbomachinery components operate at Reynolds numbers such that transition to turbulent flow occurs somewhere in the passages, or on the blades.

4.2.2 SEPARATION IN THREE-DIMENSIONAL FLOW

In three-dimensional flow it is usual to resolve the velocity vector of a velocity profile in the outer streamline co-ordinate and crossflow co-ordinate. The difference between this streamline co-ordinate system and the non-orthogonal curvilinear co-ordinate system will be presented first. The velocity profile in the streamline co-ordinate is then used to consider the three-dimensional boundary layer separation.

STREAMLINE CO-ORDINATE SYSTEM

In chapter 3, the non-orthogonal curvilinear co-ordinate system is defined by ξ = constant and η = constant lines drawn on the body surface with an angle α between them. The ζ-axis is normal to the surface. The co-ordinate system considered in this section is shown in Fig. 4.2. In the streamline co-ordinate system the s-axis is formed by the outer streamlines and the c-axis is formed by the line that is parallel to the wall and normal to s-axis (Fig. 4.2).

The velocity component along the s-axis is called streamwise velocity (u_s) while the velocity component along the c-axis is called crossflow velocity (v_c). The crossflow velocity is zero at the wall and also at the edge of the boundary layer. Thus, the crossflow components of velocity will generally reach a maximum at a point within the layer. This velocity component in some applications is referred to as the secondary flow velocity.

The velocity components in the streamline co-ordinate system (e.g. u_s, v_c) are related to the non-orthogonal curvilinear co-ordinate system (e.g. u, v) by

$$u_S = u \cos \beta + v \cos (\alpha-\beta) \qquad 4.2$$

$$v_C = -u \sin \beta + v \sin (\alpha-\beta) \qquad 4.3$$

or we can write

$$u = \{u_S \sin (\alpha-\beta) - v_C \cos (\alpha-\beta)\}/\sin \alpha \qquad 4.4$$

$$v = \{u_S \sin \beta + v_C \cos \beta\}/\sin \alpha \qquad 4.5$$

where u_S, v_C = velocity components in streamline co-ordinates (s-c)

u, v = velocity components in curvilinear co-ordinates (ξ-η)

$$\beta = \tan^{-1} \frac{v_e \sin \alpha}{u_e + v_e \cos \alpha}$$

At the boundary layer edge

$$u_{es} = \left(u_e^2 + v_e^2 + 2u_e v_e \cos \alpha\right)^{\frac{1}{2}} \qquad 4.6$$

$$u_{ec} = 0 \qquad 4.7$$

SEPARATION IN THREE-DIMENSIONAL FLOW

There are two categories of the three-dimensional boundary layer separation (Johnston (1988)). Firstly, the boundary layer separates when the skin friction tends to zero. Secondly, there is a case in which a wall streamline deviates from the outer streamline (s) and approaches the spanwise direction (η). Both types of boundary layer separation can lead to convergence difficulty in the boundary layer method.

The former case may be viewed as in the case of the two-dimensional separation that was presented in section 4.2.1. The latter case, on the other hand, occurs only in three-dimensional flow. In three-dimensional flow, the local streamlines change across the boundary layer (see Fig. 1.4). The outer streamlines (s) at the boundary layer edge and the limiting streamlines (Ψ) at the wall are not always parallel for each free-stream velocity profile. The limiting streamline as the surface is approached is called a wall streamline. The wall streamline is tangent to the direction of the local wall shear stress because the velocities vanish at the wall and the pressure gradient is completely balanced by shear forces. This is illustrated in Fig. 4.2, where it is assumed that the outer streamline (s) is the least curved and the wall streamline (Ψ) is the most curved.

The angle β_w between the limiting wall streamline (Ψ) and the outer streamline (s) can be defined as a ratio of the wall shear stress components.

$$\tan\beta_w = \frac{\tau_{wc}}{\tau_{ws}} = \left[\frac{\frac{\partial v_c}{\partial \zeta}}{\frac{\partial u_s}{\partial \zeta}}\right]_w = \lim_{\zeta \to 0} \frac{v_c}{u_s} \qquad 4.8$$

We can then say that the flow separates when (Johnston (1988))

$$\tau_{ws} \leq 0 \qquad 4.9$$

or $$(\beta+\beta_w) \geq \alpha \qquad 4.10a$$

or $$(\beta+\beta_w) \leq \alpha-180^o \qquad 4.10b$$

4.3 FLARE APPROXIMATION METHOD

FLARE approximation method is based on the assumption that the separation is small (i.e. $u < 0$ and $|u| << u_e$). Under this condition, the convective terms, such as $u\frac{\partial u}{\partial x}$, in the x-momentum equation may be written as $C|u|\frac{\partial u}{\partial x}$ where C is a constant. The value of C is made dependent on the sign of u. For example the x-momentum equation for two-dimensional flow is written as;

$$\rho\frac{\partial u}{\partial t}+C\rho|u|\frac{\partial u}{\partial x}+\rho w\frac{\partial u}{\partial z}=-\frac{\partial p}{\partial x}+\frac{\partial}{\partial z}\left(\mu\frac{\partial u}{\partial z}\right) \qquad 4.11$$

where $C = 1$ when $u > 0$ and $C = 0$ when $u < 0$.

The solutions from the FLARE approximation are straightforward and it can be implemented in the same way as the direct mode. Since the method is based on the assumption that the separation is small therefore the solutions are acceptable if the reverse flow is less than 10% of the local outer velocity, see Anderson et al (1984).

4.4 INVERSE METHOD

Another method to solve the boundary layer separation when the FLARE approximation cannot be used is the so-called inverse approach. In this method the boundary-layer equations are solved by prescribing either the displacement thickness (δ^*) or the skin friction coefficient (c_f). When δ^* is specified, the

definition of the displacement thickness generates u_e, and hence p, as part of the solution process.

In practice, we have to solve the equations by iteration until the specified displacement thickness (δ^*_{bc}) is satisfied since u_e is not known before the boundary layer calculations are completed. We prescribed displacement thickness as it can be obtained from an interaction between the boundary layer and the inviscid flow. Before the process of this interaction is discussed, the definition of the displacement thickness and momentum thickness in the streamline co-ordinate system is presented.

Displacement thickness and momentum thickness

If we define the displacement thickness (δ^*) and the momentum thickness (Θ) in the streamline co-ordinate system, we have

$$\delta^*_s = \int_0^{\delta} \left(1 - \frac{\rho u_s}{\rho_e u_{es}}\right) d\zeta \qquad 4.12$$

$$\Theta_{ss} = \int_0^{\delta} \rho u_s \frac{(u_{es} - u_s)}{\rho_e u_{es}^2} d\zeta \qquad 4.13$$

$$\delta^*_c = -\int_0^{\delta} \frac{\rho v_c}{\rho_e u_{es}} d\zeta \qquad 4.14$$

$$\Theta_{cc} = -\int_0^{\delta} \frac{\rho v_c^2}{\rho_e u_{es}^2} d\zeta \qquad 4.15$$

The definition and the physical meaning of these parameters can be seen in Appendix F.

Inverse method

In the inverse method, displacement thickness has to specify. An initial estimation of the displacement thickness may be calculated from n^{th} power formula and can be written in the streamline co-ordinate (s-c) as follow.

$$\frac{\delta^*_{s,i+1}}{\delta^*_{s,i}} = \left(\frac{s_{i+1}}{s_i}\right)^{1-n}\left(\frac{u_{csi}}{u_{csi+1}}\right)^{n} \qquad 4.16$$

where $n = \frac{1}{2}$ for laminar

$n = \frac{1}{7}$ for turbulence

From this point of view, we can see that the governing equations of the inverse mode are the same as those of the direct mode except the boundary condition at $\zeta \to \infty$ where u_{cs} is replaced by

$$\int_0^{\infty}\left(1-\frac{\rho u_s}{\rho_e u_{cs}}\right)d\zeta = \delta^*_{s,bc}(\xi,\eta) \qquad 4.17$$

At each grid point in the spanwise direction, the value of u_{cs} is obtained by an iteration of the boundary layer equations until equation (4.17) is satisfied. This iteration can be implemented by using a secant method. An algorithm for finding outer flow (u_{cs}) of a specified displacement thickness (δ^*) is presented in Appendix B. The iteration for computing $u_{cs,m}$ can be written as

$$u_{cs,m} = u_{cs,m-1} - \frac{F(u_{cs,m-1})}{F(u_{cs,m-1}) - F(u_{cs,m-2})}(u_{cs,m-1} - u_{cs,m-2}) \qquad 4.18$$

where $F(u_{cs,m}) = \delta^*_{s,m} - \delta^*_{s,bc}$

m = iteration cycle

Numerical solution algorithm

The solution procedure of inverse mode starts at any station (i's, j's) when $\tau_{ws} \leq 0$ or $(\beta+\beta_w) \geq \alpha$ or $(\beta+\beta_w) \leq (\alpha-180^o)$. It is better to start the inverse mode a little bit ahead of that point (e.g. $\tau_{ws} \leq 10^{-3}$). The inverse mode implemented in the whole spanwise direction and the procedure is continued downstream of the separation up to the trailing edge.

The numerical solution algorithm starts with an initial estimate $u_{cs,m}$. This velocity vector is resolved in non-orthogonal curvilinear co-ordinate system for three-dimensional boundary layers. The relationships between the streamline co-ordinate system and non-orthogonal co-ordinate system are given in equations (4.2-4.5). The sequence of the calculation now is exactly the same as that in the direct mode. When the solution is converged, the next step is to check that the displacement thickness (δ^*_s) from $u_{cs,m}$ satisfies the specified displacement thickness ($\delta^*_{s,bc}$). The criterion for this convergence is

$$MAX\left|\delta^*_s - \delta^*_{s,bc}\right| \leq \varepsilon \qquad 4.19$$

where ε is a convergence criterion ($\approx 10^{-4}$).

If the convergence criterion (4.19) is not satisfied, further iteration of the boundary-layer equations is required. The method in Appendix B can be used for this iteration.

It is economical if the iteration converges for $m \leq 10$. It should be noted that the solution is very non-linear and there are many parameters involved. In the case where the solution does not converge, we should employ other methods (e.g. bisection method or false position method) that guarantee the convergence.

Unfortunately most of these methods may slow the convergence down. The calculation procedure of this method is presented in Fig. 4.3.

In general the calculated values of δ^*_s and u_{es} should be iteratively coupled by using viscous-inviscid interaction in order to correct the guessed values. One suitable method is the relaxation formula. Description of this technique can be found in Carter (1978) and, Kwon and Pletcher (1986a, b). The flow diagram for this approach is shown in Fig. 2.8.

4.5 INTERACTIVE BOUNDARY LAYER METHOD

Veldman (1981) presented the interactive boundary layer model for the calculation of boundary layers with strong viscous-inviscid interaction. The method solved the boundary layer equations, through the use of the interactive boundary condition that is the combination of an external velocity and a displacement thickness. This boundary condition describes how the outer potential flow reacts to the presence of the boundary layers.

In the interaction boundary-layer model, the external velocity and the displacement thickness are combined as a boundary condition and treated as unknown quantities. Assuming that the external velocity is the sum of an inviscid velocity (u^0_{es}) and a perturbation velocity (δu_{es}). Based on these assumptions, the external boundary conditions are

$$\zeta \to \infty \qquad u_{es}(s) = u^0_{es}(s) + \delta u_{es}(s) \qquad 4.20a$$

$$\delta^*_s = \int_0^{\infty} \left(1 - \frac{u_s}{u_{es}}\right) d\zeta \qquad 4.20b$$

This boundary condition provides the basis of the method.

4.5.1 TWO-DIMENSIONAL FLOW

The simple case of two-dimensional flow is first used to illustrate the method. In this case, we assumed that the fluid flows over the curved surface with an infinite spanwise distance and an identical value in that direction. Therefore all the derivative terms in the spanwise direction are zero and the metric coefficient $h_2 = 1$. The velocity in the flow direction is u and the velocity normal to the surface is w. With this simplifications, the continuity equation of an incompressible and steady flow can be written as

$$\frac{\partial u}{\partial \xi} + \frac{h_1 \partial w}{\partial \zeta} = 0 \qquad 4.21$$

If we integrate this equation to find the normal velocity w just outside the boundary-layer edge (δ) we get

$$\begin{aligned} w_e &= \int_0^{\delta} \frac{\partial w}{\partial \zeta} d\zeta = -\int_0^{\delta} \frac{\partial u}{h_1 \partial \xi} d\zeta \\ &= -\frac{\delta}{h_1}\frac{\partial u_e}{\partial \xi} + \frac{1}{h_1}\left\{\frac{\partial}{\partial \xi}\left[\int_0^{\delta}(u_e - u)d\zeta\right]\right\} \\ &= -\frac{\delta}{h_1}\frac{\partial u_e}{\partial \xi} + \frac{1}{h_1}\left\{\frac{\partial}{\partial \xi}\left[u_e \delta^*\right]\right\} \end{aligned} \qquad 4.22$$

where $\delta^* = \frac{1}{u_e}\int_0^{\delta}(u_e - u)d\zeta$

Lighthill (1958) pointed out that the first term in the equation (4.22) represents the irrotational flow around the body, and the second term is an outflow due to the boundary layer. This additional outflow is sometime known as

a blowing-velocity and is "as if" there were a source distribution on the surface. If this source distribution of strength $\sigma(\xi)$ per length is placed along the ξ axis, the potential due to such a point source element can be obtained in the similar manner as presented in Appendix G. Using the velocity potential Φ, the velocity components, in terms of the perturbation velocity potential, are

$$w = \frac{\partial \Phi}{\partial \zeta} = \frac{\sigma(\xi)}{2} \qquad 4.23$$

$$\delta u_{\infty} = \frac{\partial \Phi}{h_1 \partial \xi} = \frac{1}{2\pi} \int_1 \frac{\sigma(\xi) h_1 d\xi}{(\xi_p - \xi)} \qquad 4.24$$

Therefore the perturbation velocity in equation (4.20a) can be written as

$$\delta u_{\infty} = \frac{1}{\pi} \int_{\xi_a}^{\xi_b} \frac{\partial (u_e \delta^*)}{\partial \xi} \frac{1}{(\xi_p - \xi)} d\xi \qquad 4.25$$

where subscript a and b mean the interaction region, and p means the point on the surface.

4.5.2 THREE-DIMENSIONAL FLOW

In the following considerations, the boundary-layer equations are defined in the three-dimensional case. The technique is similar to the two-dimensional flow. All the transformation parameters are the same as those presented in chapter 3. The continuity equation of incompressible and steady flow in the streamline co-ordinates (s-c) can be written as

$$\frac{\partial (h_c u_s)}{\partial s} + \frac{\partial (h_s v_c)}{\partial c} + \frac{\partial (h_s h_c w)}{\partial \zeta} = 0 \qquad 4.26$$

where h_s is the metric coefficient in the outer streamline direction (s)

h_c is the metric coefficient in the outer crossflow direction (c)

u_s is the velocity in the s direction

v_c is the velocity in the c direction

w is the velocity in the ζ direction (normal to the surface)

From this streamline co-ordinates, the values of u_s, v_c and w just outside the boundary-layer are u_{es}, v_{ec} and w_e respectively. This means that $v_{ec}=0$ and w_e can be written as

$$w_e = -\frac{\delta}{h_s h_c}\frac{\partial(h_c u_{es})}{\partial s} + \frac{1}{h_s h_c}\left\{\frac{\partial}{\partial s}\left[h_c \int_0^{\infty}(u_{es}-u_s)d\zeta\right]\right\} - \frac{1}{h_s h_c}\left\{\frac{\partial}{\partial c}\left[h_s \int_0^{\infty} v_c d\zeta\right]\right\} \qquad 4.27a$$

$$w_e = -\frac{\delta}{h_s h_c}\frac{\partial(h_c u_{es})}{\partial s} + \frac{1}{h_s h_c}\left\{\frac{\partial}{\partial s}\left[h_c u_{es}\delta_s^*\right]\right\} + \frac{1}{h_s h_c}\left\{\frac{\partial}{\partial c}\left[h_s u_{es}\delta_c^*\right]\right\} \qquad 4.27b$$

where $$\delta_s^* = \frac{1}{u_{es}}\int_0^{\infty}(u_{es}-u_s)d\zeta \qquad 4.28a$$

$$\delta_c^* = -\frac{1}{u_{es}}\int_0^{\infty} v_c d\zeta \qquad 4.28b$$

In equation (4.27), the first term represents the irrotational flow around the body, while the rests are additional outflow due to the boundary-layer, and are "as if" there were a source distribution on the surface, of strength per unit area

$$\sigma = \frac{2}{h_s h_c}\left\{\frac{\partial}{\partial s}\left[h_c u_{es}\delta_s^*\right]\right\} + \frac{2}{h_s h_c}\left\{\frac{\partial}{\partial c}\left[h_s u_{es}\delta_c^*\right]\right\} \qquad 4.29$$

If the source distribution is placed on the surface of the body (e.g. ζ=0), the perturbation velocity is equivalent to the flow induced region. Using the velocity potential (Φ), the influence of this distribution at a point p(s,c,0) is an integral of the influences of all the point elements (see Appendix G).

$$\delta u_{cs}(s,c,0)=\frac{1}{4\pi}\int_{surface}\sigma\frac{(s_p-s)}{\left\{(s_p-s)^2+(c_p-c)^2\right\}^{\frac{1}{2}}}h_s h_c dsdc \qquad 4.30$$

$$\delta v_{cc}(s,c,0)=\frac{1}{4\pi}\int_{surface}\sigma\frac{(c_p-c)}{\left\{(s_p-s)^2+(c_p-c)^2\right\}^{\frac{1}{2}}}h_s h_c dsdc \qquad 4.31$$

where δu_{cs} and δv_{cc} are the perturbation velocities in the streamline and crossflow direction respectively.

The effect of compressibility

The above equations are defined for incompressible flow. The effect of compressibility can be evaluated by using the co-ordinate transformation called the Prandtl-Glauert rule. Therefore the perturbation velocity is

$$\delta u_{cs}(s,c,0)=\frac{1}{4\pi\sqrt{1-M_\infty^2}}\int_{surface}\sigma\frac{(s_p-s)}{\left\{(s_p-s)^2+(c_p-c)^2\right\}^{\frac{1}{2}}}h_s h_c dsdc \qquad 4.32a$$

$$\delta v_{cc}(s,c,0)=\frac{1}{4\pi\sqrt{1-M_\infty^2}}\int_{surface}\sigma\frac{(c_p-c)}{\left\{(s_p-s)^2+(c_p-c)^2\right\}^{\frac{1}{2}}}h_s h_c dsdc \qquad 4.32b$$

where M_∞ is free stream Mach No.

Discretization

Due to the complexity of the interaction and the limited time available it is not at the present possible to perform an exact analysis of the three-dimensional

interaction equations. Therefore, we will only consider the implementation of the interactive approach in two-dimensional flow. The value of the perturbation velocity contains the displacement thickness effect and can be computed from

$$\delta u_{es}(s,0) = \frac{1}{\pi}\int_{s_a}^{s_b} \frac{\partial(u_{es}\delta_s^*)}{\partial s}\frac{1}{(s_p - s)}ds \qquad 4.33$$

where s_a and s_b define the beginning and end of the interaction region.

s_p is a field point.

Using the midpoint rule on intervals (s_m, s_{m+1})

$$\frac{\partial(u_{es}\delta_s^*)}{\partial s} = \frac{u_{es}\delta_s^*\big|_{m+1} - u_{es}\delta_s^*\big|_m}{\Delta s} \qquad 4.34$$

The integral of equation (4.33) can be represented by

$$\delta u_{es}(s,0) = \frac{1}{\pi}\sum_{m=1}^{imax-1} \frac{u_{es}\delta_s^*\big|_{m+1} - u_{es}\delta_s^*\big|_m}{s_p - s_{m+\frac{1}{2}}} \qquad 4.35$$

where $s_{m+\frac{1}{2}} = \frac{1}{2}(s_{m+1} + s_m)$

The discretization of the equation (4.35) may be rearranged to get the following form.

$$\sum_{m=1}^{imax-1} \frac{u_{es}\delta_s^*\big|_{m+1} - u_{es}\delta_s^*\big|_m}{s_p - s_{m+\frac{1}{2}}} = \sum_{m=2}^{imax} u_{es}\delta_s^*\big|_m \left[\frac{1}{s_p - s_{m-\frac{1}{2}}} - \frac{1}{s_p - s_{m+\frac{1}{2}}}\right] - \frac{u_{es}\delta_s^*\big|_1}{s_p - s_{1\frac{1}{2}}} + \frac{u_{es}\delta_s^*\big|_{imax}}{s_p - s_{imax+\frac{1}{2}}} \qquad 4.36$$

In the interaction model, all the required values of δ^*_s and u_{es} are supposed known during the i^{th} downstream march. These values are denoted with n superscript that is the iteration level. The contribution for m>i is taken from the n-1 level solution. Now the system of the equation (4.20a) at point i can be written as

$$u^{(n)}_{es,i}(s)+\alpha_{ii}\delta^{*(n)}_{s,i}=\sum_{m=2}^{i-1}\alpha_{im}\delta^{*(n)}_{s,m}+\sum_{m=i+1}^{imax}\alpha_{im}\delta^{*(n-1)}_{s,m}+\beta_i \qquad 4.37$$

$$\text{where}\quad \alpha_{im}=\frac{1}{\pi}u^{(0)}_{es,m}\left[\frac{1}{s_i-s_{m-\frac{1}{2}}}-\frac{1}{s_i-s_{m+\frac{1}{2}}}\right] \qquad 4.38$$

$$\beta_i=-\frac{1}{\pi}\frac{u^{(0)}_{es,1}\delta^*_{s,1}}{s_i-s_{1\frac{1}{2}}}+\frac{1}{\pi}\frac{u^{(0)}_{es,imax}\delta^*_{s,imax}}{s_i-s_{imax+\frac{1}{2}}} \qquad 4.39$$

From the system of the equation we can see that the external velocity (u_{es}) and the displacement thickness (δ^*_s) are treated as unknown quantities at i^{th} downstream march. For each sweep, the boundary-layer equations are solved simultaneously in an inverse mode with successive sweeps over the body surface. It should be noted that in the previous section (inverse method) the value of displacement thickness (δ^*_s) is supposed known and the external velocity (u_{es}) is the solution of the equations but in the interaction model both of them are obtained as parts of the solutions.

Numerical Solution Algorithm

Interaction between the inviscid and viscous flows can be employed through the equation (4.37). In this equation, the combination of the external velocity and displacement thickness is linked and used as the external boundary conditions in the boundary-layer equations.

The interaction calculation proceeds in the following way.

1. The boundary-layer calculation is computed up to the beginning of the interaction region (e.g. s_a, before the flow is separated) by a direct method.

2. An initial guess displacement thickness ($\delta^{*(0)}_s$) is chosen over the region (s_a, s_b) where the interaction is believed to be important. The extrapolation of $\delta^{*(0)}_s$ is an arbitrary choice. A suitable choice is using flat-plate approximation (e.g. equation 4.16).

3. The boundary-layer solution is next obtained by an inverse procedure using $\delta^{*(n)}_{s,i}$ and $u^{(n)}_{es,i}$ as boundary conditions. By guessing $\delta^{*(n)}_{s,i}$, the value of $u^{(n)}_{es,i}$ is obtained from the interaction equation (4.37). If the calculated value of displacement thickness from equation (4.20b) does not match with the guessed value of $\delta^{*(n)}_{s,i}$, then the solution has to iterate. The secant method is applied to accelerate the solution (see Appendix B).

4. Once the solutions at i^{th} downstream station are converged, the values of $\delta^{*(n)}_{s,i}$ are updated on the right hand side of the interaction equation (4.37). The implementations of the step 3-4 are carried out until the solutions are completed sweep over the body.

5. The difference between $\delta^{*(n)}_{s,i}$ calculated of this iteration and that of the previous one ($\delta^{*(n-1)}_{s,i}$) is used to check for convergence, where the convergence criterion has been taken as

$$\text{MAX} \left| \delta^{*(n)}_{s,i} - \delta^{*(n-1)}_{s,i} \right| \leq \varepsilon \qquad 4.40$$

where ε is the convergence criterion

n = iteration level

When MAX $|\delta^{*(n)}_{s,i} - \delta^{*(n-1)}_{s,i}|$ is less than a prescribed tolerance, convergence is considered to be achieved. If this criterion is not satisfied, $\delta^{*(n)}_{s,i}$ is updated and the process returns to step 3. An over relaxation value of ω (e.g. ω = 1.5) can be used in this method.

$$\delta^{*(n)}_{s,i} = \omega\delta^{*(n)}_{s,i} + (1-\omega)\delta^{*(n-1)}_{s,i} \qquad 4.41$$

The flow diagram of the interactive mode can be seen in Fig. 4.4.

4.6 ENTROPY GENERATION IN A 3-D BOUNDARY LAYER

The generation of entropy by viscous effects is governed by the equation (4.42). The procedures used to develop the equation may be seen in Appendix H.

$$\rho T\frac{Ds}{Dt} = q^{\cdot} + \mu\Phi \qquad 4.42$$

where s is entropy,

T is temperature,

$q^{\cdot}$ is heat transfer per unit time (equation H.21), and

$$\Phi = 2\left[\left(\frac{\partial u}{\partial x}\right)^2 + \left(\frac{\partial v}{\partial y}\right)^2 + \left(\frac{\partial w}{\partial z}\right)^2\right] + \left(\frac{\partial v}{\partial x} + \frac{\partial u}{\partial y}\right)^2 + \left(\frac{\partial w}{\partial y} + \frac{\partial v}{\partial z}\right)^2 + \left(\frac{\partial u}{\partial z} + \frac{\partial w}{\partial x}\right)^2 - \frac{2}{3}\left(\frac{\partial u}{\partial x} + \frac{\partial v}{\partial y} + \frac{\partial w}{\partial z}\right) \qquad 4.43$$

In order to make the use of the entropy generation equation (4.42) for boundary layers, we need to adapt some terms regarding the nature of the viscous

layers. For $q^{\cdot}$, we can see that the amount of heat transferred into volume $\Delta\vartheta$ through surface elements that are normal to the x-direction is equal to $-k\frac{\partial T}{\partial x}dydz$ (see Fig. H.1). By contrast, the amount leaving the volume is given by $\left(k\frac{\partial T}{\partial x}+\frac{\partial}{\partial x}k\frac{\partial T}{\partial x}\right)dydz$. Thus, the amount of heat added by conduction during time dt to a volume $\Delta\vartheta$ can be written

$$q^{\cdot}=\frac{\partial}{\partial x}\left(k\frac{\partial T}{\partial x}\right)+\frac{\partial}{\partial y}\left(k\frac{\partial T}{\partial y}\right)+\frac{\partial}{\partial z}\left(k\frac{\partial T}{\partial z}\right) \qquad 4.44$$

From boundary layer assumption, we found that the values of x and y are typically 0(1), and values of z (normal to the body surface) associated with the boundary layer are typically $0(\delta)$.

Thus, u, $\frac{\partial u}{\partial x}$, $\left(\frac{\partial u}{\partial x}\right)^2$, v, $\frac{\partial v}{\partial x}$, $\frac{\partial v}{\partial y}$, $\left(\frac{\partial v}{\partial y}\right)^2$, $\frac{\partial w}{\partial z}$, $\left(\frac{\partial w}{\partial z}\right)^2$, $\frac{\partial u}{\partial y}$ are 0(1) ,$\frac{\partial w}{\partial x}$, $\frac{\partial w}{\partial y}$ are $0(\delta)$ and ,$\frac{\partial u}{\partial z}$, $\frac{\partial v}{\partial z}$ are $0(1/\delta)$

Since $\delta << 1$ we can see that

$$\Phi\approx\left(\frac{\partial u}{\partial z}\right)^2+\left(\frac{\partial v}{\partial z}\right)^2 \qquad 4.45$$

In a similar manner $\frac{\partial T}{\partial z}>>\frac{\partial T}{\partial x}\&\frac{\partial T}{\partial y}$

so $$q^{\cdot}=\frac{\partial}{\partial z}\left(k\frac{\partial T}{\partial z}\right) \qquad 4.46$$

Therefore the equation for three-dimensional boundary layers reduces to

$$\rho T\frac{Ds}{Dt}=\frac{\partial}{\partial z}\left(k\frac{\partial T}{\partial z}\right)+\mu\left(\frac{\partial u}{\partial z}\right)^2+\mu\left(\frac{\partial v}{\partial z}\right)^2 \qquad 4.47$$

or $$\rho T\frac{Ds}{Dt}=\frac{\partial}{\partial z}\left(k\frac{\partial T}{\partial z}\right)+\tau_s\frac{\partial u}{\partial z}+\tau_c\frac{\partial v}{\partial z} \qquad 4.48$$

where τ_s is streamwise shearing stress = $\mu\dfrac{\partial u}{\partial z}$ 4.49

τ_c is crossflow shearing stress = $\mu\dfrac{\partial v}{\partial z}$ 4.50

Therefore the entropy generation rate inside the boundary layer is

$$\int_0^\delta \rho\frac{Ds}{Dt}dz=\int_0^\delta\frac{1}{T}\frac{\partial}{\partial z}\left(k\frac{\partial T}{\partial z}\right)dz+\int_0^\delta\frac{\tau_s}{T}\frac{\partial u}{\partial z}dz+\int_0^\delta\frac{\tau_c}{T}\frac{\partial v}{\partial z}dz \qquad 4.51$$

The term $\displaystyle\int_0^\delta\frac{1}{T}\frac{\partial}{\partial z}\left(k\frac{\partial T}{\partial z}\right)dz$ can be integrated by parts and equal

$$=\frac{k}{T}\frac{\partial T}{\partial z}\bigg|_0^\delta+\int_0^\delta\frac{k}{T^2}\left(\frac{\partial T}{\partial z}\right)^2dz$$

$$=\frac{k}{T}\frac{\partial T}{\partial z}\bigg|_0^\delta+\int_0^\delta\frac{k}{T^2}\frac{\partial T}{\partial z}dT \qquad 4.52$$

Equation (4.51) can be rewritten as:

$$\int_0^\delta \rho\frac{Ds}{Dt}dz=\frac{k}{T}\frac{\partial T}{\partial z}\bigg|_{z=\delta}-\frac{k}{T}\frac{\partial T}{\partial z}\bigg|_{z=0}+\int_0^\delta\frac{\tau_s}{T}du+\int_0^\delta\frac{\tau_c}{T}dv+\int_0^\delta\frac{k}{T^2}\frac{\partial T}{\partial z}dT \qquad 4.53$$

From the boundary condition of the boundary-layer equations, we know that $\dfrac{k}{T}\dfrac{\partial T}{\partial z}\bigg|_{z=\delta}=0$. If we let $\displaystyle\int_0^\delta\rho\frac{Ds}{Dt}dz=\xi^*$ and $k=\mu c_p/Pr$, the entropy production per unit surface area (ξ^*) is given by

$$\xi^{\bullet} = -\frac{k}{T}\frac{\partial T}{\partial z}\bigg|_{z=0} + \int_0^{\delta}\frac{\tau_s}{T}du + \int_0^{\delta}\frac{\tau_c}{T}dv + \int_0^{\delta}\frac{k}{T^2}\frac{\partial T}{\partial z}dT \qquad 4.54$$

This is the total rate of entropy creation not the change in specific entropy. We can expect that the entropy generation near the wall is higher than that near the boundary layer edge because velocities change rapidly near the wall. If we non-dimensionalise the entropy (s) in the layer by $\frac{\rho_\infty u_\infty^3}{T_\infty \mathrm{Re}^{\frac{1}{2}}}$, we can write the equation in non-dimensional form as,

$$\xi^{\bullet}(\gamma-1)M_\infty^2 = -\frac{\mu}{\mathrm{Pr}}\frac{1}{T}\frac{\partial T}{\partial z}\bigg|_{z=0} + (\gamma-1)M_\infty^2\int_0^{\delta}\frac{\tau_s}{T}du$$

$$+(\gamma-1)M_\infty^2\int_0^{\delta}\frac{\tau_c}{T}dv + \int_0^{\delta}\frac{\mu}{\mathrm{Pr}}\frac{1}{T^2}\frac{\partial T}{\partial z}dT \qquad 4.55$$

Where Re is the reference Reynolds number, $\mathrm{Re} = \rho_\infty u_\infty L/\mu_r$

R is gas constant = $c_p - c_v = c_p(\gamma-1)/\gamma$

$$M_\infty^2 = \frac{u_\infty^2}{\gamma R T_\infty}$$

From the above equations, we can see that the entropy generated in the boundary-layer is proportional to the heat transfer at the wall and the summation of viscous work per unit time in both streamwise and crosswise from the wall to the edge of the boundary-layer. In the case of adiabatic wall temperature the heat transfer at the wall is zero ($\frac{\partial T}{\partial z}\Big|_w = 0$). It should also be noted that equation (4.54) has been derived for compressible flow of a fluid.

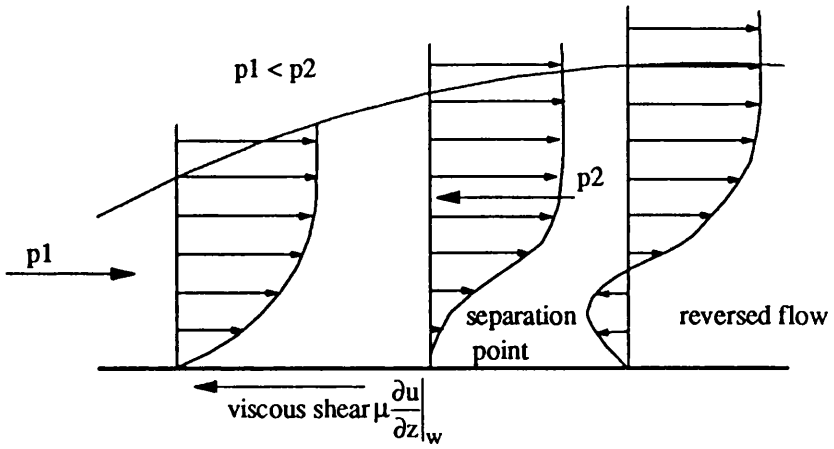

Fig. 4.1 Boundary layer separation from a two-dimensional flow

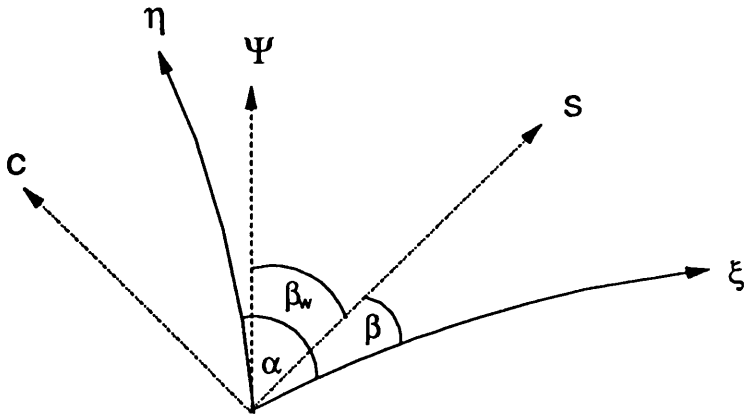

Fig. 4.2 Streamline co-ordinate system on the body surface

s-c = streamline co-ordinate system, s-axis is outer streamline in the direction of the flow at the boundary layer edge, c-axis is crossflow direction

ξ-η = non-orthogonal curvilinear co-ordinate system

Ψ = the limiting streamline

β = angle between ξ-axis and s-axis

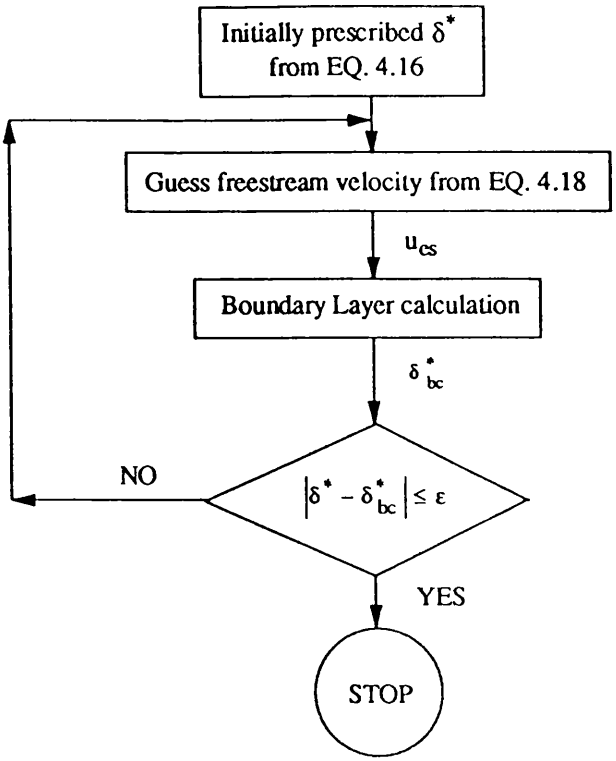

Fig. 4.3 Boundary layer calculation procedure in the inverse mode at a specific point

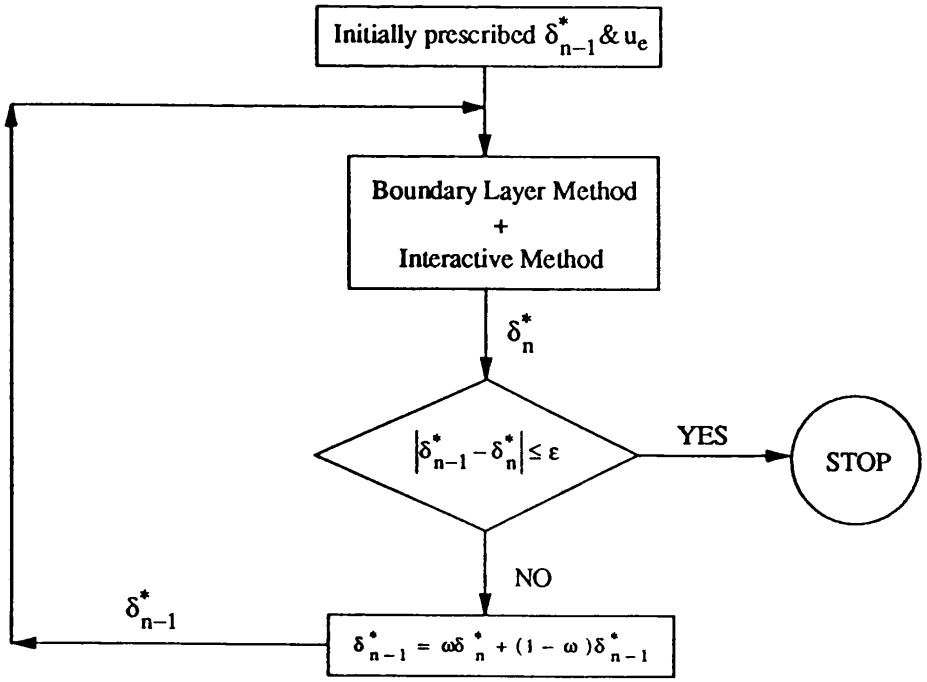

Fig. 4.4 Flow chart for the viscous-inviscid interaction: interactive model

CHAPTER 5
COMPUTATIONAL RESULTS

5.1 INTRODUCTION

The objectives of this chapter are to evaluate, compare and validate the boundary layer method described in chapter 3 and 4. Validation data comparisons ranging from two-dimensional flat plate to three-dimensional compressor are shown in this chapter to highlight the accuracy and reliability of the code. The background information and basic assumptions are given in each test case.

The code is applied to the following flow configurations:

1. Three-dimensional flow over a flat plate with the plate moving parallel to its leading edge
2. Three-dimensional flow over a flat plate with an attached cylinder
3. Rotating helical blade
4. An axial compressor
5. A centrifugal compressor rotor
6. A dented plate with a separation bubble

5.2 THREE-DIMENSIONAL FLOW OVER A FLAT PLATE WITH THE PLATE MOVING PARALLEL TO ITS LEADING EDGE

A study of three-dimensional boundary layers on a flat plate is greatly simplified by the absence of geometrical complication. Under these circumstances the solutions of the boundary-layer equations can be found by employing some forms of similarity law (e.g. Blasius-type solutions). A study of three-dimensional flow over a stationary flat plate was discussed in great detail first by Loos (1955)

and applied in the case of a moving plate parallel to its leading edge by Kitchens et al (1975). In this test case, we compare our calculations with those reported by Kitchens et al (1975).

Specification data:

For $\bar{x}$, $\bar{y}$, $\bar{z}$ co-ordinate (see Fig. 5.1), a flat plate surface is defined on the $\bar{x}$- and $\bar{y}$-axises, and the distance normal to the surface is the $\bar{z}$-axis. This plate is moving parallel to its leading edge (i.e. $\bar{y}$-axis) with a velocity of $\bar{v}_{wall}$. The boundary conditions of the boundary layer equations are given in equation (5.1-5.2).

$$\bar{z}=0 \qquad \bar{u} = \bar{w} = 0$$

$$\bar{v} = \bar{v}_{wall} \qquad 5.1$$

$$\bar{z} \to \infty \qquad \bar{u} = \bar{u}_e$$

$$\bar{v} = \bar{v}_e \qquad 5.2$$

where $\bar{u}$, $\bar{v}$ and $\bar{w}$ are the velocity components along the $\bar{x}$-, $\bar{y}$- and $\bar{z}$-direction respectively. The subscript "wall" means the value at the wall and "e" means the value at the boundary layer edge.

In this co-ordinate system, the velocity components at boundary-layer edge over the plate are given by equations 5.3 and 5.4.

$$\bar{u}_e = \text{constant} \qquad 5.3$$

$$\bar{v}_e = a - b\,\bar{x} \qquad 5.4$$

where "a" and "b" are constants.

The laminar boundary layer solution for this system can be solved by the method described in chapter 3 or by the Blasius similarity method. In the latter method, the three-dimensional boundary layers can be reduced to two ordinary differential equations by using the Blasius similarity variable, $\eta = \bar{z}\sqrt{\frac{\bar{u}_e}{\upsilon x}}$ (for detail see Yohner and Hansen (1958) or Kitchens et al (1975)). The ordinary differential equations are

$$f f'' + 2 f''' = 0 \qquad 5.5$$

$$2 h''' + f h'' - 2 f' h' + 2 = 0 \qquad 5.6$$

where the f' and h' are the first derivatives with respect to η. The boundary conditions can be written as

at $\eta=0$ $\qquad f(0) = f'(0) = h(0) = h'(0) = 0 \qquad 5.7a$

at $\eta\to\infty$ $\qquad f'(\infty) = h'(\infty) = 1 \qquad 5.7b$

The velocities (i.e. $\bar{u}$, $\bar{v}$ and $\bar{w}$) are related to two functions f and h through;

$$\bar{u} = \bar{u}_e f' \qquad 5.8$$

$$\bar{v} = \bar{u}_e\left[af' - b\bar{x}h' + \bar{v}_{wall}(1-f')\right] \qquad 5.9$$

$$\bar{w} = \tfrac{1}{2}\left(\frac{\bar{u}_e \upsilon}{\bar{x}}\right)^{\frac{1}{2}}\left[\eta f' - f\right] \qquad 5.10$$

The solutions of equation (5.5) and (5.6) can be obtained by a numerical solution (e.g. Runge-Kutta method) or from the table in Yohner and Hansen (1958). For the solutions using Runge-Kutta method see Appendix C.

Although the system of boundary layer equations is three-dimensional, the flows are identical along the $\bar{y}$-plane (e.g. $\frac{\partial}{\partial \bar{y}} = 0$). In order to avoid the identical flows in the $\bar{y}$-axis and to get a more general test case, Kitchens et al (1975) introduced the x-, y- and z-co-ordinate in which the origin of the x-, y- and z-co-ordinate is moved from the origin of the $\bar{x}$-, $\bar{y}$- and $\bar{z}$-co-ordinate by "c", and the y-axis is rotated by an angle θ to the $\bar{y}$-axis (see Fig. 5.1). The relations between the barred and unbarred co-ordinate and velocities are given by

$$\bar{x} = x \cos\theta + (y+c) \sin\theta \qquad 5.11$$

$$\bar{y} = -x \sin\theta + (y+c) \cos\theta \qquad 5.12$$

$$\bar{z} = z \qquad 5.13$$

$$\bar{u} = u \cos\theta + v \sin\theta \qquad 5.14$$

$$\bar{v} = -u \sin\theta + v \cos\theta \qquad 5.15$$

$$\bar{w} = w \qquad 5.16$$

Therefore, the system of boundary layer equations in the x-, y- and z-co-ordinate is a general three-dimensional flow. In our calculations, the x-, y- and z-co-ordinate is employed, and the solutions are compared with the analytical solutions (presented in Appendix C) of the $\bar{x}$-, $\bar{y}$- and $\bar{z}$-co-ordinate through the equations (5.11-5.16).

In this test case "a" is set equal -1.25, "b" is set equal -1.0, "c" is set equal $\sin\theta$ (1-$\sin\theta$) and $\theta = \tan^{-1}(1/6)$. The plate is moved paralleled to its leading edge with $\bar{v}_{wall} = -0.2$.

Discussion of Results

A 101×101×51 grid point of x, y and z-directions was used in the calculation. The three-dimensional velocity profiles obtained from the exact solutions were used as an initial data (only on the first row along the y-direction). Please note that the moving wall ($\bar{v}_{wall}$) has velocity components in both the x and y-directions due to the co-ordinate transformation.

The velocity profiles in all three co-ordinate directions are illustrated in Fig 5.2. We can see that they are excellent agreements in u and v of the present method and the exact solutions. In w, the present method shows a little bit downward shifts.

In order to obtain stable solutions for the three-dimensional problem, it is necessary to obey the zone of dependence condition. This concept is presented in chapter 3. Kitchens et al (1975) show that the zone of dependence for this case can be stated as

$$\Delta x \le \omega \Delta y \mathrm{Min}\left(\frac{u}{|v|}\right) \qquad 5.17$$

where the $\mathrm{Min}\left(\frac{u}{|v|}\right)$ is evaluated over the whole plane of the data. ω is a safety factor. In this calculation we set ω=1. Therefore, the choice of Δx and Δy depends on the magnitude of the local streamwise and crossflow velocities. To study the zone of dependence concept, we will use a similar approach as that reported by Kitchens et al (1975). In this study Δx is unchanged and Δy is changed. The value of Δx_p is defined as the largest permissible step size that is calculated from equation (5.17).

The calculated values of zone of dependence are given in table 5.1. The results of this table are subjected to constant step size Δx. The step size of Δy was changed until the results are no longer acceptable. As the mesh size in the y direction is decreased, the error in the calculation increases even though the truncation error decreases. This is caused by the violation of the zone of dependence principle. The highest value of $\frac{\Delta x}{\Delta x_p}$ is about 12 with $\frac{\Delta x}{\Delta y} = 2$. In general, the results agree well with the exact solution even though the zone of dependence concept is violated.

Table 5.1 Summary of the zone of dependence (Δx=0.01 and ω=1)

$\frac{\Delta x}{\Delta x_p}$	$u_{rms\ error}$	$v_{rms\ error}$	$w_{rms\ error}$
5.96	5.8×10^{-5}	1.1×10^{-4}	5.3×10^{-3}
8.52	5.8×10^{-5}	1.2×10^{-4}	5.1×10^{-3}
11.92	7.3×10^{-5}	1.2×10^{-4}	1.0×10^{-2}

Note: $u_{rms\ error} = \Sigma\ (u_{exact\ solution} - u)^2$/ (total number of grid points)

5.3 THREE-DIMENSIONAL FLOW OVER A FLAT PLATE WITH AN ATTACHED CYLINDER

The boundary layer approaching a cylinder with its axis normal to a plate (Fig. 5.3) was computed extensively and accurately by Sowerby (1965) with a Blasius-type series solution, by Fillo and Burbank (1972) with two stream functions, and by Cebeci (1975) with a two-point finite-difference method. For this flow, the free-stream is assumed as a potential (i.e. inviscid) flow around the cylinder and the boundary layer is formed on the plate upstream of the cylinder.

This test case gives a three-dimensional boundary layer on a flat plate. It is used as a test for the accuracy and the suitability of the method (i.e. discretization) discussed in chapter 3. In this test case, we compare our calculations with those reported by Fillo and Burbank (1972).

Specification data:

The co-ordinate system used in this study is shown in Fig. 5.3. In this system, the plate surface is defined on the x-y co-ordinate and the z-axis is normal to the surface. The velocity components along the x-, y- and z-co-ordinates are u, v and w respectively. The x-axis (e.g. y=0) is a symmetry plane at which v = 0 and the y-axis (e.g. x=0) is a leading edge plane at which velocity profiles have been assumed corresponding to the Blasius solutions. A circular cylinder of radius "a" is mounted at distance x_0 downstream from the leading edge of the plate. The calculation domain is limited only up to x/a=4.2 on the symmetry plane, and y/a=1.5 on the y-axis before separation occurred.

If the main stream has uniform velocity u_∞ at infinity in the x-direction, the potential flow arising from the disturbance of a circular cylinder of radius a has components

$$u_e = u_\infty \left\{ 1 + \frac{y^2 - (x - x_0)^2}{\frac{1}{a^2}\left[(x - x_0)^2 + y^2\right]^2} \right\} \qquad 5.18$$

$$v_e = -\frac{2u_\infty y(x - x_0)}{\frac{1}{a^2}\left[(x - x_0)^2 + y^2\right]^2} \qquad 5.19$$

These velocity profiles are used to specify the boundary conditions at boundary layer edge (δ). In order to make a direct comparison between our

calculated results and those obtained by Fillo and Burbank (1972), we have chosen u_∞=3050 cm./sec., a = 5.1 cm. and x_0= 45.7 cm.

Fillo and Burbank (1972) represent the results of their calculations in terms of function F and G which are related to the wall shear stress as follows:

$$\tau_{xz} = \mu \left.\frac{\partial u}{\partial z}\right|_{z=0} = \mu u_e \left(\frac{u_e}{2\upsilon x}\right)^{\frac{1}{2}} F|_{z=0} \qquad 5.20$$

$$\tau_{yz} = \mu \left.\frac{\partial v}{\partial z}\right|_{z=0} = \mu v_e \left(\frac{u_e}{2\upsilon x}\right)^{\frac{1}{2}} G|_{z=0} \qquad 5.21$$

Discussion of Results

In our calculation the convergence criterion for laminar flow was based on the requirement that the difference between two successive values of u and v, for the y-z plane, be less than a specific number ε which was taken as 10^{-5}.

We found that for the calculation domain, the maximum values of $\left|u^{n+1} - u^n\right|$ and $\left|v^{n+1} - v^n\right|$ are at the edges of the plate (i.e. y = 0 or y = y_{max}) and, for all x-stations the solutions near the leading edge converge faster than those near the trailing edge. This may be from the discretization scheme that employed to approximate the solutions. The error in the calculation also will be moved downstream and will influence the whole of the downstream flow.

A 43x16x51 grid point of x, y and z-directions was used in the calculation. To keep the error and iterations down, the calculations were started with Blasius solutions at the first and the second grid points from the leading edge. The computing time required per grid point was 0.0368 seconds on a VAX Workstation.

The predicted variation of F and G in the streamwise distance is compared with the Fillo and Burbank (1972) in Fig. 5.4 and 5.5, respectively. The function F, which determines the streamwise shear stress, decreases as the distance from the leading edge increases for a fixed value of y. For the function G, which determines the cross-flow shear stress, its value increase with distance from the leading edge. At the plate leading edge both functions are independent of y and their values are identical with the Blasius solution, 0.4696 (Fillo and Burbank (1972)). The resulting solutions for the streamwise and crossflow components of wall shear, F and G, at four different spanwise locations are in an excellent agreement with the analytical results of Fillo and Burbank.

5.4 ROTATING HELICAL BLADE

5.4.1 LAMINAR FLOW

To explore the possible extension of our method for complex geometry, we considered the three-dimensional boundary layers on a rotating blade. The laminar boundary layer on a rotating blade such as a rotor blade of an axial turbomachine or a helicopter rotor was first studied by Fogarty (1951) with an assumption that the blades were two-dimensional. Morris (1981) analysed a laminar boundary layer on a twisted helical blade that rotates in an axis perpendicular to its leading edge and solved the boundary-layer equations by using a double series expansion in powers of distance from the leading edge and the cosine of the blade twist angle. The blade's geometry is similar to that of the rotor blades of an axial turbomachine and this boundary-layer flow is three-dimensional because of the centrifugal force due to rotation, so we employ it as a test case to verify the effect of blade rotation on the boundary-layer development.

Specification Data:

The blade geometry with a straight leading edge that rotates in a uniform stream u_∞ with angular velocity Ω is shown in Fig. 5.6a. The blade rotates about the x-axis and the leading edge is parallel to the r-axis. The blade geometry in cylindrical co-ordinate can be written in the following way:

$$\begin{aligned} &x = b\,\theta \\ &0 \le r \le 1 \\ &0 \le \theta \le \pi/4 \end{aligned} \qquad 5.22$$

It is noted that a line of constant radius (r) is also the line along which helix angle (ϕ) remains constant. "b" is a constant and in this case we set b = 1. The body surface (ξ,η) co-ordinate system is formed with intersection of lines of constant radius (r) and lines of constant polar angle (θ). The normal lines (ζ) to the blade surface are described in section of the governing equation in chapter 3.

The free-stream velocity in cylindrical co-ordinate system has components

$$u_x = u_\infty \qquad 5.23$$

$$u_r = 0 \qquad 5.24$$

$$u_\theta = \Omega r \qquad 5.25$$

where u_∞ is a reference velocity, and u_x, u_r, u_θ are the free-stream velocity components in the x-, r-, θ-directions, respectively. For zero angle of incidence at the leading edge, the free-stream velocity in body surface (ξ, η, ζ) co-ordinate system has components

$$u = \left[u_\infty^2 + (\Omega r)^2\right]^{\frac{1}{2}} \qquad 5.26$$

$$v = 0 \qquad 5.27$$

$$w = 0 \qquad 5.28$$

where u, v and w are the velocities along the ξ, η, ζ curves. From the calculation, it is found that these velocities are identical to the transformed velocities that are described in Appendix A.

Discussion of Results

The co-ordinate systems used in this study are the cylindrical co-ordinate. This physical domain (x, r, θ) is then transformed to computational domain (ξ, η, ζ) as presented in chapter 3.

In this test case the convergence criterion (ε) was taken as 10^{-5}. The solution proceeds in the x-direction and requires a large number of iterations ($\approx$ 41) at lateral boundaries to satisfy the convergence criterion.

A 51x25x31 grid point of ξ, η and ζ directions was used. The calculations were started at a next grid point downstream from the leading edge (i.e. x = 0 radians). The computing time required was about 1 and a half minutes for the whole plane on a VMS AXP (TM) Operating System.

The streamwise and crossflow velocity profiles for various polar distances from the blade leading edge, at ϕ=45°, are presented in Fig. 5.7. These velocity profiles have been scaled by the local free-stream velocity magnitude ($\frac{\Omega r}{\sin\phi}$) in the case of u and the free-stream velocity magnitude (Ωr) in the case of v. They show good agreement with those obtained by Morris when polar distance, $\theta \leq 30°$. The main reason for the high errors when θ is increased may be due to the fact that the solutions of Morris are neglecting higher order terms of θ in the series

and the error is high when the value of the distance from the leading edge (θ) is increased. It should be noted that for a fixed value of ϕ = 45° (Fig. 5.7 a-f) the magnitudes of the crossflow velocity near the wall increase as the magnitude of the polar distance from the leading edge increases.

Crossflow skin friction coefficient along the blade shows good agreement with that obtained by Morris (Fig. 5.8) but for streamwise skin friction coefficient the error is high at the leading edge when ϕ=45°. These skin friction coefficients have been scaled by the square root of local Reynolds number, Re_θ. The values increase with distance from the leading edge along the line of constant helix angle, ϕ=45°. At the leading edge the value of crossflow skin friction is zero since there is no crossflow and that of streamwise skin friction is 0.6641 since $c_{f\theta}$ is independent of the twist angle ϕ (Morris (1981)) and corresponds to the Blasius flat-plate boundary layer.

5.4.2 TURBULENT FLOW

It is of interest to extend the application of the code to the conditions under which the boundary-layer flow is turbulent. In most practical situations of fluid flow through a turbomachinery, we encounter fairly large values for the Reynolds number and we must regard turbulence as the normal state of fluid motion. The turbulent boundary layer that develops on a rotating helical blade of large chord length, enclosed in an annulus is investigated by Lakshminarayana et al (1972). Their experimental values may therefore be taken as our verification. A further purpose of the study is to show the suitability of Baldwin-Lomax turbulent model for obtaining accurate solutions for three-dimensional boundary layers.

Specification Data:

The turbulent boundary layer development on a single rotating helical blade was reported by Lakshminarayana et al (1972). The blade geometry is

similar to Fig. 5.6b. In this experiment, the hub radius is 9 inches and the tip radius is 18.30 inches. The maximum angle θ measured from the leading edge is 300°, with pitch of 10 inches. The blade rotates with an angular velocity of 57 rad/sec (450 rev/min) corresponding to a Reynolds number of 7×10^5 base on the tip radius and kinematic viscosity of 160×10^{-6} ft²/sec. With a suitable adjustment, i.e. the blade geometry, to fit the experimental data, we could compare calculated values with those reported by Lakshminarayana et al (1972).

Discussion of Results

The blade's leading edge may be approximated by a flat circular plate since its pitch is very small compared to a chord length. The transition from laminar to turbulent flow occurs at $\theta = 0.73$ radians (Groves and Change (1984)). Base on this analysis, present calculations begin at the leading edge with Blasius solutions and with transition set to $\theta = 0.73$ radians. The convergence criterion (ε) was taken as 2.5×10^{-5}. A 18x18x31 grid point of ξ, η and ζ direction was used. The computing time required per grid point was 0.087 seconds on a VAX Workstation.

The predicted momentum thickness, Θ_{ss} at various distances from the leading edge, is plotted in Fig. 5.9 for a rotating blade at r/r_{tip} =0.55, 0.72, 0.82 and 0.93. The prediction is excellent away from the endwalls. Near the endwalls, the values agree closely with the experimental data. In our analysis of boundary layer, the constraints of the annulus wall and hub are neglected. The predictions of the momentum thickness grow rapidly at the transition point from laminar to turbulent flow ($\theta > 0.73$ radians) and the growth is almost stable near the trailing edge.

5.5 AN AXIAL COMPRESSOR

To account for the effect of viscosity on turbomachinery blade, there are a number of problems that have to be considered, such as the three-dimensional nature of the free-stream velocity, blade geometry and the rotation. Up to this point we can conclude that the method can cope with such problems.

Olsson (1962) carried out comprehensive measurements of the mean flow field on an axial compressor blade. The experiments were conducted in a stationary annular cascade. In order to eliminate the endwalls boundary layer, the endwalls of the cascade and the duct-walls approximately two chord-length upstream of the cascade were made of perforated material. The measurements of free-stream velocity were taken by using three-hole cobra-probe and five-hole direction probe. For velocity profiles inside the boundary layers, a specially made probe of the cobra-type was used. Details of the construction and measurement of these probes can be found in Olsson (1962). He reported that there are larger uncertainties in the crossflow measurements than that in the streamwise measurements. The uncertainty in the streamwise measurement $(\frac{u}{u_e})$ was ±1.5 percent while in the crossflow measurement $(\frac{v}{u_e})$ was ±10 percent. The error for integrated quantities in streamwise direction (e.g. δ^*_s, Θ_s) was ±4 percent and that in crossflow direction (e.g. δ^*_c, Θ_c) was ±10-15 percent.

To demonstrate the rotating effect, Olsson used the experimental blade geometry of the stator blade. Then, he assumed that the rotating stage is both preceded and followed by the stator vanes. The layout of this cascade is shown in Fig. 5.10b. The velocity triangle is then constructed in such a way that the inlet relative angle to the rotor is the same as the inlet absolute angle to the stator. Under this assumption, the data at 50% span-position is used to approximate the

angular velocity and this gives the angular velocity (Ω) of 123 rad/sec. This value can be used for the boundary layer calculation concerning the blade rotation. Although this angular velocity is based on the 50% span data, it can be used on the other span position to show the trend in change of the rotation.

Specification data:

The blade is typical of compressor practice. The key parameters are

Circular arc camber line

NACA Four Digit Series thickness distribution with 9% maximum thickness

Chord; c = 2.8 inches

Camber angle = -35°

Pitch-chord ratio at mid-span; s/c = 1.0

Aspect ratio; l/c = 1.8

Diameter ratio; Di/Dy = 0.65

Chord angle to tangential direction = -45°

The blade was tested in incompressible flow with the Reynolds number based on upstream velocity and chord-length of 1.2×10^5. Details of the blade geometry are available in Appendix E and given in Fig. 5.10. The % chord means the chord position in percent of chord length, starting at the leading edge and % span means the span position in percent of span length, starting at the hub. The measured free-steam velocities on the blade for suction side and pressure side are presented in Fig. 5.11. These data are used as input to the code. Efforts were made to fit the free-stream velocities to give the fully three-dimensional velocities by using two-dimensional cubic spline method.

For the present study, the flow was assumed turbulent throughout. The calculations have been done for both the pressure and suction sides. In order to investigate the effect of rotation, the calculations also have been done for both stator and rotor cases. The calculations were started from the leading edge to the trailing edge using only the free-stream velocities and the blade geometry from the experimental data. The initial velocity profiles were obtained by specifying the flow with no-slip condition at the wall.

Discussion of Results

The flow over pressure surface

The computed mean velocity profiles in the streamwise and crossflow directions are shown in comparison with experimental data at several locations in Fig. 5.12-5.14. The streamwise velocity ($\frac{u}{u_e}$) is well predicted at all locations. The agreement between the prediction and the measurement of crossflow velocity ($\frac{v}{u_e}$) is good near the leading edge and fair near the trailing edge. The effect of rotation is found to have less significant on the velocity profile in the streamwise direction. The magnitude of the crossflow velocity is increased when the blade is rotating, especially near the trailing edge where the magnitude of the flow is increased more than double.

The displacement thickness (δ^*), momentum thickness (Θ) and shape factor in the streamwise, and crossflow predicted from the boundary-layer code are shown in Fig. 5.15-5.17. The definition and the physical meaning can be seen in chapter 4 and appendix F. The predictions of streamwise displacement thickness (δ^*_s) and momentum thickness (Θ_{ss}) show fairly good agreement with those of the experimental data and those of the crossflow (δ^*_c and Θ_{cc}) are in reasonably good agreement when $\Omega = 0$. The poor prediction in the crossflow direction is probably caused by inadequate prediction of the crossflow velocity

profiles. The momentum thickness Θ_{cc}, that is expressed as $\Theta_{cc} = -\int_0^{\delta} \frac{vu}{u_e^2} d\zeta$, is shown to give reasonable agreement with the experimental data except near the leading edge. The predictions for shape parameter of the velocity profile ($H_s = \frac{\delta^*_s}{\Theta_{ss}}$) agree closely with experimental result.

In the case of rotation, the predicted values in the streamwise direction (e.g. δ^*_s, Θ_{ss}) are not much changed while the predicted values in the crossflow direction (e.g. δ^*_c, Θ_{cc}) are considerably increased especially for the crossflow momentum thickness. This is from the effect of the blade rotation to the velocity profiles as shown in Fig. 5.12-5.14 where the magnitude of the crossflow is dramatically increased while that of the streamwise is slightly changed. Therefore, we can expect the high loss of crossflow momentum in the boundary layer due to the rotation.

The predicted velocity vectors near the pressure surface are presented in Fig. 5.18 where the flow can be seen to be strongly three-dimensional. From the boundary layer equations we can see that the flow inside the boundary-layer is driven by two applied forces; the pressure gradient and the force due to rotation. When $\Omega = 0$ there is only the pressure gradient that affects the flow as shown in Fig. 5.18a. In this figure we can see the strong radial pressure gradient that tends to drive the flow radially inward (i.e. secondary flow). This force tends to drive the flow axially near the leading edge and radially inward near the trailing edge.

When Ω = -123 rad/sec, the forces due to the pressure gradient and the rotation are applied to the flow. The predicted velocity vectors of this flow are shown in Fig. 5.18b. Comparing between the two cases (Fig. 5.18a -b), we can see that the rotating force tend to drive the flow radially inward as the secondary flow is stronger when Ω = -123 rad/sec than that when $\Omega = 0$.

In both cases the local streamline velocity is stronger near the hub than that near the tip. This is due to the strong free-stream velocity. It should be noted that the effect of viscosity generates the secondary flow as shown in Fig. 5.18. In the absent of viscosity (i.e. inviscid flow) there is no secondary flow and the flow will go along the outer streamline.

The flow over the suction surface

The computation was also carried out on the suction surface. Comparisons between result of the code (e.g. u, v) and the measurements are shown in Fig. 5.19-5.24. Good predictions are also obtained for the boundary layers on the suctions surface. The mean velocity profiles on the surface are shown in Fig. 5.19-5.21. The magnitude of the secondary flow trends to increase when the blade is rotating. The other predictions (e.g. δ^*, Θ) are shown in similar manner as those on the pressure surface. Overall these predictions show good correlation with the experimental results.

From Fig. 5.11 on the suction side of the blade, the free-steam velocity gradually accelerates from the leading edge and reaches the maximum value at about 50% of the chord. This region represents as a favourable pressure gradient that is discussed in chapter 4. Between that point and the trailing edge of the blade, the pressure rise is sufficiently large to cause flow separation in the case of $\Omega = 0$ as we can see in Fig. 5.25a that near the trailing edge the magnitude of the local secondary flow is higher than that of the local streamline velocity.

When $\Omega = -123$ rad/sec, the balance of the pressure gradient and rotating forces tends to prevent the separation near the trailing edge as indicated in Fig. 5.25b. The rotation effect, on this surface, tends to drive the flow radially inward at about 40% of the chord and generates high secondary flow. Near the trailing

edge, the angle (β_w) between the local streamline and the outer streamline when Ω = 0 is higher than the angle β_w when Ω = -123 rad/sec. This is because the direction of the rotating force depends on the sign of the blade rotation vector and a normal vector to the surface. Therefore, in this surface when the blade is rotating, the angle β_w near the trailing edge is reduced.

The above computations were carried out using a VAX AXP computer. Convergence of the solution is good. The convergence criteria used in the computation is 1×10^{-4}. For a grid 51×21×31, it takes about 1 minute of CPU time except in the case of suction surface with zero angular velocity which takes about 3 minutes of CPU time. This is because the flow is separated and the FLARE approximation is employed in this case.

From this calculation we can conclude that the effects of the boundary layer on turbomachines can be analysed using the fully three-dimensional method. The rotation effect makes the magnitude of the crossflow larger than in the stationary case. The momentum thickness as well as displacement thickness in the crossflow direction trends to increase rapidly when the blade is rotating. Therefore, secondary losses generated by the crossflow will be higher in a rotating than in a stationary case.

5.6 A CENTRIFUGAL COMPRESSOR

In this test case, the code is applied to the study of the three-dimensional compressible flow field in a high-speed, back swept centrifugal compressor impeller. The main objectives are to investigate the physical flow and loss generation due to viscosity in the machine. It is hoped that the accurate prediction of the flow can be used to improve the performance of the machine by altering the impeller blade. However, in this study no attempt was made to redesign the blade.

Specification data:

The compressor rotor is according to the design of Eckardt (1976). Basic parameters are:

impeller LE radius at hub	=	60 mm
impeller LE radius at tip	=	140 mm
impeller TE radius	=	200 mm
impeller axial distance	=	130 mm
blade back swept angle (from radial)	=	30°
rotational seed	=	1466 rpm

The machine has axial inlet flow and radial outflow and the flow is highly three-dimensional. The free-stream velocity vectors (inviscid flow) of the pressure and the suction surfaces are shown in Fig. 5.26-5.27, respectively. These were computed by using Denton's (1983) three-dimensional Euler solver. From these figures, we can see that there is no secondary flow on the pressure surface but there is weak secondary flow near the trailing edge of the suction surface. This is not a physical effect. It is caused by numerical viscosity. The free-stream velocity of this flow is shown in Fig. 5.28. The contours of these velocities are presented in Fig. 5.29a for the pressure surface and in Fig. 5.29b for the suction surface. In both figures, we can see that the highest velocity is near the tip at the leading edge for both surfaces. The lowest velocity is about 15% of the impeller distance from the leading edge near the hub for the pressure surface and about 70% of the impeller distance from the leading edge near both the hub and the tip of the blade for the suction surface. All of these data are used as input to the code.

The code has been applied to simulate the three-dimensional compressible boundary-layer in the above configuration. The energy equation for the analysis of the total enthalpy has been approximated by using the conservation of rothalpy. In

this case the flow is assumed to be adiabatic and the Prandtl number is unity (a fair approximation for gases). If the flow separates, the code uses the FLARE approximation. This is done solely to save computer time and to reduce the complexity of the coding.

A 51×13×31 grid point is used in this calculation. The convergence criterion of the solution is 1×10^{-4}. The computations were carried on VAX AXP computer. The CPU time for the pressure surface was 1 minute and 2 seconds, and for the suction surface was 1 minute and 40 seconds. The results of the computations are in the followings.

Discussion of Results

Pressure side

The predicted velocity vectors near the pressure surface are shown in Fig. 5.30. The figure shows that the flow is separated near the leading edge of the hub. The flow generates strong secondary flows from about the beginning of the axial-radial bend up to the trailing edge. The secondary flows grow dramatically from hub to tip. The effect of the secondary flows will be to transport the fluid particles toward the tip of the blade. Compare these velocity vectors (Fig. 5.30) to those of free-stream in Fig. 5.26, we can see that there are secondary flows in the former figure especially near the trailing edge. These secondary flows are generated due to three-dimensional boundary-layer.

Fig. 5.31 shows contours of the predicted displacement thickness on the pressure surface. There is substantial growth of displacement thickness near the shroud at the trailing edge where the secondary flows are very strong. Near the leading edge of hub, the displacement thickness is also high because the flow is reversed. Compare this result (Fig. 5.31) to the velocity vector in Fig. 5.30, the

displacement thickness seems to be high in a region where the secondary flows are strong.

Fig. 5.32 shows numerical predictions of entropy generation on the pressure surface. This illustrates the high loss on the shroud at rotor inlet, outflow and especially along the shroud of the blade. The high loss at the inlet is due to the high inlet flow. From this result it has shown that the inlet region of the blade is the major cause of lost efficiency in the machine and the dominant loss generation is on the shroud. The main contribution of the high loss along the shroud is due to the secondary flow. It transports the losses toward the shroud. The major source of entropy at the trailing edge comes from the subsequent mixing of the flow towards the exit.

Suction side

The similar results of the suction surface as those from the pressure surface are obtained. Fig. 5.33 shows the predicted velocity vectors near the suction surface. From this figure, we can see that the secondary flow is very strong at about 1/3 of the streamline from the leading edge where the flow is separated at the shroud. The results indicate that the fluid is migrating from the hub toward the shroud. The secondary flows are stronger than those on the pressure surface (Fig. 5.30). Compare these velocity vectors (Fig. 5.33) to those of free-stream in Fig. 5.27, the secondary flows in the former figure are generated earlier and stronger than those in the latter figure. The secondary flows near the shroud at the trailing edge of Fig. 5.33 are moved in the opposite direction of the other region. The main cause may be come from the free-steam velocity that already shown secondary flow near the trailing edge.

The predicted displacement thickness is presented in Fig. 5.34. The thicknesses grow dramatically at the separation points. The displacement

thickness is also high in the region where the secondary flows are strong (compare this result (Fig. 5.34) to velocity vectors in Fig. 5.33). This indicates that the secondary flows move low momentum fluids (in this calculation from hub to shroud) and therefore increase the overall displacement thickness.

Fig. 5.35 shows contours of the predicted entropy generation on the suction surface. From this result it has been shown that the entropy generation is very high at the inlet region of the blade. At each meridional distance, the major source of loss is near the shroud. Compare this result to the free-stream velocities in Fig. 5.32 and to the velocity vectors near the surface in Fig. 5.33, it is likely that the major cause of high loss at the inlet region is due to high inlet free-stream velocities and the major cause of high loss near the shroud is the subsequent mixing out of the secondary flows. It should be noted that the secondary flow is responsible for transporting the low-momentum fluid from the hub region to the shroud region.

Compare the predicted entropy generation on both the pressure surface and the suction surface with the contours of free-stream velocity and the secondary flows, we can conclude that the rate of entropy production is high in the direction of the secondary flow and its value is dependent on the free-stream velocity. The secondary flows are not responsible for loss generation with in the impeller but simply transport the loss.

5.7 A BOUNDARY LAYER WITH A SEPARATION BUBBLE

In this section, we considered the two-dimensional incompressible laminar boundary layer with a separation bubble. This problem was presented in Briley (1971) by solving the Navier-Stokes equations, in Carter and Wornom (1975) by

solving the inverse method boundary-layer equations (the vorticity transport) and in Veldman (1981) by using the interactive boundary layer method.

The purposes of comparison are: (1) application of the present method in separation flow problem and (2) the use of veldman's interaction method. In this calculation we do not use Blasius-type solution as an initial condition but specify velocities (e.g. u, w) at a solid wall are zero and the rests are equal the outer flow. This is because we want to check the convergence of the code. The results of the calculation are compared with those reported by Carter and Wornom (1975).

Specification data

Consider a flow parallel to a dented plate with the configuration given by

$$z_b = -0.03 \text{ sech } \{4(x-2.5)\} \qquad 0 \le x \le \infty \qquad 5.29$$

and presented in Fig. 5.36.

The potential flow past the body can be represented by thin airfoil theory; viz.;

$$u_e(x) = 1 + \frac{1}{\pi}\int_0^{\infty} \frac{dz_b / d\xi}{x - \xi} d\xi \qquad 5.30$$

Veldman (1981) assumed that the interaction takes place between x = 1 and 4 but in our calculation we assumed that the interaction takes place from the leading edge of the plate. In the present calculations, the Reynolds number (Re) is 8×10^4, the length of the plate is 4 ($0 \le x \le 4$).

Discussion of results

In this calculation the convergence criterion (ε) was taken as 1×10^{-4} and relaxation factor (ω) for updating δ^* is 1. A 51×31 grid point of x and z-directions was used. To check the convergence of the method, the calculations were started without using Blasius solution but with specifying the flow with no-slip at wall. The calculation needs 64 iterations to pass the convergence criterion, which requires about 5 minutes computation time on a VAX workstation. This is may be the reason why the present calculation takes more iterations than those of Veldman (1981).

Fig. 5.17 shows the excellent agreement between the skin friction obtained from the present method and that from Carter and Wornom (1975). There is no difference near the point x = 1 where Veldman (1981) solution has. This is because the domain of integration of the interaction boundary layer is extended upstream as he pointed out.

The computed displacement thickness distribution is compared with Carter's predictions in Fig. 5.38. Also shown on this figure is the initial guess for displacement thickness. These values are calculated from the $\frac{1}{2}$-power formula. A difference between the present results and those of Carter and Wornom (1975) is visible at about x≈2.25 where our result is a little bit higher. In general, this agreement is quite good.

Finally Fig. 5.39 presents the pressure, $p=\frac{1}{2}(1-u_e^2)$ obtained with interaction and that without interaction. The difference between the two curves indicates the influence of the interaction (Veldman, 1981).

In conclusion it is deduced that the present method is quite accurate and can be implemented in the case of separation flow. The solutions showed the

reverse flow velocity with the help of Veldman's interaction boundary layer method.

5.8 CONCLUSION

The three-dimensional, compressible boundary-layer solution method is applied to predict the behaviour of the boundary layers on a wide variety of flow situations and configurations. The predictions are in good agreement with analytical results and experimental measurements.

The method employs the non-orthogonal curvilinear co-ordinate system on the body surface and the finite difference approximation to solve the equation accurately and efficiently. In this method the boundary layer equations are marched in time by using a time stepping method and their truncation error has been shown to be numerically second-order accurate in space and first-order accurate in time. The equations are solved without employing the similarity law. The solution of the equations is obtained in an uncoupled manner using a simple iterative procedure to update the coefficients in the next time step. This new development shows that the method is straightforward and easily adapted to flow situations and configurations.

We may conclude that the present prediction method provides generally satisfactory results for all the test cases. Some of the major conclusions are as follows.

1. The analysis is accurate for the prediction of the three-dimensional boundary-layer with or without surface curvature and rotation. The method is simple and requires reasonable computer storage. Although the method has the

capability to predict unsteady flow, our main development is to predict the steady flow.

2. The additional effect of the rotation tends to increase the magnitude of the crossflow but the limiting streamline angle (β_w) increases or decreases depending on the sign of the blade rotation vector and the unite normal vector to the blade surface. The secondary losses in this case, therefore, will be high.

3. The method shows poor convergence when the flow is reversed. Two methods are employed for calculating of the flow. The first method is based on an interactive scheme. The second method is based on FLARE approximation scheme. Due to the complexity of the interaction, it is not at the present to perform the three-dimensional interaction scheme. Therefore, FLARE approximation scheme is applied for the three-dimensional calculation. Theoretically, the FLARE approximation method is inaccurate beyond the flow separation point when the reverse flow is high.

4. The total enthalpy may be approximated by using the conservation of rothalpy. This approximation results from the assumption of adiabatic wall and the Prandtl number is unity in the energy equation of compressible boundary layer.

5. The boundary-layer induced loss is dependent on its free-stream velocity and the secondary flow. When the flow is separated, the displacement thickness increases rapidly and the secondary flow is strong. These make the flow non-uniform. The entropy generation is high in the direction of the secondary flow because it transports the loss. To improve the efficiency of a machine, the level of secondary flow has to reduce.

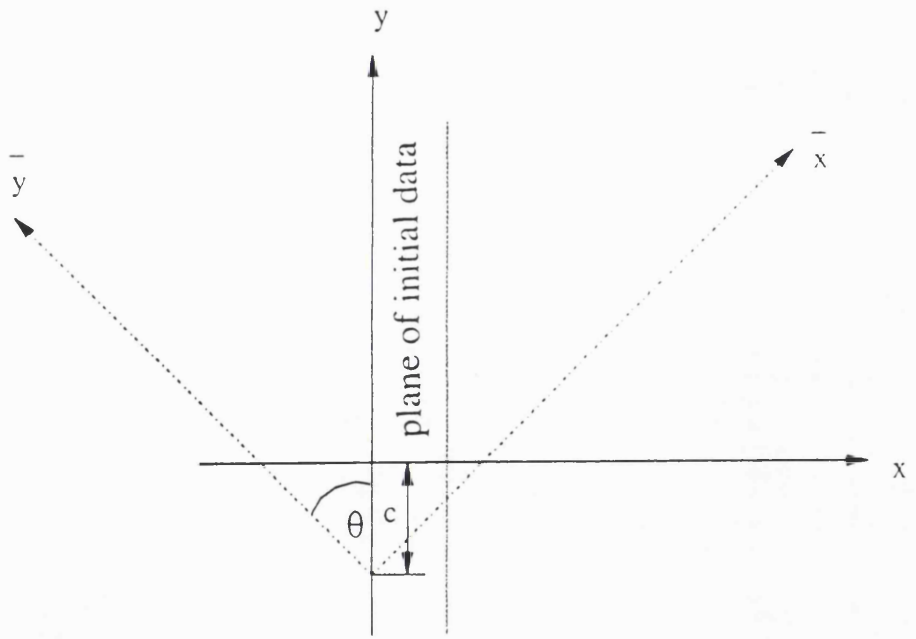

Fig.5.1 Co-ordinate system for three-dimensional flow over a flat plate with the plate moving parallel to its leading edge

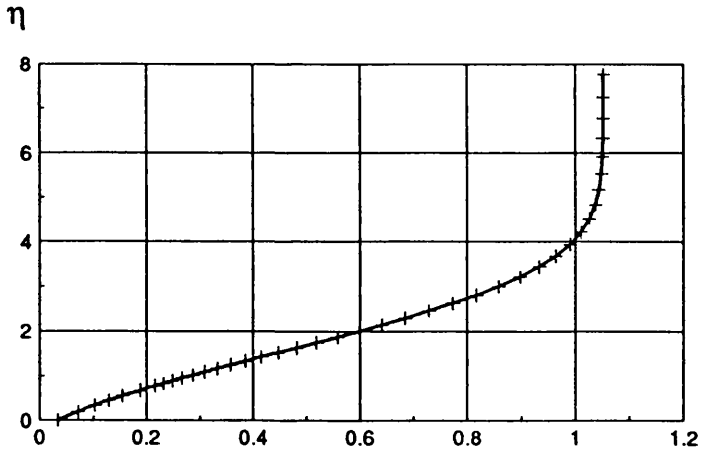

a) u

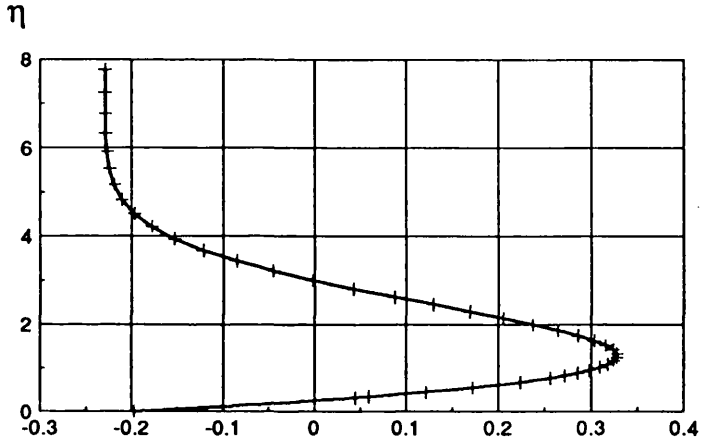

b) v

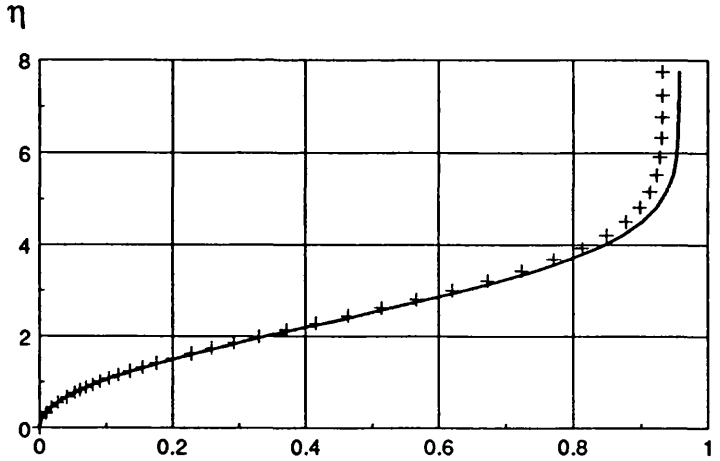

c) w

Fig. 5.2 Three-dimensional boundary-layer velocity profiles for flow over a flat plate moving wall ($\bar{v}_{wall}$ = -0.2) at x = 0.80, y = 0.24

\+ analytical solution ——— present method

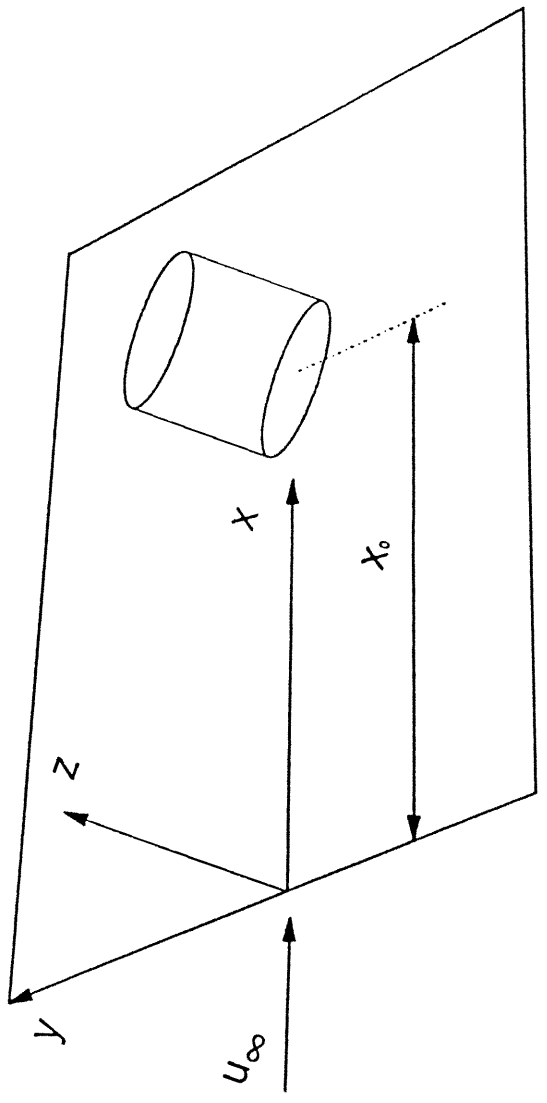

Fig. 5.3 Flow past a flat plate with attached cylinder

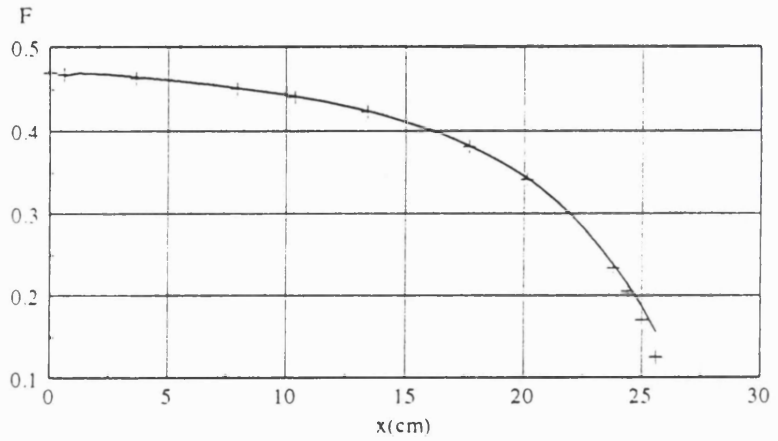

a) y/a = 0.5

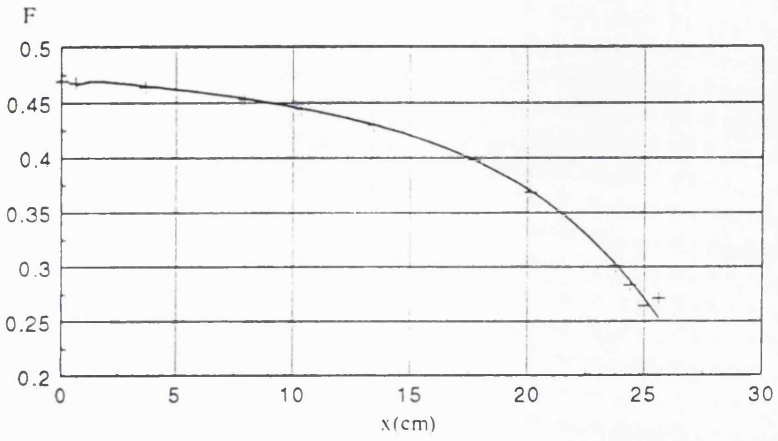

b) y/a = 1.0

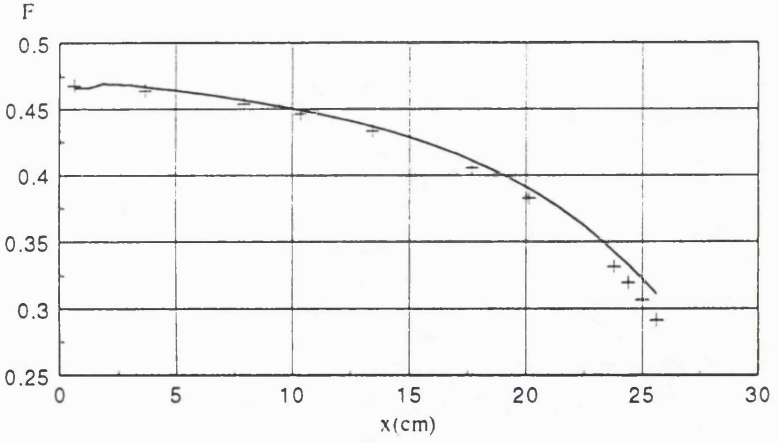

c) y/a = 1.2

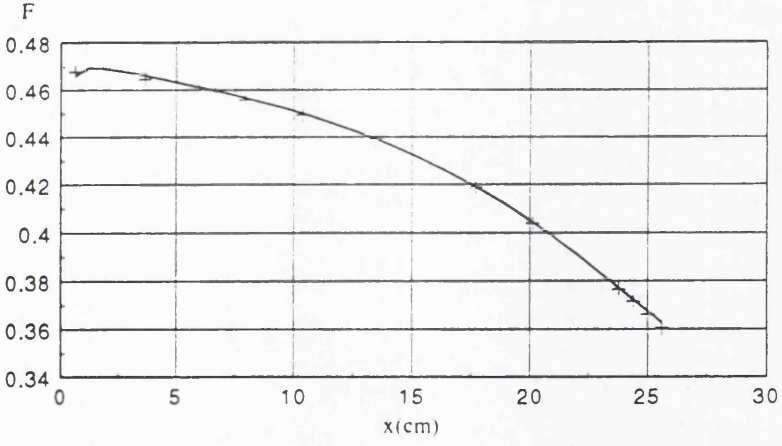

d) y/a = 1.5

Fig. 5.4 Wall shear F distribution for flat plate with attached cylinder, + analytical result (Fillo and Burbank 1972) —— present method

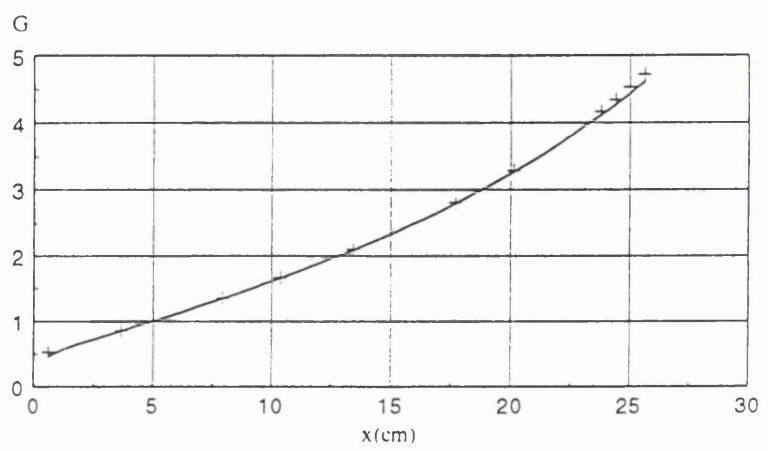

a) y/a = 0.5

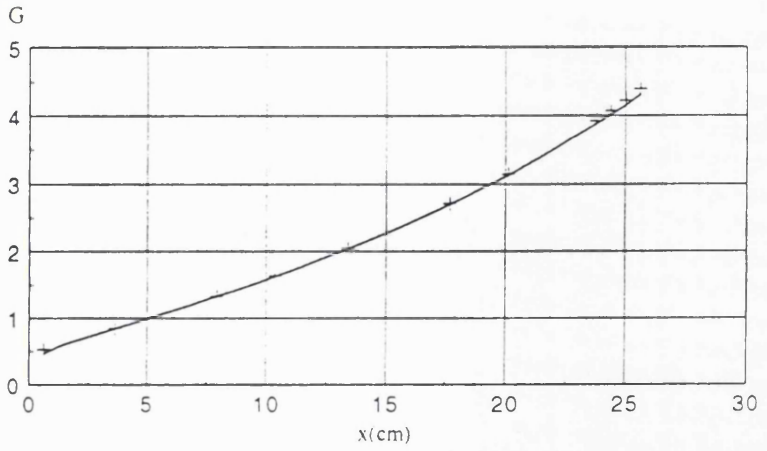

b) y/a = 1.0

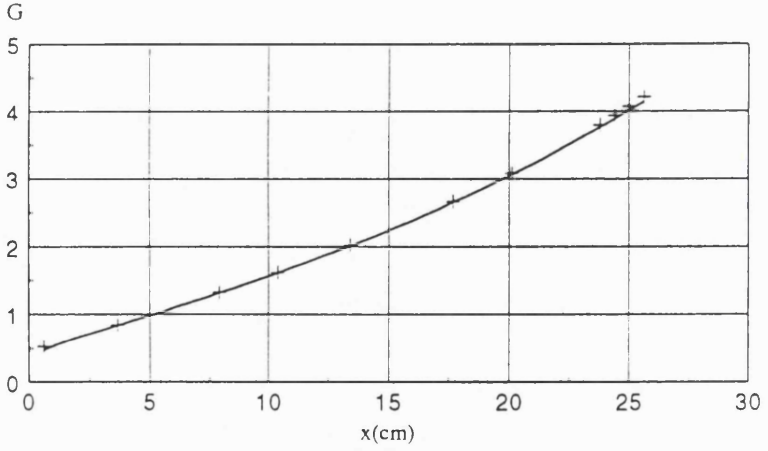

c) y/a = 1.2

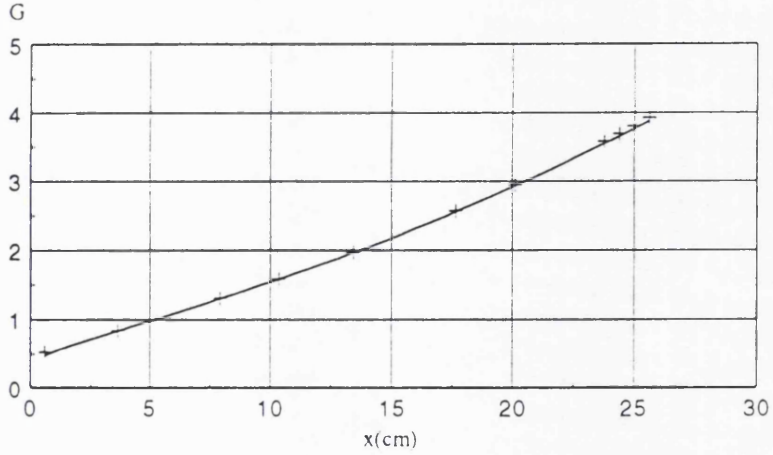

d) y/a = 1.5

Fig. 5.5 Wall shear G distribution for flat plate with attached cylinder, + analytical result (Fillo and Burbank 1972) ——— present method

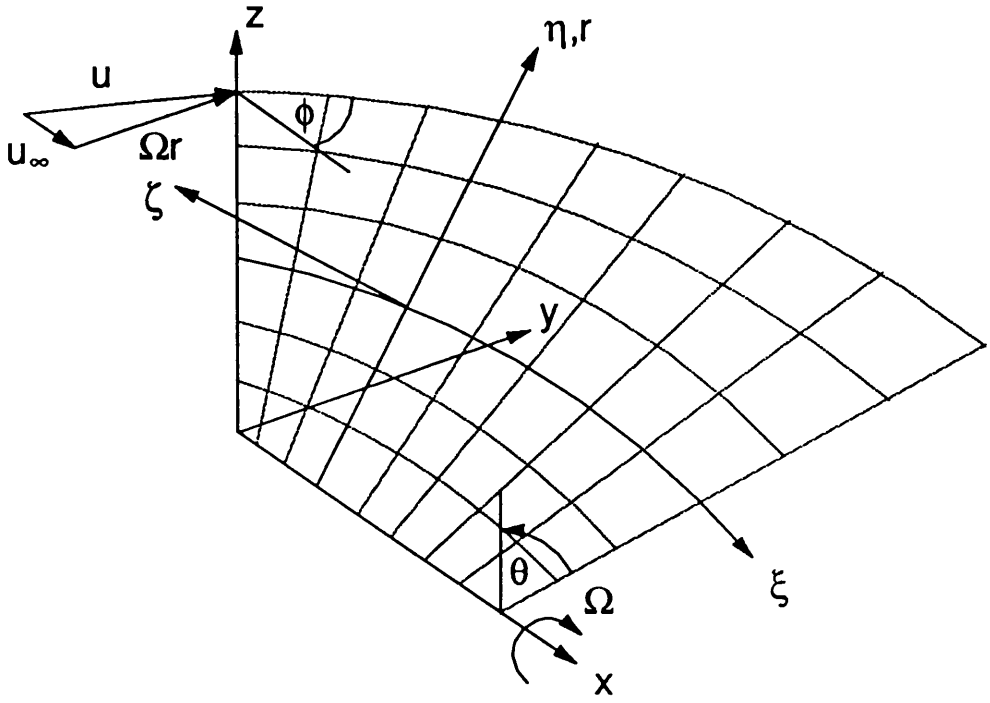

a) helical blade co-ordinate system

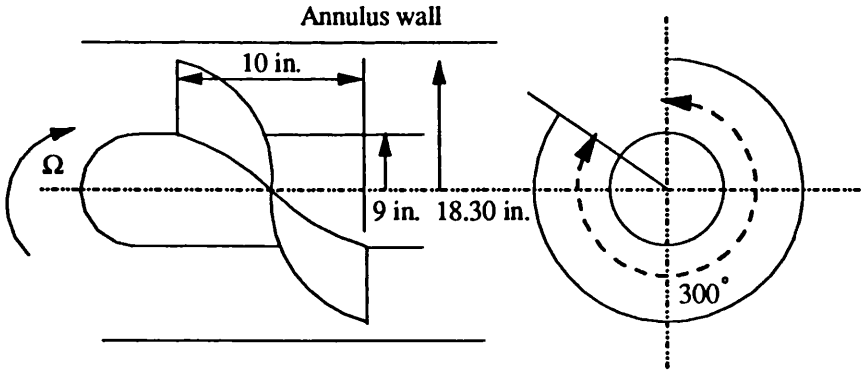

Not to scale

b) helical blade due to Lakshminarayana, et al (1972)

Fig. 5.6 Schematic of rotating helical blade

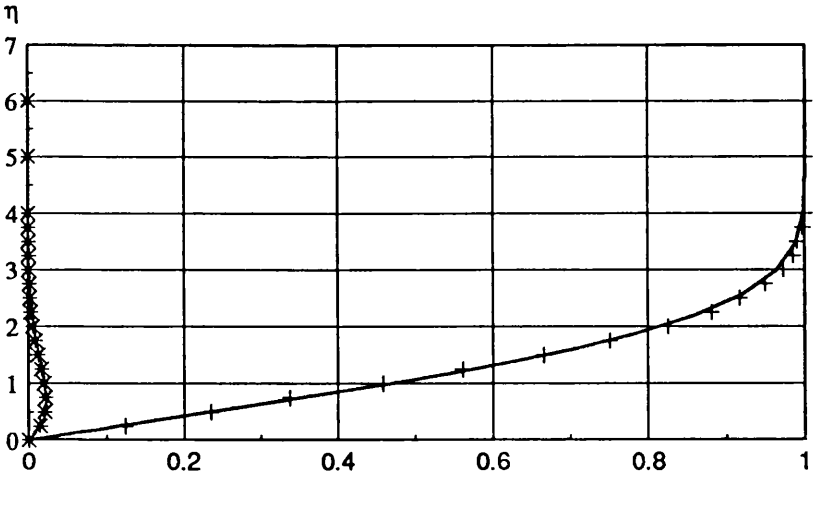

a) $\theta = 4.50^{o}$

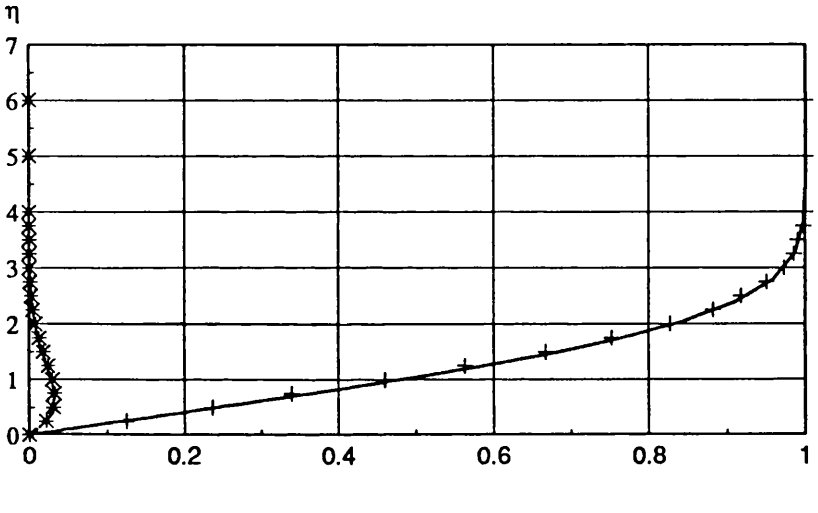

b) $\theta = 5.75^{o}$

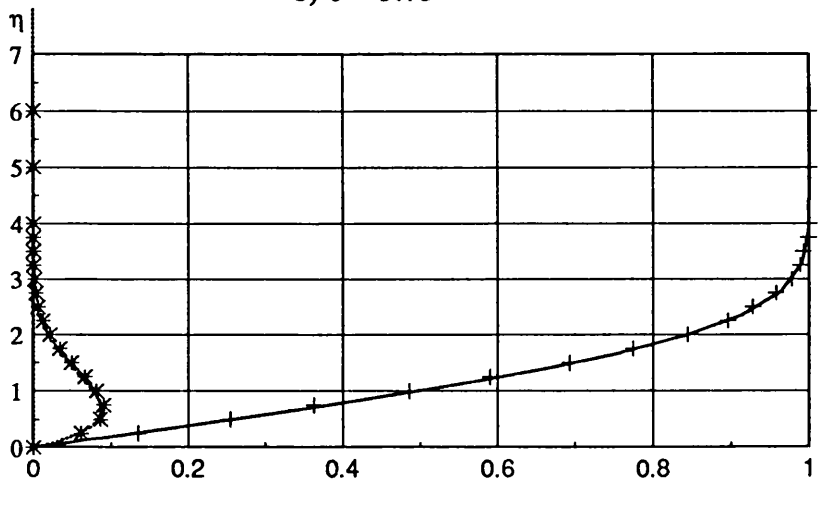

c) $\theta = 20.25^{o}$

\+ * streamwise & radial velocities from analytical result (Morris, 1981)

— ----- streamwise & radial velocities from present method

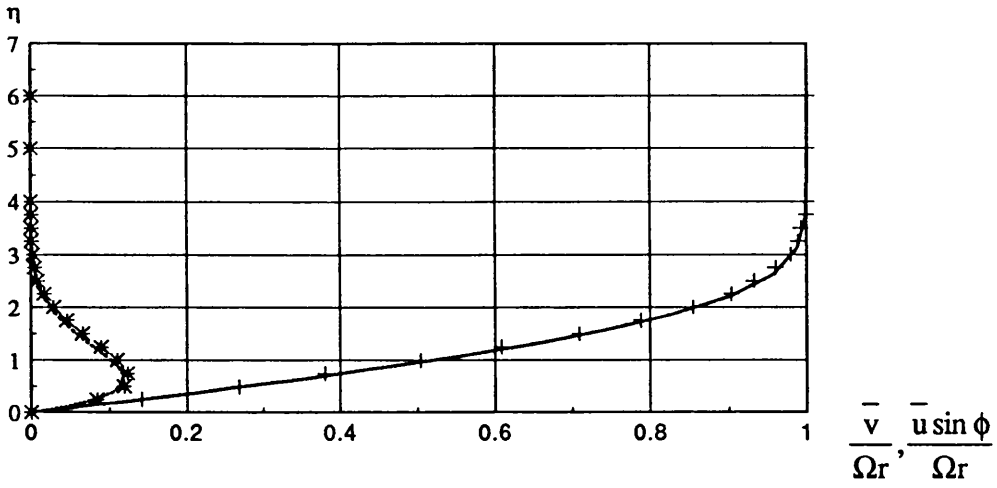

d) $\theta = 29.25^{o}$

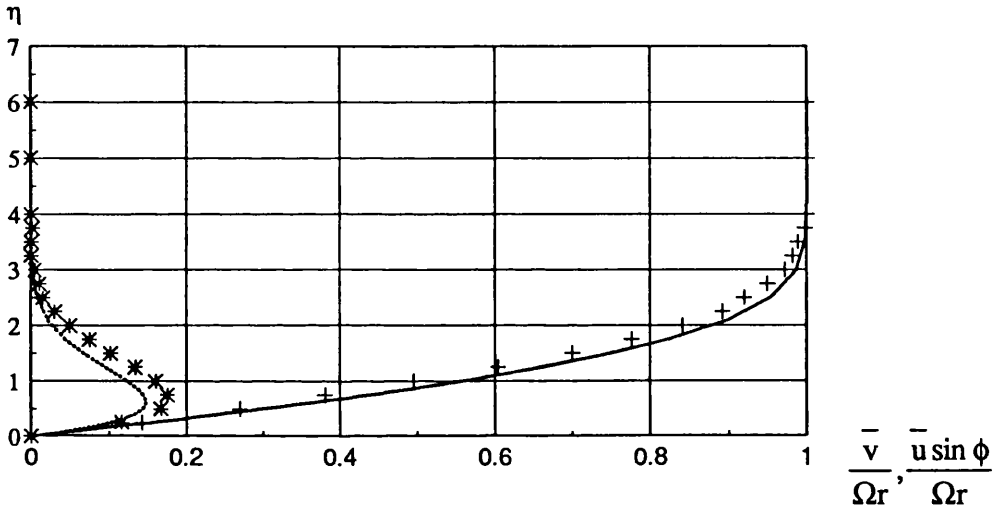

e) $\theta = 40.00^{o}$

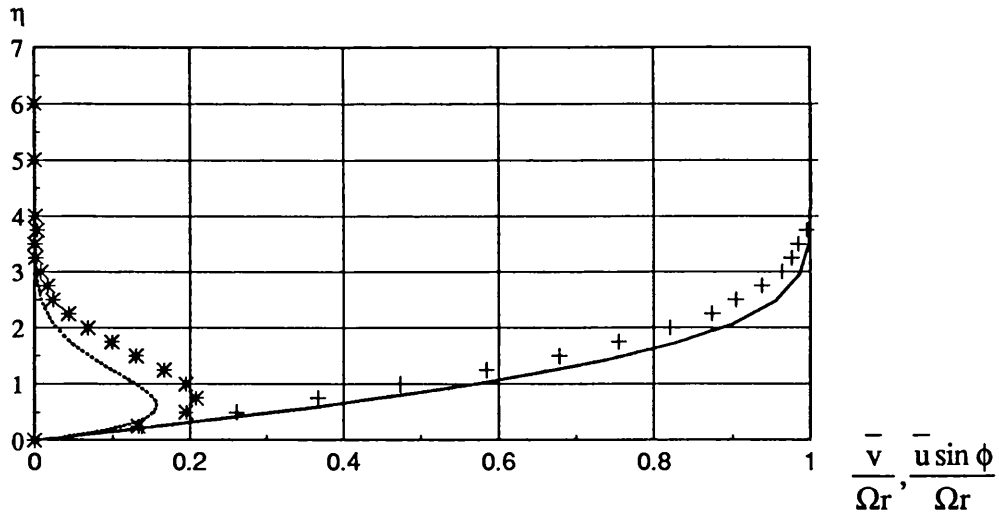

f) $\theta = 45.00^{o}$

Fig. 5.7 Streamwise $\left(\frac{\bar{u}\sin\phi}{\Omega r}\right)$ and radial $\left(\frac{\bar{v}}{\Omega r}\right)$ velocity profiles for various polar distances from the leading edge, $\phi = 45^{o}$, $\eta = \zeta\left(\frac{\Omega}{2\upsilon\theta}\right)^{\frac{1}{2}}$

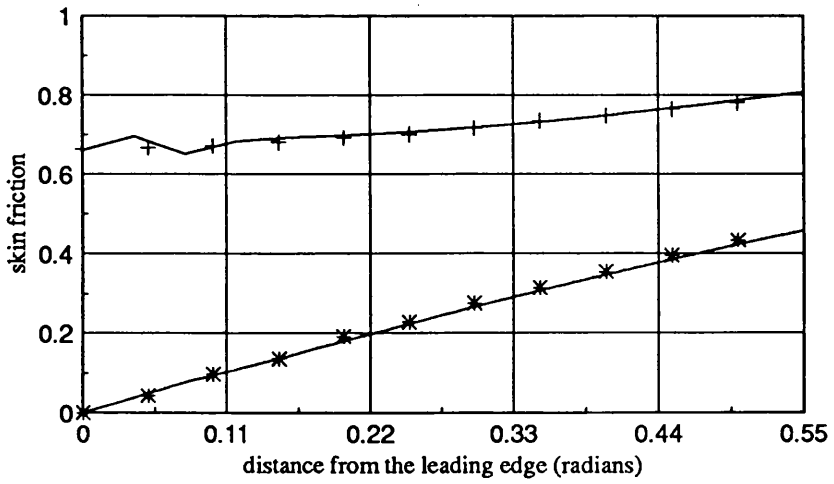

Fig. 5.8 Skin friction $\left(c_{f\theta}\,Re_{\theta}^{\frac{1}{2}}, c_{fr}\,Re_{\theta}^{\frac{1}{2}}\right)$

\+ * $\left(c_{f\theta}\,Re_{\theta}^{\frac{1}{2}}, c_{fr}\,Re_{\theta}^{\frac{1}{2}}\right)$ from analytical result (Morris, 1981)

— ----- $\left(c_{f\theta}\,Re_{\theta}^{\frac{1}{2}}, c_{fr}\,Re_{\theta}^{\frac{1}{2}}\right)$ from present method

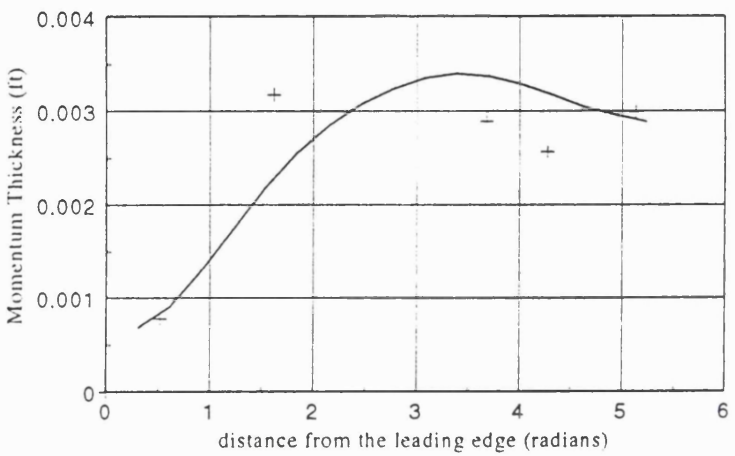

a) $r/r_{tip} = 0.55$

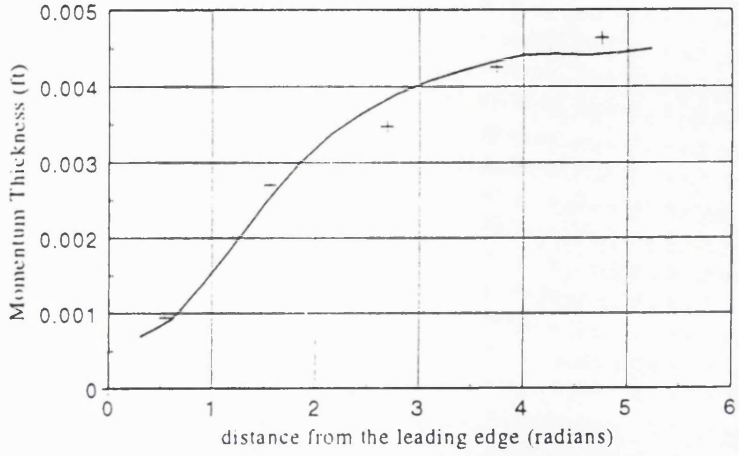

b) $r/r_{tip} = 0.72$

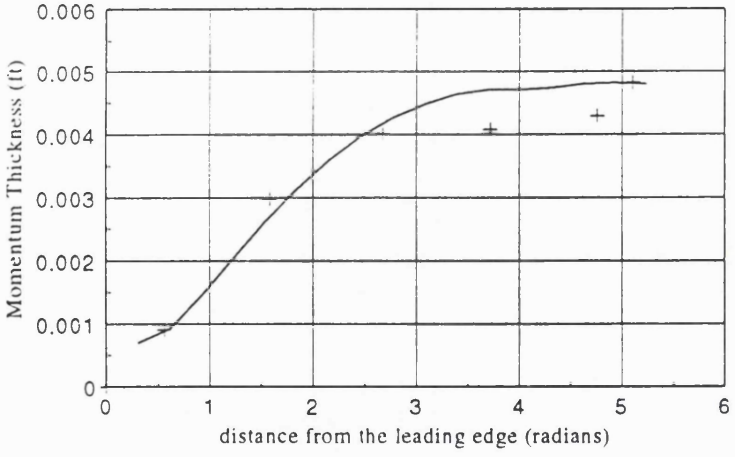

c) $r/r_{tip} = 0.82$

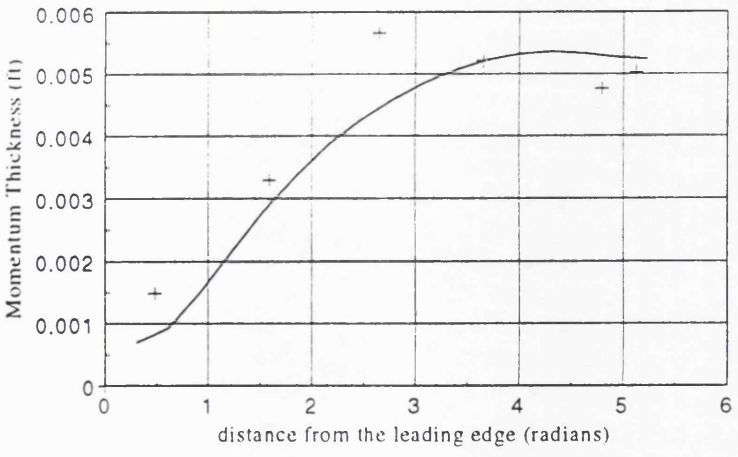

d) $r/r_{tip} = 0.93$

Fig. 5.9 Variation of momentum thickness on rotating helical blade, + measured (Lakshminarayana et al 1972) ——— present method

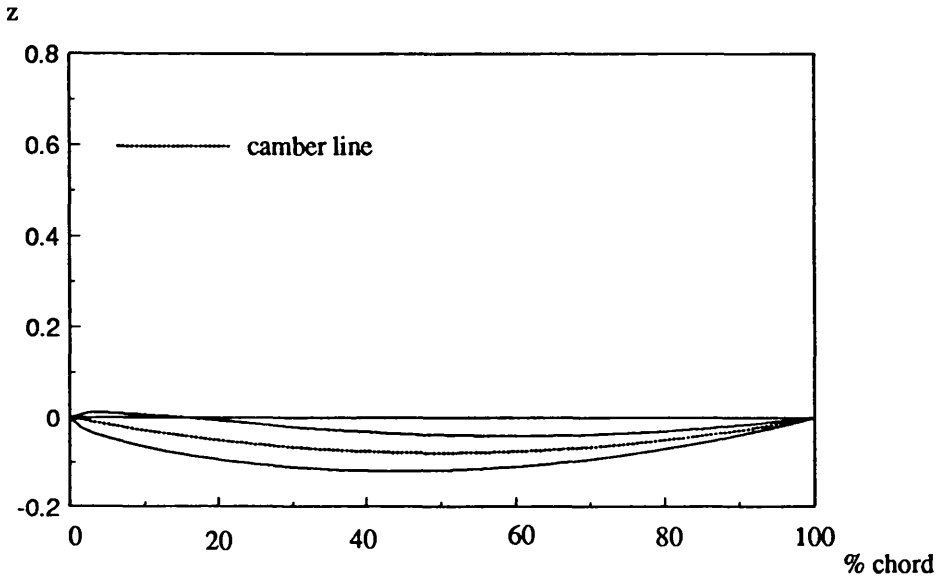

a) the blade geometry

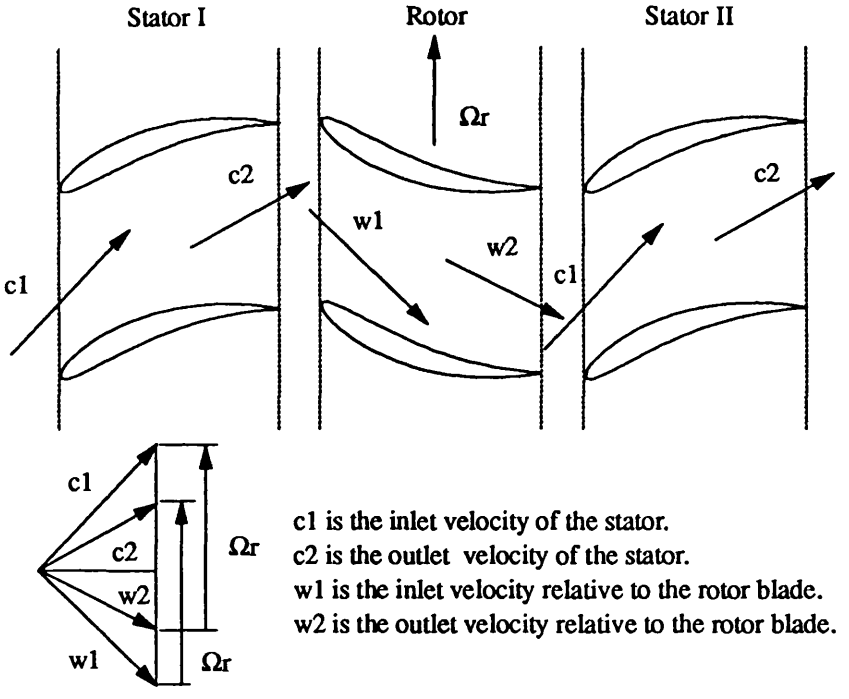

b) velocity triangle (Olsson (1962))

Fig. 5.10 Blade co-ordinate for the test case (NACA Blade)

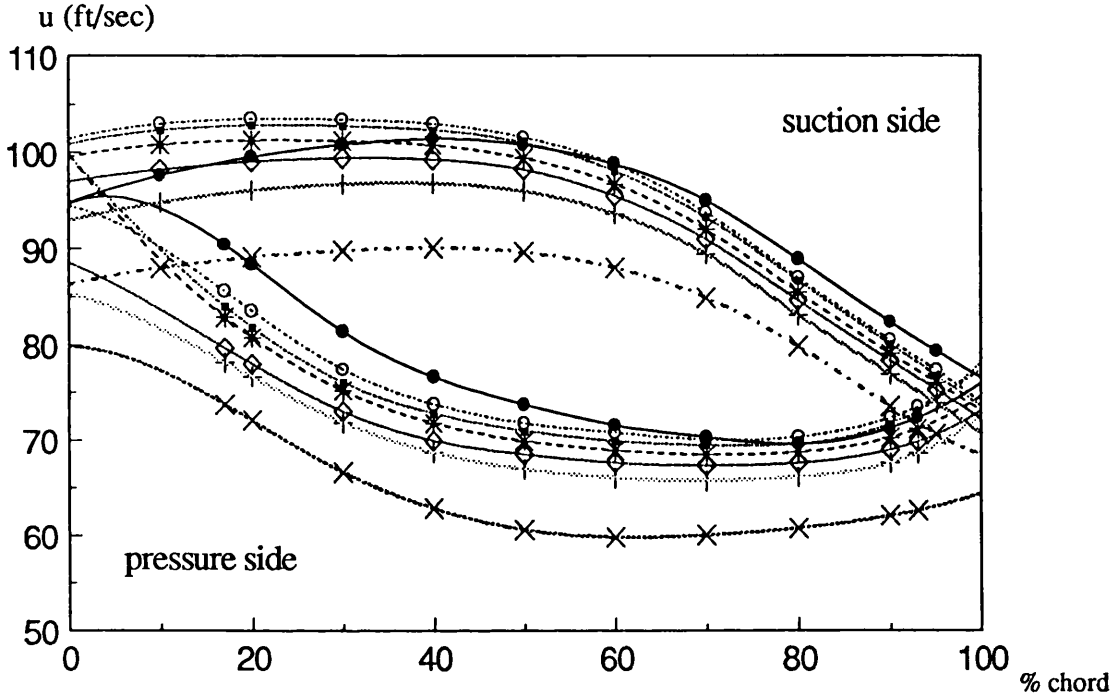

Fig. 5.11 Free-stream velocity on the NACA blade

• 10% span ○ 30% span ■ 40% span

* 50% span ◊ 60% span + 70% span

× 90% span

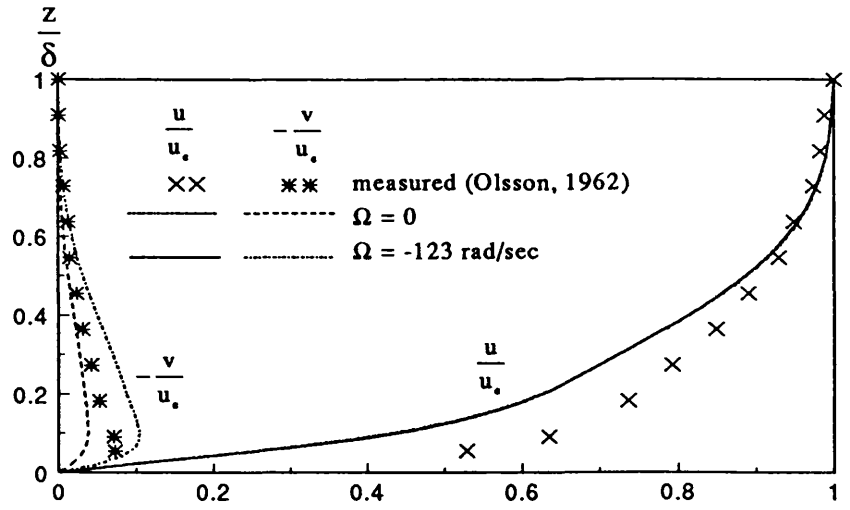

a) 30% chord, 10% span

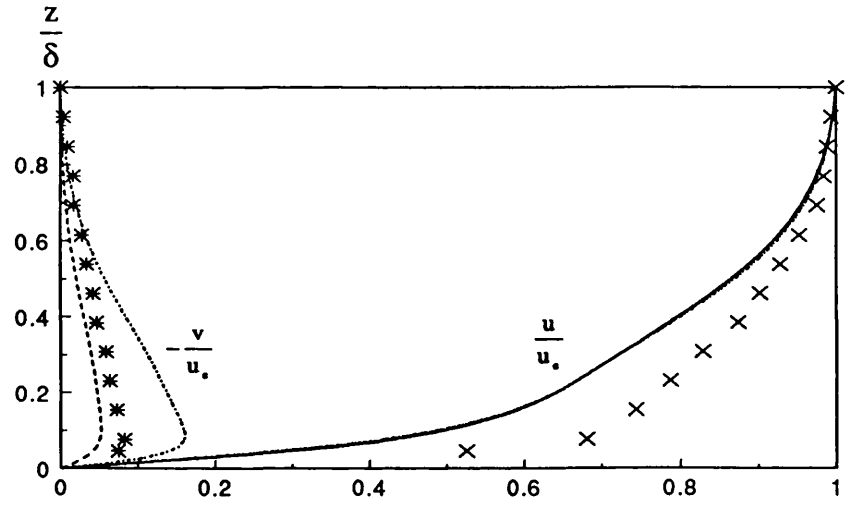

b) 50% chord, 10% span

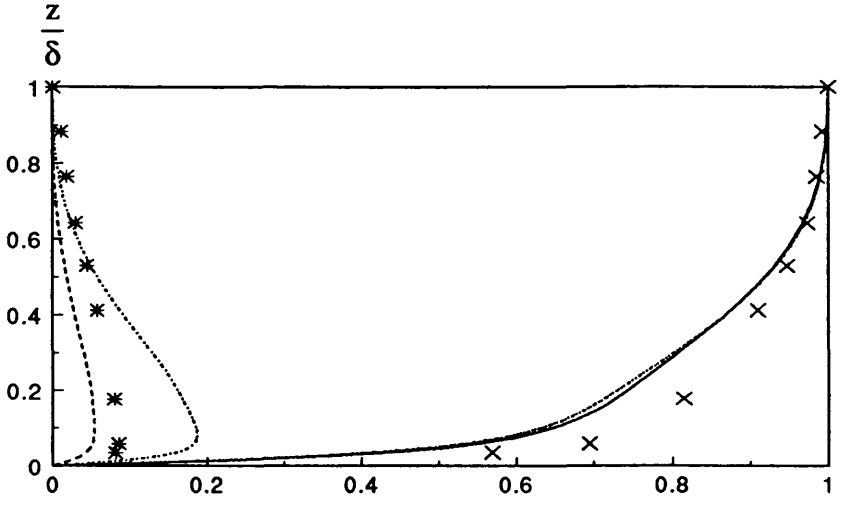

c) 90% chord, 10% span

Fig. 5.12 Mean velocity u and v profiles of three-dimensional boundary layer 10% span for NACA Blade (pressure side)

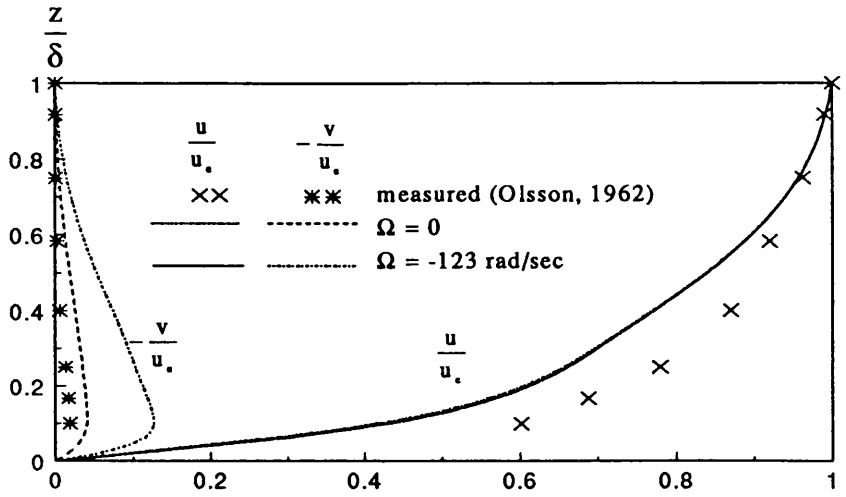

a) 30% chord, 50% span

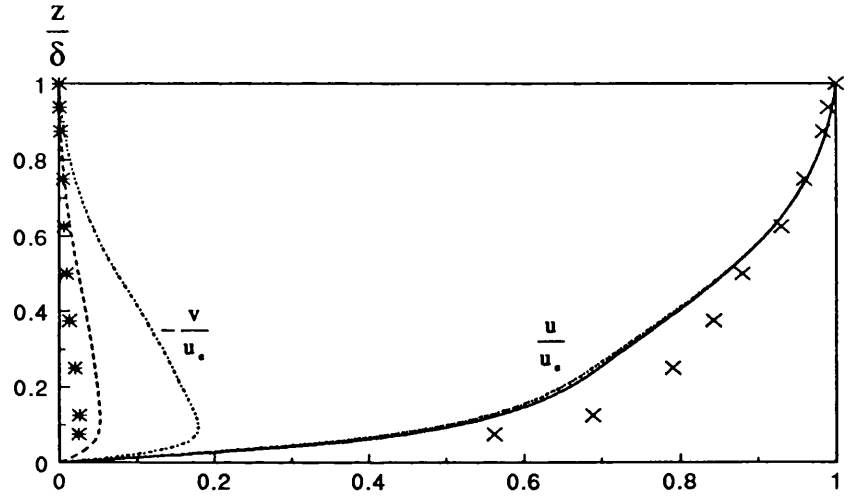

b) 50% chord, 50% span

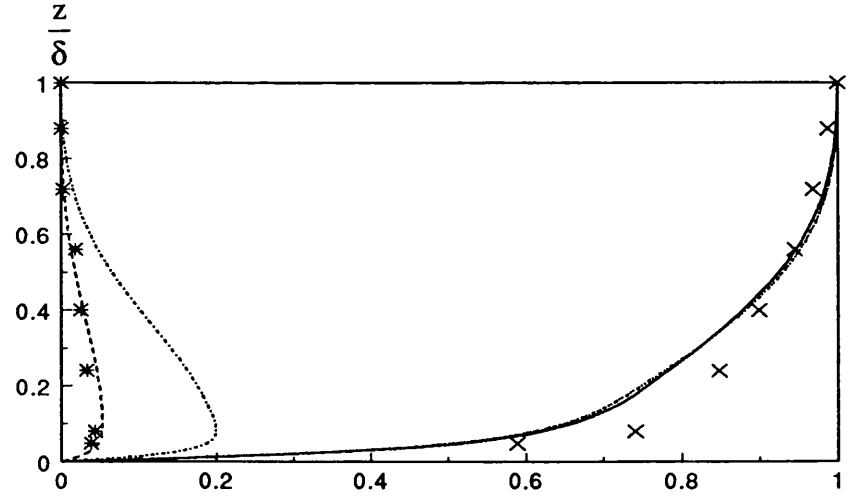

c) 90% chord, 50% span

Fig. 5.13 Mean velocity u and v profiles of three-dimensional boundary layer 50% span for NACA Blade (pressure side)

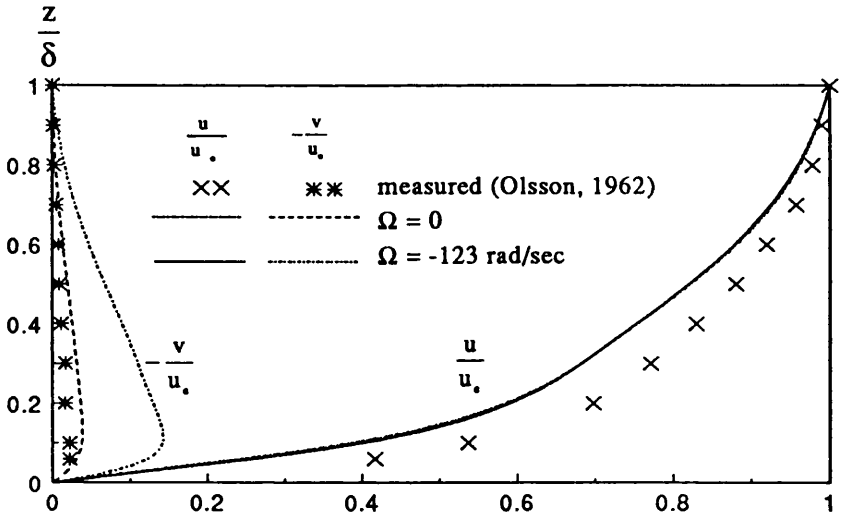

a) 30% chord, 90% span

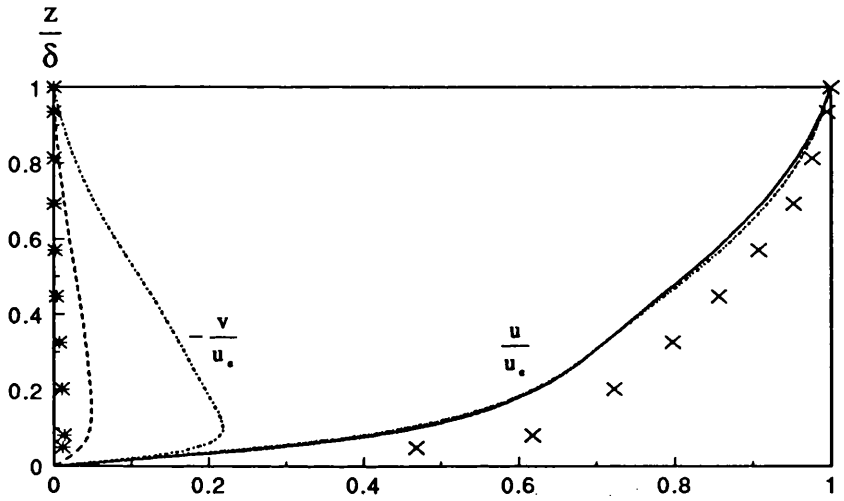

b) 50% chord, 90% span

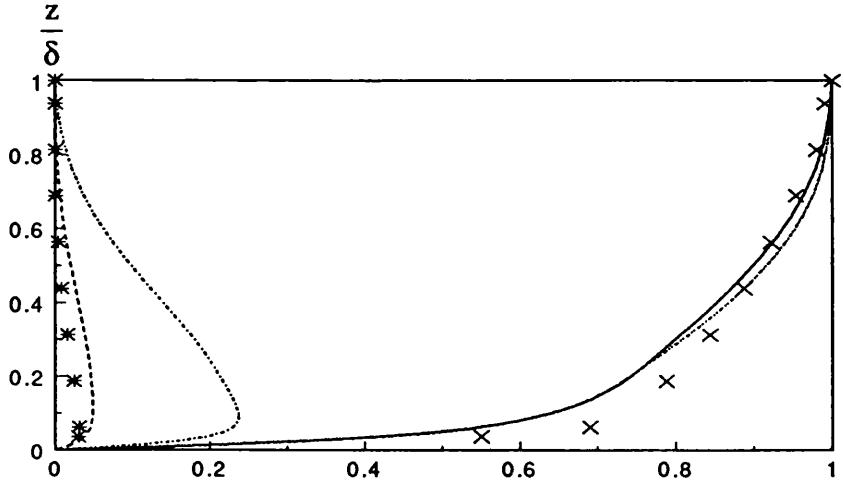

c) 90% chord, 90% span

Fig. 5.14 Mean velocity u and v profiles of three-dimensional boundary layer 90% span for NACA Blade (pressure side)

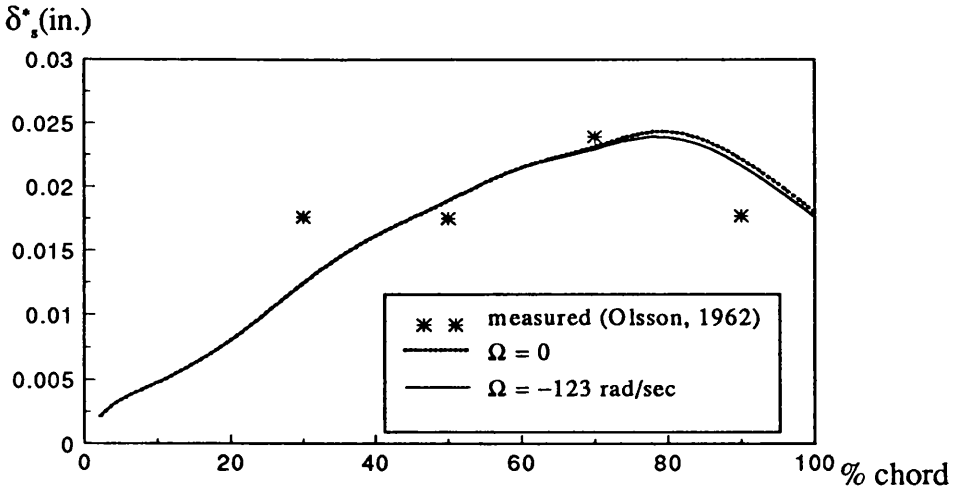

a) displacement thickness in the streamline direction

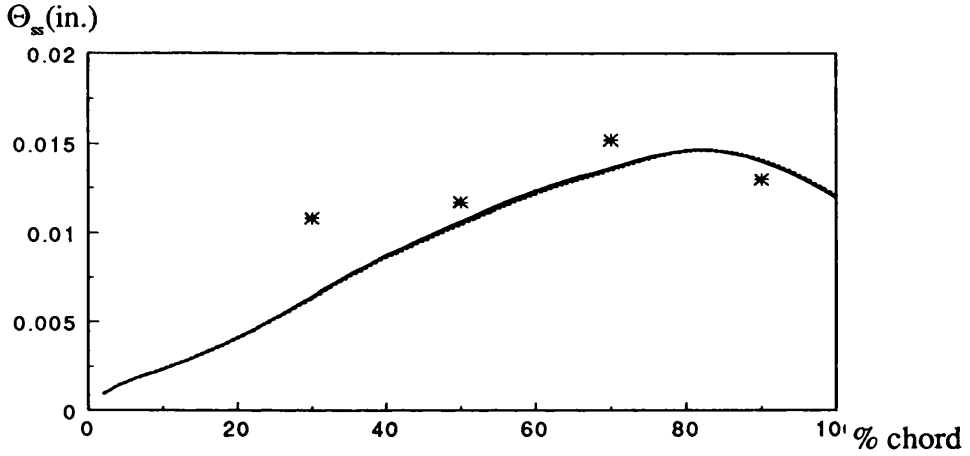

b) momentum thickness in the streamline direction

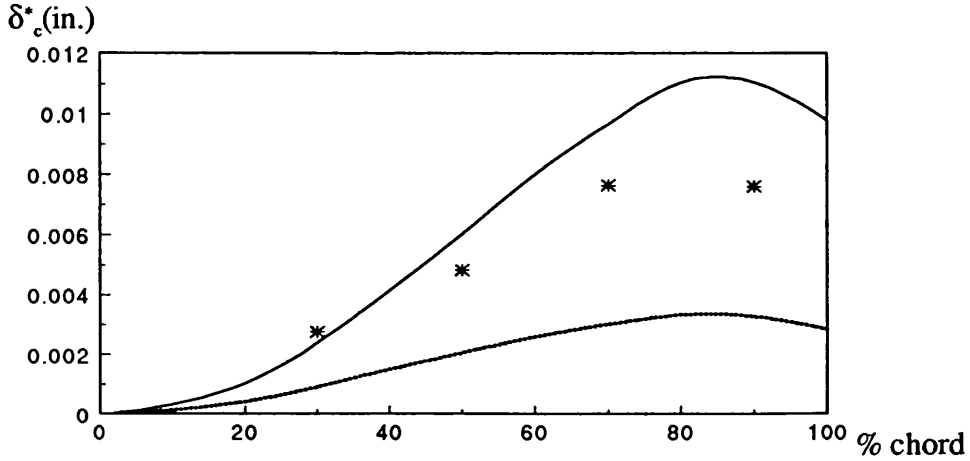

c) displacement thickness in the crossflow direction

Fig. 5.15 Comparison of calculated and measured quantities for pressure surface of NACA Blade, 10% span

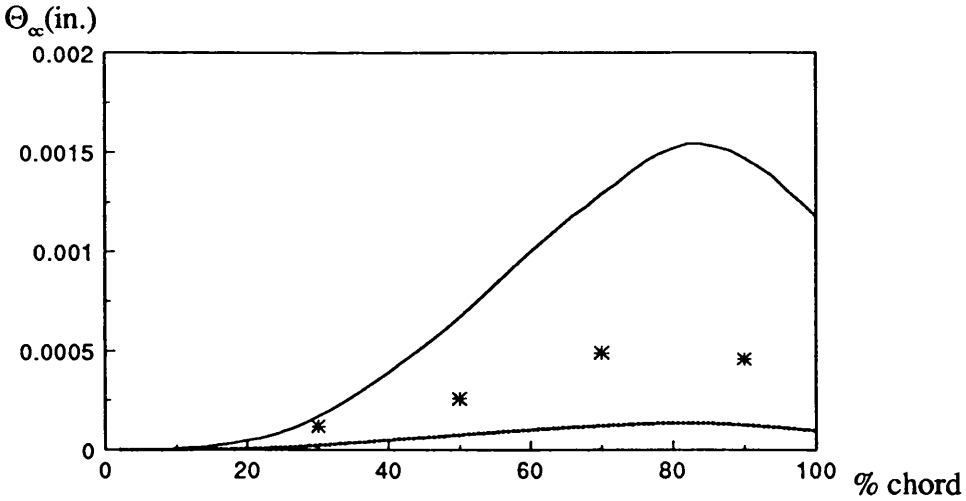

d) displacement thickness in crossflow direction

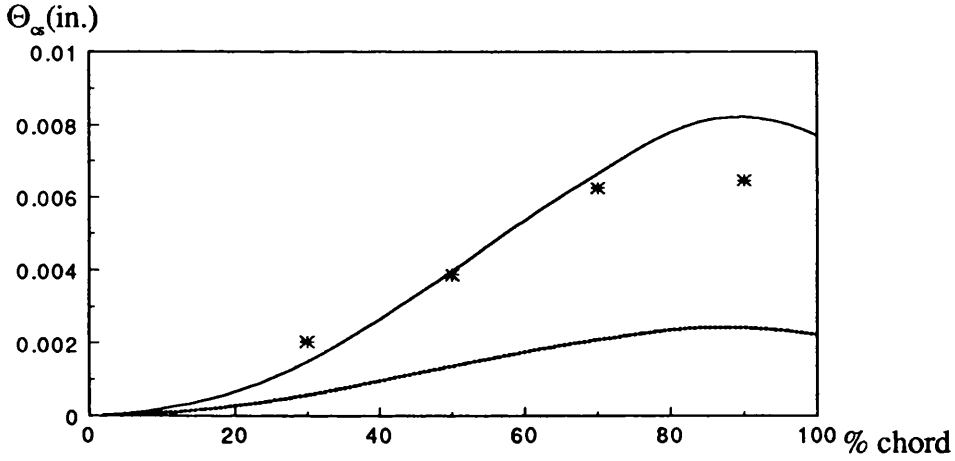

e) momentum thickness in crossflow-streamline direction

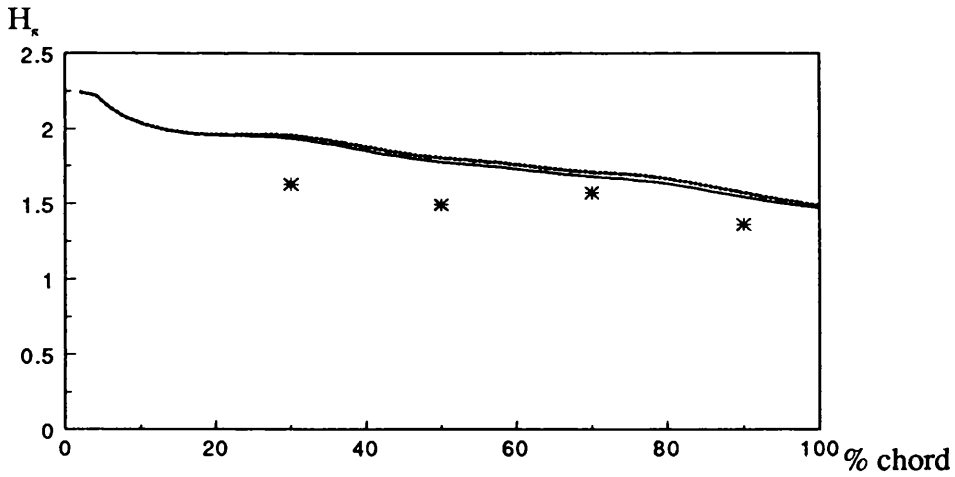

f) shape factor

Fig. 5.15 Comparison of calculated and measured quantities for pressure surface of NACA Blade, 10% span

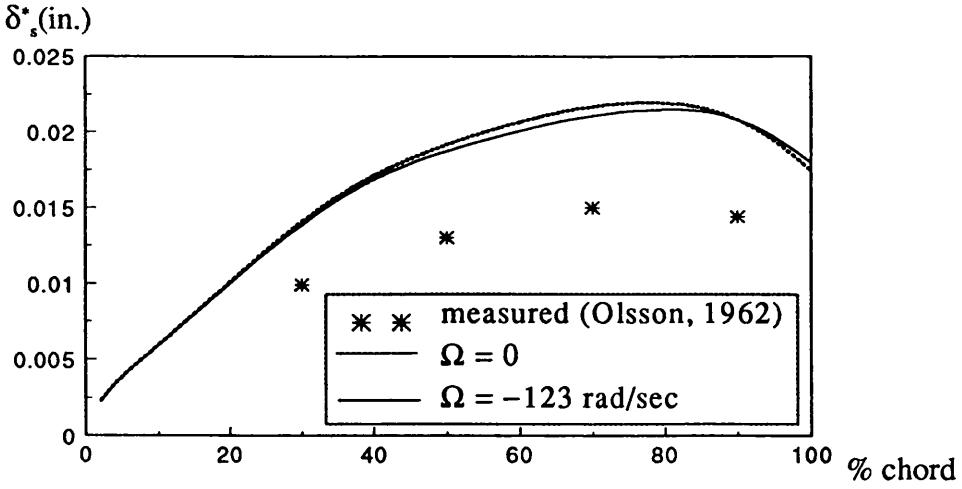

a) displacement thickness in the streamline direction

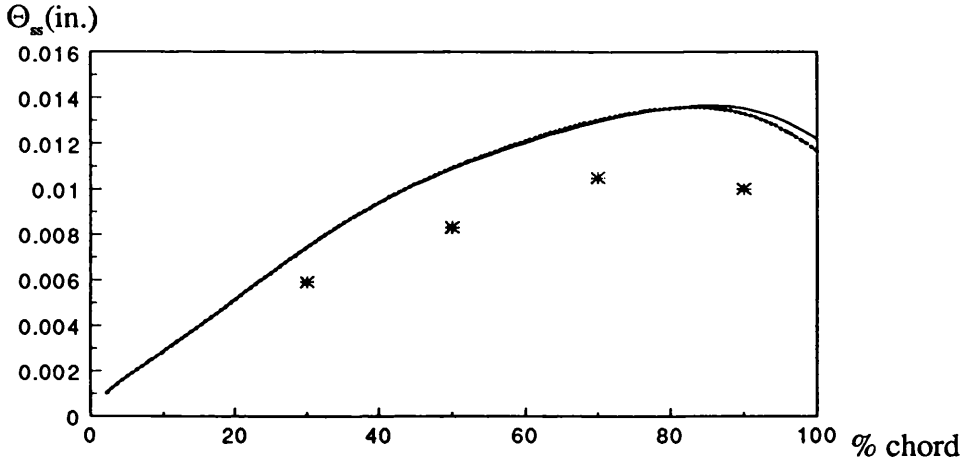

b) momentum thickness in the streamline direction

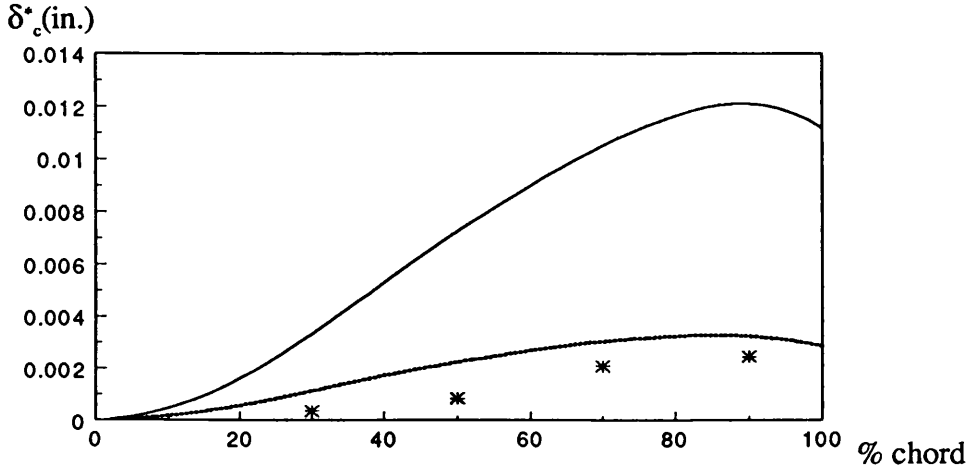

c) displacement thickness in the crossflow direction

Fig. 5.16 Comparison of calculated and measured quantities for pressure surface of NACA Blade, 50% span

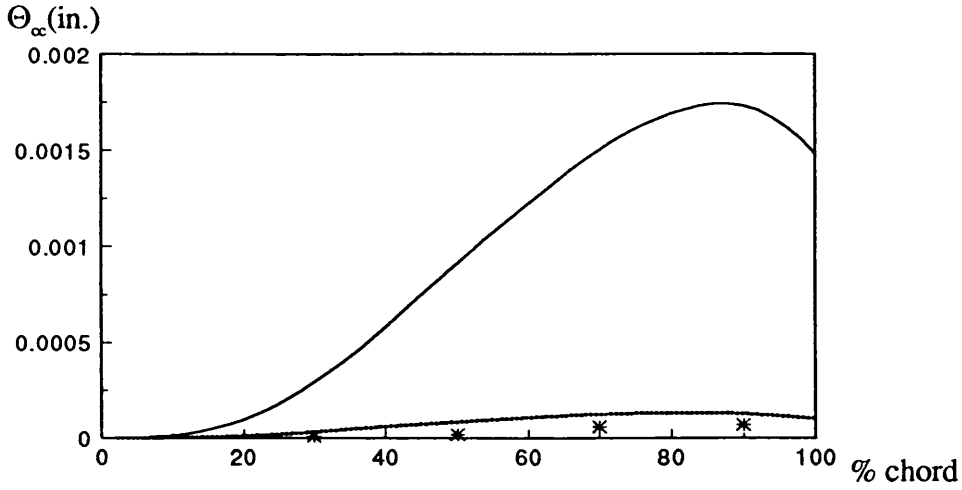

d) displacement thickness in crossflow direction

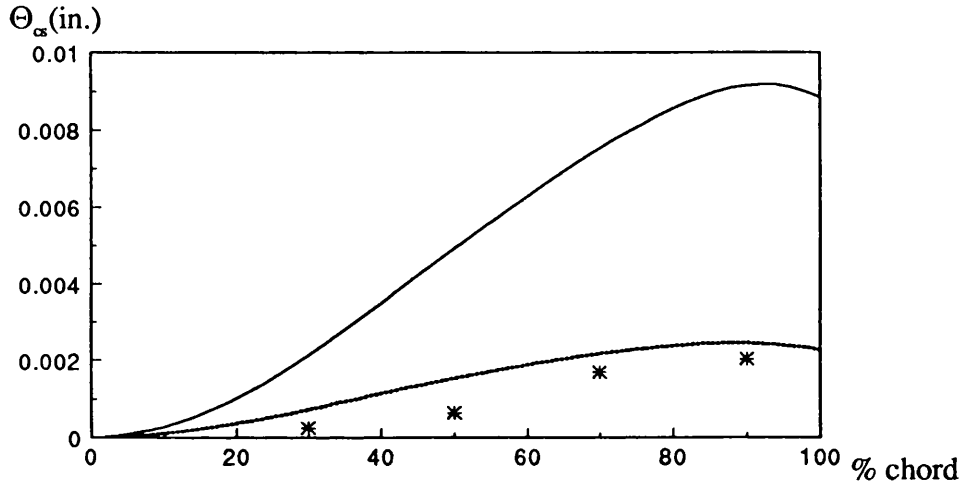

e) momentum thickness in crossflow-streamline direction

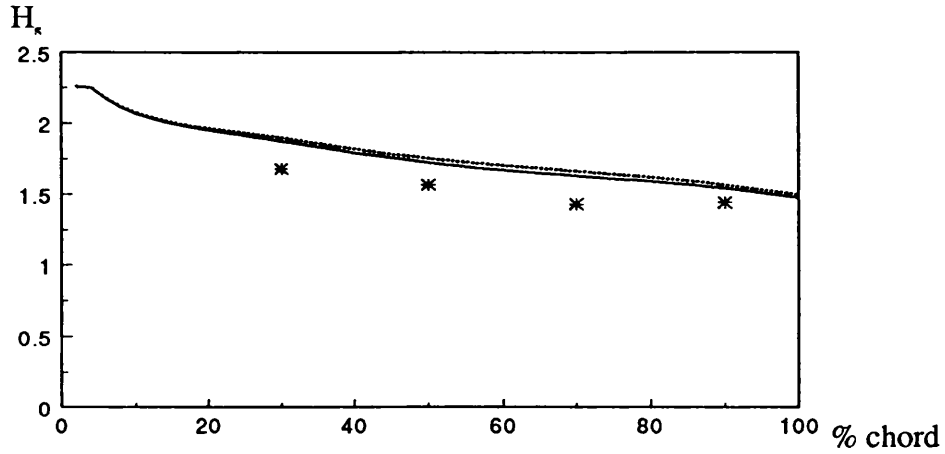

f) shape factor

Fig. 5.16 Comparison of calculated and measured quantities for pressure surface of NACA Blade, 50% span

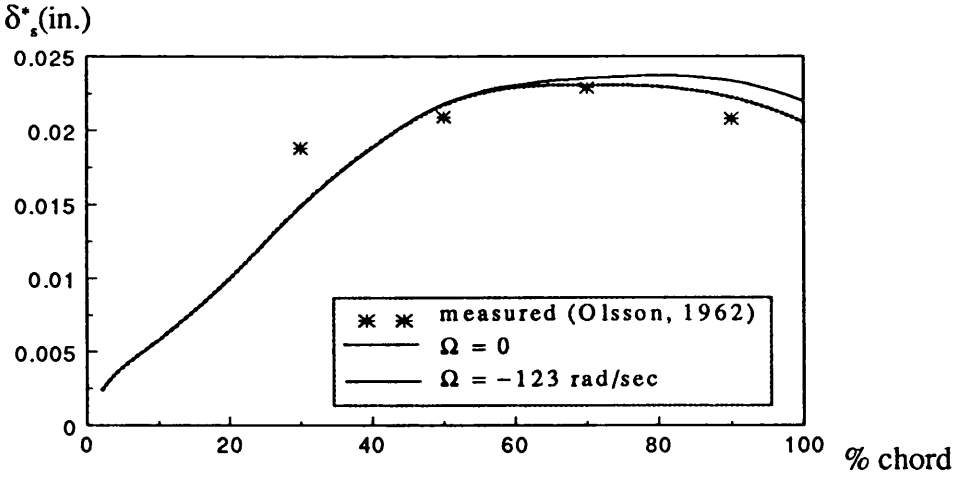

a) displacement thickness in the streamline direction

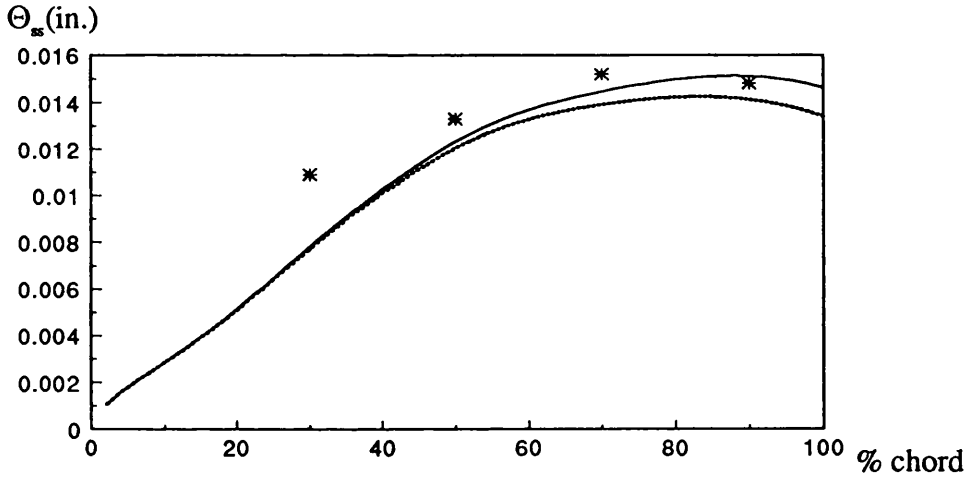

b) momentum thickness in the streamline direction

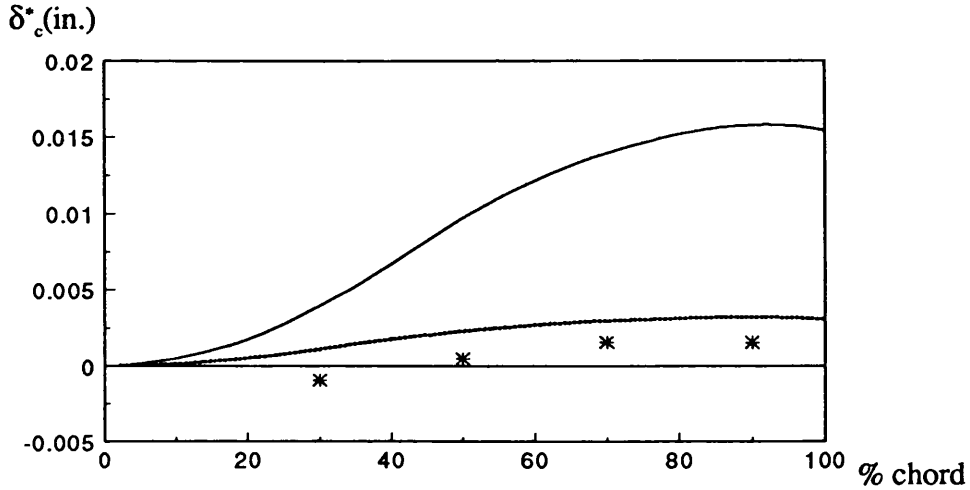

c) displacement thickness in the crossflow direction

Fig. 5.17 Comparison of calculated and measured quantities for pressure surface of NACA Blade, 90% span

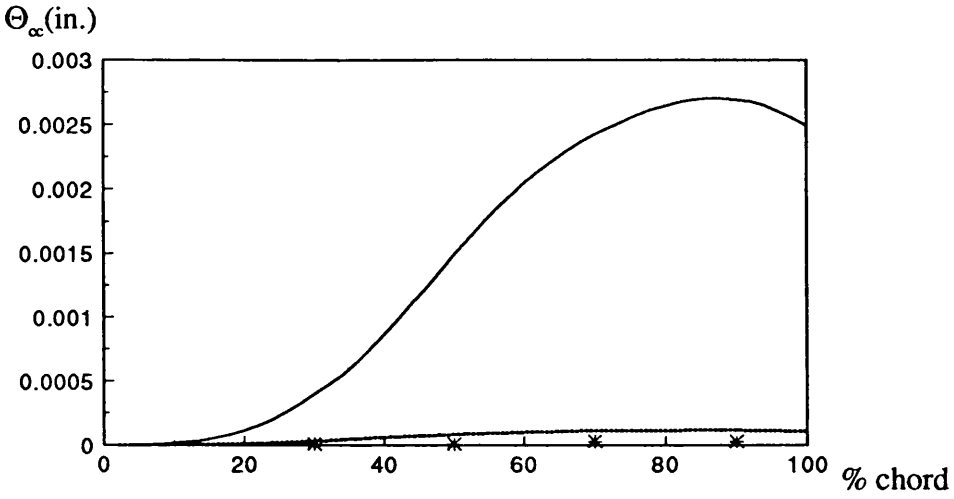

d) displacement thickness in crossflow direction

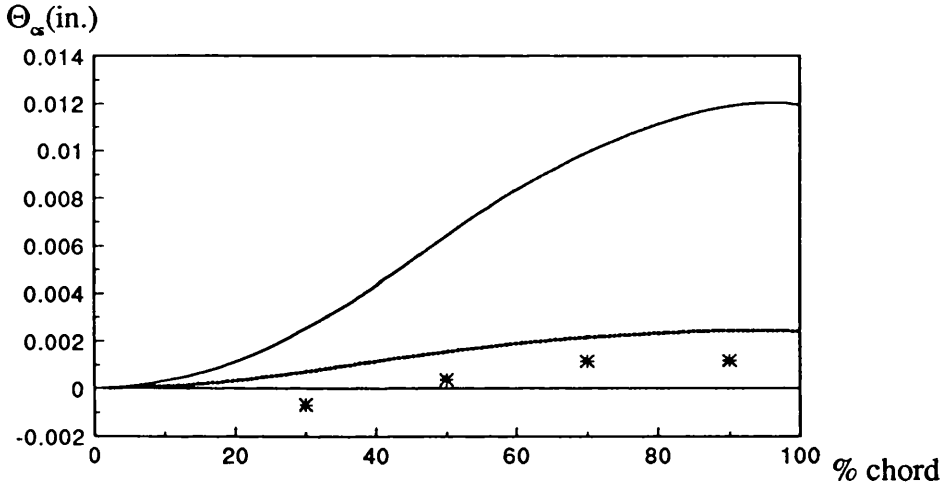

e) momentum thickness in crossflow-streamline direction

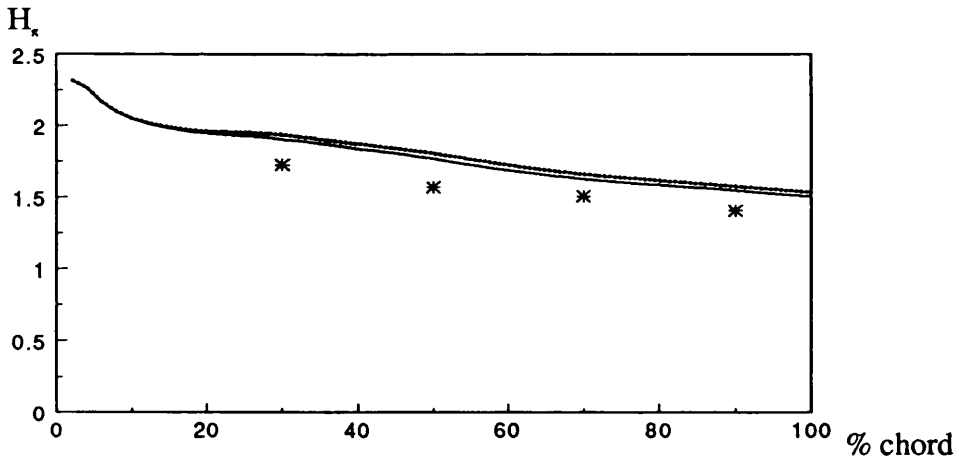

f) shape factor

Fig. 5.17 Comparison of calculated and measured quantities for pressure surface of NACA Blade, 90% span

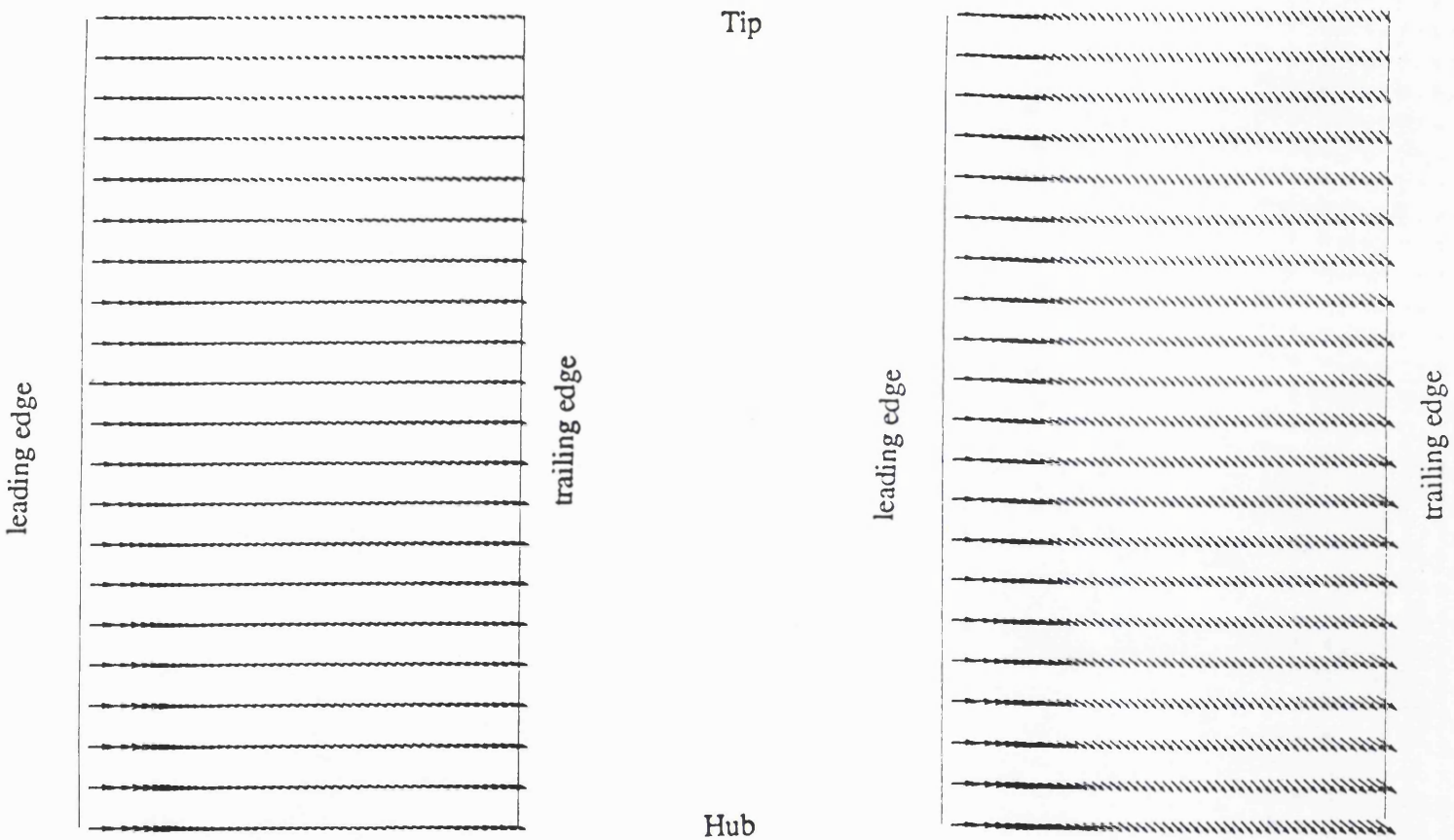

Fig. 5.18 Flow on NACA Blade (pressure surface)

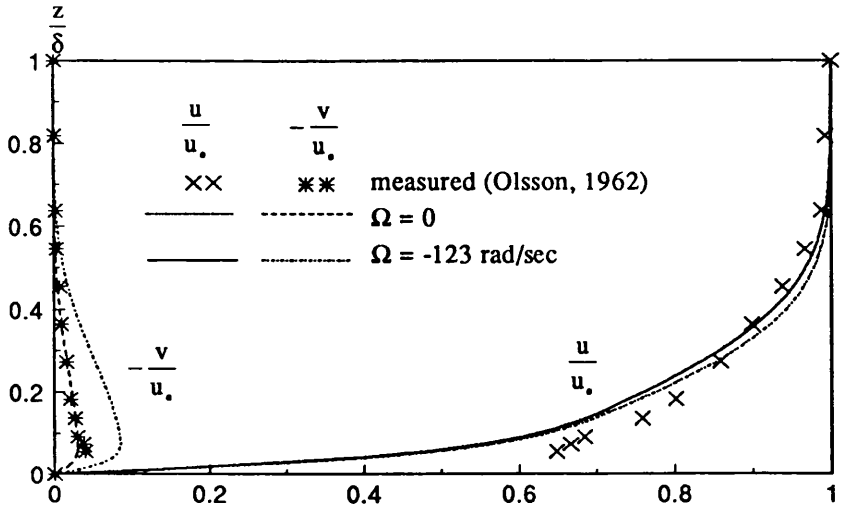

a) 50% chord, 10% span

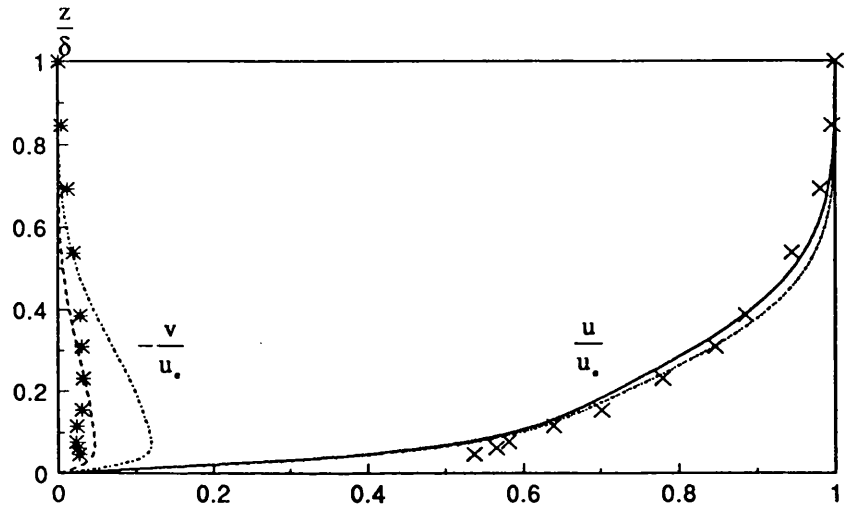

b) 70% chord, 10% span

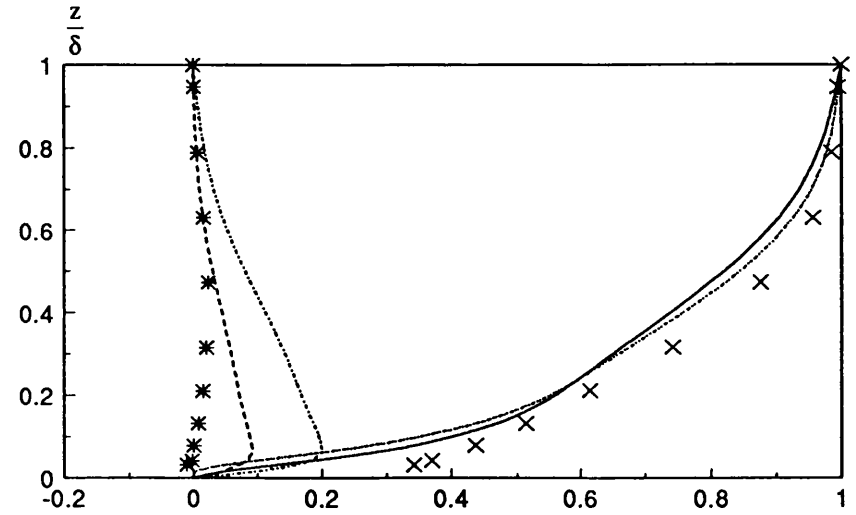

c) 90% chord, 10% span

Fig. 5.19 Mean velocity u and v profiles of three-dimensional boundary layer 10% span for NACA Blade (suction side)

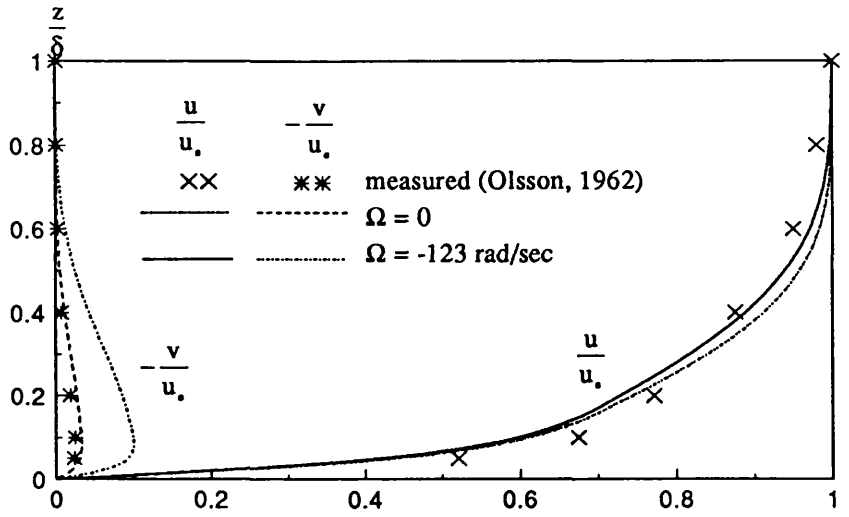

a) 50% chord, 50% span

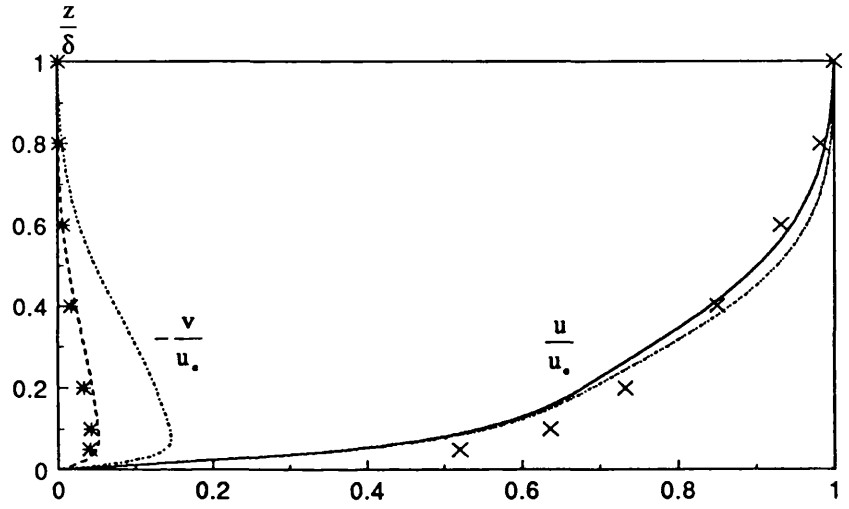

b) 70% chord, 50% span

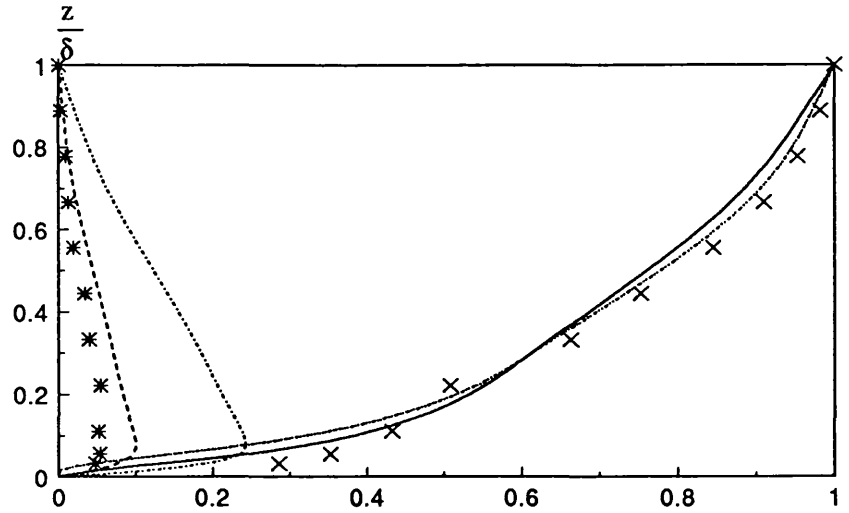

c) 90% chord, 50% span

Fig. 5.20 Mean velocity u and v profiles of three-dimensional boundary layer 50% span for NACA Blade (suction side)

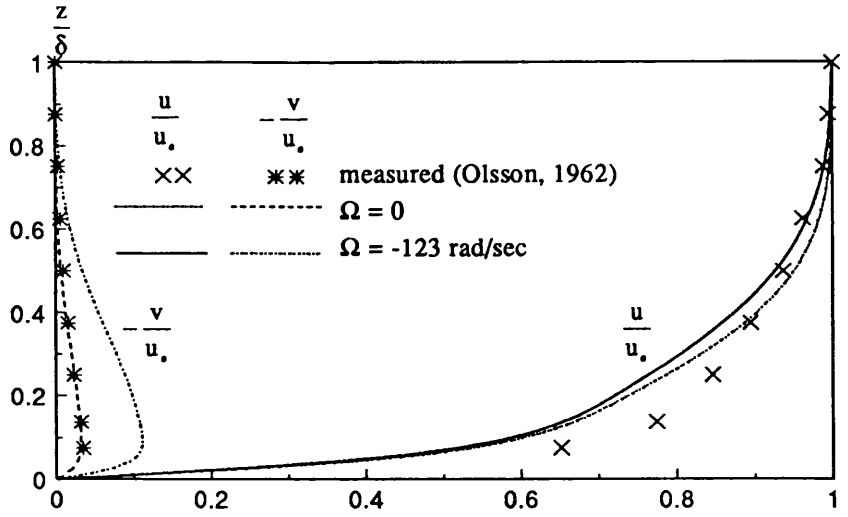

a) 50% chord, 90% span

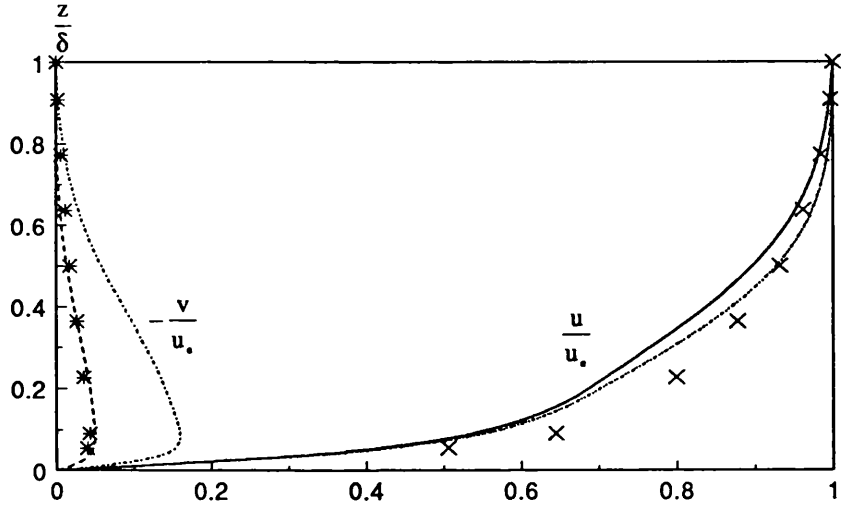

b) 70% chord, 90% span

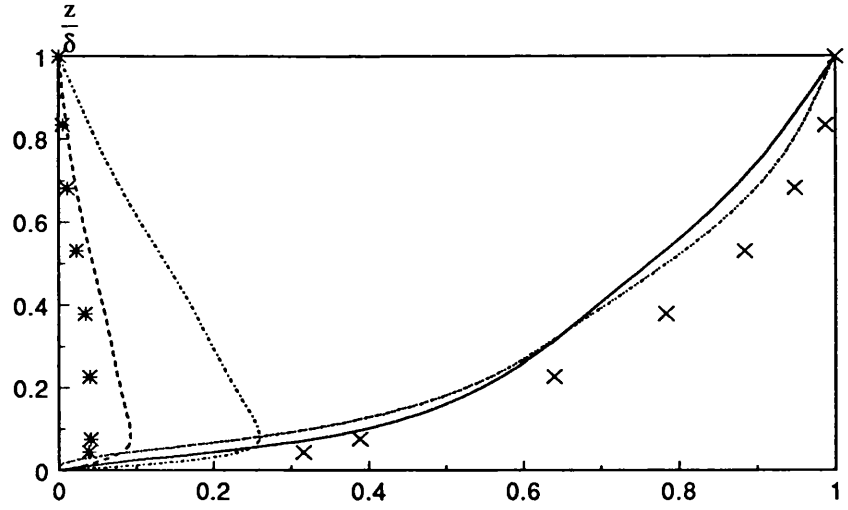

c) 90% chord, 90% span

Fig. 5.21 Mean velocity u and v profiles of three-dimensional boundary layer 90% span for NACA Blade (suction side)

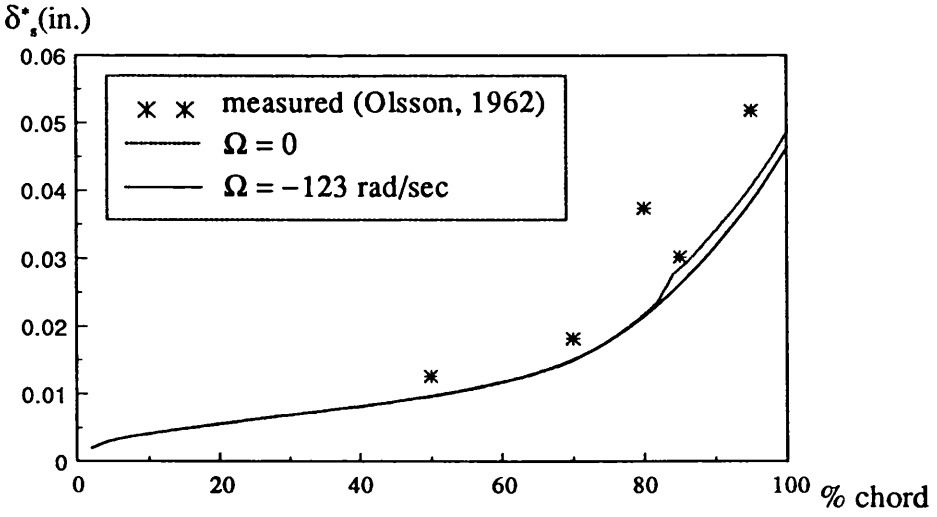

a) displacement thickness in the streamline direction

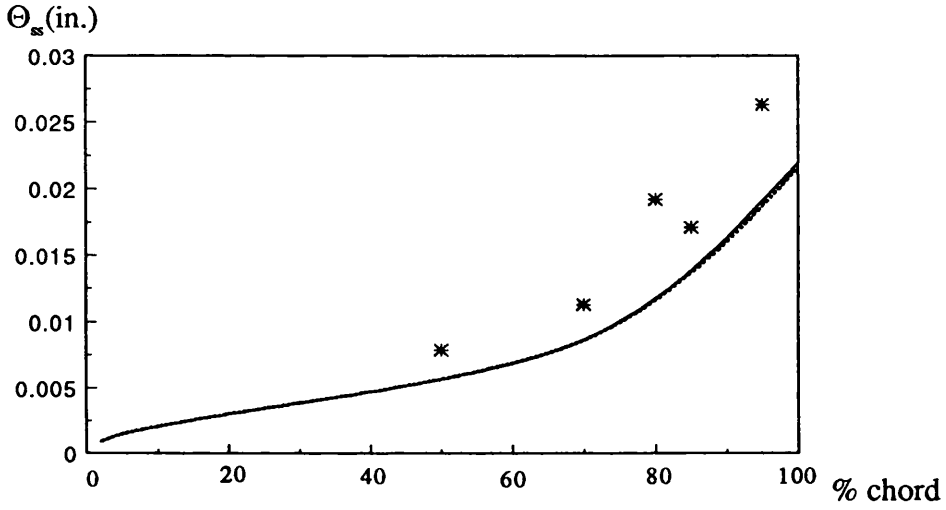

b) momentum thickness in the streamline direction

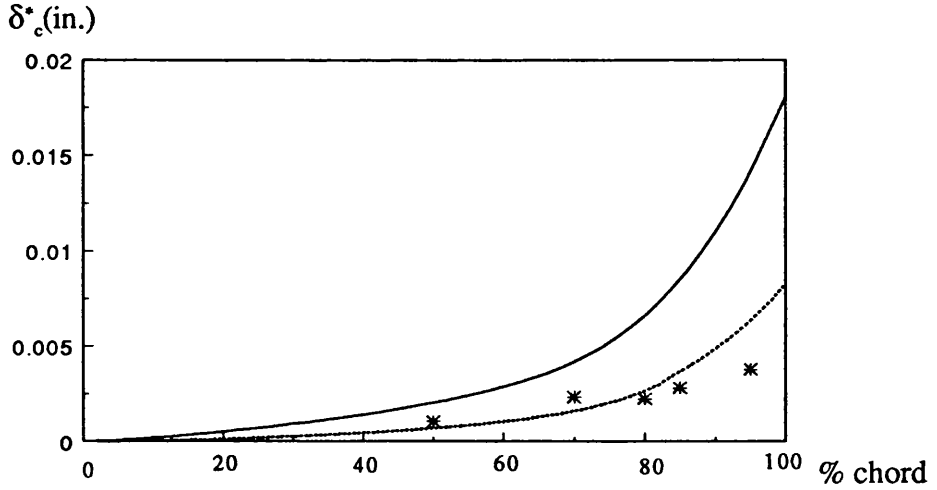

c) displacement thickness in the crossflow direction

Fig. 5.22 Comparison of calculated and measured quantities for suction surface of NACA Blade, 10% span

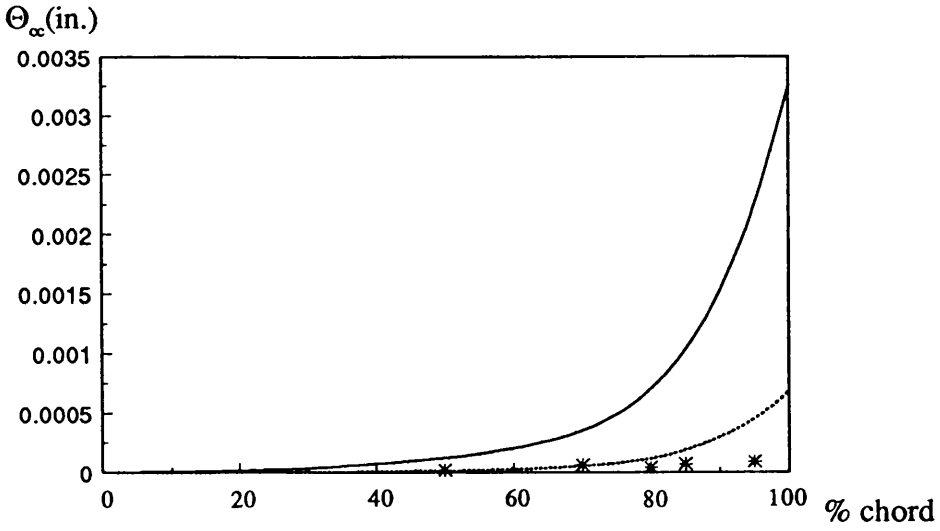

d) displacement thickness in crossflow direction

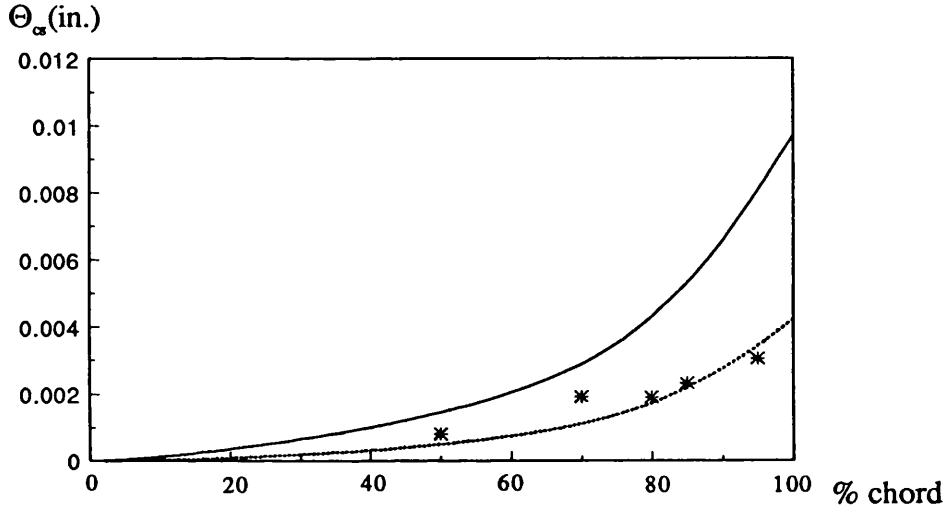

e) momentum thickness in crossflow-streamline direction

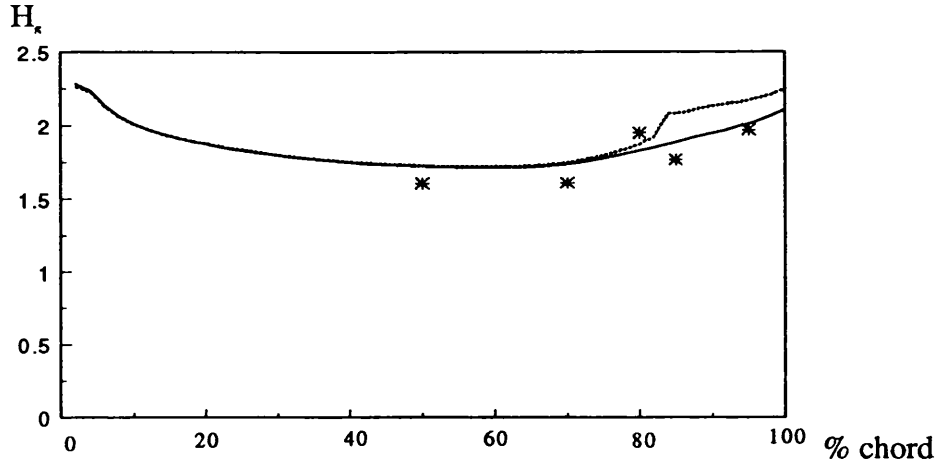

f) shape factor

Fig. 5.22 Comparison of calculated and measured quantities for suction surface of NACA Blade, 10% span

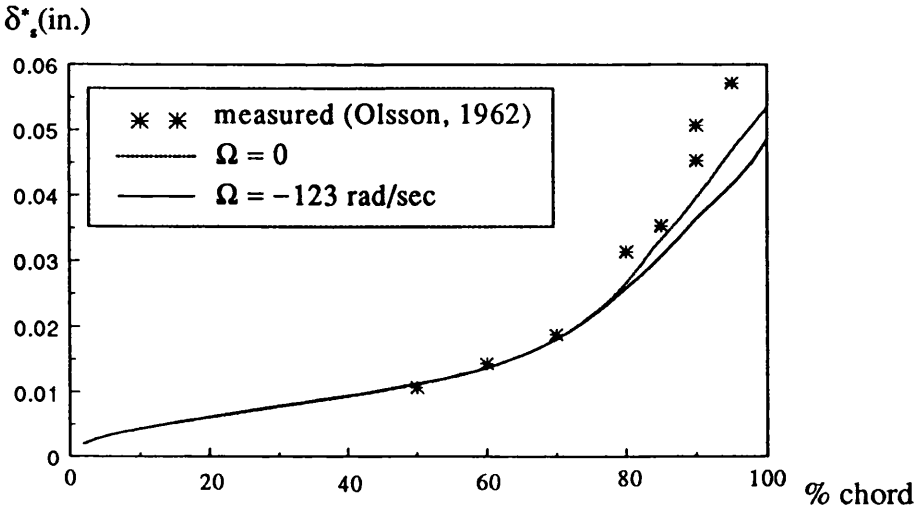

a) displacement thickness in the streamline direction

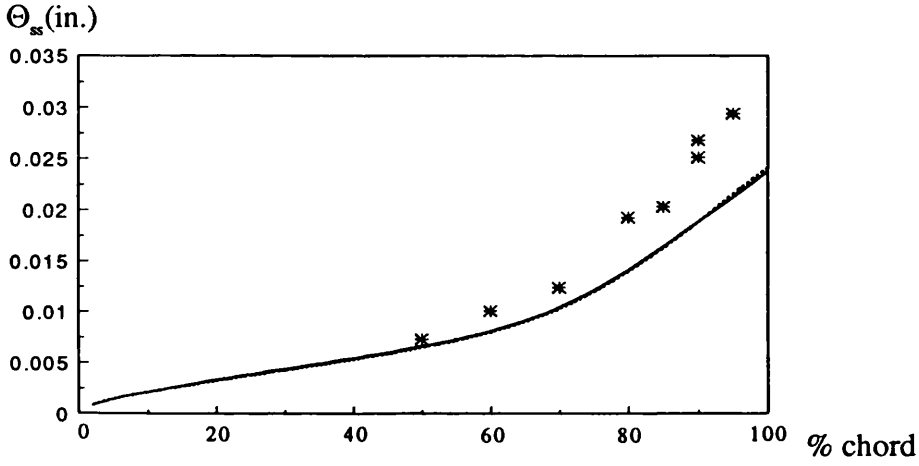

b) momentum thickness in the streamline direction

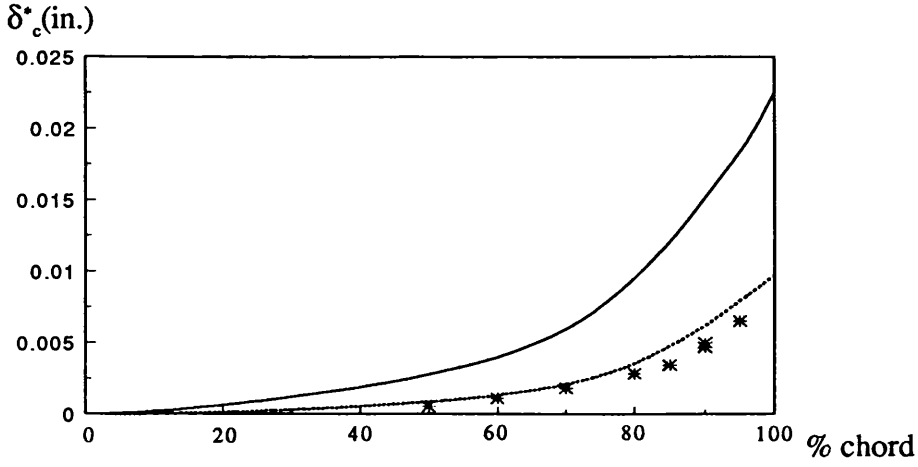

c) displacement thickness in the crossflow direction

Fig. 5.23 Comparison of calculated and measured quantities for suction surface of NACA Blade, 50% span

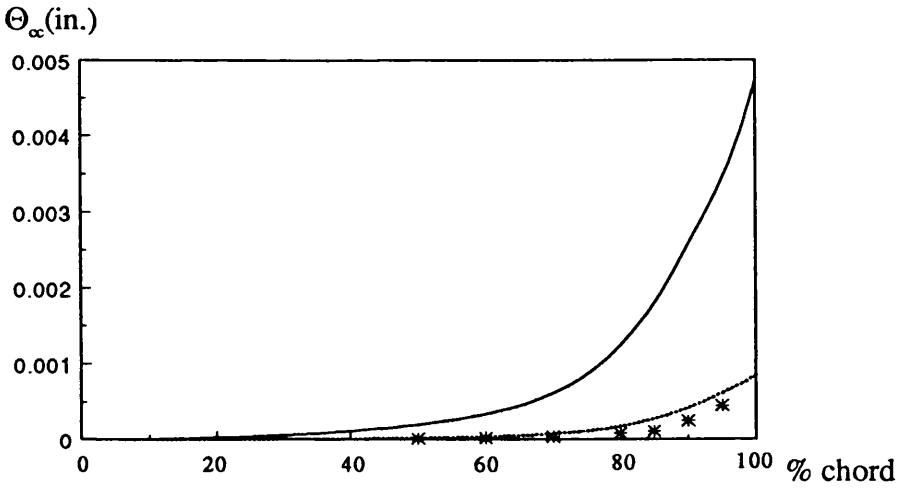

d) displacement thickness in crossflow direction

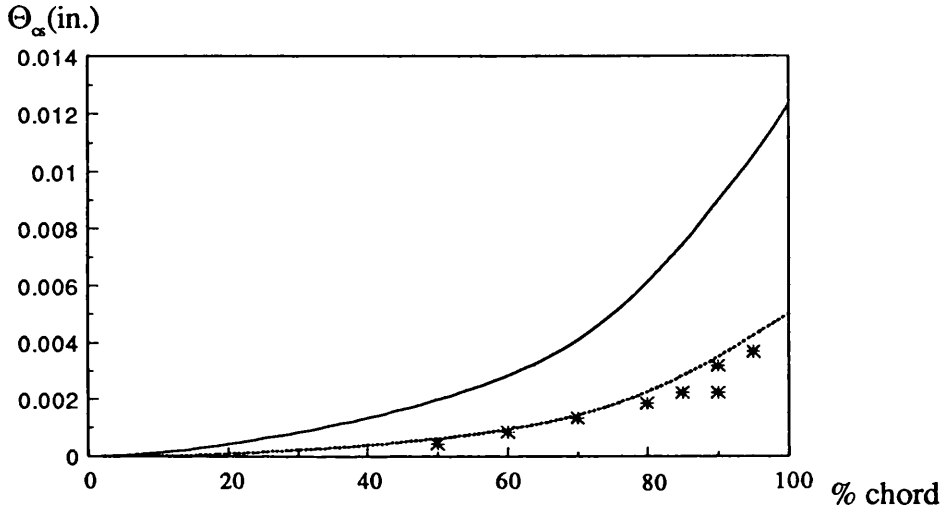

e) momentum thickness in crossflow-streamline direction

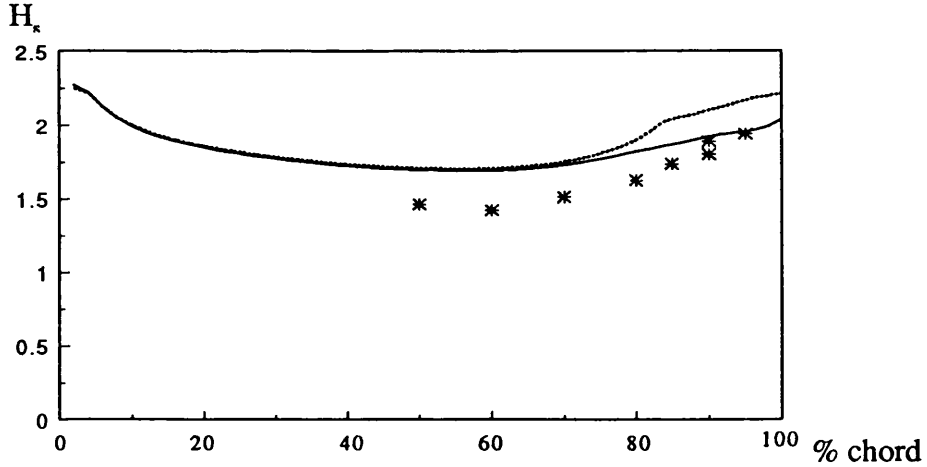

f) shape factor

Fig. 5.23 Comparison of calculated and measured quantities for suction surface of NACA Blade, 50% span

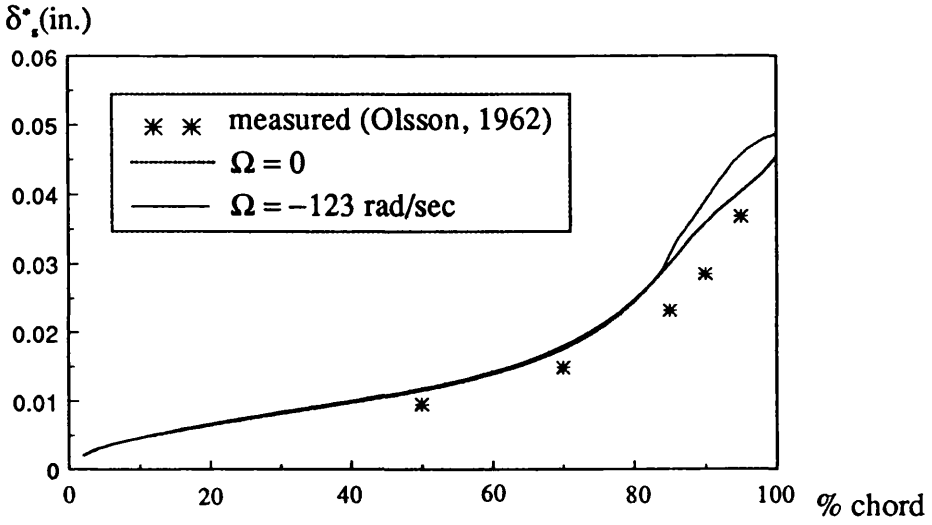

a) displacement thickness in the streamline direction

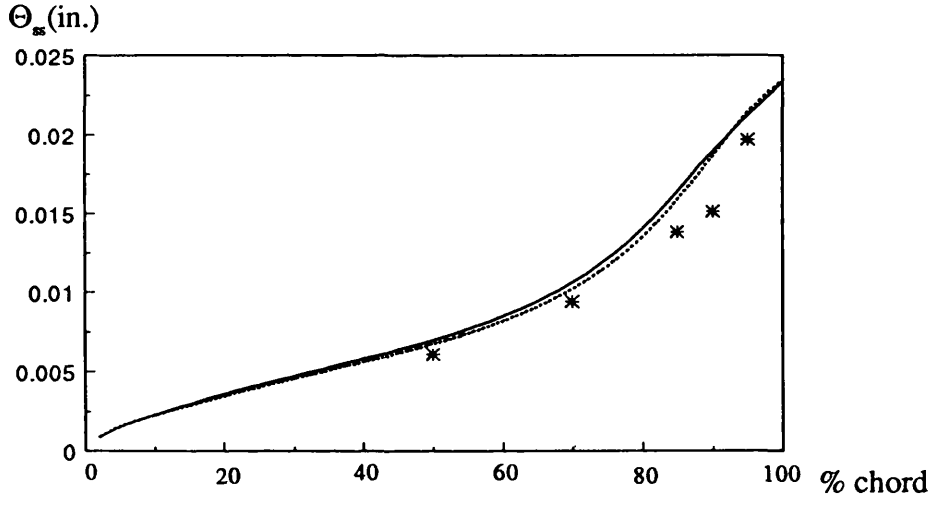

b) momentum thickness in the streamline direction

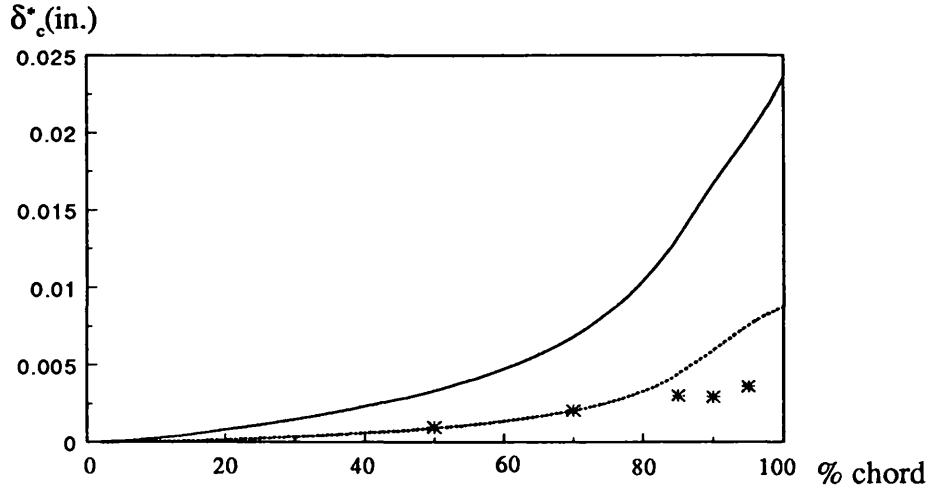

c) displacement thickness in the crossflow direction

Fig. 5.24 Comparison of calculated and measured quantities for suction surface of NACA Blade, 90% span

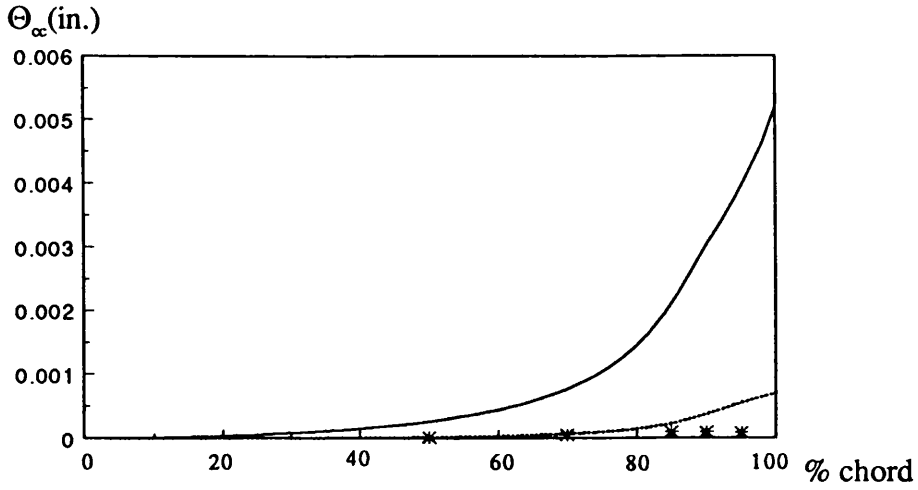

d) displacement thickness in crossflow direction

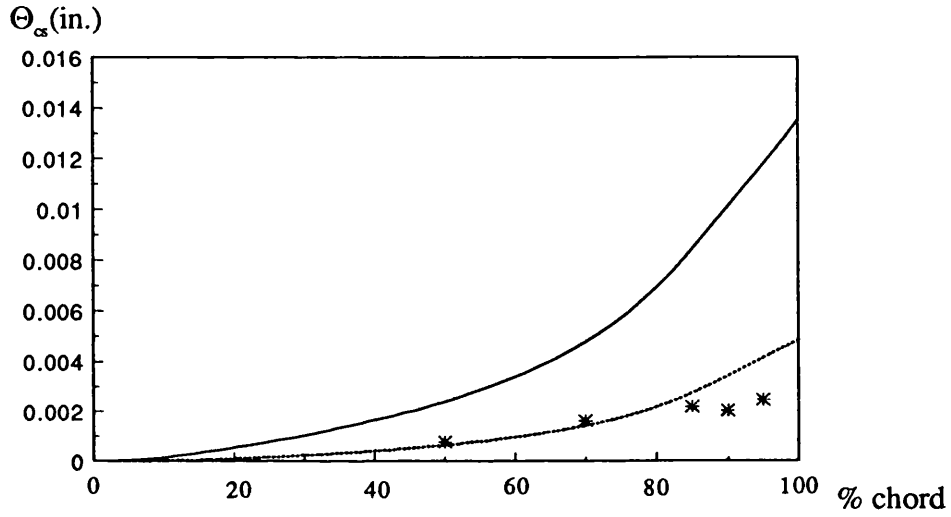

e) momentum thickness in crossflow-streamline direction

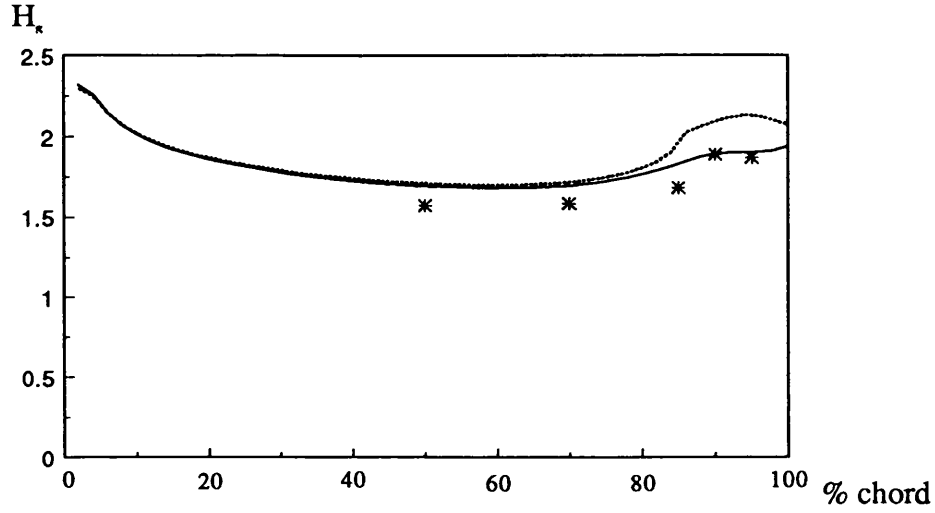

f) shape factor

Fig. 5.24 Comparison of calculated and measured quantities for suction surface of NACA Blade, 90% span

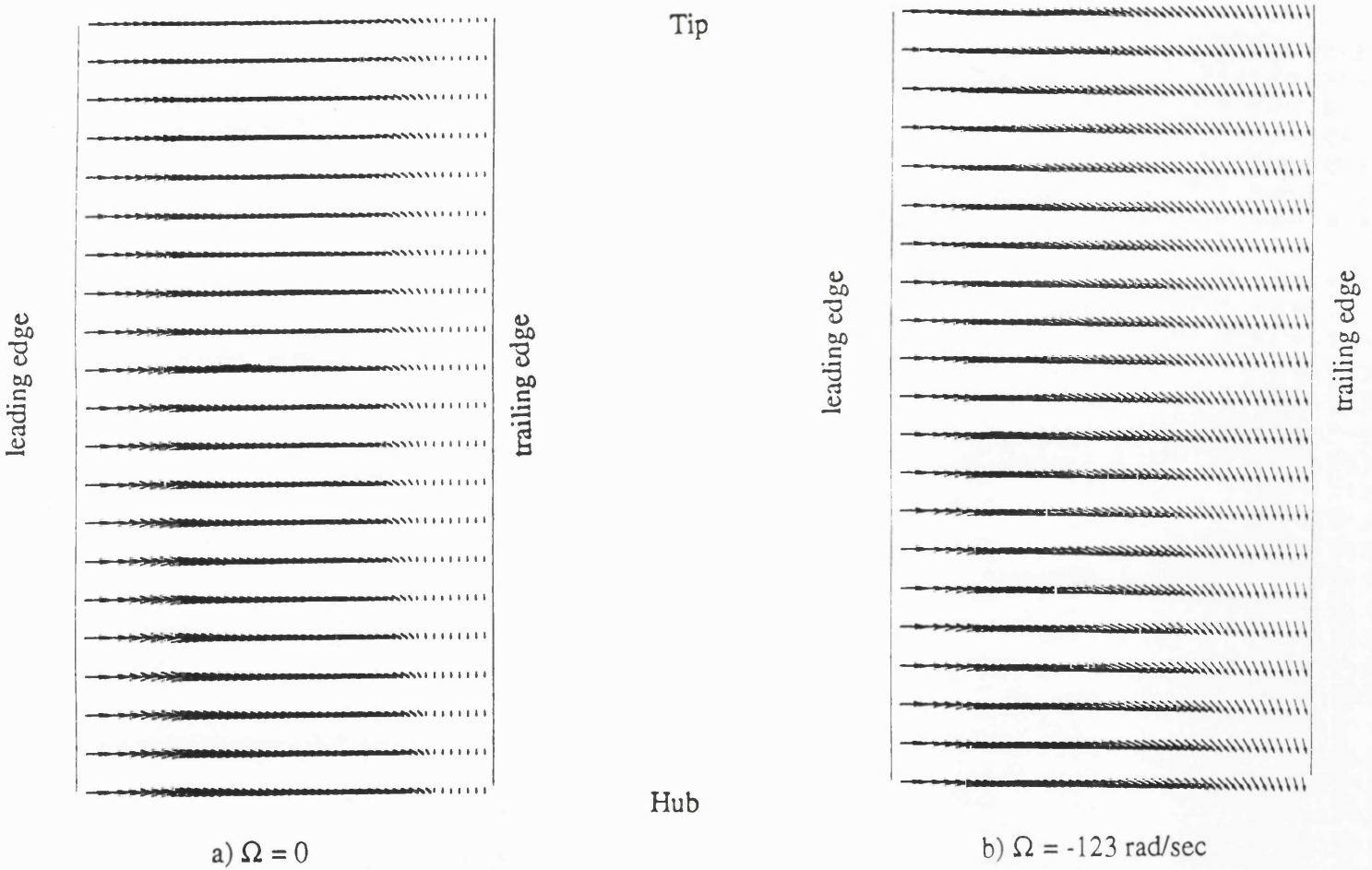

Fig. 5.25 Flow on NACA Blade (suction surface)

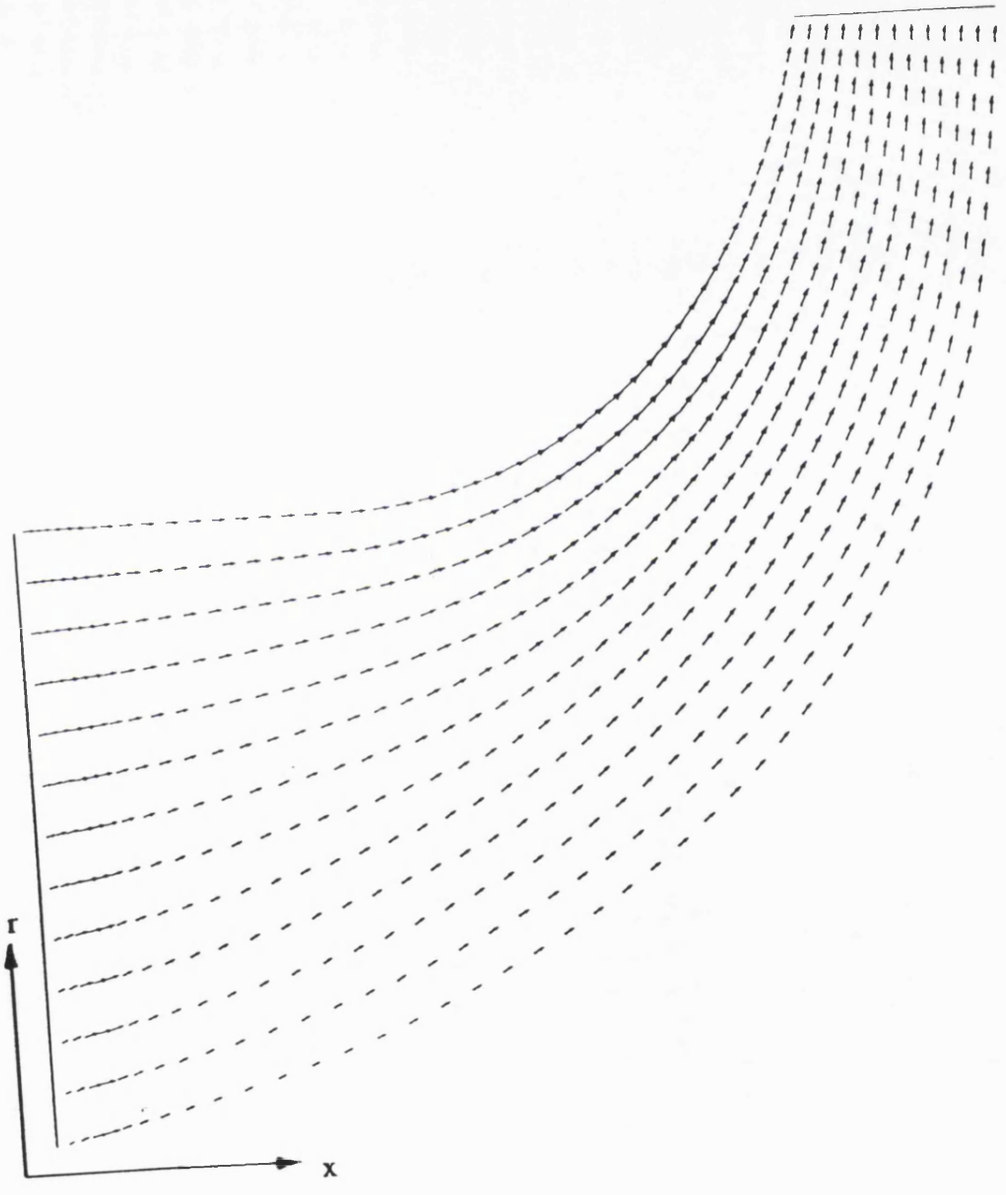

Fig. 5.26 Free-stream velocity vectors (outside the boundary-layer) of pressure surface on Eckardt's impeller

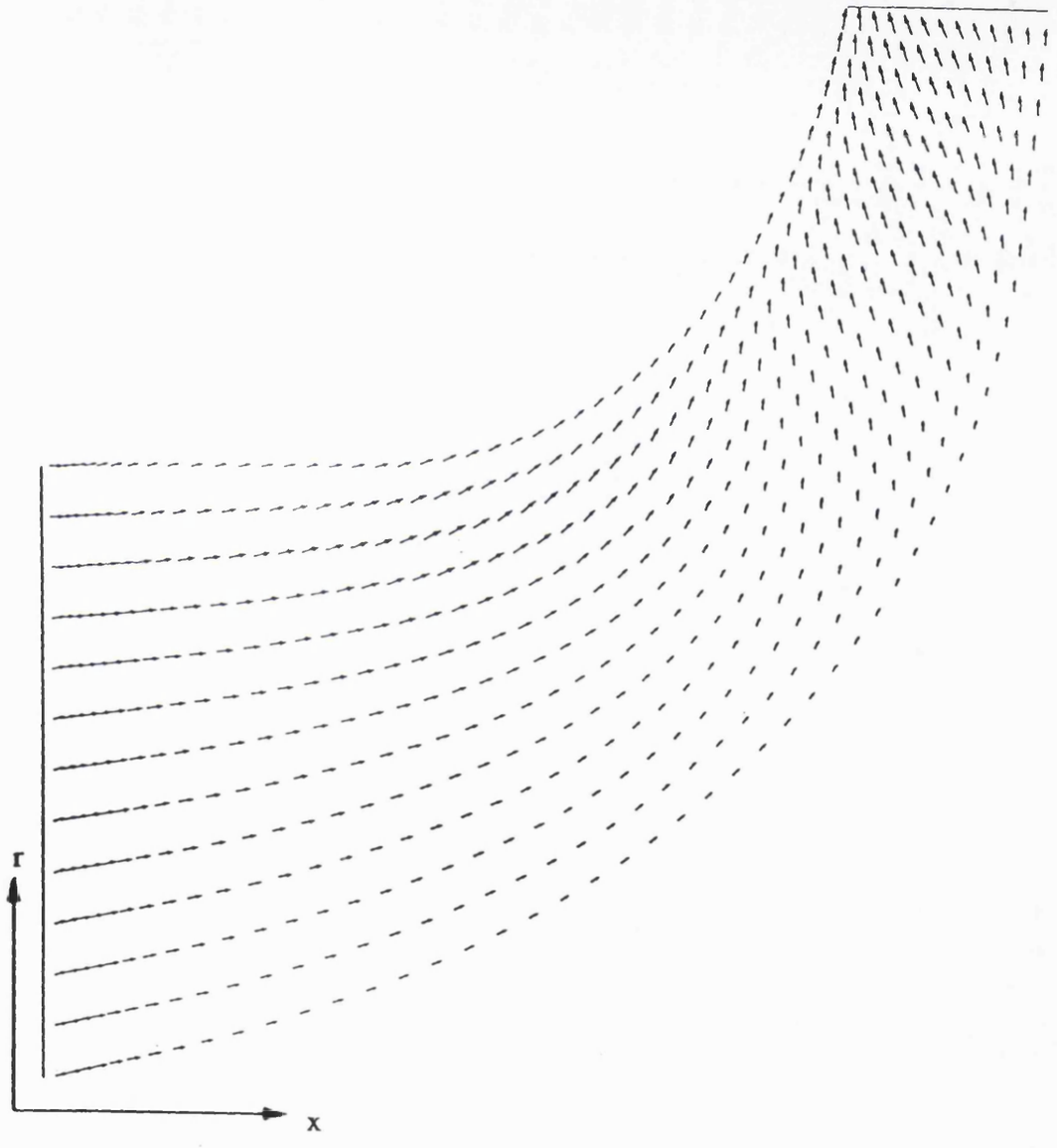

Fig. 5.27 Free-stream velocity vectors (outside the boundary-layer) of suction surface on Eckardt's impeller

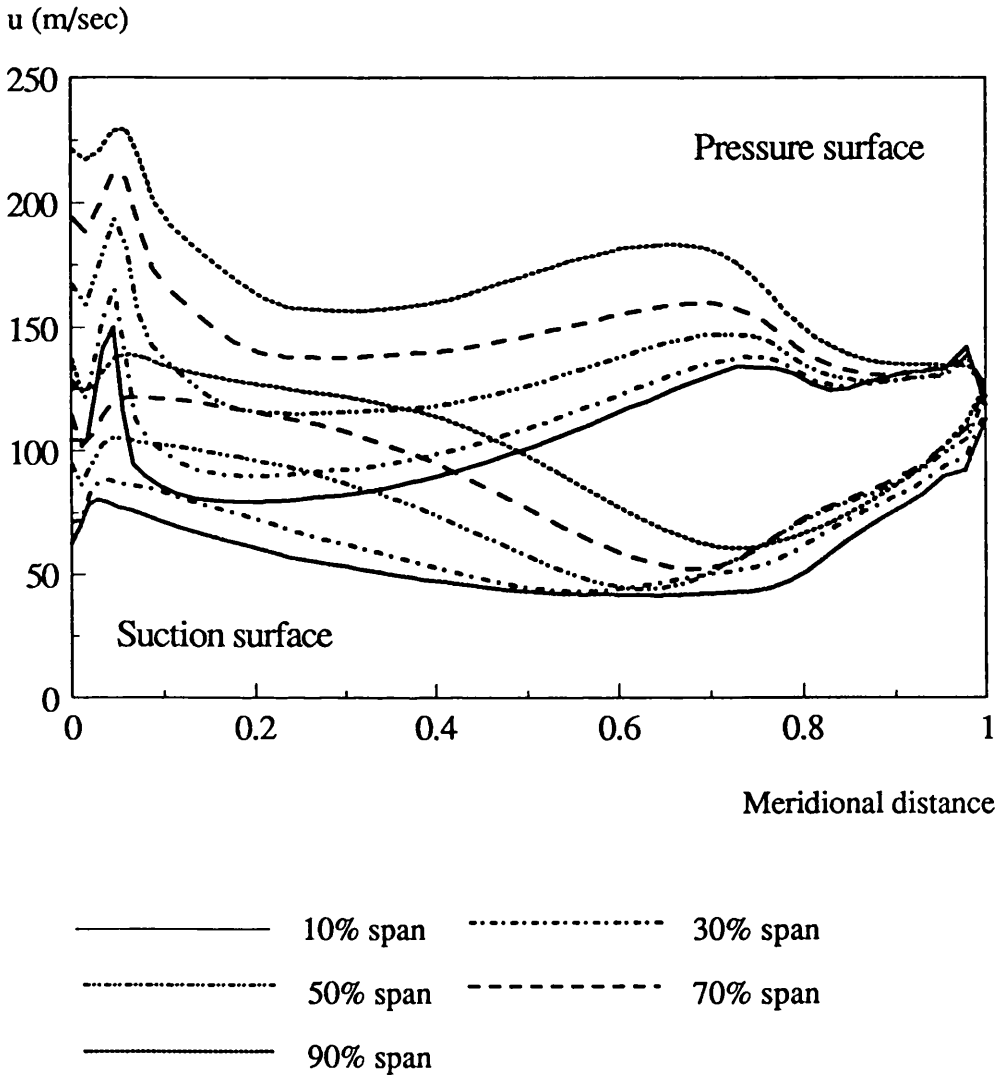

Fig. 5.28 Free-stream velocities on the Eckardt's impeller

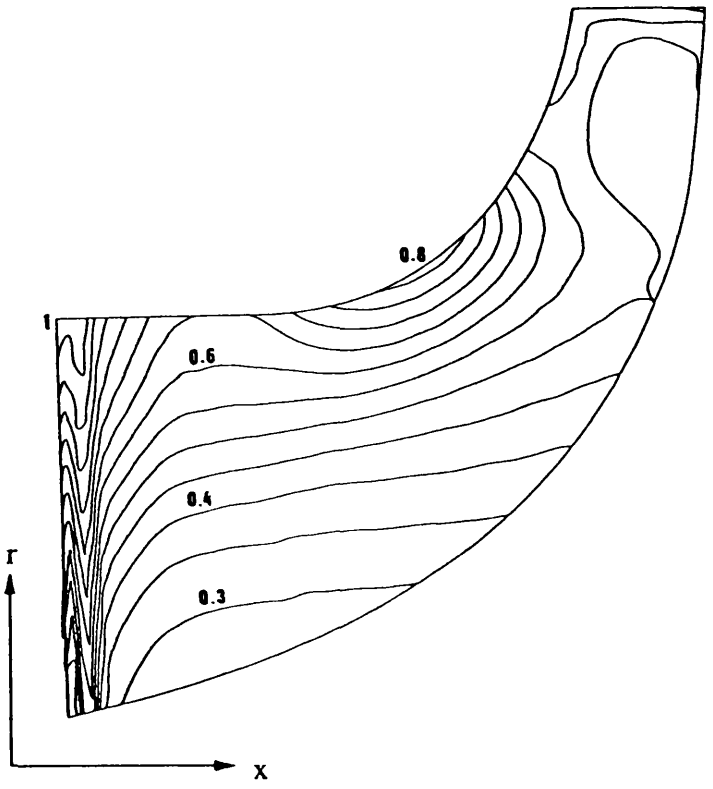

a) pressure surface

All figures are in non-dimensional values.

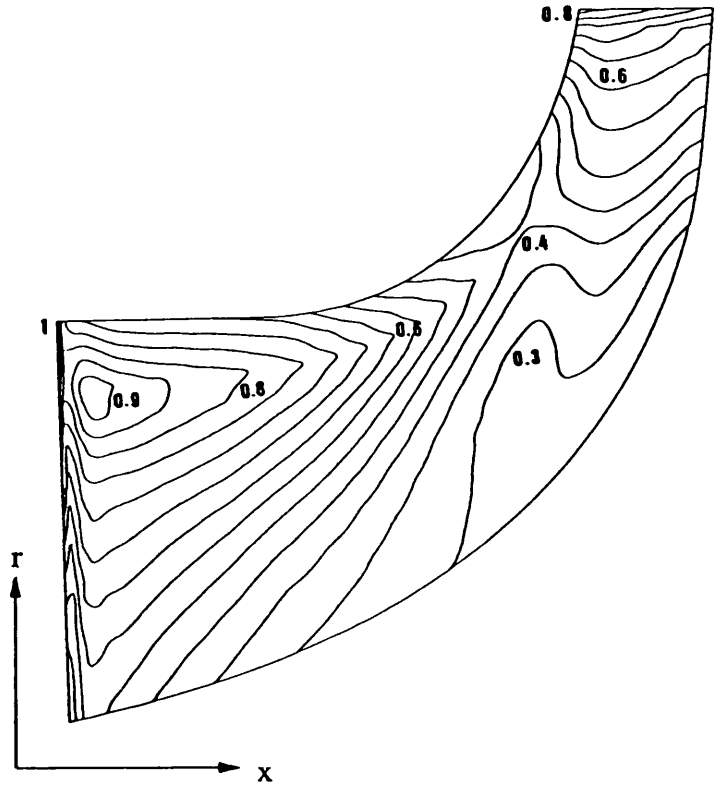

b) suction surface

Fig. 5.29 Contours of free-stream velocities on surface of Eckardt's impeller

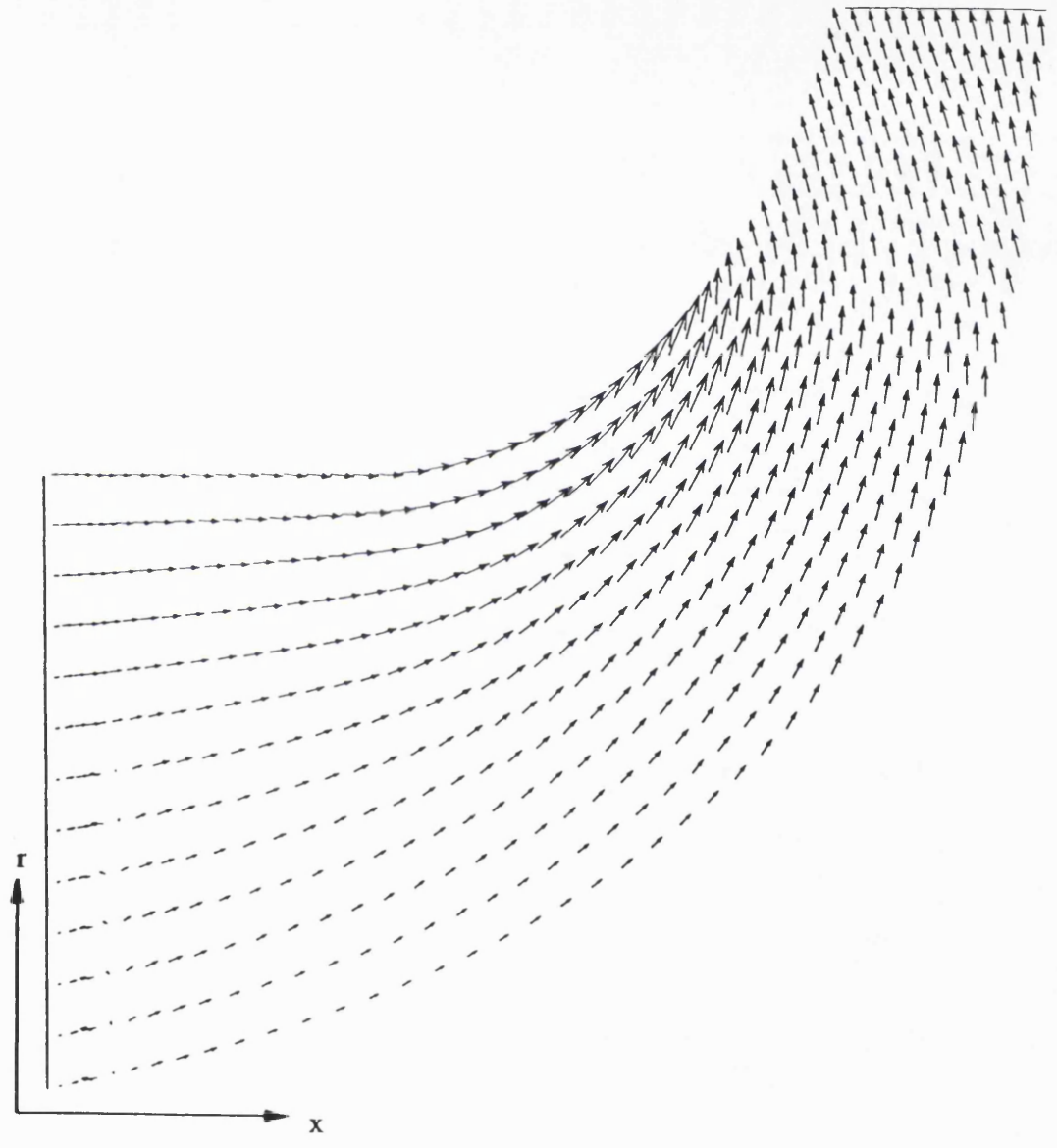

Fig. 5.30 Predicted velocity vectors (near the pressure surface) on Eckardt's impeller

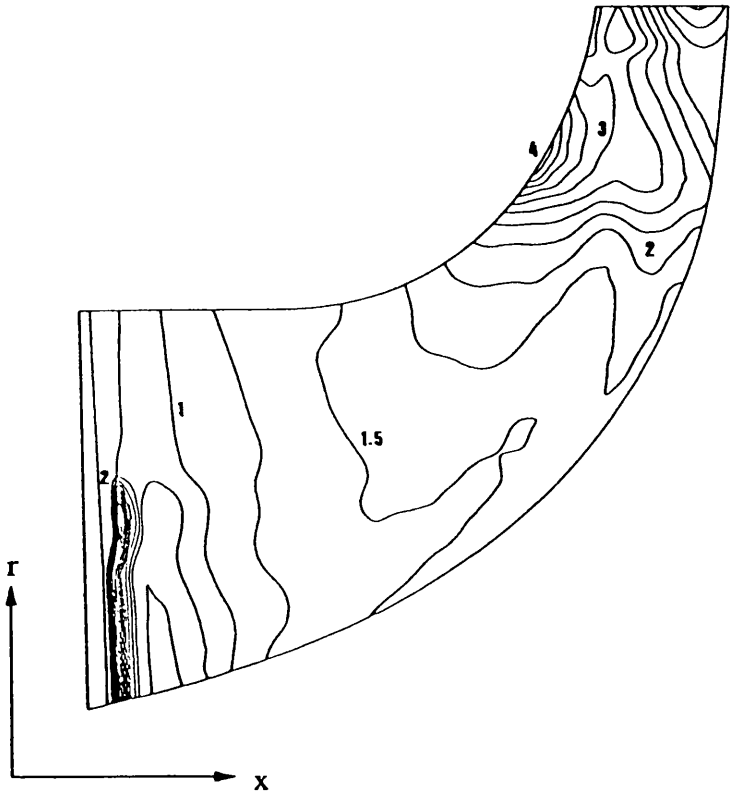

All figures are in non-dimensional values.

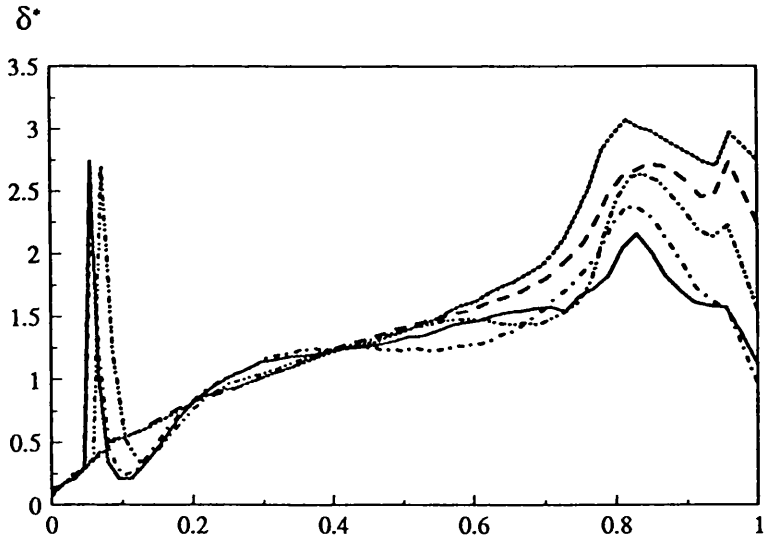

——— 10% span ····· 30% span ····· 50% span

- - - - - 70% span ——— 90% span

Fig. 5.31 Contours of the predicted displacement thickness on the pressure surface (Eckardt's impeller)

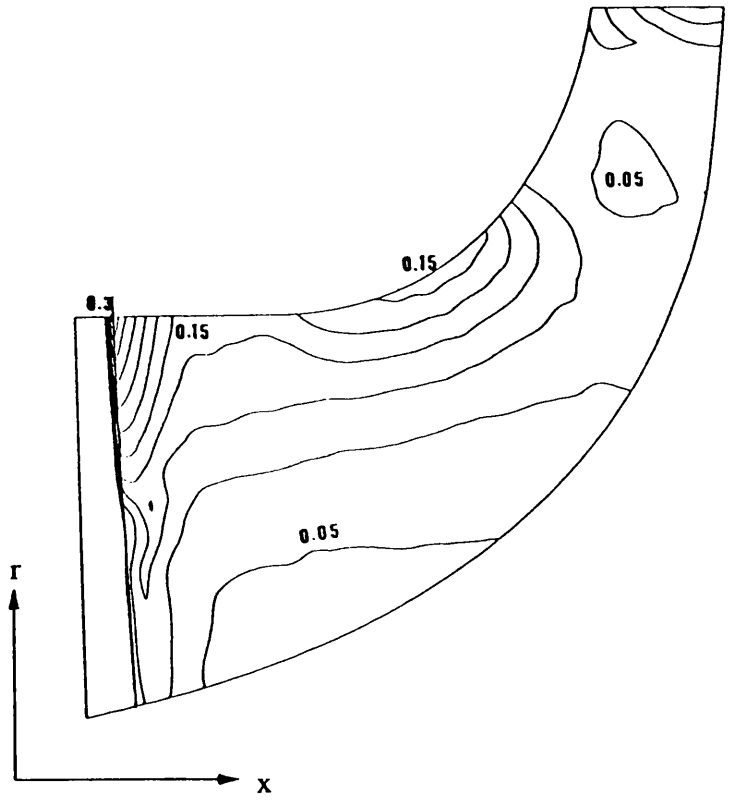

All figures are in non-dimensional values.

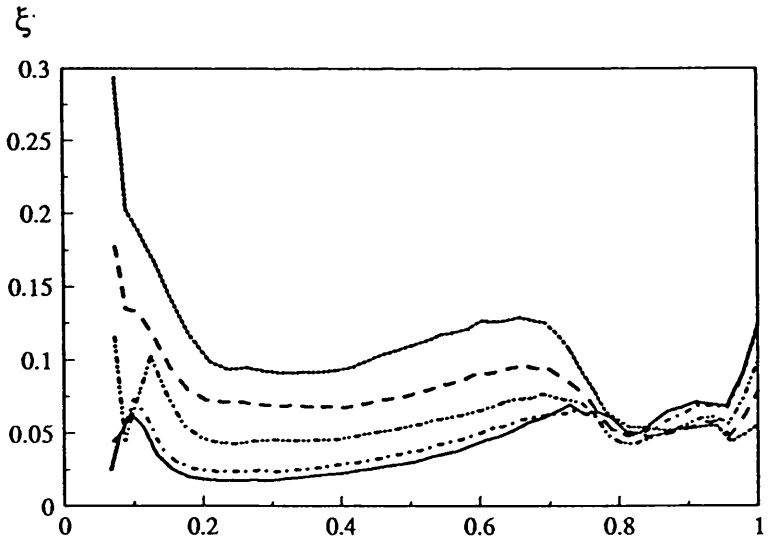

——— 10% span ····· 30% span ····· 50% span

- - - - - 70% span ——— 90% span

Fig. 5.32 Contours of the predicted entropy generation on the pressure surface (Eckardt's impeller)

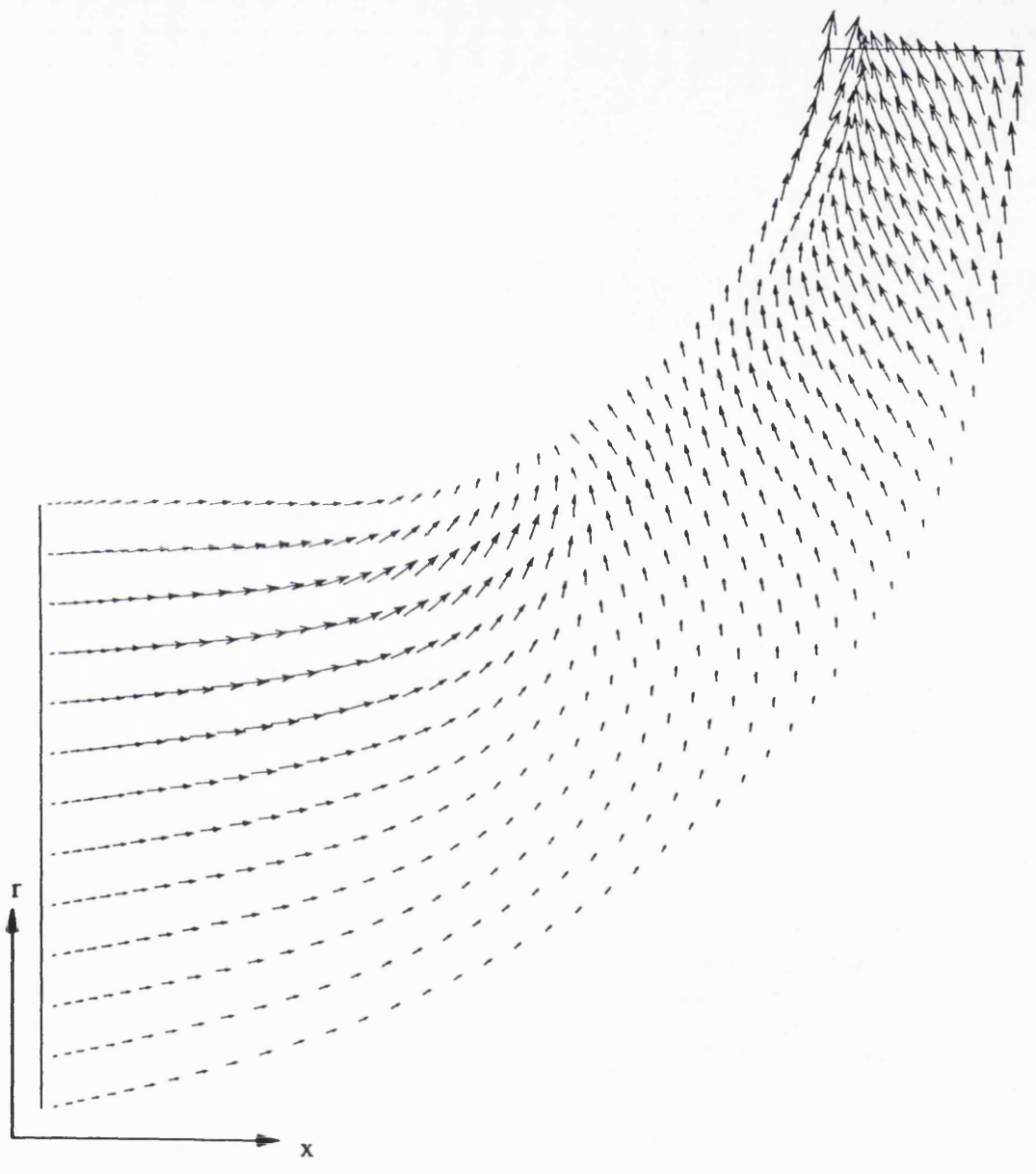

Fig. 5.33 Predicted velocity vectors (near the suction surface) on Eckardt's impeller

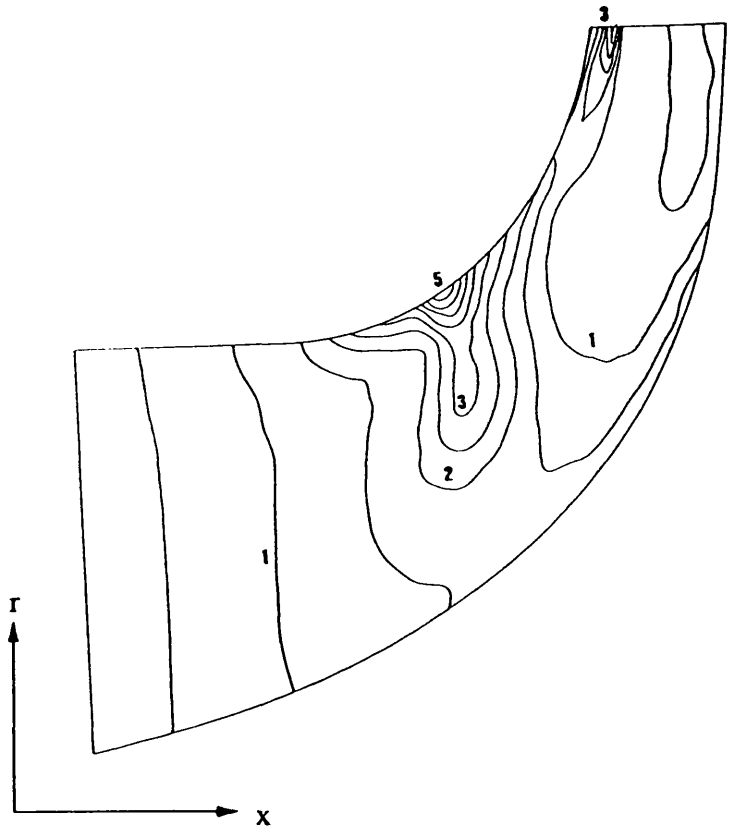

All figures are in non-dimensional values.

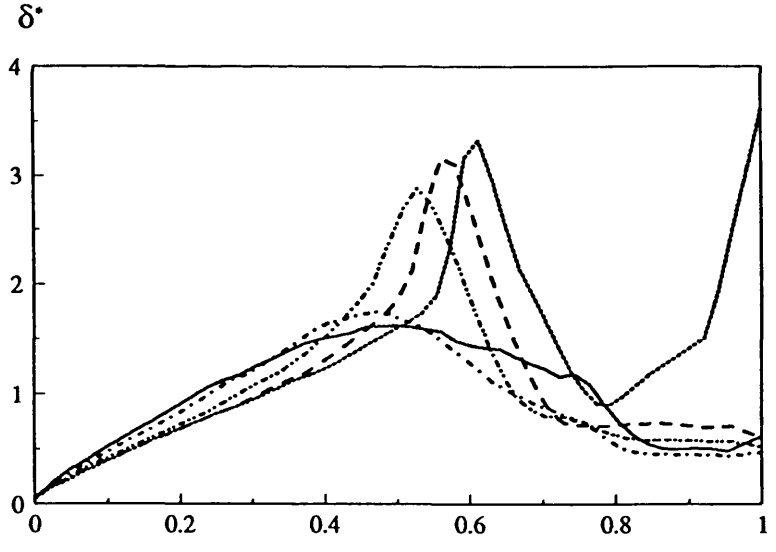

——— 10% span ····· 30% span ····· 50% span

- - - - - 70% span ——— 90% span

Fig. 5.34 Contours of the predicted displacement thickness on the suction surface (Eckardt's impeller)

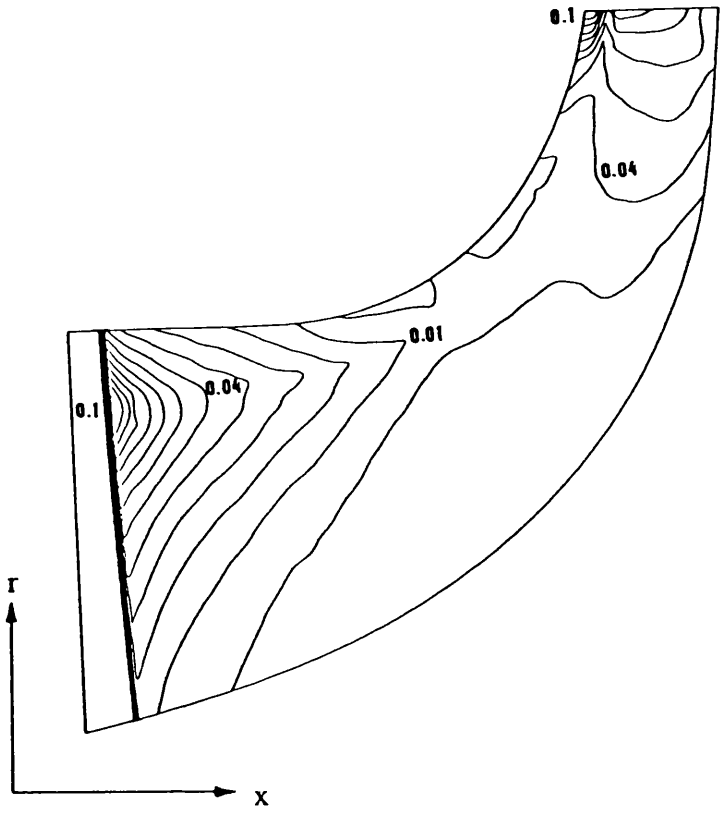

All figures are in non-dimensional values.

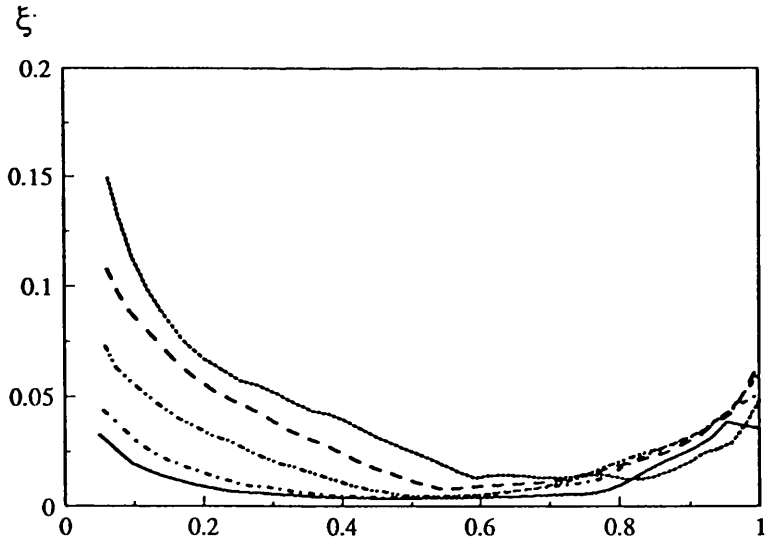

——— 10% span ····· 30% span ····· 50% span

- - - - - 70% span ——— 90% span

Fig. 5.35 Contours of the predicted entropy generation on the suction surface (Eckardt's impeller)

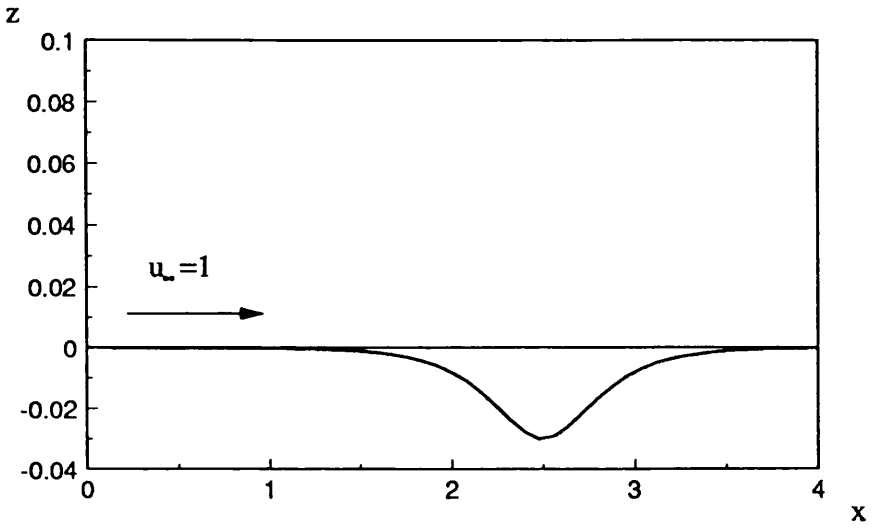

Fig. 5.36 Dented plate for a boundary layer with a separation bubble

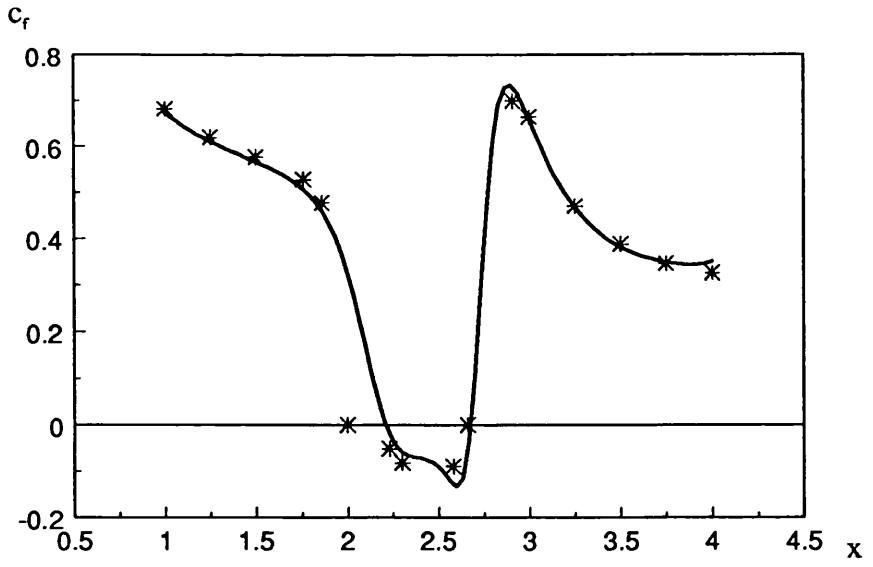

Fig. 5.37 Wall shearing stress

* Carter's data ——— present method

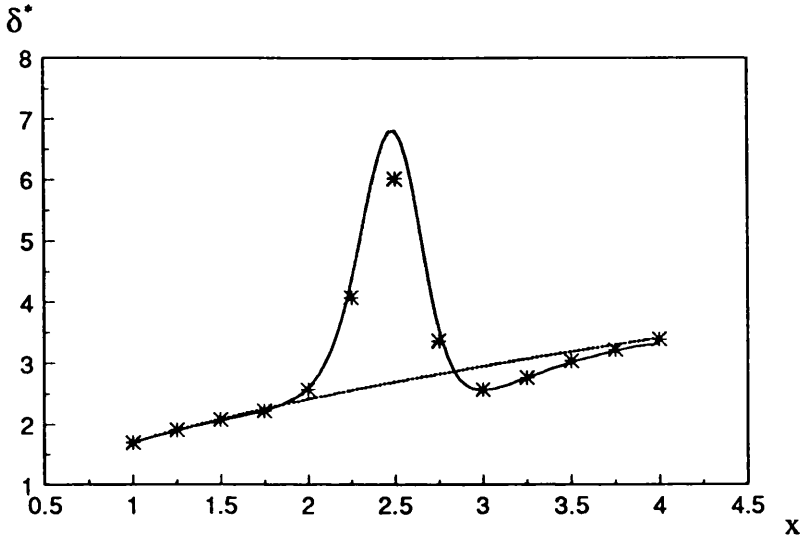

Fig. 5.38 Displacement thickness

* Carter's data ——— present method

····· 1st approximation

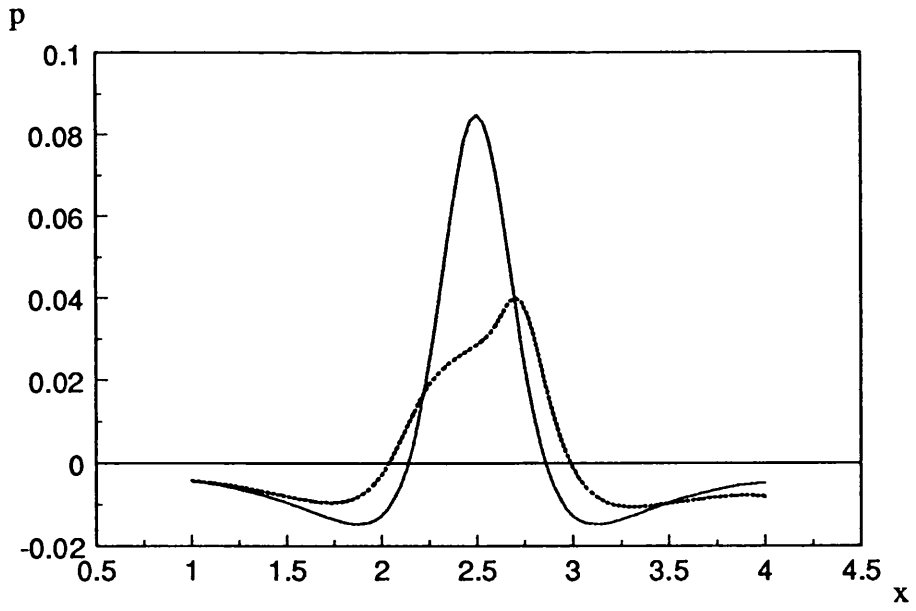

Fig. 5.39 Pressure distribution, $p=\frac{1}{2}(1-u_e^2)$

——— without interaction ····· with interaction

CHAPTER 6
CONCLUSIONS AND SUGGESTIONS FOR FURTHER WORK

The summary of each chapter is presented in the first section of this chapter. The contribution of this dissertation to the three-dimensional boundary-layer on the turbomachinery blades is given in section two. A discussion for further work is in the final section.

6.1 CONCLUSIONS

6.1.1 CHAPTER 2

The literature review of current developments in the calculations of boundary-layer flows were discussed in this chapter. The boundary layer methods applicable to turbomachinery are the highlight of the chapter. In the design of turbomachinery blades, inviscid methods are routinely used. To improve design methods, the fluid mechanics theory of turbomachinery should integrate all the factors that contribute to the flow and the energy transfer about the blades. This means that the effects of three-dimensional flow, compressibility, rotation and viscosity have to be taken into account.

There have been several recent attempts, as shown in chapter 2, to use Navier-Stokes as well as boundary layer methods to predict the viscous effect in turbomachinery blade analysis and design. The Navier-Stokes methods are usually too slow and expensive for routine design work. The boundary layer methods, on the other hand, can provide a better resolution of the viscous layers at the wall with little computational cost. Among the boundary-layer methods in recent years, the method due to Vatsa (1985) seems to be the most suitable for turbomachinery analysis. In this method the steady three-dimensional boundary-layer equations are solved using finite-difference techniques. The Levy-Lees transformation is

employed in the system of the equations in order to capture the viscous-layer growth. He employed a first-order formulation for spatial derivatives and an upwind scheme in the crossflow direction. The resulting linear algebraic equations are solved using a block tridiagonal solver. This method, however, is not applicable to encounter reversal of velocity within a three-dimensional boundary layer. In addition the implementation and application of the similarity transformation to solve the equations are not straightforward since the transformation is varied according to the flow conditions such as laminar, turbulent, compressible, incompressible, two-dimensional flow, three-dimensional flow.

6.1.2 CHAPTER 3

The method to solve the boundary-layer equations applicable to turbomachinery blades is presented in this chapter. The main difference between the present method and the method used by Vatsa is the numerical solution algorithm of the boundary-layer equations. In the present method, the solutions of the equations are obtained by time integration. In addition, the transformations used to stretch the co-ordinate normal to the solid surface as well as the numerical method used to solve the boundary-layer equations are considerably different.

The basic methodology of the present method is to time-march the unsteady boundary-layer equations of flow to steady state with a multi-relaxation factor to enhance convergence rate. The solutions are obtained in an uncoupled manner with a simple iteration of tridiagonal matrix. The implementation and application of the method are simple and straightforward since the governing equations are solved directly without employing similarity transformation.

Two different approaches for energy equation were presented. One is for the approximate and the other is for the exact form of the equation. The

approximate equation is based upon the conservation of rothalpy. The flow is assumed to be adiabatic and the Prandtl number is one. The results, under such conditions, show that the approximate equation give reasonable value with less computer time than that of the exact one.

Turbulent flow modelling is also an important feature in the computation of the equations. In this study, the Baldwin-Lomax model is extended for three-dimensional flow over a non-orthogonal surface. The model is simple to implement and gives reasonable solution for the test cases. However, this model does not account for rotation and other complex phenomenon, such as surface curvature.

6.1.3 CHAPTER 4

The calculation method presented in the previous chapter has the weakness that the computation will break down as soon as there is a flow reversal. This is the main concern about the stability of the solution and the highlight of this chapter. There are a number of solutions to this problem. But in this study we will consider only the FLARE approximation method, conventional inverse method and the implicit interactive method.

Among the three methods, the FLARE approximation method is the simplest to implement. In this approach, the streamwise velocity and its products are neglected when there is a flow reversal. The solution from this method is good only for regions of small reverse flow.

The main difference between the "inverse" approach and the "direct" approach is on the type of boundary condition specified. In the case of the inverse approach, the displacement thickness or skin friction has to be prescribed and used as a boundary condition instead of the outer flow conditions. The problem of

implementation of the method is that the displacement thickness or skin friction is not known beforehand. Therefore, the solutions from the boundary-layer (viscous region) have to be approximated and iteratively coupled with the solutions from the outer flow (inviscid region). This technique is called the viscous-inviscid interaction.

One of the best interactive methods, which is implemented in two-dimensions in this work is the method of Veldman. The method makes use of the Hilbert integral to couple the solutions of the inviscid and viscous flow equations. The essence of the method is that both pressure and displacement thickness are treated as boundary conditions.

The flow behaviour about the turbomachinery blade is changed due to viscous effects, especially when there is a flow reversal. This change also affects the design condition that relates to the efficiency of the machine. Therefore, it is of interest to investigate the loss generation by the boundary-layer. The benefits of this knowledge can be used as a tool to improve the design and to identify loss sources and mechanism. The loss in this study is investigated in term of entropy generation. The entropy generation is deduced from the Thermodynamics laws and the viscous fluid flow equations. From the equation, we can see that the entropy generation is proportional to the heat transfer at the wall and the viscous work inside the boundary-layer in both streamwise and crossflow direction.

6.1.4 CHAPTER 5

In this chapter, the code based on the proposed method was applied to a number of test cases to highlight the accuracy and reliability of the model. The test cases are in the following configuration.

1. Three-dimensional flow over a flat plate with the plate moving parallel to its leading edge

2. Three-dimensional flow over a flat plate with an attached cylinder

3. Rotating helical blade (both laminar and turbulent flow)

4. An axial compressor

5. A centrifugal compressor rotor

6. A dented plate with a separation bubble

The predictions provide generally satisfactory results for all the test cases. Several specific conclusions can be drawn from the study:

This boundary layer method has been applied in three-dimensional time marching technique for the computational of the above test cases. The convergence of the solutions is fast since the tridiagonal elimination scheme is formed and a multi-relaxation factor method is employed.

The computer time and storage are also reduced when the total enthalpy in the energy equation is approximated by employing the conservation of rothalpy. This approximation is resulted from the assumption of adiabatic wall and the Prandtl number is one in the energy equation of compressible boundary layer.

The direct method shows poor convergence when there is a flow reversal. For the two-dimensional flow, the interactive scheme is employed. The interactive method was not implemented in three-dimensional cases due to limited time available to the author, and were not straightforward, as shown in chapter 4. Therefore, the FLARE approximation scheme is employed for such cases. However, the application of interactive method in two-dimensional calculation is designed to lay the foundation for three-dimensional calculation.

The influence of the rotation in the test case tends to increase the magnitude of the secondary velocity. The predicted momentum thickness and

displacement thickness are also increased. Therefore, secondary losses will be high in a rotating case.

The viscous losses, expressed in terms of entropy generation, is shown to be dependent on the free-stream velocity and the secondary flow. The results indicate that the entropy generation is high in the direction of the secondary flow because it transports the loss. The displacement thickness increases rapidly and the secondary flow is strong when there is a flow reversal. To improve the efficiency of a machine, the level of secondary flow has to be reduced.

6.2 CONTRIBUTIONS OF THE WORK

This thesis outlines a three-dimensional boundary-layer solver developed for application to turbomachinery blades. The work solved unsteady boundary-layer equations of the rotating cylindrical co-ordinate system. The main attraction of solving the unsteady equations is the ability to compute steady and unsteady solutions. In this study, we consider only the steady state solutions. In order to cope with the separated flows, the method used the FLARE approximation as well as an interactive approach. The concept of the interactive approach, presented in chapter 4, is general but its application has so far been restricted to two-dimensional flow. In an attempt to understand the loss generation mechanisms in the flow, the entropy generation rate is calculated from the computed flowfield.

6.3 SUGGESTIONS FOR FURTHER WORK

6.3.1 DEVELOPMENTS OF THE METHOD FOR UNSTEADY FLOW

The method presented in this study solves the boundary layer equations using a finite difference technique in which the solution proceeds by marching in time. A first order integration in time is then used to advance the dependent variables forward to a steady state solution. Since the flow through turbomachinery blades are inherently unsteady and unsteady viscous effects can impact the time-averaged or steady-state performance, efficient calculation methods for unsteady viscous flow are an important goal for current and future research. As a step toward this goal, the time integration should be improved. A second order integration in time, such as RRK, or an explicit 4-state Runge-Kutta scheme may be employed. However, some acceleration parameter, such as multigrid scheme, may be needed to enhance the convergence of the solutions. The works on the unsteady flow may be seen in Power et al (1991), Walker and Dawes (1990), and Doorly (1987).

6.3.2 DEVELOPMENTS OF THE METHOD FOR HEAT TRANSFER ON GAS TURBINE BLADE

The thermal efficiency of gas turbines is improved by increasing the turbine inlet temperature. In order to increase the inlet temperature, it is important to obtain a better understanding of heat transfer around the turbine blades. The method developed in this study has a potential to predict blade heat transfer. However, some fluid properties, such as viscosity obtained from Sutherland's theory, have to be modified since the gas turbine operates at very high temperatures (above 1250 K). The turbine blade heat transfer predictions using

two-dimensional boundary layer can be seen in Rodi and Scheuerer (1985), and using quasi-three-dimensional Navier-Stokes equations can be seen in Boyle (1991).

6.3.3 DEVELOPMENTS OF THE METHOD USING A ZONAL FORMULATION

Most of the Navier-Stokes solutions can only provide accurate prediction of inviscid flowfield. The major concerns are the grid resolution of viscous layers at the wall, and the computing cost for the Navier-Stokes solutions. One way to obtain a better resolution at the wall with little computational cost is to use a so-called zonal approach. In a zonal approach, the boundary layer equations are solved at the solid boundary in a fine grid and the Navier-Stokes equations are solved outside the Boundary layer in a coarse grid together with appropriate matching boundary conditions. The Navier-Stokes solutions provide an outer boundary condition for boundary equations in the viscous layer. In return, the boundary layer solutions provide information near the solid boundary. The solutions are advanced simultaneously on a coarse and on a fine grid. Implementation of the zonal approach may be seen as the extension for the present study. Methods outlined for zonal formulations may be seen in Tang and Hafez (1993), and Hafez et al (1991).

6.3.4 DEVELOPMENTS OF THE METHOD FOR SEPARATED FLOW

In this study, the FLARE approximation and the interactive scheme were used when flow reversal was presented. The present evaluation indicates that the two approaches are capable of dealing with the boundary-layer problems. The interactive scheme is preferable because as it can deal with the large separation region while the FLARE approximation scheme is not accurate. The main concern

about the interactive scheme especially in three-dimensional flow is that it may be too complicated to implement.

Although this work concentrated on solving the boundary-layer equations, the framework gives the general steps that can be adapted to other equations. One of the set of equations that falls between full Navier-Stokes and boundary-layer equations is the thin-layer Navier-Stokes equations. This set of equations is similar to that of boundary-layer equations. The main difference is that it retains all three of the momentum equations and makes no assumption about the pressure. In this way, the equations can be solved in "direct mode" even in the presence of flow reversal. However the computer storage and time have to be considered since very fine grids are required to order to resolve the normal gradients in the boundary-layer.

6.3.5 TURBULENT MODEL

The Baldwin-Lomax model was extended to three-dimensional flow and used in this calculation. The model is used in many Navier-Stokes and related equations. The use of turbulent models in turbomachinery blades makes it necessary to account for the effects of curvature and rotation. At the moment, it seems that only Reynolds stress model (RSM) can capture these effects. Lakshminarayana (1991) has reviewed the turbulent models for three-dimensional boundary-layer. The method due to Zhang and Lakshminarayana (1990) is probably the most suitable for turbomachinery flows. So further work should be undertaken in order to implement a Reynolds stress model into the programs.

REFERENCES

Abbott, IRA H. and Doenhoff, A.E. Von (1959): "Theory of Wing Sections", Dover Publication, Inc., New York

Anderson, D.A., Tannehill, J.C., and Pletcher, R.H. (1984): "Compuational Fluid Mechanics and Heat Transfer", Hemisphere Publishing Corporation

Anderson, O.L. (1987): "Calculation of Three-dimensional Boundary Layers on Rotating Turbine Blades", Journal of Fluids Engineering, vol.109, March 1987, pp.41-50

Aronne, A. and Swanson, R.C. (1993): "A Navier-Stokes Solver for Turbomachinery Applications", Journal of Turbomachinery, April 1993, Vol. 115

Baldwin, B., and Lomax, H. (1987): "Thin-layer Approximation and Algebraic Model for Separate Turbulent Flows", AIAA Paper 78-257

Boyle, R.J. (1991) "Navier-Stokes analysis of turbine blade Heat Transfer", Journal of turbomachinery ASME, vol.113, pp.392-403, July 1991

Bradshaw, P., Cebeci, T., and Whitelaw J.H. (1981): "Engineering calculation methods for turbulent flow", Academic, London

Briley, W.R. (1971): "A Numerical Study of Laminar Separation Bubbles using the Navier-Stokes Equations", J. Fluid Mech., vol.47, part 4, pp.713-736

Buchanam, J.L. and Turner, P.R. (1992): "Numerical Methods and Analysis", McGraw-Hill, Inc.

Carter, J.E. (1978): "A new boundary layer interaction techniques for separated flows", NASA, June 1978

Carter, J.E., and Wornom, S.F. (1975): "Solution for Incompressible Separated Boundary Layers Including Viscous-Inviscid Interaction", Aerodynamic analysis requiring advanced computers, NASA SP-347, pp.125-150

Catherall, D. and Mangler, K.W. (1966) "The integration of the two-dimensional laminar boundary-layer equations past the point of vanishing skin friction", J. Fluid Mech., vol.26, part 1, pp.163-182

Cebeci, T. (1975): "Calculation of Three-Dimensional Boundary Layer II. Three-Dimensional Flows in Cartesian Co-ordinates", AIAA Journal, vol.13, No.8, August, 1975

Cebeci, T. (1984): "Numerical and Physical Aspects of Aerodynamic Flows II", New York, Springer

Cebeci, T., Platzer, M.F., Jang, H.M. and Chen, H.H. (1992): "An inviscid-viscous interaction approach to the calculation of dynamic stall initiation on airfoils", ASME paper no 92-GT-128

Cebeci, T. and Smith, A.M.O. (1970): "A Finite-Difference Method for calculating Compressible Laminar and Turbulent Boundary Layers", Journal of Basic Engineering, September, 1970

Cebeci, T. and Smith, A.M.O. (1974): "Analysis of turbulent boundary layers", Academic, New York

Chow, Chuen-Yen (1979): "An Introduction to Computational Fluid Mechanics", New York, Wiley

Conte, S.D. and Carl de Boor (1980): "Elementary numerical analysis: an algorithmic approach", 3rd edition, McGraw-Hill

Cousteix, J. (1987): "Computation of Three-Dimensional Boundary Layers including Separation", AGARD Report No. 741, February 1987.

Cumpsty, N.A. (1989): "Compressor Aerodynamics", Longman Scientific & Technical

Das, D.K. (1988): "A simple theory for calculating turbulent boundary layers under arbitrary pressure gradients", Journal of engineering fluid mechanics, vol. 1, no. 1, pp.83-99

Dawes, W.N. (1986): "Numerical Techniques for Viscous Flow Calculations in Turbomachinery Bladings", von Karman Institute for Fluid Dynamics, Lecture Seriess 1986-02

Dawes, W.N. (1987): "Application of a Three-Dimensional Viscous Compressible Flow Solver to a High-Speed Centrifugal Compressor Rotor-Secondary Flow and Loss Generation", Proceedings of the Institution of Mechanical Engineers International Conference: Turbomachinery-Efficiency Prediction and Improvement

Denton, J.D. (1983): "An improved time marching method for Turbomachinery flow calculations", Trans. ASME, Journal of Engineering for Power, Vol.105, No.3, pp.514

Denton, J.D. (1986): "The Use of a Distributed Body Force to Simulate Viscous Effects in Three-Dimensional Flow Calculations", ASME paper no. 86-GT-144

Denton, J.D. (1993): "Loss Mechanisms in Turbomachines", Journal of Turbomachinery, Vol.115, October 1993

Denton, J.D. and Cumpsty N.A. (1987): "Loss Mechanisms in Turbomachines", Proceedings of the Institution of Mechanical Engineers International Conference: Turbomachinery-Efficiency Prediction and Improvement

Doorly, D.J. (1987): "Modelling the unsteady flow in a turbine rotor passage", ASME Paper No.87-GT-197, May 1987

Eckardt, D. (1976): "Detail Flow Investigation Within a High-Speed Centrifugal Compressor Impeller", Transactions of ASME, Journal of Fluids Engineering, pp.390-402

Ekaterinaris, J.A. and Menter, F.R. (1994): "Computation of oscillating airfoil flows with one- and two-equation turbulence models", AIAA Journal, vol.32, No.12, December 1994

Fillo, J.A. and Burbank, R. (1972): "Calculation of 3D Laminar Boundary Layer Flows", AIAA Journal, vol.10, no.3, pp.353-355

Fletcher, C.A.J. (1991): "Computational Techniques for Fluid Dynamics", Volume I-II, Second Edition, Springer-Verlag

Fogarty, L.E. (1951): "The Laminar Boundary Layer on a Rotating Blade", Journal of the Aeronautical Sciences, April 1951

Gill, P.E. and Miller, G.F. (1972): "An Algorithm for the Integration of Unequally Spaced Data", The Computer Journal, vol.15, No.1, pp.80-83

Groves, N.C. and Change, M.S. (1984): "A differential prediction method for 3-D Laminars and turbulent boundary layers of rotating propeller blades", 15th symposium on naval hydro-dynamics, 6 Sep 1984

Hafez, M.M., Habashi, W.G. and Przybytkowski, S.M. (1991): "Transonic viscous-Inviscid Interaction by a finite element method", International Journal for Numerical methods in fluids, vol.13, pp.309-319

Hara, K., Furukawa, M. and Inoue, M. (1994): "Behavior of three-dimensional boundary layers in a radial inflow turbine scroll", Journal of Turbomachinery, vol.116, July 1994

Humphreys, D.A. and Lindhout, J.P.F. (1988): "Calculation methods for three-dimensional turbulent boundary layers", Prog. Aerospace sci., vol.25, pp.107-129

Jang, H.M., Ekaterinaris, J.A., Platzer, M.F. and Cebeci, T. (1991): "Essential ingredients for the computaion of steady and unsteady blade boundary layers", Journal of Turbomachinery ASME, Vol. 113, October 1991, pp.608-616

Johnston, L.J. (1988): "A Calculation Method for Compressible Three Dimensional Boundary Layer Flows", von Karman Institute for fluid dynamics, technical note 167, July 1988

Johnston, L.J. (1990): "An upwind scheme for the Three-dimensional boundary layer equations", International Journal for Numerical methods in fluids, vol.11, pp.1043-1073

Karimipanah, M.T. and Olsson, E. (1992): "Calculation of Three-dimensional Boundary Layers on Rotor Blades Using Integral Methods", ASME paper 92-GT-210

Katz, J. and Plotkin, A. (1991): "Low-speed aerodynamics from wing theory to panel methods", McGraw-Hill

Kay, J.M. and Nedderman, R.M. (1990):, "Fluid Mechanics and Transfer Process", Cambridge University Press

Keller, H.B. (1978): "Numrical Methods in Boundary-Layer Theory", Ann. Rev. Fluid Mech, 10, pp. 417-433

Keller, H.B. and Cebeci, T. (1972): "Accurate Numerical methods for boundary-layer flows II: two-dimensional turbulent flows", AIAA Journal, September, 1972

Kitchens, C.W. Jr., Sedney, R. and Gerber, N. (1975): "The Role of the Zone of Dependence Concept in Three-Dimensional Boundary-Layer Calculations", Proc. AIAA computational Fluid Dynamics

Kwon, O.K. and Pletcher, R.H. (1986a): "A Viscous-Inviscid Interaction Procedure-Part I: Method for Computing Two-Dimesnsional Incompressibel Separated Channel Flows", Journal of Fluids Engineering ASME, Vol. 108, March 1986, pp.64-70

Kwon, O.K. and Pletcher, R.H. (1986b): "A Viscous-Inviscid Interaction Procedure-Part 2: Application to Turbulent Flow over a Rearward-Facing Step", Journal of Fluids Engineering ASME, Vol. 108, March 1986, pp.71-75

Lakshminarayana, B. (1991): "An Assessment of Coputational Fluid Dynamic Techniques in the Analysis and Dssign of Turbomachinery-The 1990 Freeman Scholar Lecture", Journal of Fluid Engineering, Vol.113, September 1991, pp.315-352

Lakshminarayana, B. and Govindan, T.R. (1981): "Analysis of Turbulent Boundary Layer on Cascade and Rotor Blades of Turbomachinery", AIAA Journal, Vol.19, No.10, October 1981, pp.1333-1341

Lakshminarayana, B., Jabbari, A. and Yamaoka H. (1972): "Turbulent Boundary Layer on a Rotating Helical Blade", J. Fluid Mech., vol. 51, part 3, 1972, pp.545-569

Lemmerman, L.A. and Atta, E.H. (1980): "Three-dimensional boundary layer calculation methods", AIAA-80-0133, AIAA 18th aerospace science meeting 14-16 Jan 1980

Lighthill, M.J. (1958): "On Displacement Thickness", J. Fluid Mech., vol.4, pp.383-392

Liu, Feng and Jameson, Antony (1993): "Multigrid Navier-Stokes calculations for three-dimensional cascades", AIAA Journal, vol.31, No.10, October 1993

Loos, H.G. (1955): "A Simple Laminar Boundary Layer with Secondary Flow", Journal of the Aeronautical Sciences, January, 1955, pp.35-40

McNally, W.D. (1985): "Review-computational methods for internal flows with emphasis on Turbomachinery", Journal of Fluids Engineering, vol. 107, March 1985, pp.6-22

Morinishi, Koji and Satofuka, N. (1991): "Convergence acceleration of the rational runge-kutta scheme for the Euler and Navier-Stokes equations", computers and fluids, vol.19, no.3/4, pp.305-313

Morris, P.J. (1981): "Three-Dimensional Boundary Layer on a Rotating Helical Blade", J. Fluid Mech., vol. 112, pp.283-296

Ng, E. Y-K and Dawes W.N. (1992): "A Novel Approach to High Resolution Compressible Cascade Flow Analysis Using the Navier-Stokes Equations", ASME Paper No. 92-GT-419

Olsson, E.K.A. (1962): "Centrifiugal Effect on the Boundary Layer on a Blade of an Axial Turbomachine", Gas Turbine Laboratory, MIT., Report No.66, April 1962

Oshima, A. (1994): "Analysis of three-dimensional boundary-layer on propeller blade", propellers/shafting'94 symposium, September 20-21,1994

Pletcher, R.H. (1969): "On a Finite-Difference Solution for the Constant-Property Turbulent Boundary Layer", AIAA Journal, vol. 7, NO. 2, February 1969

Power G.D., Verdon, J.M. and Kousen, K.A. (1991): "Analysis of unsteady compressible viscous layer", Journal of Turbomachinery ASME, Vol. 113, pp.644-653, October 1991

Ralston, A. (1965): "A First Course in Numerical Analysis", McGraw-Hill (International series in pure and applied mathematics)

Rodi, W. and Scheuerer, G. (1985): "Calculation of Heat Transfer to convection-cooled gas turbine blades", Journal of Engineering for gas turbines and power ASME, vol.107, pp.620-627, July 1985

Schlichting, H. (1979): "Boundary-Layer Theory", Seventh Edition, McGraw-Hill, Inc.

Sondak, D.L. and Pletcher, R.H. (1995): "Application of wall functions to generalized nonorthogonal curvilinear coordinate systems", AIAA Journal, vol.33, No.1, January 1995

Sowerby, L. (1965): "Three-Dimensional Laminar Boundary Layer on a Flat Plate", J. Fluid Mech., vol.22, part 3, pp.587-598

Steger, J.L. and Van Dalsem, W.R. (1985): "Development in the Simulation of Separated Flows using Finite Difference Methods", Proceeding of the Third Symposium on Numerical and Physical Aspects of Aerodynamic Flows, California State University, Long Beach, Cal., January, 1985

Stewartson, K. (1964): "The Theory of Laminar Boundary Layers in Compressibel Fluids", Oxford University Press

Tang, C.Y. and Hafez, M.M. (1993): "Finite element/finite volume simulations of viscous flows based on zonal Navier-Stokes formulations: Part I", American Society of Mechanical Engineering, Fluid Engineering Division (Publication) FED: Advances in Finite Element Analysis in Fluid Dynamics vol.171, pp.53-65

Tani, I (1977): "History of Boundary-Layer Theory", Ann. Rev. Fluid Mech., vol.9, pp.87-111

Thompkins, W.T. Jr. and Usab, W.J. Jr. (1982): "A quasi-Three-dimensional blade surface Boundary Layer analysis for rotating blade rows", Journal of engineering for power, vol.104, April 1982, pp.439-449

Thwaites, B. (1949): "Approximate Calculation of the Laminar Bondary layer", Aeronautical Quarterlly, vol.1, pp.245-280

Van Dalsem, W.R. (1984): "Simulation of Separated Transonic Airfoil Flow by Finite-Difference Viscous Inviscid Interaction", Ph.D. thesis, Stanford University, June, 1984

Van Dalsem, W.R. and Steger, J.L. (1985): "The Efficient Simulation of Separated Three-Dimensional Viscous Flows using the Boundary-Layer Equations", AIAA Pager 85-4064

Vatsa, V.N. (1985):"A Three-Dimensional Boundary-Layer Analysis Including Heat-Transfer and Blade-Rotation Effects", Third Symposium on Numerical and Physical Aspects of Aerodynamic Flows, Long Beach, CA

Veldman, A.E.P. (1981): "New, Quasi-Simultaneous Method to Calculate Interacting Boundary Layers", AIAA Journal, vol.19, No.1, January 1981, pp.79-85

Walker, P.J. and Dawes, W.N. (1990): "The extersion and application of three-dimensional time-marching analyses to incompressible turbomachinery flows",Journal of Turbomachinery ASME, Vol. 112, pp.385-390, July 1990

Warsi, Z.U.A. (1992): "Fluid Dynamics Theoretical and Computational Approaches", CRC Press

White, F.M. (1991): "Viscous Fluid Flow", Second Edition, McGraw-Hill, Inc.

Yamazaki, R. (1981): "On the Theory of Marine Propellers in Non-uniform Flow", Memoirs of the Facculty of Engineering, Kyushu University, vol. 41, No. 3, September 1981

Yohner, P.L. and Hansen, A.G. (1958): "Some Numerical Solutions of Similarity Equations for Three-Dimensional Laminar Incompressible Boundary-Layer Flows", National Advisory Committee for Aeronautics, Technical note 4370

Zhang, J. and Lakshminarayana, B. (1990): "Computation and turbulence modelling for Three-dimensional Boundary Layers including turbomachinery rotor flows", AIAA Journal, November 1990, pp.1861-1869

APPENDIX A
VELOCITY TRANSFORMATION

The system of three-dimensional boundary-layer governing equations (3.18-3.21) is expressed in the co-ordinate surface $(\bar{\xi},\bar{\eta},\bar{\zeta})$. The body surface is defined in the co-ordinate lines $\bar{\xi}$ and $\bar{\eta}$, and $\bar{\zeta}$ normal to that surface. The velocities u, v and w are velocities, respectively, along the $\bar{\xi}$, $\bar{\eta}$, and $\bar{\zeta}$ curves. In the case where the velocities u_x, u_r and u_θ of a standard co-ordinate (e.g. x, r, θ) are known, we have to transformed these velocities in the direction of the curvilinear co-ordinate $(\bar{\xi}, \bar{\eta}, \bar{\zeta})$.

Let **U** is the velocity vector relative to the rotating system where its components in $(\bar{\xi}, \bar{\eta}, \bar{\zeta})$ co-ordinate are u, v and w, and in (x, r, θ) co-ordinate are u_x, u_r and u_θ. In terms of the unit base vectors, the velocity vector **U** is now written as:

$$\mathbf{U} = u_x \mathbf{e}_x + u_r \mathbf{e}_r + u_\theta \mathbf{e}_\theta \qquad \text{A.1a}$$

$$\mathbf{U} = u \mathbf{e}_1 + v \mathbf{e}_2 + w \mathbf{e}_3 \qquad \text{A.1b}$$

Using the dot product property and the relationships among the unit vectors equations (3.14), we can write the equations (A.1a,b) in the form

$$u_x = (\mathbf{e}_1 \cdot \mathbf{e}_x)u + (\mathbf{e}_2 \cdot \mathbf{e}_x)v + (\mathbf{e}_3 \cdot \mathbf{e}_x)w \qquad \text{A.2}$$

$$u_r = (\mathbf{e}_1 \cdot \mathbf{e}_r)u + (\mathbf{e}_2 \cdot \mathbf{e}_r)v + (\mathbf{e}_3 \cdot \mathbf{e}_r)w \qquad \text{A.3}$$

$$u_\theta = (\mathbf{e}_1 \cdot \mathbf{e}_\theta)u + (\mathbf{e}_2 \cdot \mathbf{e}_\theta)v + (\mathbf{e}_3 \cdot \mathbf{e}_\theta)w \qquad \text{A.4}$$

In matrix form the equations (A.2-A.4) becomes

$$\begin{bmatrix} u_x \\ u_r \\ u_\theta \end{bmatrix} = \begin{bmatrix} \mathbf{e}_1 \cdot \mathbf{e}_x & \mathbf{e}_2 \cdot \mathbf{e}_x & \mathbf{e}_3 \cdot \mathbf{e}_x \\ \mathbf{e}_1 \cdot \mathbf{e}_r & \mathbf{e}_2 \cdot \mathbf{e}_r & \mathbf{e}_3 \cdot \mathbf{e}_r \\ \mathbf{e}_1 \cdot \mathbf{e}_\theta & \mathbf{e}_2 \cdot \mathbf{e}_\theta & \mathbf{e}_3 \cdot \mathbf{e}_\theta \end{bmatrix} \begin{bmatrix} u \\ v \\ w \end{bmatrix} \qquad \text{A.5}$$

Then, the velocity vectors along the $\bar{\xi}$, $\bar{\eta}$ and $\bar{\zeta}$ curves are

$$\begin{bmatrix} u \\ v \\ w \end{bmatrix} = \begin{bmatrix} \mathbf{e}_1 \cdot \mathbf{e}_x & \mathbf{e}_2 \cdot \mathbf{e}_x & \mathbf{e}_3 \cdot \mathbf{e}_x \\ \mathbf{e}_1 \cdot \mathbf{e}_r & \mathbf{e}_2 \cdot \mathbf{e}_r & \mathbf{e}_3 \cdot \mathbf{e}_r \\ \mathbf{e}_1 \cdot \mathbf{e}_\theta & \mathbf{e}_2 \cdot \mathbf{e}_\theta & \mathbf{e}_3 \cdot \mathbf{e}_\theta \end{bmatrix}^{-1} \begin{bmatrix} u_x \\ u_r \\ u_\theta \end{bmatrix} \qquad \text{A.6}$$

For boundary-layer problem, w should be zero or nearly zero when compare with u. If w is not zero and has a significant value, this means that the velocity vector **U** does not parallel to the body surface. The values of the directional cosines between the systems (e.g. $\mathbf{e}_1 \cdot \mathbf{e}_x$) are given in equation (3.15).

APPENDIX B
AN ALGORITHM FOR FINDING OUTER FLOW (u_{es}) OF A SPECIFIED DISPLACEMENT THICKNESS (δ^*)

A direct boundary-layer solution method that specifies the outer flow as a boundary condition and calculates displacement thickness as part of the solutions, fails to converge as the flow separation point is approached. It is well known that this singularity point may be removed by using the inverse boundary-layer solution method. The usual procedure in an inverse calculation method is to replace the outer flow boundary condition by the specification of a displacement thickness or wall shear stress that must be satisfied by the solution.

In this appendix we describe an algorithm that accelerates the convergence of finding the outer flow when displacement thickness is a prescribed function.

The boundary conditions for the inverse procedure are

at $\zeta=0$ $\quad u_s(\xi,\eta,0) = v_c(\xi,\eta,0) = w(\xi,\eta,0) = 0$ B.1

and at $\zeta\to\infty$ $\quad v_c(\xi,\eta,\infty) = 0$

$$\int_0^\infty \left(1-\frac{\rho u_s}{\rho_e u_{es}}\right) d\zeta = \delta^*_{s,bc}(\xi,\eta) \qquad \text{B.2}$$

where the subscribe "s" means streamwise direction

the subscribe "c" means crossflow direction

the subscribe "e" means at the boundary-layer edge

$\delta^*_{s,bc}(\xi,\eta)$ is a prescribed displacement thickness in the streamwise direction

The implementation of the inverse mode begins by varying $u_{es}(\xi,\eta)$ in successive iterations at each streamwise calculation station until the solution satisfies the specified value of $\delta^*_{s,bc}(\xi,\eta)$ in the plane of η. In each value of $u_{es}(\xi,\eta$), the numerical solutions for the boundary-layer equations are implemented in the same ways as for the direct method. When the solution is obtained, the displacement thickness is evaluated from equation (B.2). The integration of the computed velocity distribution in unequalled grid spacing data may be seen in Appendix D.

To accelerate the trial-and-error process, Anderson et al (1984) suggested to adopt secant method that usually converges in three or four iterations. In this method, two initial guesses are required.

In the application of the secant method, a function of $u_{es}(\xi,\eta)$ (i.e. $F(u_{es})$) at each streamwise station is $\delta^*_s(\xi,\eta)$-$\delta^*_{s,bc}(\xi,\eta)$ and we are seeking the value of $u_{es}(\xi,\eta)$ required to establish $F(u_{es})=0$. Where $\delta^*_s(\xi,\eta)$ is the displacement thickness from the computed velocity distribution of $u_{es}(\xi,\eta)$.

If $u_{es,n-1}$ and $u_{es,n-2}$ are two approximations to the solution of the equation $F(u_{es})=0$, then the secant method for finding the root is obtained from

$$u_{es,n} = u_{es,n-1} - \frac{F(u_{es,n-1})}{F(u_{es,n-1}) - F(u_{es,n-2})} (u_{es,n-1} - u_{es,n-2}) \qquad \text{B.3}$$

with a convergence criteria $|u_{es,n} - u_{es,n-1}| < \varepsilon$

where n = iteration cycle

ε = convergence criteria, e.g. 1×10^{-4}

$F(u_{es,n-1}) = \delta^*_{s,n-1} - \delta^*_{s,bc}$

If $|u_{es,n} - u_{es,n-1}| < \varepsilon$ is not satisfied, the process is repeated by using the two most recent iterates $u_{es,n-1}$ and $u_{es,n}$ to generate $u_{es,n+1}$. The iterative process is illustrated in Fig. B.1. From this figure, you can see that an estimate of $u_{es,n}$ is predicted by a tangent of the function to the u_{es} axis.

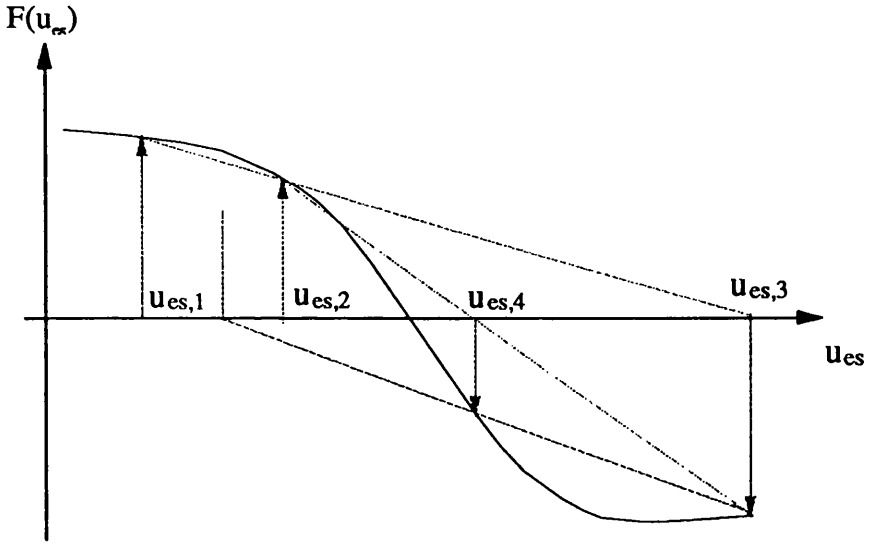

Fig. B.1 Graphical depiction of the secant method

Although the method required two initial guesses to generate the new one, it is not necessary to start the method with the two points that bracket the solution. In the case where the two iterations bracket the solution, the next iteration is obtained by linear interpolation that is a reliable process. While in the case where the two iterations do not bracket the solution, the next iteration is obtained by extrapolation. In some cases, the extrapolation feature of the secant method may cause difficulties, resulting in very slow convergence. Buchanam and Turner (1992), recommended a combination of secant and bisection methods to guarantee a convergence of the function. Another way of improving the convergence is by using the δ^2 process. This method was developed from an extrapolation method. Ralston (1965) used it to accelerate the Gauss-Seidel iteration method. The new approximation to the root is obtained from

$$u_{cs,n} = \frac{u_{cs,n-3}u_{cs,n-1} - (u_{cs,n-2})^2}{u_{cs,n-1} - 2u_{cs,n-2} + u_{cs,n-3}} \qquad \text{B.5}$$

However, it is important that the δ^2 process not be used too early in the computation in which case it may give poorer results than the last iteration.

APPENDIX C

NUMERICAL SOLUTIONS FOR THREE-DIMENSIONAL FLOW OVER A FLAT PLATE WITH THE PLATE MOVING PARALLELED TO ITS LEADING EDGE

Here we will find the solutions of two ordinary differential equations of three-dimensional flow over a flat plate with the plate moving paralleled to its leading edge. The equations of $f=f(\eta)$, $h=h(\eta)$ and their derivatives are (for detail see section 5.2).

$$f f'' + 2 f''' = 0 \qquad \text{C.1}$$

$$2 h''' + f h'' - 2 f' h' + 2 = 0 \qquad \text{C.2}$$

with the associated boundary conditions

at $\eta=0$ $\quad f(0) = f'(0) = h(0) = h'(0) = 0$

at $\eta\to\infty$ $\quad f'(\infty) = h'(\infty) = 1$ C.3

The fourth-order Runge-Kutta method may be utilised to find the solution of (C.1), if f, f' and f'' are known at $\eta=0$. Since we know the boundary conditions at $\eta=0$ of f and f', and at $\eta\to\infty$ of f', the numerical integration of (C.1) has to begin with a guessed value of f'' at $\eta=0$. The solutions are accepted until the boundary conditions at $\eta\to\infty$ of f' is satisfied. This trial-and-error process is time consuming. Chow (1979) suggested a better method that can be derived for finding f'' at $\eta=0$. He introduced a linear transformation for the independent variable

$$\eta = k z \qquad \text{C.4}$$

and a function g such that

$$f(\eta) = \frac{g(z)}{k} \qquad \text{C.5}$$

where k is a constant.

The differentiation of $f(\eta)$ with respect to η can be written in a general form as

$$\text{for } n \geq 1 \qquad \frac{d^n f}{d\eta^n} = \frac{1}{k^{n+1}} \frac{d^n g}{dz^n} \qquad \text{C.6}$$

Substitution into equation (C.1) gives an ordinary differential equation.

$$g\, g'' + 2\, g''' = 0 \qquad \text{C.7}$$

with the associated boundary conditions

$$\text{at } z=0 \qquad g(0) = g'(0) = 0$$

$$\text{at } z \to \infty \qquad g'(\infty) = k^2 \qquad \text{C.8}$$

Since k is arbitrary and appears only in the condition at infinity, there is no restriction on the magnitude of g'' at the plate. We can choose any values for $g''(0)$ (e.g. $g''(0)=1$). Now, the fourth-order Runge-Kutta method can be implemented without any difficulties. The third order equations equation (C.7) is first written as three first-order simultaneous equations

$$g' = p, \qquad p' = q, \qquad q' = -\tfrac{1}{2}\, g\, q \qquad \text{C.9}$$

The fourth-order Runge-Kutta method (Chow (1979)) is applied to get

$$\Delta_1 g_i = \Delta\eta\, p_i$$

$$\Delta_1 p_i = \Delta\eta\, q_i$$

$$\Delta_1 q_i = -\tfrac{1}{2}\,\Delta\eta\, g_i\, q_i$$

$$\Delta_2 g_i = \Delta\eta\,(p_i + \tfrac{1}{2}\,\Delta_1 p_i)$$

$$\Delta_2 p_i = \Delta\eta\,(q_i + \tfrac{1}{2}\,\Delta_1 q_i)$$

$$\Delta_2 q_i = -\tfrac{1}{2}\,\Delta\eta\,(g_i + \tfrac{1}{2}\,\Delta_1 g_i)\,(q_i + \tfrac{1}{2}\,\Delta_1 q_i)$$

$$\Delta_3 g_i = \Delta\eta\,(p_i + \tfrac{1}{2}\,\Delta_2 p_i)$$

$$\Delta_3 p_i = \Delta\eta\,(q_i + \tfrac{1}{2}\,\Delta_2 q_i)$$

$$\Delta_3 q_i = -\tfrac{1}{2}\,\Delta\eta\,(f_i + \tfrac{1}{2}\,\Delta_2 f_i)\,(q_i + \tfrac{1}{2}\,\Delta_2 q_i)$$

$$\Delta_4 g_i = \Delta\eta\,(p_i + \tfrac{1}{2}\,\Delta_3 p_i)$$

$$\Delta_4 p_i = \Delta\eta\,(q_i + \tfrac{1}{2}\,\Delta_3 q_i)$$

$$\Delta_4 q_i = -\tfrac{1}{2}\,\Delta\eta\,(g_i + \tfrac{1}{2}\,\Delta_3 g_i)\,(q_i + \tfrac{1}{2}\,\Delta_3 q_i) \qquad \text{C.10}$$

The values of g, p and q at point i+1 are computed from:

$$g_{i+1} = g_i + \tfrac{1}{6}(\Delta_1 g_i + 2\Delta_2 g_i + 2\Delta_3 g_i + \Delta_4 g_i)$$

$$p_{i+1} = p_i + \tfrac{1}{6}(\Delta_1 p_i + 2\Delta_2 p_i + 2\Delta_3 p_i + \Delta_4 p_i) \qquad \text{C.11}$$

$$q_{i+1} = q_i + \tfrac{1}{6}(\Delta_1 q_i + 2\Delta_2 q_i + 2\Delta_3 q_i + \Delta_4 q_i)$$

When the calculation with an arbitrary value of $g''(0)$ is completed, the value of k can be calculated from

$$k = \sqrt{g'(\infty)} \qquad \text{C.12}$$

The values of η, f, f' and f'' can be obtained by using the transformations (C.4, C.5 and C.6). Once the values of f, f' and f'' are known the value of h' can be computed from equation (C.2) using the finite-difference approach. The differentiated components, h'' and h''', are central differences with second-order accuracy in $\Delta\eta$. Substitution of the differentiated components into equation (C.2) and rearrangement gives the following tridiagonal system of equations:

$$(4 - \Delta\eta\, f_i)\, h'_{i-1} - (8 + 4\,\Delta\eta^2 f'_i)\, h'_i + (4 + \Delta\eta\, f_i)\, h'_{i+1} = -4\,\Delta\eta^2 \qquad \text{C.13}$$

Equation (C.13) is applied for $2 \le i \le IMAX-1$. For the equation formed at i=1 and i=IMAX the value of h'_i is obtained from the boundary condition (C.3).

The numerical result is shown in table C.1. The velocity profiles of this three-dimensional flow are:

$$\bar{u} = \bar{u}_e f'$$

$$\bar{v} = \bar{u}_e \left[af' - b\bar{x}h' + \bar{v}_{wall}(1-f') \right] \qquad \text{C.14}$$

$$\bar{w} = \tfrac{1}{2}\left(\frac{\bar{u}_e \upsilon}{\bar{x}} \right)^{\frac{1}{2}} [\eta f' - f]$$

where $\eta = \bar{z}\sqrt{\dfrac{\bar{u}_e}{\upsilon \bar{x}}}$

a, b and $\bar{v}_{wall}$ are constants (in this case a=-1.25, b=-1.0 and $\bar{v}_{wall}$=-0.2)

Table C.1 Numerical solutions of equations (C.1 and C.2).

η	f	f'	f''	h'
0.00	0.0000000	0.0000000	0.3320574	0.0000000
0.39	0.0256118	0.1303754	0.3315011	0.3208094
0.79	0.1023272	0.2599889	0.3276353	0.5700335
1.18	0.2295099	0.3869232	0.3173901	0.7534750
1.57	0.4055489	0.5081798	0.2984343	0.8798628
1.96	0.6275071	0.6200985	0.2698389	0.9598057
2.36	0.8909855	0.7190220	0.2326064	1.0045818
2.75	1.1902783	0.8020837	0.1897116	1.0249364
3.14	1.5188235	0.8678786	0.1454596	1.0301020
3.54	1.8698521	0.9167671	0.1043187	1.0272063
3.93	2.2370608	0.9506937	0.0697122	1.0211310
4.32	2.6151319	0.9726124	0.0432951	1.0147635
4.71	2.9999871	0.9857675	0.0249464	1.0094725
5.11	3.3887780	0.9930922	0.0133220	1.0056442
5.50	3.7796872	0.9968729	0.0065897	1.0031444
5.89	4.1716533	0.9986810	0.0030184	1.0016457
6.28	4.5641088	0.9994820	0.0012801	1.0008119
6.68	4.9567738	0.9998107	0.0005026	1.0003794
7.07	5.3495221	0.9999356	0.0001827	1.0001690
7.46	5.7423010	0.9999797	0.0000615	1.0000730
7.86	6.1350899	0.9999940	0.0000192	1.0000314
8.25	6.5278826	0.9999984	0.0000055	1.0000142
8.64	6.9206758	0.9999996	0.0000015	1.0000070
9.03	7.3134689	1.0000000	0.0000004	1.0000036
9.43	7.7062616	1.0000000	0.0000001	1.0000017
9.82	8.0990543	1.0000000	0.0000000	1.0000000

APPENDIX D
AN ALGORITHM FOR THE INTEGRATION OF UNEQUALLY SPACED DATA

In this appendix we will describe the methods for the numerical integration of unequally spaced data. These techniques are used to evaluate displacement thickness. The displacement thickness (δ^*) of the boundary-layer is calculated from equation (D.1). Many numerical integration methods (e.g. trapezoidal rule, Simpson's rule) are based on equally spaced data points. These methods are not applicable to evaluate δ^* because the assumption of equally spaced data points does not hold and we must deal with unequal-sized segments.

$$\delta^* = \int_0^\infty \left(1 - \frac{\rho u}{\rho_e u_e}\right) dz \qquad \text{D.1}$$

For simplification, the function $\left(1 - \frac{\rho u}{\rho_e u_e}\right)$ will be written as f(z) and the integration of the equation (D.1) can be replaced by a summation.

$$\delta^* = \sum_{k=0}^{N} f(z) dz_k \qquad \text{D.2}$$

For this case, one method is to apply the trapezoidal rule to each segment and sum the results:

$$\delta^* = \sum_{k=0}^{N-1} \frac{[f(z_{k+1}) + f(z_k)]h_k}{2} \qquad \text{D.3}$$

where $h_k = z_{k+1} - z_k$, is the width of segment k.

The truncation error of the integral of equation (D.3) may be substantial since we employ the integral under a straight-line segment to approximate the integral under a curve. One way to improve the accuracy is using cubic interpolation. The method is due to Gill and Miller (1972). Instead of integration the equation term-by-term, they used cubic interpolation to compute the integration over successive sub-intervals. We do not dwell on the details of this method here but will implement it to our problems.

The integral at the first interval is calculated by four-point forward difference formula. The integral can be represented as

$$\frac{1}{h_0}\int_{z_0}^{z_1} f(z)dz = f(z_0) + A_1 f[z_0z_1] + A_2 f[z_0z_1z_2] + A_3 f[z_0z_1z_2z_3] + A_4 f[z_0z_1z_2z_3z_4] \qquad \text{D.4}$$

where $A_1 = \frac{1}{2}h_0$

$A_2 = -\frac{1}{6}h_0^2$

$A_3 = (\frac{1}{4}+\frac{1}{6}e_1)h_0^3$

$A_4 = -\{\frac{19}{30} + \frac{2}{3}e_1 + \frac{1}{4}e_2 + \frac{1}{6}e_1(e_1+e_2)\}h_0^4$

$e_r = \left(\frac{h_r}{h_0}\right)-1$

$$f[z_rz_{r+1}\ldots z_{r+s}] = \frac{f[z_{r+1}z_{r+2}\ldots z_{r+s}]-f[z_rz_{r+1}\ldots z_{r+s-1}]}{z_{r+s}-z_r} \qquad \text{D.5}$$

For the end interval, the integral is obtained by using four-point backward difference formula which can be written as

$$\frac{1}{h_N}\int_{z_{N-1}}^{z_N} f(z)dz = f(z_N) + B_1 f[z_{N-1}z_N] + B_2 f[z_{N-2}z_{N-1}z_N] + B_3 f[z_{N-3}z_{N-2}z_{N-1}z_N] + B_4 f[z_{N-4}z_{N-3}z_{N-2}z_{N-1}z_N] \qquad \text{D.6}$$

where $B_1 = -\frac{1}{2} h_{N-1}$

$B_2 = -\frac{1}{6} h_{N-1}^2$

$B_3 = -(\frac{1}{4} + \frac{1}{6} e_{N-2}) h_{N-1}^3$

$B_4 = -\{\frac{19}{30} + \frac{2}{3} e_{N-2} + \frac{1}{4} e_{N-3} + \frac{1}{6} e_{N-2}(e_{N-2}+e_{N-3})\} h_{N-1}^4$

$$e_r = \left(\frac{h_r}{h_{N-1}}\right) - 1 \qquad \text{D.7}$$

The integral between these two end-intervals is calculated by a four-point finite-difference formula centred on the interval concerned. The equation for this integration over the range (z_0,z_1) is given in equation (D.8).

$$\frac{1}{h_0}\int_{z_0}^{z_1} f(z)dz = \frac{1}{2}[f(z_0) + f(z_1)] - \frac{1}{6} h_0^2 [\mu D_{\frac{1}{2}}^{\ 2} + \frac{1}{2} h_0 (e_{-1} - e_1) D_{\frac{1}{2}}^{\ 3}] \qquad \text{D.8}$$

where $\mu D_{\frac{1}{2}}^{\ 2} = \frac{1}{2}(D_0^2 + D_1^2)$

$D_0^2 = f[z_{-1}z_0z_1]$

$D_1^2 = f[z_0z_1z_2]$

$D_{\frac{1}{2}}^{\ 3} = f[z_{-1}z_0z_1z_2]$

$$e_r = \left(\frac{h_r}{h_0}\right) - 1 \qquad \text{D.9}$$

The equation (D.2) now can be evaluated by using the formula (D.8) to integrate between consecutive pairs of points from z_1 to z_{N-1}, the formula (D.4) to integrate the first interval (z_0,z_1) and the formula (D.6) to integrate the end interval (z_{N-1},z_N). Hence the total integration is obtained by summation over the range (z_0,z_N). It should be noted that the application of equations (D.4, D.6 and D.8) is valid when $N>3$. If $N\leq 3$, the equation (D.3) should be implemented.

APPENDIX E
NACA FOUR-DIGIT WING SECTION

The blade profile used in section 5.5 is described here. The blade is NACA four-digit of 9 per cent maximum thickness (t). The camber angle (θ) is -35°, the camber line is a circular arc. The chord-length (c) is 2.8 inches.

Let θ_1 and θ_2 be the angles between the tangent to the camber line and the chord line at inlet and outlet. The total camber $\theta_T = \theta_1 + \theta_2$. Since the blade is a circular arc camber line, we get $\theta_1 = \theta_2 = \theta_T/2$ and the maximum camber (a) occurs at the mid-chord (i.e. a = c/2). According to Cumpsty (1989), the maximum distance of the camber line from the chord line (b) can be calculated from equation E.1.

$$\frac{b}{c} = \frac{1}{4\tan\theta_T}\left\{-1+\sqrt{\left[1+(4\tan\theta_T)^2\left\{\frac{a}{c}-\left(\frac{a}{c}\right)^2-\frac{3}{16}\right\}\right]}\right\} \qquad \text{E.1}$$

Mean Lines:

The camber line (i.e. the mean line) is expressed analytically as two parabolic arcs tangent at the position of maximum camber. The equations defining the camber lines are taken to be (Abbott et al (1959))

$$y_c = \frac{m}{a^2}(2ax - x^2) \qquad \text{for } x \le a \qquad \text{E.2}$$

$$y_c = \frac{m}{(1-a)^2}\left[(1-2a)+2ax-x^2\right] \qquad \text{for } x > a \qquad \text{E.3}$$

where $m = \frac{b}{c}$, the maximum distance of the camber line from the chord line expressed as fraction of chord (E.1).

Thickness Distributions:

The thickness distribution for the NACA four-digit sections is giving by the following equation:

$$\pm y_t = \frac{t}{0.2}\left(0.2969\sqrt{x} - 0.126x - 0.3516x^2 + 0.2843x^3 - 0.1015x^4\right) \quad \text{E.4}$$

where t is the maximum thickness express as a fraction of the chord.

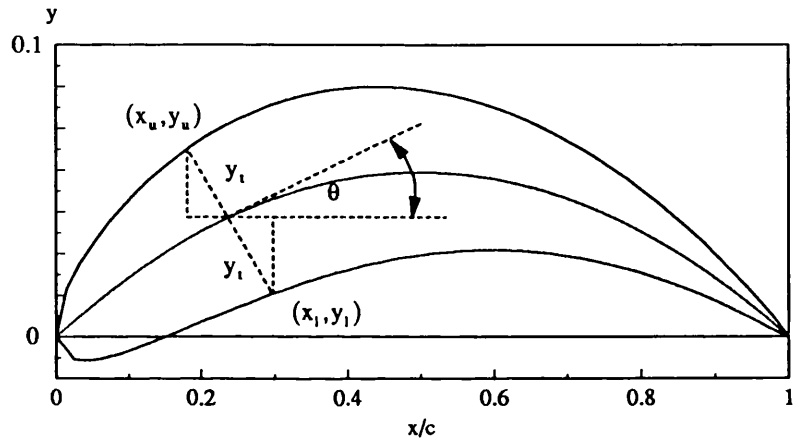

Fig. E.1 Method of combining mean lines and a thickness distribution (Abbott et al (1959))

The blade section now can be obtain by combining a mean line and a thickness distribution. The process is illustrated in Fig. E.1. From this figure we can define the co-ordinates of the upper-surface and lower-surface in the following relations:

For upper-surface co-ordinate:

$$x_u = x - y_t \sin\theta \quad \text{E.5}$$

$$y_u = y_c + y_t \cos\theta \quad \text{E.6}$$

For lower-surface co-ordinate:

$$x_l = x + y_t \sin\theta \qquad \text{E.7}$$

$$y_l = y_c - y_t \cos\theta \qquad \text{E.8}$$

where x_u, y_u are the abscissa and ordinate, respectively, of a typical point of the upper surface and x_l, y_l are the abscissa and ordinate, respectively, of a typical point of the lower surface.

The result of the calculation is shown in table E.1.

Table E.1 Calculation for the NACA Four-digit
Circular arc camber line
max. thickness % of chord = 9.00
camber angle (degree) = -35.00
max. camber is = -0.07882 at x/c = 0.50

x/c	y_t	y_c	θ(degree)	x_u	y_u	x_l	y_l
0.00	0.00000	0.00000	-17.500	0.00000	0.00000	0.00000	0.00000
0.10	0.03512	-0.02838	-14.157	0.10859	0.00568	0.09141	-0.06243
0.20	0.04303	-0.05045	-10.713	0.20800	-0.00817	0.19200	-0.09273
0.30	0.04501	-0.06621	-7.188	0.30563	-0.02155	0.29437	-0.11087
0.40	0.04352	-0.07567	-3.608	0.40274	-0.03224	0.39726	-0.11911
0.50	0.03971	-0.07882	0.000	0.50000	-0.03912	0.50000	-0.11853
0.60	0.03423	-0.07567	3.608	0.59785	-0.04151	0.60215	-0.10983
0.70	0.02748	-0.06621	7.188	0.69656	-0.03895	0.70344	-0.09348
0.80	0.01967	-0.05045	10.713	0.79634	-0.03112	0.80366	-0.06978
0.90	0.01086	-0.02838	14.157	0.89734	-0.01785	0.90266	-0.03891
1.00	0.00095	0.00000	17.500	1.00000	0.00000	1.00000	0.00000

APPENDIX F
DEFINITION OF BOUNDARY-LAYER THICKNESS

This appendix is presented the definition and physical meaning of the boundary-layer thickness or boundary-layer edge (δ). This description is taken from Kay and Nedderman (1990), and Schlichting (1979).

The boundary-layer edge (δ) is an ambiguous layer since it defines as the thickness across the boundary-layer when $u \rightarrow u_e$. Another interesting effect of the boundary-layer is displacement thickness (δ^*). As shown in Fig. F.1, displacement thickness (δ^*) represents the distance by which an equivalent uniform stream would have to be displaced from the surface to give the same total volume flow. Therefore, the displacement thickness (δ^*) can be defined in a precise way and we can say that

$$Q = \int_0^{\delta} u dz = u_e(\delta - \delta^*) \qquad \text{F.1}$$

$$\delta^* = \int_0^{\delta} \left(1 - \frac{u}{u_e}\right) dz \qquad \text{F.2}$$

where Q is the volume flow in the boundary layer.

Thus the ratio $\frac{\delta^*}{\delta}$ varies only with the non-dimensional velocity-profile shape $\frac{u}{u_e}$. For boundary-layer flow over flat plate, we can conclude that $\frac{\delta^*}{\delta} \approx \frac{1}{3}$. Therefore we can approximate the boundary layer edge from the displacement thickness. In general the boundary-layer edge (δ) may be written as

$$\delta = \omega\delta^* \qquad \text{F.3}$$

where ω is a safety factor (say ≈ 5).

δ^* can be approximated from flat plate boundary-layer.

A similar definition may be evaluated for the momentum-displacement thickness (δ^{**}). As indicated in Fig. F.2, if the momentum flow in the boundary layer is M, we can say that

$$M = \int_0^{\delta} \rho u^2 dz = \rho u_e^2 (\delta - \delta^{**}) \qquad \text{F.4}$$

$$\delta^{**} = \int_0^{\delta} \left(1 - \frac{u^2}{u_e^2}\right) dz \qquad \text{F.5}$$

We may relate the momentum displacement thickness (δ^{**}) and displacement thickness (δ^*) as another quantity Θ that is called momentum thickness as indicted in Fig. F.2. Therefore, we get

$$\Theta = \delta^{**} - \delta^* = \int_0^{\delta} \frac{u}{u_e}\left(1 - \frac{u}{u_e}\right) dz \qquad \text{F.6}$$

Physically, the momentum thickness (Θ) represents the thickness of the main-stream flow necessary to make up the deficiency in momentum flux within the boundary layer (or the loss of momentum in the boundary layer).

Both the displacement thickness (δ^*) and the momentum thickness (Θ) play an important role in the momentum equation for boundary layer.

The relation between the displacement thickness (δ^*) and the momentum thickness (Θ) may be defined in term of shape factor (H). This shape factor is the ratio of the thicknesses and is defined by

$$H = \frac{\delta^*}{\Theta} \qquad \text{F.7}$$

This shape factor is use as an approximated value for describing the velocity profiles especially in the integral method of solving the boundary layer equations. The application of this factor can be seen in the work of Truckenbrodt (appeared in Schlichting (1979)).

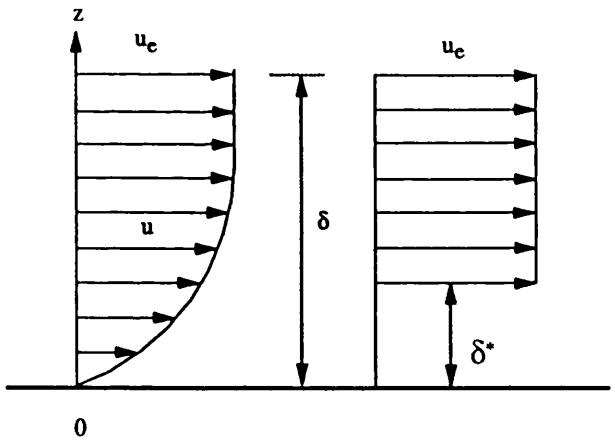

Fig. F.1 Displacement thickness (Kay and Nedderman (1990))

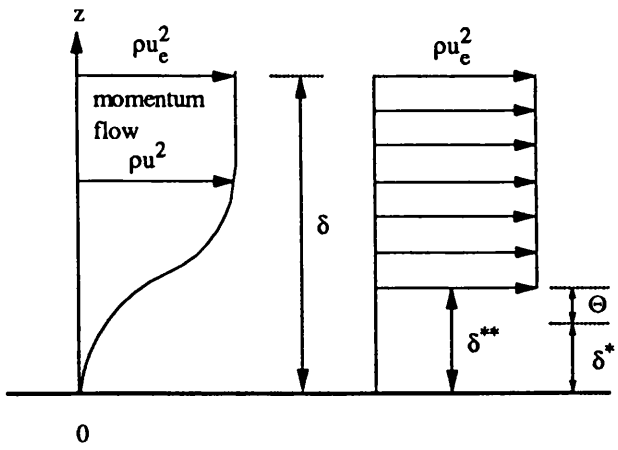

Fig. F.2 Momentum thickness (Kay and Nedderman (1990))

APPENDIX G
PERTURBATION VELOCITY POTENTIAL ON A SURFACE

In this appendix we will consider a fundamental concept of potential flow about a surface. This concept is used to calculate the velocity components in terms of the perturbation velocity potential that used in the interactive boundary layer approach.

Two-dimensional flow

If a source element of strength σ is placed along the x-axis (see Fig. G.1), the potential (Φ) due to such a point source element at (x_0, 0) is

$$\begin{aligned}\Phi &= \frac{\sigma}{2\pi}\ln r \\ &= \frac{\sigma}{2\pi}\ln\left\{(x-x_0)^2+z^2\right\}^{\frac{1}{2}} \\ &= \frac{\sigma}{4\pi}\ln\left\{(x-x_0)^2+z^2\right\}\end{aligned} \qquad \text{G.1}$$

The influence of this strength $\sigma(x)$ distribution at a point P(x,z) is an integral of the influences of all the point element:

$$\Phi(x,z) = \frac{1}{2\pi}\int_{x_1}^{x_2}\sigma(x_0)\ln\left\{(x-x_0)^2+z^2\right\}^{\frac{1}{2}}dx_0 \qquad \text{G.2}$$

The velocities u and w, along x-axis and z-axis, are obtained by differentiating $\Phi(x,z)$ with respect to x and z respectively (from the continuity equation: $\nabla^2\Phi = 0$):

$$u = \frac{\partial \Phi}{\partial x} = \frac{1}{2\pi} \int_{x_1}^{x_2} \sigma(x_0) \frac{(x - x_0)}{(x - x_0)^2 + z^2} dx_0 \qquad \text{G.3}$$

$$w = \frac{\partial \Phi}{\partial z} = \frac{1}{2\pi} \int_{x_1}^{x_2} \sigma(x_0) \frac{z}{(x - x_0)^2 + z^2} dx_0 \qquad \text{G.4}$$

The value of w as $z \to 0$ can be obtained by taking a limit to the equation (G.4) and we obtain (Katz and Plotkin (1991))

$$w(x,0\pm) = \lim_{z \to 0} w(x,z) = \pm \frac{\sigma(x,z)}{2} \qquad \text{G.5}$$

Therefore, the perturbation velocity in the x-axis is

$$u(x,0\pm) = \frac{1}{2\pi} \int_{x_1}^{x_2} \sigma(x_0) \frac{1}{(x - x_0)} dx_0 \qquad \text{G.7a}$$

$$= \frac{1}{\pi} \int_{x_1}^{x_2} w(x,0\pm) \frac{1}{(x - x_0)} dx_0 \qquad \text{G.7b}$$

Three-dimensional flow

In the similar manner to the above consideration, the potential (Φ) due to a point source element (σ) at (x_0, y_0, 0) is

$$\Phi = \frac{-\sigma}{4\pi r} \qquad \text{G.8}$$

where r is the distance from the point (x_0, y_0, 0) to (x, y, z)

The potential at an arbitrary point (x, y, z) can be obtained by integration the equation (G.8) over a surface (s). The velocity components u(x,y,z), v(x,y,z) and w(x,y,z) are presented in equations (G.10-12).

$$\Phi(x,y,z)=\frac{-1}{4\pi}\int_s\frac{\sigma(x_0,y_0)}{r}ds$$

$$=\frac{-1}{4\pi}\int_s\frac{\sigma(x_0,y_0)}{\sqrt{(x-x_0)^2+(y-y_0)^2+z^2}}dx_0dy_0 \qquad \text{G.9}$$

$$u(x,y,z)=\frac{\partial\Phi}{\partial x}=\frac{1}{4\pi}\int_s\sigma(x_0,y_0)\frac{(x-x_0)}{\left\{(x-x_0)^2+(y-y_0)^2+z^2\right\}^{\frac{1}{2}}}dx_0dy_0 \qquad \text{G.10}$$

$$v(x,y,z)=\frac{\partial\Phi}{\partial y}=\frac{1}{4\pi}\int_s\sigma(x_0,y_0)\frac{(y-y_0)}{\left\{(x-x_0)^2+(y-y_0)^2+z^2\right\}^{\frac{1}{2}}}dx_0dy_0 \qquad \text{G11}$$

$$w(x,y,z)=\frac{\partial\Phi}{\partial z}=\frac{1}{4\pi}\int_s\sigma(x_0,y_0)\frac{z}{\left\{(x-x_0)^2+(y-y_0)^2+z^2\right\}^{\frac{1}{2}}}dx_0dy_0 \qquad \text{G.12}$$

To find w(x,y,0), a limit process is required (see Katz and Plotkin (1991)) and the result is:

$$w(x,y,0\pm)=\lim_{z\to 0}w(x,y,z)=\pm\frac{\sigma(x,y)}{2} \qquad \text{G.13}$$

Therefore, the perturbation velocity in the x-axis and y-axis are

$$u(x,y,0)=\frac{1}{2\pi}\int_s w(x,y,0)\frac{(x-x_0)}{\left\{(x-x_0)^2+(y-y_0)^2+z^2\right\}^{\frac{1}{2}}}dx_0dy_0 \qquad \text{G.14}$$

$$v(x,y,0)=\frac{1}{2\pi}\int_s w(x,y,0)\frac{(y-y_0)}{\left\{(x-x_0)^2+(y-y_0)^2+z^2\right\}^{\frac{1}{2}}}dx_0dy_0 \qquad \text{G15}$$

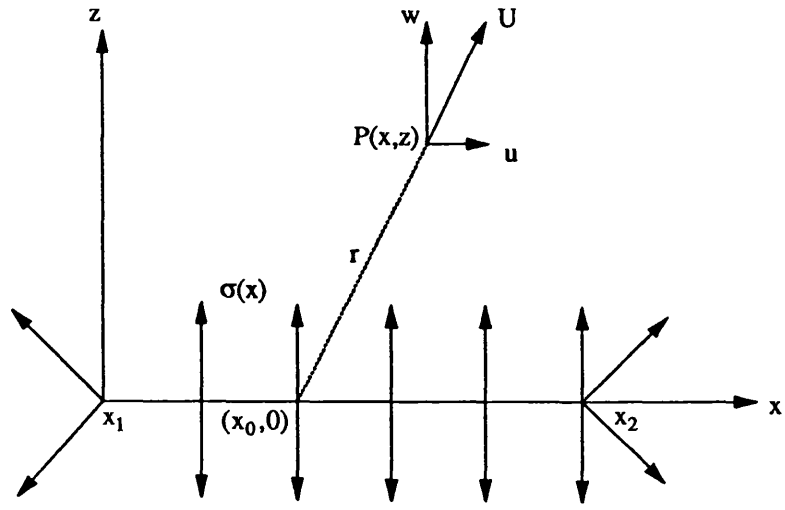

Fig. G.1 Source distribution along the x-axis

APPENDIX H
LOSS DUE TO VISCOSITY

In this appendix, we will discuss loss in the viscous fluid flow in terms of entropy generation. This viscous loss is presented in three-dimensional flow and may be used in estimating the entropy generation in a boundary layer that is presented in chapter 4.

BASIC PRINCIPLE

The first law of thermodynamics expresses the relationship among heat, internal energy and work. It may be written mathematically for a closed system as

$$dQ = dE + dW \qquad \text{H.1}$$

However, it will be appropriate to apply this law to a moving fluid and to obtain a general statement of the law as it applies to a three-dimensional flow system. For compressible flow this law applied to an open system. If the heat transfer dQ, the change in energy dE, and the work dW take place in time dt, we may write the equation as

$$\frac{dQ}{dt} = \frac{dE}{dt} + \frac{dW}{dt} \qquad \text{H.2}$$

Rate of heat transfer: $\frac{dQ}{dt}$

The heat transfer can take place by conduction, convection and radiation. To simplify the equation, we shall consider that heat enters or leaves the system only through conduction across a fluid control surface area ds. According to Fourier's Law, the quantity of heat transfer per unit time ($\frac{dQ}{dt}$) is given by

$$\frac{dQ}{dt} = -\int_s k\nabla T \cdot \mathbf{n} dS \qquad \text{H.3}$$

where k is the thermal conductivity, T is temperature and **n** the unit outward normal on the surface. The negative sign indicates that heat flux flows down a temperature gradient from a region of higher temperature to a region of lower temperature. Suppose the mass of our system contains in volume ϑ, from vector calculus we know that

$$\int_s k\nabla T \cdot \mathbf{n} dS = \int_\vartheta \nabla \cdot k\nabla T d\vartheta \qquad \text{H.4}$$

Rate of change of the internal energy: $\frac{dE}{dt}$

If we consider the movement of a small material volume $d\vartheta$, the rate of change of the internal energy $(\frac{dE}{dt})$ of the fluid contained within this material volume is

$$\frac{dE}{dt} = \int_s \rho \frac{De}{Dt} d\vartheta \qquad \text{H.5}$$

where e is the energy of the fluid expressed per unit mass of the system.

$\frac{De}{Dt}$ is a substantial derivative, $\frac{De}{Dt} = \frac{\partial e}{\partial t} + \mathbf{U} \cdot \nabla(e)$.

U is the fluid velocity.

Fluid power: $\frac{dw}{dt}$

In order to determine the work performed, we shall consider two types of the work term: the work done by the pressure forces $(\frac{dW_i}{dt})$ for the inviscid case and the work done by the viscous forces $(\frac{dW_v}{dt})$ for the viscous case.

Inviscid Work

In the absence of chemical, electrical, viscous, magnetic, or body forces, the work done by the system will be entirely against the surrounding pressure forces. It can be shown that

$$\frac{dW_i}{dt} = \int_S pU \cdot ndS \qquad \text{H.6}$$

where p is pressure of the systems

From the divergence theorem,

$$\int_S pU \cdot ndS = \int_\vartheta \nabla \cdot (pU) d\vartheta \qquad \text{H.7}$$

Viscous Work

The work performed due to viscous forces is evaluated over the boundary of the volume or element and it is analogous to the flow work associated with the normal and shearing stresses. If we consider a small material element of fluid (see Fig. H.1), we can define the work per unit time by the normal stress σ_x as

$$\frac{dW_{\sigma_x}}{dt} = -dydz\left\{-u\sigma_x + \left(u + \frac{\partial u}{\partial x}dx\right)\left(\sigma_x + \frac{\partial \sigma_x}{\partial x}dx\right)\right\} \qquad \text{H.8a}$$

$$= -d\vartheta \frac{\partial}{\partial x}(u\sigma_x) \qquad \text{H.8b}$$

The negative sign means work is added to the fluid from the outside. We can apply a similar method to the other surfaces involving the stresses. Therefore, the total work performed by the normal and shearing stresses per unit time is the

summation of all viscous work acting over the boundary surface. Thus we can say that

$$\frac{dW_v}{dt} = -\left[\frac{\partial}{\partial x}\left(u\sigma_x + v\tau_{xy} + w\tau_{xz}\right)\right]d\vartheta - \left[\frac{\partial}{\partial y}\left(u\tau_{yx} + v\sigma_y + w\tau_{yz}\right)\right]d\vartheta$$

$$-\left[\frac{\partial}{\partial z}\left(u\tau_{zx} + v\tau_{zy} + w\sigma_z\right)\right]d\vartheta \qquad \text{H.9}$$

where σ_x, σ_y, ..., τ_{zy} denote the normal and shearing stresses.

We can expand the equation (H.9) into two parts, noting that

$$\frac{dW_v}{dt} = -\mu\Psi d\vartheta - \mu\Phi d\vartheta \qquad \text{H.10}$$

where $$\mu\Psi = u\left(\frac{\partial\sigma'_x}{\partial x} + \frac{\partial\tau_{yx}}{\partial y} + \frac{\partial\tau_{zx}}{\partial z}\right) + v\left(\frac{\partial\tau_{xy}}{\partial x} + \frac{\partial\sigma'_y}{\partial y} + \frac{\partial\tau_{zy}}{\partial z}\right)$$

$$+ w\left(\frac{\partial\tau_{xz}}{\partial x} + \frac{\partial\tau_{yz}}{\partial y} + \frac{\partial\sigma'_z}{\partial z}\right) \qquad \text{H.11}$$

and $$\mu\Phi = \left(\sigma'_x\frac{\partial u}{\partial x} + \tau_{xy}\frac{\partial v}{\partial x} + \tau_{xz}\frac{\partial w}{\partial x}\right) + \left(\tau_{yx}\frac{\partial u}{\partial y} + \sigma'_y\frac{\partial v}{\partial y} + \tau_{yz}\frac{\partial w}{\partial y}\right)$$

$$+ \left(\tau_{zx}\frac{\partial u}{\partial z} + \tau_{zy}\frac{\partial v}{\partial z} + \sigma'_z\frac{\partial w}{\partial z}\right) \qquad \text{H.12}$$

Since $$\sigma'_x = 2\mu\frac{\partial u}{\partial x},\ \sigma'_y = 2\mu\frac{\partial v}{\partial y},\ \sigma'_z = 2\mu\frac{\partial w}{\partial z} \qquad \text{H.13}$$

$$\tau_{xy} = \mu\left(\frac{\partial u}{\partial y} + \frac{\partial v}{\partial x}\right),\ \tau_{yz} = \mu\left(\frac{\partial v}{\partial z} + \frac{\partial w}{\partial y}\right),\ \tau_{zx} = \mu\left(\frac{\partial w}{\partial y} + \frac{\partial v}{\partial z}\right) \qquad \text{H.14}$$

Thus, $$\Phi = 2\left[\left(\frac{\partial u}{\partial x}\right)^2 + \left(\frac{\partial v}{\partial y}\right)^2 + \left(\frac{\partial w}{\partial z}\right)^2\right] + \left(\frac{\partial v}{\partial x} + \frac{\partial u}{\partial y}\right)^2 + \left(\frac{\partial w}{\partial y} + \frac{\partial v}{\partial z}\right)^2$$

$$+\left(\frac{\partial u}{\partial z}+\frac{\partial w}{\partial x}\right)^2-\frac{2}{3}\left(\frac{\partial u}{\partial x}+\frac{\partial v}{\partial y}+\frac{\partial w}{\partial z}\right) \qquad \text{H.15}$$

The total work performed by the normal and shearing stresses per unit time can be written as

$$\frac{dW_v}{dt}=-\int_{\vartheta}[\mu\Psi+\mu\Phi]d\vartheta \qquad \text{H.16}$$

GOVERNING EQUATION

Substitution equations (H.3, H.4, H.5, H.6 and H.16) in the open system (H.2) we get

$$-\int_{\vartheta}\nabla\cdot k\nabla T d\vartheta=\int_{\vartheta}\rho\frac{De}{Dt}d\vartheta+\int_{\vartheta}\nabla\cdot(pU)d\vartheta-\int_{\vartheta}[\mu\Psi+\mu\Phi]d\vartheta \qquad \text{H.17}$$

Since this equation must be valid for any volume ϑ no matter how small,

$$-\nabla\cdot k\nabla T=\rho\frac{De}{Dt}+\nabla\cdot(pU)-\mu\Psi-\mu\Phi \qquad \text{H.18}$$

If we drop the change in the potential energy due to a displacement in the gravitational field, we can write the energy term as

$$\rho\frac{De}{Dt}=\rho\left\{\frac{De_t}{Dt}+\frac{1}{2}\frac{D}{Dt}\left(u^2+v^2+w^2\right)\right\} \qquad \text{H.19}$$

where e_t is the internal energy per unit mass.

Also, $\nabla\cdot(pU)=p(\nabla\cdot U)+U\cdot\nabla p$ H.20

and let $-\nabla\cdot k\nabla T=q$ H.21

We can write the above equation (H.18) as

$$q^{\cdot} = \rho\frac{De_t}{Dt} + \rho\frac{D\frac{1}{2}|U|^2}{Dt} + p(\nabla\cdot\mathbf{U}) + \mathbf{U}\cdot\nabla p - \mu\Psi - \mu\Phi \qquad \text{H.22}$$

We may write the equation of motion for a viscous fluid as

$$\rho\frac{Du}{Dt} = -\frac{\partial p}{\partial x} + \frac{\partial \sigma_x'}{\partial x} + \frac{\partial \tau_{xy}}{\partial y} + \frac{\partial \tau_{xz}}{\partial z} \qquad \text{H.23}$$

$$\rho\frac{Dv}{Dt} = -\frac{\partial p}{\partial y} + \frac{\partial \tau_{xy}}{\partial x} + \frac{\partial \sigma_y'}{\partial y} + \frac{\partial \tau_{yz}}{\partial z} \qquad \text{H.24}$$

$$\rho\frac{Dw}{Dt} = -\frac{\partial p}{\partial z} + \frac{\partial \tau_{xz}}{\partial x} + \frac{\partial \tau_{yz}}{\partial y} + \frac{\partial \sigma_z'}{\partial z} \qquad \text{H.25}$$

Multiplying these three equations by u, v and w, respectively, and adding we get,

$$\rho\frac{D\frac{1}{2}|U|^2}{Dt} = -\mathbf{U}\cdot\nabla p + \mu\Psi \qquad \text{H.26a}$$

or

$$\rho\frac{D\frac{1}{2}|U|^2}{Dt} + \mathbf{U}\cdot\nabla p - \mu\Psi = 0 \qquad \text{H.26b}$$

Using this relation, the energy equation (H.22) can be written as

$$q^{\cdot} = \rho\frac{De_t}{Dt} + p(\nabla\cdot\mathbf{U}) - \mu\Phi \qquad \text{H.27}$$

Since $e_t + p/\rho = h$ H.28

and $$p(\nabla \cdot U) = -\frac{Dp}{Dt} + \rho \frac{D}{Dt}\left(\frac{p}{\rho}\right) \qquad \text{H.29}$$

We have $$\rho \frac{Dh}{Dt} - \frac{Dp}{Dt} = q^{\cdot} + \mu\Phi \qquad \text{H.30}$$

With the aid of this equation and of $$T\frac{Ds}{Dt} = \frac{Dh}{Dt} - \frac{1}{\rho}\frac{Dp}{Dt} \qquad \text{H.31}$$

where h is enthalpy and s is entropy.

we can write the equation (H.30) in the form

$$\rho T \frac{Ds}{Dt} = q^{\cdot} + \mu\Phi \qquad \text{H.32}$$

Equation (H.32) represents the rate of entropy generation applied to a material element of fluid that is viscous and compressible flow.

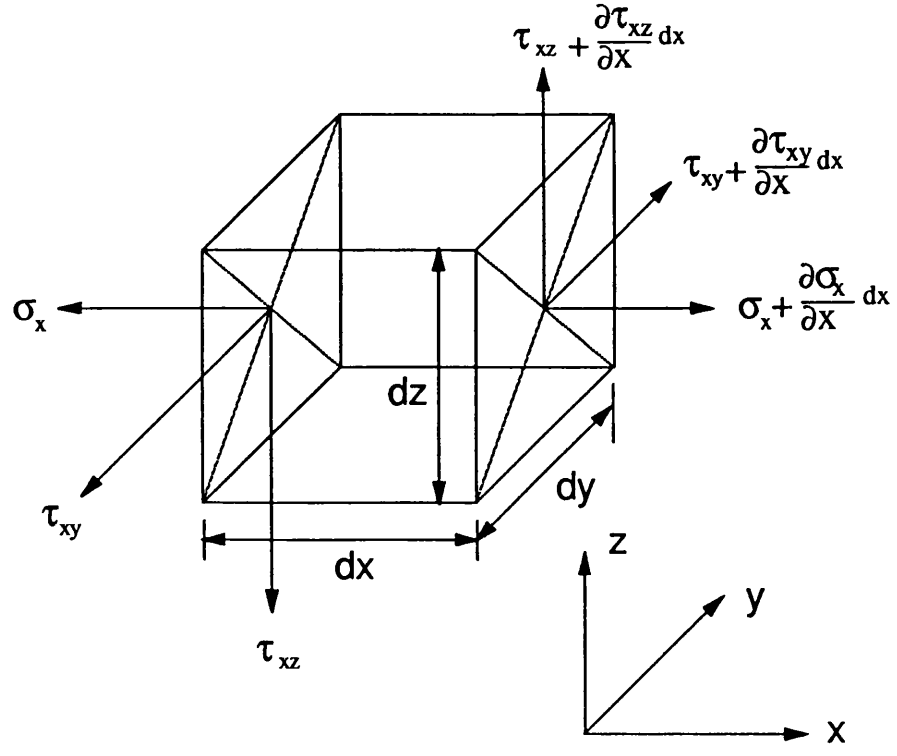

Fig.H.1 Stresses acting on a fluid element (show only on the dy dz surface)